Improving seasoned hardwood timber quality

with particular reference to collapse

by

Trevor Craig Innes
B.E. (Hons.)

Submitted in fulfilment of the requirements for the degree of
Doctor of Philosophy

in the Faculty of Engineering
UNIVERSITY OF TASMANIA

Australia

July 1996

I hereby declare that, except as stated herein, this thesis contains no material which has been accepted for the award of any other degree or diploma in any university and that, to the best of my knowledge and belief, this thesis contains no copy or paraphrase of material previously published or written by any other person, except where due reference is made in the text of the thesis.

T.C. Innes

This thesis may be made available for loan and limited copying in accordance with the Copyright Act 1968.

T.C. Innes

Abstract

This thesis principally concentrates on the prevention of degrade due to collapse during the controlled kiln drying of timber. Collapse is an abnormal shrinkage which occurs in wood during drying to fibre saturation point (FSP). Formation of internal checking is often associated with it. Collapse is particularly common in native Australian eucalypt timbers.

Specific work was also performed on the drying of karri (*Eucalyptus diversicolor* F.Muell) and brushbox (*Tristania conferta* R.Br.) as part of the commercialisation process of the Clever Kiln Controller® (CKC). The CKC is a personal computer based kiln control package which uses sensed acoustic emissions (AE) and on-line modelling of drying to optimise the seasoning process.

Collapse shrinkage occurs as a result of the physical flattening of water filled fibre cells due to the action of internal tension. The work on collapse presented in this thesis begins with stress-strain modelling of a single fibre under such conditions. This model predicted that collapse of fibres is precipitated at the inner fibre wall, and that fibre collapse is strongly dependant on temperature.

Following the predictions of the single fibre model and observations of drying trials, the concept of a "collapse threshold temperature" was introduced. If wood at moisture content (MC) above FSP is dried at temperatures above the collapse threshold temperature, then it will collapse. If it is dried at temperatures below the collapse threshold temperature, then it will not collapse. This concept was first tested on a $20m^3$ kiln load of *Eucalyptus regnans* F.Muell. The timber was successfully dried to 40% MC free of collapse.

An existing model of the timber seasoning process was modified to model wood as a heterogeneous material. This model showed that if the dry bulb temperature exceeded the collapse threshold temperature during drying to FSP (that is, if collapse shrinkage occurred), then checking was very difficult to avoid, even if the humidity of the modelled schedule was very high, and the drying thus very slow.

It is common practice in industry to increase the dry bulb temperature during drying to FSP. This does not always induce collapse. That is, the collapse threshold temperature varies during drying. Mathematical modelling predicted that the effect was not due to the lowering of water surface tension with increase in temperature, or

strain relaxation by creep or mechano-sorptive deformation. The most likely cause for the variation of collapse threshold temperature during drying was shown to be the effect of bulk stress in the board due to drying.

Drying trials controlled by the CKC were conducted on batches of karri and brushbox. The drying trials yielded information on the two species which allowed accurate modelling of their behaviour. The work on karri revealed a stress raiser effect from opened vessels lying along the surfaces of boards; modelling of the effect produced results consistent with those from drying trials and acoustic emission monitoring.

This study has established the link between collapse in Australian hardwoods and temperature. Mathematical models developed to quantify the effect predicted that collapse induced checking could best be avoided by using drying conditions which did not cause collapse shrinkage; collapse was shown to be very sensitive to drying temperature. Collapse checking was shown to be due to stresses resulting from localised collapse shrinkage. Optimisation of dry bulb temperature during drying has not yet been achieved by mathematical modelling. Suitable non-collapsing dry bulb temperature schedules can be determined by small-scale drying trials.

Acknowledgments

The author gratefully acknowledges the assistance and support of the following individuals and companies throughout the project:

Emeritus Professor Arch Oliver, supervisor, for his enthusiastic guidance, support and many discussions.

Associate Professor Peter Doe, supervisor, for his excellent advice and organisational assistance.

James Booker and Jason Woolley, fellow postgraduate students, for their helpful discussions and good company.

Helen Tonks for assistance with proof reading.

Australasian Furnishing Research and Development Institute Ltd. for financial assistance, and Michael Lee in particular for his valuable advice.

My family and friends for their encouragement and support. Special thanks to Kathy for helping me to maintain my perspective.

This project was undertaken with the assistance of an Australian Postgraduate Award.

Additional publications

The following papers were either published or in press at the time of submission of this thesis:

1. Innes, T.C. 1995. Stress model of a wood fibre in relation to collapse. Wood Sci. Tech. 29(5): 363-376.

2. Innes, T.C. 1995. Collapse free pre-drying of *Eucalyptus regnans* F.Muell. Holz als Roh- und Werkstoff 53(6): 403-406.

3. Innes, T.C. 1996. Collapse during seasoning of eucalypt timbers. Paper presented at 5th IUFRO International Wood Drying Conference, Quebec City, Canada August 13-17 1996.

4. Innes, T.C. 1996. Collapse and internal checking in the latewood of *Eucalyptus regnans* F.Muell. Wood Sci. Tech. 30(6): 373-383.

5. Innes, T.C. 1996. Pre-drying of collapse prone wood free of surface and internal checking. Holz als Roh- und Werkstoff 54(3): 195-199.

6. Innes, T.C. 1997. Vessels as surface stress raisers during drying of *Eucalyptus diversicolor* F.Muell. Wood Sci. Tech. *in press*.

7. Doe, P.E., Booker, J.D., Innes, T.C., and Oliver, A.R. 1996. Optimal lumber seasoning using acoustic emission sensing and real time strain modelling. Paper presented at 5th IUFRO International Wood Drying Conference, Quebec City, Canada August 13-17 1996.

Contents

Chapter 1. Introduction and literature review

The emphasis of the hardwood sawmilling industry in Australia is slowly shifting away from the traditional base of structural grade timber towards value added products. Sawn timber seasoned with very little or no degrade, suitable for furniture manufacture, is such a product. To this end, timber seasoning research at the University of Tasmania has been directed at the production of sawn native hardwood timber free of seasoning induced degrade. Prior to the work detailed in this thesis, the research here has focused on prevention of surface checking through the use of mathematical modelling of the seasoning process and, more recently, through on-line monitoring of acoustic emission (AE). These two processes were combined in the Clever Kiln Controller® (CKC), (Booker, 1994a; Doe et al, 1996), a personal computer based kiln control package.

This thesis covers two broad areas of research into the controlled kiln drying of eucalypt timber. The first area, and the one which makes up the bulk of the thesis, is research into the problem of collapse during drying of wood to fibre saturation point. The second area is specific work on the drying of two species of timber, karri (*E. diversicolor*) and brushbox (*Tristania conferta*). This work was performed as part of the development of the CKC. The controller has previously been tested on *E. regnans, E. delegatensis* R.T. Bak. and *E. obliqua* L'Herit. and is nearing commercial application.

The work presented here consists of mathematical modelling in conjunction with physical observation and measurement to gain further insight into the processes involved in seasoning. Several extensions to an existing timber drying simulation model (**KilnSched**, see Section 4.1) were developed, and have shed light on some problems in drying.

Work performed by the timber research group at the University of Tasmania over the last fifteen years has been summarised at the end of this chapter to provide a background to the work contained in this thesis.

1.1 The phenomenon of collapse

Collapse has been defined as an abnormal shrinkage of wood. It appears to have been first explained by Tiemann (1915). Collapse shrinkage occurs as a result of physical collapse of fibre cells within the wood. There is still debate in the literature about the actual mechanism and causes of collapse.

As wood dries, it undergoes a volumetric shrinkage. This shrinkage can be separated into two distinct components. The first component is normal shrinkage, which always occurs. The second is collapse shrinkage, which does not always occur.

Water within timber is generally accepted to exist in one of two states. Bound water is chemically bound to the wood cell wall material. Free water exists within the lumens of the wood cells, and is not so bound. The fibre saturation point (FSP) is defined as that moisture content at which all of the free water has been removed, but none of the bound water (Tiemann, 1906 as cited in Siau, 1984). Sharp changes in the behaviour of many wood properties are observed to occur at FSP. Although this model of the wood-water relationship is a simplification of the real situation, it is a useful concept for wood drying research.

Normal shrinkage occurs as a result of removal of moisture from the cell wall material of timber. Thus, normal shrinkage is associated with bound water removal, and will not take place in this simplified model until the moisture content of the timber has been reduced below FSP. In practice, a small amount of normal shrinkage does occur above FSP, because the levels of bonding of water to the cell wall material are complex, and it appears that bound water can be removed from some parts of the wood before all free water has been removed.

Collapse shrinkage occurs when the timber is at a moisture content above fibre saturation. It is a result of physical flattening of the cells. It is usually a very local phenomenon, normally occurring in one or more discrete earlywood bands, often for the whole length of the board. Collapse is often seen as a corrugation, or "washboarding" of the board surface.

1.2 Tiemann's liquid tension theory

It is widely accepted in the literature that the driving force behind collapse shrinkage is hydrostatic tension forces within the fibre lumens. This theory, proposed by Tiemann (1915), is based on the fact that wherever a curved meniscus is formed at a liquid-gas interface, the pressure in the liquid behind the meniscus will be reduced. Correspondingly, there will exist a three dimensional tension stress field at all points on the curved surface of the meniscus. This is the basis for the formation of a droplet of liquid in a gas. The basis for the application of this theory to the problem of collapse is that, as water evaporates out of the pits of fibres, a meniscus forms at the pit. If the radius of the pit (and thus of the meniscus) is sufficiently small, the water inside the cell lumen develops negative pressure. The magnitude of this pressure depends on the principal radii of the meniscus (and hence on the size of the pits).

A liquid held in a capillary behind a meniscus will be at a state of negative pressure P relative to the pressure of the gas with which it is in contact given by

$$P = \sigma\left(\frac{1}{r_1} + \frac{1}{r_2}\right) \tag{1.2.1}$$

where P = total liquid tension
σ = surface tension
r_1, r_2 = principal radii of meniscus

A correction is necessary for the vapour pressure over the curved meniscus

$$\ln\left(\frac{p_1}{p}\right) = -\frac{2\sigma M}{rDRT} \tag{1.2.2}$$

where:

p_1 = vapour pressure over the curved surface
p = vapour pressure over plane surface
M = molecular mass of liquid
D = density of liquid
R = gas constant
T = absolute temperature
σ = surface tension
r = radius of meniscus

This theory may explain collapse in timber which has open pits, but in Australian eucalypts, the pits are generally occluded. Cronshaw (1960) found that the pit openings in *E. regnans* were less than 64nm in diameter. Thus the movement of

water out of the cell lumens is dominated by molecular diffusion, hence the finding by Schaffner and Doe (1981) that water movement through Tasmanian Oak could be adequately described by Fick's law. There is no certainty that surface tension relationships which describe macro liquid-gas interfaces apply on a molecular scale.

1.3 Classical boiling theory

It is well known in the theory of boiling that a certain minimum size of vapour bubble can grow against surface tension forces. Surface tension forces as described above act in opposition to the internal pressure of a vapour bubble. That is, the pressure inside a vapour bubble must be sufficiently greater than the pressure outside the bubble to overcome the tension field at the interface. Since surface tension forces increase with decreasing bubble radius, there will exist a critical bubble radius at which the system will be metastable. If a vapour bubble forms at a smaller radius than this critical value, it will collapse, given a constant pressure differential across the liquid-vapour interface.

The critical bubble radius as predicted by classical thermodynamics is given by

$$r_k = \frac{2\sigma}{\Delta p} \tag{1.3.1}$$

where r_k = critical bubble radius
Δp = isothermal pressure difference to the saturation line
σ = surface tension

The activation energy necessary for formation of this bubble may be given by

$$A_k = \frac{16\pi\sigma^3}{3(p_k - p_i)} \tag{1.3.2}$$

from theory developed by Volmer (1939) as quoted by Gerum et al (1977).

where A_k = activation energy
p_k = pressure inside the bubble ($\cong$ saturation pressure at temperature T)
p_i = pressure of the liquid phase

The same source quotes a formula for the probability of this activation energy becoming available

$$J = Z_1 \exp\left(-\frac{\lambda}{kT}\right)\sqrt{\frac{6\sigma}{(3-b)\pi m}}\exp\left(-\frac{16\pi\sigma^3}{3kT(p_k - pi)^2}\right) \tag{1.3.3}$$

J = frequency of bubble formation

Z_l = number of molecules per unit volume

λ = latent heat of vaporisation per molecule

where k = Boltzmann' s constant

$b = (p_k - p_i) / p_k$

m = mass per molecule

Close inspection of equations 1.3.1 to 1.3.3 show that they are very sensitive to the variables input. In equation 1.3.3, the two exponential terms are very small, whilst Z_1 is very large (of the order of 10^{28}), so that the formulation is practically unworkable, although Kauman (1965) calculated some results based on this and some slightly more refined theory. The applicability of this theory to this problem is questionable as it was originally designed for pure liquids, and does not take into account surface effects. Many later researchers (eg. Gerum et al 1977) have investigated surface and nucleation effects, and this is still an area of active research among physicists.

If we assume that the pressure inside the bubble is equal to the vapour pressure of the water (that is, a saturated atmosphere), then we can get at room temperature from equation 1.3.1, values for critical bubble radius corresponding to particular values of water pressure. These values are shown in Table 1.3.1.

P_{water}	r_k (μm)
0.337 Pa	72.8
-17.7 kPa	7.28
-97.7 kPa	1.46
-1 MPa	0.146
-10 MPa	0.015

Table 1.3.1 Critical radius

Table 1.3.1 shows that, as the tension in water increases, so the critical bubble size decreases. A bubble less than the critical bubble size will collapse while one larger than the critical size will expand. If a capillary were of a smaller diameter than the critical bubble size, then the corresponding tension could be sustained indefinitely, irrespective of the presence of gases or bubble nucleation points.

1.4 Contraction theory

R.E. Booker (1994) postulated that contraction of fibres filled with water under tension causes differential stresses which lead to internal checking. Collapse of the cells would then follow the release of restraint caused by checking. This poses the

question - what is collapse? The single fibre stress model presented in Chapter 2 of this thesis predicts that round fibres collapse away from radial symmetry with a relatively small loss of free water, and a correspondingly very small contraction - around 0.4%, certainly not enough to cause checking. The near square tracheids in *Pinus radiata* studied by Booker may contract more, but buckling of the cell walls seems likely to occur at a similar order of magnitude of contraction to the round fibres. The tracheids would have to maintain their square shape during contraction to maintain the integrity of the wood. The buckling of square tracheids is a complex problem. Simplifying the structure by modelling it as a series of plates or beams seems unlikely to be successful because of the complex fixity conditions at the corners of the tracheids.

1.5 Shrinkage stress induced collapse

It has been postulated by some researchers (Clarke, 1927; Stamm and Loughborough, 1942) that collapse may be induced by compressive stresses resulting from drying of the wood. The liquid tension theory of collapse depends upon the negative pressure developed in the liquid filled lumen becoming sufficiently great to overcome the compressive strength of the cell wall. If this occurs, then the cell will collapse. Theories based solely on shrinkage stress induced collapse do not include any effect of negative pressure in the fibre lumens.

Keylwerth (1951) states that internal cracking may occur in the later stages of drying, when the core of the wood is subjected to tensile stresses due to tensile set at the board surfaces. However, he does not provide experimental evidence to support this claim.

Collapse can be brought about very early in the drying process by high temperatures. This would tend to discount the theory of stress induced collapse, as at a very early stage of drying, there has been no opportunity for compressive stresses due to normal shrinkage to build up to a significant level. Generally, only the very outer parts of the board are under tension in drying to FSP in the centre, since the outer parts are the only parts of the board to attain MC below FSP and hence undergo significant shrinkage. Thus, since a great deal more of the board is under compression than is under tension, the magnitude of the compression in the middle is very much less than

the magnitude of the tension at the surface. The effect of shrinkage stresses on collapse has been investigated in Section 5.4 of this thesis.

Kauman (1960, 1965a, 1965b) presented a comprehensive theory of collapse incorporating liquid tension and compressive stress induced components. According to his theory, collapse is produced when P from equation 1.2.1 is greater than the stress, Q which acts in the wood at the limit of plastic flow. Thus liquid tension collapse C_L is given by:

$$C_L = k_L\left(P - Q\right)\left(1 - \exp\left(\frac{-t}{\tau}\right)\right) \qquad (1.5.1)$$

k_L is a deformation coefficient

where t = time

τ = relaxation time of the collapse process

For compression stress collapse, Kauman replaces the factor (P-Q) by the compressive stress. The compressive stress he calculated as a linear function of the potential difference in shrinkage between case and core.

Kauman found that in *E. regnans* τ was of the order of 2 hours at 20°C and 0.5 hours at 53°C, so that the factor $(1-\exp(-t/\tau))$ could be taken as constant. He took the remaining factors as being linearly dependant on wood temperature so that total collapse C^i could be written as:

$$C^i = a_0 + b_0 n + \left[a_1 + b_1(1-n)\right]T_w + b_2(1-n)S_0^j \qquad (1.5.2)$$

T_w = wood temperature

S_0 = collapse free shrinkage

where a_k, b_k depend only on surface tension and wood properties

n depends mainly on end drying

i, j represent the structural directions of the wood

Kauman determined capillary radii from sorption isotherm and mercury porosimetry measurements. He approximated pure liquid tension collapse by drying 2.5cm cubes through exposed end grain. His calculations agreed closely with experimental results on total collapse at temperatures between 20°C and 100°C.

Banks and Barkas (1946) proposed a modified liquid tension theory. They based their theory on the fact that a hydrostatic tension acting on the walls of an elastic capillary

reduces the diameter of the capillary, and thus increases the hydrostatic tension (equation 1.2.1). For initial radii smaller than a critical value, the system is unstable, and the capillary will collapse. They showed that for capillaries of the size of wood fibres, the fibre wall elasticity would have a value around that for soft rubber. The applicability of this theory to the problem of fibre collapse thus seems doubtful.

1.6 Factors which affect collapse during drying

Gottstein and McCombe (1956) reported that 'both field and laboratory experiments have indicated that temperature is a factor of major importance, independent of other drying conditions'. Their experimental work consisted of pre-heating veneers of *E. delegatensis* and *E. obliqua* to temperatures between 21°C and 66°C and comparing the resultant shrinkage. They found that wood preheated to higher temperature invariably displayed more collapse than wood preheated to lower temperatures.

Vermaas and Bariska (1994) found that *Eucalyptus grandis* Hill ex Maid. collapsed approximately 2.5% when dried at 20°C, and 3.2% when dried at 30°C, whereas *Pinus silvestris* dried under the same conditions exhibited less than 0.5% collapse. Examination of scanning electron micrographs revealed no collapse in *P. silvestris* but substantial collapse in *E. grandis*.

Keylwerth (1951) recommends that "one should only increase the initial low drying temperature when the timber does not contain any more free water". For eucalypt timbers he suggests limiting the dry bulb temperature to a maximum of 40°C until the timber reaches FSP.

Kemp (1959) found that time to collapse for aspen (*Populus tremuloides* Michx.) increased slightly with increase in temperature or humidity. However, his experiments invariably induced collapse within the first three hours of drying. His experiments were carried out between 60°C and 77°C.

Booker (1994a) reported drying two eucalyptus samples from one board, one at 22°C, the other at 20°C. The sample dried at 22°C collapsed, whilst that dried at 20°C did not. Ellwood et al (1963a, 1963b, 1963c) found that chemical degradation caused by soaking wood in certain organic solvents increased collapse. Kauman (1961)

considered that increase in collapse with increase in temperature was due to hydrolysis of the fibre wall. His experiments were carried out between 38°C and 137°C. The hydrolysis process was monitored by measuring the pH of the wood. A significant drop in pH was found at the higher temperatures. This effect does not seem to explain the sensitivity of collapse to changes in temperature of approximately 2°C, particularly at lower temperatures.

Position within the tree, both radially and longitudinally, has been found to affect the amount of collapse shrinkage undergone by wood. Pankevicius (1961) found that collapse in *E. regnans* varied consistently within a tree, decreasing with increase in height. Chafe (1985, 1986b), Cuevas (1969), and Bisset and Ellwood (1951) found that the amount of collapse shrinkage increased with radial distance from the outside of the tree, reaching a peak at approximately 85% of the distance to the centre, and then decreased into the pith.

Collapse is generally located in discrete earlywood bands, so that the occurrence of collapse may coincide with the occurrence of a particular earlywood band rather than with any particular radial position. The location of this band appears likely to be determined by environmental (growth) conditions during its formation. Thus, in a stand of similar trees from the same area, it is expected that the earlywood bands corresponding to the same year of growth would have a similar propensity to collapse in all trees. This has in fact been observed by Amos (1954), who counted internal checks formed in living *Pinus radiata*. Lutz (1952) similarly observed internal checks in particular growth rings of living white spruce (*Picea glauca* Moench) in Alaska. Lutz concluded that the checks formed as a result of high internal tension in the tracheids when absorption of water was prevented by the freezing of the ground. Miller and Simpson (1992) found that collapse-associated internal checking in *Pinus radiata* was concentrated in the annual rings corresponding to the time just after second thinning. Presumably this corresponded to a time of accelerated growth, leading to lower density. Kemp (1959) reported that collapse in aspen started in the springwood.

Greenhill (1938) and Miller and Simpson (1992) reported high initial moisture content as important for development of collapse shrinkage, although actual initial moisture contents associated with collapse reported by Kauman (1965a) were quite different. It seems that collapse can occur as long as some fibre lumens remain saturated.

Since collapse is clearly related to fibre wall stiffness, and hence thickness, and density of the cell wall material varies within small limits (Stamm, 1929 as cited in Bisset and Ellwood, 1951) many researchers have looked for a relationship between collapse shrinkage and bulk density (Chafe, 1985, 1986a; Hillis, 1978). Collapse is found to decrease with increase in density. Normal shrinkage generally increases slightly with increase in density, as all of the fibre wall material shrinks, and there is more of it in denser material (Bisset and Ellwood 1951).

1.7 Cell wall structure

The wood cell walls are composed of three main structural constituents. These are, the framework, the matrix and encrusting materials. The framework consists of cellulose in the form of microfibrils. The matrix is composed of hemicelluloses and other carbohydrate materials. The encrusting materials are lignin and associated amorphous compounds.

The framework and matrix materials can be enzymatically removed to leave exposed the lignin skeleton. This reveals a microcapillary system within the cell wall. This is the area where bound water exists within the cell wall in the green state. Removal of this bound water allows the microfibrils around these microcapillaries to realign closer together. Thus, removal of bound water causes shrinkage of the cell wall material.

Development of the light microscope enabled the first detailed examination of the construction of the wood cell wall. According to Stamm (1964), the first observations of spiral lines on the cell walls were made by Valentin (1837). Eventually, these sub-fibre structures were separated and examined more closely. They were named *fibrils*.

1.7.1 Microfibrils

X-ray diffraction and polarisation microscopy revealed the crystalline nature of cellulose in wood. The strand-like nature of the cellulose chains called fibrils was proven by electron microscopy.

Elementary fibrils are assumed to be the smallest possible diameter cellulose strands. According to Kollmann and Côté (1984), Mühlethaler (1960, 1965) termed fibrils with diameter of approximately 35Å elementary fibrils. Such a fibril could consist of about forty cellulose chains.

Elementary fibrils are bundled together to make up microfibrils. These can be typically 100 to 300Å wide, according to Kollmann and Côté (1984). In turn, microfibrils aggregate to form macrofibrils. These then join together to form lamellae, which make up the cell wall layers.

Along the elementary fibrils there exist sections where the cellulose chains are so closely oriented that X-ray diffraction produces images just like those for pure crystals. These crystalline regions are termed *micelles*. Between these, where the cellulose chains of the elementary fibrils do not appear to be as closely aligned, are amorphous zones.

1.7.2 Wall structure

Between the individually identifiable cells in dicotyledonous angiosperms such as eucalypts, there is amorphous material known as the simple middle lamella. The cell wall itself consists of two distinct layers. The first of these is the primary wall. This is a very thin layer with a high proportion of lignin and hemicellulose, and as such acts as a chemical transition between the simple middle lamella and the secondary cell wall. The primary wall has approximately 20 to 25% cellulosic content in the form of loosely packed fibril wrappings (Stamm 1964). The inner microfibrils are oriented at approximately 90° to the cell axis, whilst the outer microfibrils are often disordered. The primary wall is formed in the cambium, and is the first part of the cell wall to form. The large lignin content causes the removal of most of the primary wall with the simple middle lamella when the wood is placed in a lignin dissolving solution.

Thus, the simple middle lamella and the primary wall are sometimes collectively known as the compound middle lamella.

The secondary wall usually consists of three distinct layers in normal wood. Reaction wood, wood which has formed to counterbalance a leaning tree, can have a fourth layer (Wardrop and Dadswell 1955). The three secondary cell wall layers in normal wood are labelled the S1, S2 and S3 layers, from the outermost layer in. The secondary wall forms inside, and after, the primary wall.

The S1 layer typically consists of 4 to 6 lamellae of microfibrils oriented at approximately 50° to 70° to the cell axis. The lamellae may be crossed, but there is usually a dominant direction, so that the S1 layer is essentially made up of microfibril helices in one direction. Like the primary wall, the S1 layer is thin.

The S2 layer is much thicker than the S1. It usually has between 30 and 150 lamellae (Wardrop 1964a). The predominant microfibril direction is approximately perpendicular to that of the S1, at 10° to 30° to the cell axis and the microfibrils in the central part of the S2 are highly oriented. There exist transition lamellae on the outer and inner surfaces of the S2. These transition lamellae vary in orientation from the S1 to the main S2, and from the main S2 to the S3, on the outside and inside of the S2 layer respectively.

The S3 layer usually has a similar thickness to that of the S1 layer. It has loosely arranged microfibrils crossed at approximately 20° to 30° to the fibre axis.

1.7.3 Pit structure

In the cell walls there are pits, openings between vessels or fibres. Usually in hardwoods they are blocked by a pit membrane of primary cell wall material. Hence in Tasmanian eucalypts, moisture transport is by molecular diffusion. Thus the pits are of little importance to moisture movement during seasoning of these timbers. However, they probably form a weak point in the structure of a fibre cell wall, so that collapse may well occur at lower tension in a fibre with large pits.

Bryan (1960) reported that collapse in Pacific madrone (*Arbutus menziesin* Pursh) was most intense in areas of heartwood which were dark red. It seems plausible that the dark red colour was the result of extractives which could occlude the pits, increasing the induced surface tension, leading to the increase in collapse.

1.8 Collapse related to wood microstructure

Collapse shrinkage is clearly related to the stiffness of the fibre walls subjected to the collapse inducing internal tension. This stiffness of the fibres is difficult to measure itself, but can be inferred from measurements on wood samples.

Bisset and Ellwood (1951) demonstrated that greatest collapse occurred within the earlywood in *E. delegatensis*. The diameter of the earlywood fibres was approximately 20 μm, and diameter of latewood fibres was approximately 12 μm. Wall thicknesses were approximately 3 μm and 5 μm respectively. Hasan (1994) measured earlywood fibre widths of approximately 15.0 μm, and wall thickness of approximately 2.3 μm for regrowth *Eucalyptus globulus* Labill., while the corresponding values for the latewood were 12.4 μm and 3.8 μm.

Another important parameter in determining fibre wall resistance to collapse is microfibril angle in the S1, S2 and S3 layers within the fibre secondary wall. Panshin and de Zeeuw (1980) report that the microfibrillar orientation in the S1 layer is close to 90° on the outside, with a transition to between 50° and 70° on the inside. The S2 layer microfibrils lie parallel between 10° and 30° from the longitudinal direction, while the S3 layer has 60° to 90° microfibrils. Layer thicknesses are 0.1 to 0.2 μm for the S1 and slightly less for the S3 with the bulk of the wall made up of the S2 layer.

The size of the pores in the fibre walls determine the tension induced in the fibre lumens according to liquid tension collapse theory (Tiemann 1915). Cronshaw (1960) reported that colloidal gold of 64 nm would not pass through the fibre pits of *E. regnans*. Indeed, Cronshaw says "..a direct flow of liquid through the pits, such as can occur through the pits of softwoods, is unlikely in view of the structure of their closing membranes." This is supported by Schaffner and Doe (1981) who found that Fick's law of diffusion adequately described the moisture transport through drying eucalypt wood. Bariska (1975) used mercury porosimetry to determine that the pores

in beechwood (*Fagus sylvatica* L.) were predominantly approximately 8 nm in diameter.

Hattori et al (1981) induced collapse in cells of *Shorea almon* Foxw. by immersing specimens in solutions of polyethylene glycol (PEG). The PEG induced osmotic pressure across the cell walls, which were assumed to act as semi-permeable membranes. The liquid tension in the cell was assumed to be equal to the osmotic pressure induced by the PEG. They found that the ray cell walls were impermeable to PEG of average molecular weight 20000, but permeable to PEG 8100 and PEG 2900. Palin and Petty (1981) quote 3000 as being the lower limiting molecular weight for cell wall impermeability. One would expect this figure to be highly species dependant, as pit size varies significantly from species to species.

1.9 Pre-treatments to reduce collapse

There are two different philosophies for reducing collapse by pre-treatment. The first is to increase the diffusivity of the wood by treatments which open up occluded pits, so that the liquid tension induced is lower. The second is to alter the liquid properties, usually to reduce the surface tension, or to provide nuclei for bubble formation.

Chafe (1993) found that pre-boiling *E. regnans* resulted in greater shrinkage before reconditioning in the heartwood, but less in the sapwood. Chafe (1990) reported that brief presteaming increased total volumetric shrinkage and collapse shrinkage after drying. Campbell (1960) reported that presteaming for less than six hours increased drying rate without increasing degrade, while presteaming for longer than six hours increased both recoverable and irrecoverable collapse.

Choong et al (1973) reported that collapse in *E. delegatensis* may be completely eliminated by freeze-drying. It appears that the liquid surface tension may be completely eliminated by sublimation of the water, thus avoiding collapse.

Ilic (1993) reported that pre-freezing to -20°C (as distinct from freeze-drying) of *E. regnans* significantly reduced collapse shrinkage, but not the number of internal checks. Wright (1967) found that pre-freezing decreased the amount of collapse, and that the lower the freezing temperature, the less collapse shrinkage resulted.

Bariska (1975) found that wood which had been soaked in anhydrous ammonia shrank much more after drying than wood which had not been soaked in ammonia. He reports that "In many respects, this excessive shrinkage resembles the collapse of wood". Interestingly, the surface tension of ammonia is approximately 0.02 at room temperature, about a third that of water (Weast, 1981). It appears likely that ammonia acts as a chemical plasticiser of the wood. Pankevicius (1960) reports unsuccessful attempts to induce bubble formation by impregnation with carbon dioxide gas at pressures of 25 MPa.

Ellwood et al (1963a, 1963b, 1963c) successfully prevented collapse and internal checking by replacing the water in wood with several organic solvents. They attributed this success to three effects; reduction of liquid tension by decrease in liquid surface tension, possible reduction of core compression stresses by modification of liquid (and hence shrinkage) gradients, and greater cell wall stiffness as a result of the swelling effect of the organic liquids. They also found that solvents which were significantly basic or acidic caused an increase of collapse by wood deterioration. Collapse in such wood was generally unrecoverable. They attributed some of the reduction in collapse to decreased adhesion between the solvents and the wood cell surfaces relative to that between water and the wood cell surfaces

1.10 Tension in water and cavitation

It has been known since the mid 1800's that liquids can be subjected to tension forces, that is, absolute pressures less than zero (Trevena, 1987). In this way, the liquid acts more like a solid (which can of course be stressed in tension) than a gas (which always exerts a positive pressure on the walls of its surroundings). A gas will always expand to fill a container, whereas a liquid will not due to the higher cohesive forces between the molecules. Liquid in tension is in a metastable phase. The liquid can be taken to a similar metastable phase by superheating. Superheating is the cause of "bumping", sudden violent boiling of a heated liquid.

Experiments on tension in static liquids began with Donny (1846) as cited in Trevena (1987). Donny used an inverted U-tube, sealed at one end, to generate negative pressure at the sealed end when filled with sulfuric acid. Donny also discovered that

the amount of tension the liquid could withstand was strongly dependent on the amount of air dissolved in the liquid.

The next important work on liquid tension was carried out by Berthelot (1950). His apparatus became known as the Berthelot tube. He took a sealed tube, mostly filled with liquid, but also containing an air cavity. The tube was heated, the liquid expanding more than the tube so that the air was forced into solution. The tube was then cooled, thus placing the liquid into tension. Eventually, the liquid column fractured, resulting in a sudden increase in volume of the Berthelot tube. This increase in volume was used to calculate the tension just before fracture.

Several other techniques have been used to measure the tensile strength of liquids (Trevena, 1987). These have all seemingly tested the adhesive strength of the liquid to the apparatus rather than the cohesive strength of the molecules to each other. The highest value for the tensile strength of water appears to be 27.7 MPa, measured by Briggs (1950) using a centrifugal method.

Water containing dissolved air and wood fibres was found to be capable of sustaining a tension in excess of 16 MPa (Dixon, 1909 as cited in Dorsey, 1968) using the Berthelot tube method. It seems likely that the dissolved wood fibres affected the surface of the Berthelot tube chemically, improving the adhesion.

Water fractures under tension at much lower stresses than those predicted by theory based on the cohesion of water molecules between each other. The reason for this weakening seems to be the existence of impurities in the water which provide nuclei for cavitation to occur. This is probably also the reason why the adhesive strength of liquids to experimental equipment is less than the cohesive strength of pure water.

Trevena (1987) reports that "there seems to be reasonable conclusive evidence that large negative pressures do exist in the sap columns of high trees". It appears that the transpiration of water through leaf stomata leads to the development of negative pressure there, thus sucking up the water from the bottom of the tree. This cohesion theory of sap ascent in trees is usually attributed to Dixon (1914). Alternative theories to explain sap ascent have been advanced by others (Amin, 1982; Plumb and Bridgman, 1972), but the cohesion theory is generally accepted as the most plausible model.

One way in which this tension is measured is now known as the Scholander pressure bomb, or balancing pressure technique (Scholander et al, 1965). A leaf is excised, and then enclosed in a pressure chamber. The cut petiole will have had water at high tension in it, so that when the petiole is severed and the water column fractured, the water will suddenly retreat up into the leaf. Positive pressure is then applied to the leaf, with the cut end of the petiole exposed. When the water re-appears at the cut surface, it is assumed that the tension previously existent in the petiole is equal to the opposite of the positive pressure applied to the leaf. Scholander et al (1965) report up to 8MPa tension in some plants using this technique.

Balling and Zimmermann (1990) measured xylem pressure directly with pressure probes. They measured lower values for the tension with the pressure probes than they did with the Scholander pressure bomb. The two measurement techniques disagreed even when they were used on the same plant.

Recently, Pockman et al (1995) and Holbrook et al (1995) increased water tension directly in plant tissue until the onset of cavitation. The two studies used similar techniques. They induced water tension in plant tissue by centrifugal means. Xylem conductance was measured before and after testing; a substantial drop in conductivity was assumed to correspond to cavitation. Holbrook et al (1995) induced pressures of less than -1.5MPa before cavitation occurred; these pressures were compared directly with simultaneous Scholander bomb measurements. The Scholander bomb technique was validated. Pockman et al (1995) measured pressures as low as -3.5MPa in *Juniperus monosperma* before cavitation occurred. These two studies, as well as validating balancing pressure technique measurements, showed that xylem pressure probe measurements probably provide inaccurate measures of water tension. It seems possible that the xylem pressure probe induces premature cavitation.

The largest tensions measured in water were found in the smallest compartments; approximately 35 MPa in fern sporangia of diameter 10-20 μm (Renner, 1915; Ursprung, 1915; both as cited in Zimmermann 1983). It seems possible, then, that the tension maintained in a liquid column is dependent on the capillary diameter. This implies that the internal tensions which could be sustained in fibres are greater than those measured in xylem.

One would expect that, if the water in the xylem of the tree were subject to tension, the tree trunk would be subject to diameter changes as the tension changed. This has been observed by Huber and Schmidt (1936, as cited in Zimmermann 1983). They

measured shrinkage of the trunk at two heights as transpiration began in the morning. The upper point shrunk first as it was subjected first to tension, before water uptake from the soil began.

When the tension in water within plants is increased, the water column will eventually fracture. This can be detected acoustically. This appears to have been first performed by Milburn and Johnson (1966), using normal acoustic microphones, amplification, and band-pass filtering. The technique was further refined (Milburn, 1973a, 1973b), and used to monitor cavitation in whole plants. It was acknowledged that there are other potential sources within the plant material for such acoustic emissions, but there was significant circumstantial evidence pointing to cavitation being the most energetic noise source in the live plant. West and Gaff (1976) used apparatus similar to that of Milburn to detect cavitation in excised leaves.

Tyree and Dixon (1983) monitored ultrasonic acoustic emissions from *Thuja occidentalis* L. in the frequency range of 0.1 to 1 MHz. Circumstantial evidence again pointed to cavitation as the cause of this AE.

1.11 Detection of collapse prone wood

Numerous attempts have been made to find ways of identifying collapse prone wood before it is seasoned. If this were possible, then drying schedules could be modified to avoid collapsing sensitive wood, or overly collapse prone wood could be discarded from the drying charge.

Ilic and Hillis (1986) dried small "predictor samples" at 100°C and measured the resultant changes in shape and area with an image processor. They expressed these measurements as a collapse factor (CF) and as volumetric shrinkage (VS), where:

$$CF = \frac{(\text{perimeter of cross section of board including internal checks})^2}{\text{cross-sectional area of board}} \qquad (1.11.1)$$

and $$VS = 1 - \frac{D}{G}; \qquad (1.11.2)$$

where D = area of dry cross section (not including area of internal checks)

G = area of green cross-section

They found highly significant linear correlations between collapse in kiln dried boards and the CF and VS measurements of predictor samples. They did not specify the temperatures at which the kiln dried boards were seasoned.

Ilic and Chafe (1986) found that collapse was significantly related to depth of penetration of electrodes of a Shigometer (Shigo and Shigo, 1974). In this case, the Shigometer was being used initially like a Pilodyn which provides a direct indication of basic density (Cowen, 1978 as cited in Ilic and Chafe, 1986), and then the resistance to a pulsed electrical current tested. Collapse was not significantly related to pulse resistance.

1.12 Collapse recovery by reconditioning

Collapse shrinkage can often be largely recovered by reconditioning. Reconditioning is the process of subjecting timber to live steam after it has been dried to a moisture content less than FSP. In 1917 an Australian, James Grant, noticed that accidental soaking of bluegum in boiling water removed most of the collapse shrinkage from the wood (Kauman, 1965a). His son, George Grant, a timber seasoning kiln operator, applied this by subjecting kiln charges to an application of steam after drying. This process is now known as reconditioning, and is widely used throughout Australia for the recovery of collapse in eucalypt timbers.

1.12.1 MC for reconditioning

There is some debate about the best moisture content at which to recondition. A CSIRO seasoning correspondence course (Campbell, date unknown) recommended an average MC of 18% to 20% for reconditioning. The same document suggests that drying to MC below 12% before steaming may result in incomplete recovery. It also reported that some *E. delegatensis* from Tasmania was found to require an average MC of 11% to 12%, with a core MC below 16% for successful reconditioning. Lee (1993) performed experiments on Tasmanian *E. regnans* in a commercial seasoning environment, and found that reconditioning at average MC less than 15.5% was

ineffective. Greenhill (1938) recommended a MC of 15% for the commencement of reconditioning for *E. delegatensis*. Bryan (1960) found that collapse recovery in Pacific madrone was most satisfactory at lower MC of around 8% to 12%.

Clearly, the timber MC must be below FSP before reconditioning can occur, as otherwise there may still be fibre lumens full of water, which will then collapse on final drying. It seems likely that the optimum MC at which to recondition will vary between species, and quite likely between or even within trees. The fact that there is a minimum average MC below which reconditioning is ineffective is a clear indication that the mechanism for recovery by reconditioning depends upon moisture as well as heat.

1.12.2 Usefulness of reconditioning

Successful reconditioning reverses most collapse shrinkage: it returns the board to the dimensions it would have had if the collapse had not occurred. That is, the reconditioned board will only be subject to normal shrinkage. If performed correctly it can also relieve residual stresses from the drying process. However, there is currently insufficient understanding of the high temperature behaviour of wood to allow this process to be repeatably performed successfully.

It is often found that collapse will have associated with it internal checking, due to differential shrinkages imposed by the collapse. If this is the case, then the process of reconditioning, although it returns the board to the required external dimensions, cannot repair the effects of internal checking. If the board is machined sufficiently to expose these internal checks, then it will be of no use for high grade applications.

1.12.3 Introduction and removal of steam

The mechanism by which steam replaces air at the beginning of a reconditioning (or a presteaming) treatment is poorly understood. Modelling has shown that this is important, because if the steam is introduced in the wrong manner, surface checking

may be rapidly induced. For instance, if the steam were introduced at the top of the reconditioning chamber and the air was to escape from the bottom, then the less dense steam would sit at the top of the chamber, heating the drier air below it. Thus, the cold timber near the bottom of the chamber would be exposed to warm dry air instead of steam.

Development of the boundary layers of steam which replace the air across the surface of a wide board could also cause checking, if the heat transfer through the board is sufficiently rapid for the timber to become sufficiently hot to dry quickly to the low humidity air before it is replaced by steam.

Thus steam must be introduced rapidly from the bottom of the kiln, and the stack left in the reconditioning chamber to cool to ambient temperature after reconditioning has been completed.

1.12.4 Mechanism of collapse recovery

The generally accepted mechanism of collapse recovery is that there are two different portions of the cell wall, one of which remains elastic under all normal conditions, whereas the other becomes plastic with elevated temperatures. When the cell collapses, it reaches a stable (ie. low) energy state with the plastic component in a collapsed condition. Reconditioning increases the temperature of the wood sufficiently to cause softening of the plastic component so that the elastic component can spring back to its lowest energy level, which corresponds to the cell being in its normal state.

The elastic and inelastic layers have not as yet been clearly identified. Kauman (1965) suggests that the elastic layer may be the S3 (innermost) layer of the secondary wall, and that the inelastic layer may be in the matrix and encrusting components of the primary wall. However, Wardrop and Dadswell (1955) suggest that lignin increases cell wall elasticity. Ilic (1990) hypothesised that the elastic component consists of the S1 and S3 layers, with essentially circumferential fibril wrappings providing stiffness against collapse, and that the inelastic component is the S2 layer, its longitudinal wrappings not providing much stiffness against collapse, but its greater thickness accounting for the cell not returning to its original shape of its own

accord. This model provides the mechanism for formation of irrecoverable collapse, as, if the S2 layer breaks away from the S1 or S3 layers, the remaining layer may not be sufficiently strong to return the cell to its original configuration upon softening of the S2 layer.

Wardrop and Dadswell (1955) report that tension wood often has no S3 layer. Collapsed tension wood can not usually be recovered by reconditioning, so it seems likely that the S3 layer is a necessary part of the recovery process.

1.13 Work by the timber research group at the University of Tasmania

Research on timber seasoning at the University of Tasmania began with a masters thesis by Schaffner (1981). The aim of his work was to develop an economically viable means of seasoning backsawn Tasmanian eucalypts with minimum degrade and in the minimum time.

Schaffner (1981) developed a one-dimensional stress and drying model of timber. His drying model used Fick's law of diffusion to study the drying process. Diffusion coefficients were either measured directly in diffusion cells, or inferred from comparison of measured and calculated drying curves. Shrinkage was measured directly on thin slices of wood. He modelled the development of drying stresses in wood using theory of elasticity in anisotropic bodies; Airy stress functions were used to solve for stresses. Only purely backsawn or purely quartersawn boards far from the centre of the tree were modelled; this restriction applies to all of the drying models developed thus far by this group. Some elastic properties of Tasmanian eucalypts were measured for use in his model. Wood was assumed to be linearly elastic, and free from hysteresis, creep, and mechano-sorptive effects.

Schaffner (1981) used his model to assess the effectiveness of semi-permeable coatings on the wood surface in reducing drying stresses. Tests on timber coated with animal glue (collagen) showed significantly decreased occurrence of surface checking from seasoning.

In 1986 the Pascal program DRYWOOD (Oliver et al 1986) was released. This was a development of Schaffner's modelling, and was the first of the Tasmanian timber seasoning simulation programs to include non-linearities. This program simulates only fixed schedules. DRYWOOD was intended as a training tool for industry.

Wu (1989) performed detailed measurements of the air flow through a timber stack. He monitored the boundary layer development across the board surface. He then used the Reynolds analogy to model heat and mass transfer through the boundary layer. He used a Fickian diffusion model for moisture movement within the wood, with a diffusion coefficient dependent on temperature, but not on moisture content, and with moisture concentration as the driving force for moisture movement. Heat transfer was modelled by consideration of the convective heat transfer over the board surface, and the conductive heat transfer within the board. The model's predictions of moisture content distribution were validated by measuring moisture contents of slices from sections of boards during drying trials. Wu (1989) also performed some introductory work on the mechano-sorptive effect.

Following the work of Schaffner (1981), Oliver et al (1986) and Wu (1989), the stress and drying model **KilnSched** (Oliver, 1991; Doe et al, 1994; Booker 1994b) was developed. **KilnSched** accepts variable schedules, and includes creep and mechano-sorptive effect, as well as using non-linear stress-strain relationships. A more complete summary of **KilnSched** is presented in Section 4.1. **KilnSched** provides the basis for all of the drying modelling performed within this thesis. It has been extensively tested over many hours of drying trials, and shown to consistently predict the moisture content distribution and time to surface check formation of eucalypt boards with an accuracy of approximately 15%.

Innes (1992) measured the stress-strain properties of Tasmanian eucalypts in the tangential direction at various temperatures and moisture contents. The results supported the formulations used in **KilnSched**, agreeing within approximately 15%.

Parsons (1989) completed preliminary investigations into the possibility of using acoustic emissions (AE) from drying timber as feedback for kiln control. Booker (1990) furthered these investigations as an honours program and later (Booker, 1994a) as a PhD project. His investigations revealed a close correlation between peak AE rate and surface instantaneous strain predicted by **KilnSched**, two completely different measures of tendency to failure (Booker, 1994b). Further work revealed that cumulative AE counts were representative of unrecoverable strain energy at the board

surface, but were not a useful measure of the propensity for surface checking (Booker, 1995).

The advances in utilisation of AE and drying modelling were combined in the Clever Kiln Controller® (CKC), (Booker, 1994a; Doe et al, 1996). This is a personal computer based kiln control package, and was largely developed by Booker in conjunction with a professional computer programmer. It is designed for control of medium-sized batch kilns and laboratory or experimental kilns. The CKC uses sensed acoustic emission in conjunction with on line predictive mathematical modelling using **KilnSched** to optimise the process of drying wood to FSP free of surface checking. One of the aims of the work contained in this thesis was to determine how to avoid degrade due to collapse, a problem which had not yet been tackled in the development of the CKC.

Chapter 6 provides a more detailed description of the CKC. The final chapter details work performed as part of the commercialisation of the CKC. It covers work on the drying of Western Australian karri. Similar work on the drying of brushbox from New South Wales is covered in Appendix B.

Chapter 2. Stress-strain modelling of a fibre cell subjected to internal tension

Collapse shrinkage occurs at moisture contents above the fibre saturation point (FSP). Drying causes tension in the water within the fibre lumens (Kauman, 1965). A physical flattening of fibres induced by this internal tension causes collapse shrinkage. A problem in the study of collapse has been the lack of information in the literature as to the conditions which accompany the onset of collapse. As a guide to what to look for in experimental work, a stress model of a fibre has been written to predict the onset of collapse. This model computes the stress and strain distributions within the fibre wall as a function of temperature, moisture content, and fibre wall strength properties and size in the early stages of drying. The fibre cell has been modelled as a thick walled cylinder, as eucalypt fibres are typically approximately round with a ratio of outside diameter to wall thickness of the order of 5:1. The length to diameter ratio of fibre cells is typically of the order of 50:1, so that longitudinal effects are negligible, and hence are not considered in the model. It is assumed that plane transverse sections remain plane (Navier hypothesis). Thus the problem is essentially one-dimensional.

This chapter outlines the development of the model, and presents some results from the model in its final form. There is a preliminary section on water removal from the fibre lumens; water is treated as an elastic fluid. The model development begins with simple thick cylinder theory, extends to three isotropic layers, then treats the layers as linear orthotropic, then finally models each layer with different non-linear orthotropic properties. The model's results were compared at each stage of development with the results from the previous version.

2.1 Water removal from a fibre lumen

Consider the process of removal of a small amount of water from an initially saturated fibre lumen:

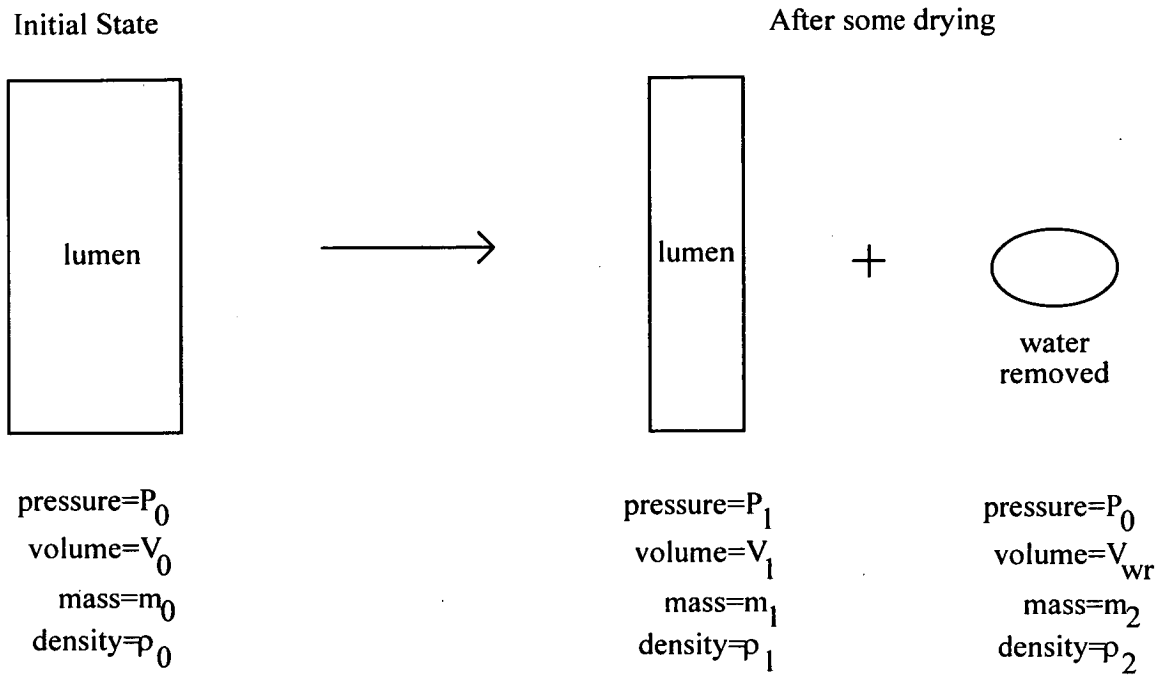

Figure 2.1.1 Water loss from a fibre lumen

Fig. 2.1.1 represents the fibre lumen decreasing in volume as water is removed. V_{wr} is the volume of water removed from the fibre by drying. It is expressed at the starting pressure of P_0 for convenience. Note that the fibre lumen is completely filled with water both before and after the drying shown.

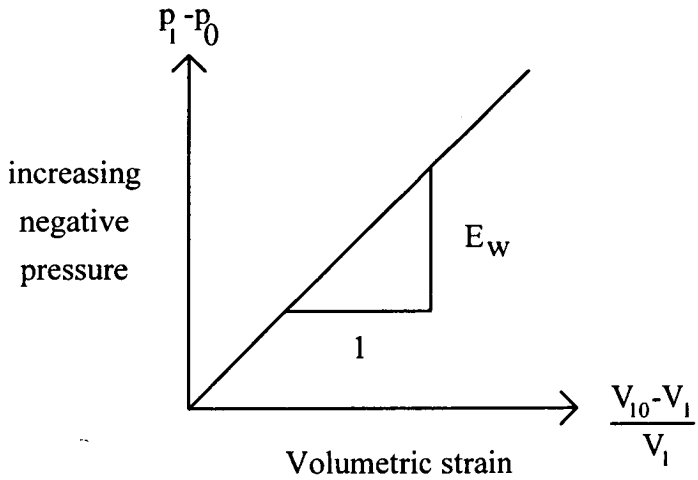

Figure 2.1.2 Elastic modulus of water

Fig. 2.1.2 shows a graphical definition of elastic modulus of water in tension. Axes are non-dimensional. The volume of water in the fibre lumen after some drying, V_1, is at a lower absolute pressure, P_1, than that at the start of drying. This volume of water would occupy a volume V_{10} at the initial

pressure P_0, where V_{10} is given by:

$$V_{10} = V_1 - \frac{P_0 - P_1}{E_w} V_1 \tag{2.1.1}$$

where E_W is the elastic modulus of water. Equation 2.1.1 follows directly from the definition of E_W shown in Fig. 2.1.2.

To conserve mass, we have:

$$m_0 = m_1 + m_2 \tag{2.1.2}$$

Since density is constant for constant pressure and temperature, we have that

$$\rho_2 = \rho_0 \tag{2.1.3}$$

Substituting 2.1.3 into 2.1.2 and using ρ=m/V we get:

$$\rho_0 V_0 = \rho_1 V_1 + \rho_0 V_{wr} \tag{2.1.4}$$

Using (2.1.1) we get:

$$\rho_0 V_0 = \rho_0 V_{10} + \rho_0 V_{wr} \tag{2.1.5}$$

and hence:

$$V_0 = V_{10} + V_{wr} \tag{2.1.6}$$

and thus, substituting for V_{10} from 2.1.6 into 2.1.1, we get:

$$V_{wr} = V_0 - V_1\left(1 - \frac{P_0 - P_1}{E_w}\right) \tag{2.1.7}$$

The variation with temperature of the elastic modulus of water was taken from Appendix 2 in Vennard & Street (1982). Intermediate values were found by linear interpolation. These data were for water at atmospheric pressure. No values for elastic modulus could be found for water under tension although Dorsey (1968) states that "There is no discontinuity in the value of the compressibility as P changes from positive (=pressure) to negative (=tension)." The water is thus assumed to have the same elastic properties in tension and compression for the range of pressures of interest.

The new lumen radius was calculated from the tangential strain on the inside surface, and thus V_1 was calculated. Hence, from the user specified internal tension the volume of water removed per unit length of fibre was calculated.

2.2 Elastic isotropic analysis

This discussion gives an outline of elastic analysis of an isotropic thick cylinder (Lamé problem) filled with water (an elastic fluid). This analysis can be found in many text books on elasticity, but is included here to provide a background to the following models, and because it has proved beneficial to look at simple models first.

The process has been thought of as follows. As the cell dries out, water moves by diffusion out of the cell. This removal of water induces a negative pressure in the cell lumen. The result of this negative pressure is that the water expands, and the cylinder contracts until they are at equilibrium. During wood drying, this equilibrium will be a dynamic one as water is being continually removed, but is very slow so that the problem is treated as static.

Consider a section of a thick walled cylinder, taken perpendicular to the cylinder's axis. The cylinder has inner radius r_1, outer radius r_2, internal pressure p_1, external pressure p_2. An element at radius r is subject to radial displacement u.

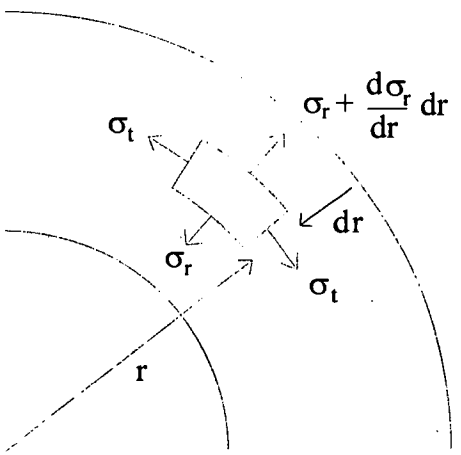

Figure 2.2.1 Element in static equilibrium

The components of strain are defined by

$$\varepsilon_r = \frac{du}{dr} \text{ and } \varepsilon_t = \frac{u}{r} \quad . \tag{2.2.1}$$

Generalised Hooke's law for a body is given by

$$\varepsilon_r = \frac{1}{E}(\sigma_r - \mu\sigma_t - \mu\sigma_z)$$
$$\varepsilon_t = \frac{1}{E}(\sigma_t - \mu\sigma_r - \mu\sigma_z) \qquad (2.2.2)$$
$$\varepsilon_z = \frac{1}{E}(\sigma_z - \mu\sigma_r - \mu\sigma_t)$$

The plane strain approximation ($\varepsilon_z = 0$) reduces the third of equations 2.2.2 to

$$\sigma_z = \mu(\sigma_r + \sigma_t) \qquad (2.2.3)$$

Substituting 2.2.1 into the first two equations of 2.2.2 and solving for σ_r and σ_t gives

$$\sigma_r = \frac{E}{(1+\mu)(1-2\mu)}[(1-\mu)\varepsilon_r + \mu\varepsilon_t]$$
$$\sigma_t = \frac{E}{(1+\mu)(1-2\mu)}[\mu\varepsilon_r + (1-\mu)\varepsilon_t] \qquad (2.2.4)$$

Using the plane strain assumption, the equation for static (planar) equilibrium of an element of a thick walled cylinder as shown in Fig. 2.2.1 above is

$$\sigma_t - \sigma_r - r\frac{d\sigma_r}{dr} = 0 \text{ or}$$
$$\frac{d\sigma_r}{dr} + \frac{\sigma_r - \sigma_t}{r} = 0 \qquad (2.2.5)$$

Substituting 2.2.4 into 2.2.5 yields

$$\frac{d^2u}{dr^2} + \frac{1}{r}\frac{du}{dr} - \frac{u}{r^2} = 0 \qquad (2.2.6)$$

Thus the solution

$$u = A_1 r + \frac{A_2}{r} \qquad (2.2.7)$$

gives the radial deflection of a point at radius r, where A_1 and A_2 are given by boundary conditions.

In this case, it can easily be shown that

$$A_1 = \frac{(1+\mu)(1-2\mu)}{E}\frac{p_1 r_1^2 - p_2 r_2^2}{r_2^2 - r_1^2}$$
$$A_2 = \frac{(1+\mu)}{E}\frac{(p_1 - p_2)r_1^2 r_2^2}{r_2^2 - r_1^2} \qquad (2.2.8)$$

Thus the internal radius of the cylinder when it is subject to the pressures p_1 and p_2 is:

$$r_{1_{new}} = r_1 + u|_{r_1} \qquad (2.2.9)$$

Substituting the solution for u in 2.2.9 gives

$$r_1 = r_{1_{old}} + \frac{(1+\mu)(1-2\mu)}{E}\left(\frac{p_1 r_1^2 - p_2 r_2^2}{r_2^2 - r_1^2}\right)r_1 + \frac{(1+\mu)}{E}\left(\frac{(p_1 - p_2)r_1^2 r_2^2}{r_2^2 - r_1^2}\right)\frac{1}{r_1} \qquad (2.2.10)$$

where r_1 and r_2 are the new values of the inner and outer radii respectively, and r_{1old} is the old value of r_1.

A similar equation exists for r_2:

$$r_2 = r_{2_{old}} + \frac{(1+\mu)(1-2\mu)}{E}\left(\frac{p_1 r_1^2 - p_2 r_2^2}{r_2^2 - r_1^2}\right) r_2 + \frac{(1+\mu)}{E}\left(\frac{(p_1 - p_2) r_1^2 r_2^2}{r_2^2 - r_1^2}\right)\frac{1}{r_2} \tag{2.2.11}$$

Solution of these equations is considerably simplified when the original values of r_1 and r_2 are used on the RHS of the equation. This is acceptable for small deflections.

In the specific case of drying timber, the initial cell sizes are known, and the cell wall properties can be inferred from bulk properties. Thus 2.2.10 gives the variation of internal radius with internal pressure of the cylinder (subject of course to the limitations and assumptions mentioned above).

General equations for the radial and tangential stress at any point in the cylinder are easily obtained, and take the form of:

$$\sigma_r = C_1 - \frac{C_2}{r^2} \tag{2.2.12}$$

and

$$\sigma_t = C_1 + \frac{C_2}{r^2} \tag{2.2.13}$$

where

$$C_1 = \frac{p_1 r_1^2 - p_2 r_2^2}{r_2^2 - r_1^2}$$

$$C_2 = \frac{(p_1 - p_2) r_1^2 r_2^2}{r_2^2 - r_1^2}$$

The convention of tensile stresses being positive, and compressive stresses being negative is used.

2.3 Three layer isotropic analysis

The next complication after the single isotropic layer model is to apply the Lamé theory to three layers, corresponding to the S1, S2, and S3 layers.

Consider a section through a three layer cylinder:

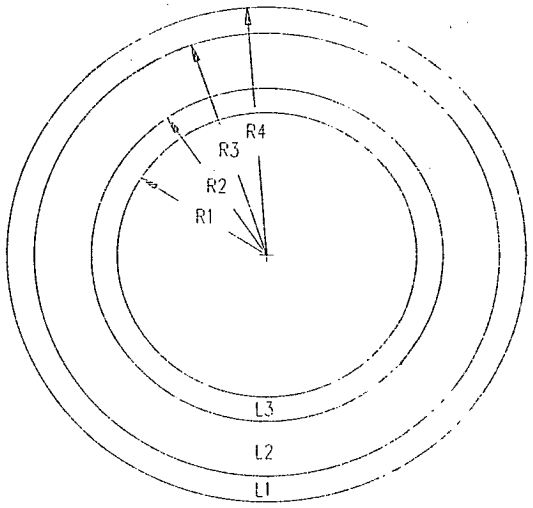

Figure 2.3.1 Three layered cylinder

The layers are labelled L1, L2, and L3 from the outside in. The inner radius is labelled R1, and the outer radius R4. The two interface radii are labelled as R2 and R3.

For each layer, the theory as outlined in the previous section on elastic isotropic analysis applies. It remains to determine the boundary conditions for each layer, so that we may solve for the deflections throughout the cylinder wall. The boundary conditions are stated as:

$\sigma_{r3}\big|_{r1} = -p_1$; - internal pressure = radial stress at inside

$\sigma_{r1}\big|_{r4} = -p_2$; - external pressure = radial stress at outside

$\sigma_{r1}\big|_{r3} = \sigma_{r2}\big|_{r3}$; radial stress at interface r_3 is equal in layers 1 and 2

$\sigma_{r2}\big|_{r2} = \sigma_{r3}\big|_{r2}$; radial stress at interface r_2 is equal in layers 2 and 3

$\varepsilon_{t1}\big|_{r3} = \varepsilon_{t2}\big|_{r3}$; tangential strain at interface r_3 is equal in layers 1 and 2

$\varepsilon_{t2}\big|_{r2} = \varepsilon_{t3}\big|_{r2}$; tangential strain at interface r_2 is equal in layers 2 and 3

$u_2\big|_{r3} = u_1\big|_{r3}$; radial displacement at interface r_3 is equal in layers 1 and 2

$u_3\big|_{r2} = u_2\big|_{r2}$; radial displacement at interface r_2 is equal in layers 2 and 3

$u_3\big|_{r1} + r_1 = r_{1n}$; radial displacement at inner surface plus original inner radius = new inner radius

and writing out the equations for the above boundary conditions we get:

$$-p_1 = \frac{E_3}{(1+\mu_3)(1-2\mu_3)}\left(A_{13} - (1-2\mu_3)\frac{A_{23}}{r_1^2}\right) \tag{2.3.1}$$

$$-p_2 = \frac{E_1}{(1+\mu_1)(1-2\mu_1)}\left(A_{11} - (1-2\mu_1)\frac{A_{21}}{r_4^2}\right) \tag{2.3.2}$$

$$\frac{E_1}{(1+\mu_1)(1-2\mu_1)}\left(A_{11} - (1-2\mu_1)\frac{A_{21}}{r_3^2}\right) = \frac{E_2}{(1+\mu_2)(1-2\mu_2)}\left(A_{12} - (1-2\mu_2)\frac{A_{22}}{r_3^2}\right) \tag{2.3.3}$$

$$\frac{E_2}{(1+\mu_2)(1-2\mu_2)}\left(A_{12}-(1-2\mu_2)\frac{A_{22}}{r_2^2}\right)=\frac{E_3}{(1+\mu_3)(1-2\mu_3)}\left(A_{13}-(1-2\mu_3)\frac{A_{23}}{r_2^2}\right) \tag{2.3.4}$$

$$A_{11}+\frac{A_{21}}{r_3^2}=A_{12}+\frac{A_{22}}{r_3^2} \tag{2.3.5}$$

$$A_{12}+\frac{A_{22}}{r_2^2}=A_{13}+\frac{A_{23}}{r_2^2} \tag{2.3.6}$$

$$A_{13}r_1+\frac{A_{23}}{r_1}+r_1=r_{1_n} \tag{2.3.7}$$

where A_{ij} is the i^{th} deflection equation constant for layer j (equation 2.2.7).

Note that from the given nine boundary conditions, there are only seven used here. The conditions for equality across interfaces of tangential strains and radial displacements are in fact the same conditions, so that of the four equations, two are redundant.

The first six boundary equations, equations 2.3.1 to 2.3.6 are solved for the six coefficients A_{ij} after specifying the internal and external pressures. Equation 2.3.7 then gives the new internal radius, which is used in equation 2.1.7 to calculate the volume of water removed.

The values of A_1 and A_2 for each layer are then substituted into equation 2.2.7 to solve for the displacements.

2.4 Three layer linear orthotropic analysis

The elastic isotropic model, although simple and easy to implement, is probably not a particularly realistic representation of the real situation. The next complicating step is to extend the model to incorporate orthotropic material properties. To realistically represent the cell wall, the model must incorporate three distinct layers with accompanying different orthotropic properties to represent the S1, S2, and S3 layers. This modification is performed here.

The equations for static equilibrium and strain are the same as for the isotropic case,

ie. $$\frac{d\sigma_r}{dr}+\frac{\sigma_r-\sigma_t}{r}=0 \tag{2.4.1}$$

$$\varepsilon_r = \frac{du}{dr} \tag{2.4.2}$$

and $$\varepsilon_t = \frac{u}{r} \tag{2.4.3}$$

The three dimensional Hooke's law relationship for an orthotropic material is:

$$\varepsilon_r = \frac{\sigma_r}{E_r} - \mu_{tr}\frac{\sigma_t}{E_t} - \mu_{zr}\frac{\sigma_z}{E_z} \tag{2.4.4}$$

$$\varepsilon_t = \frac{\sigma_t}{E_t} - \mu_{rt}\frac{\sigma_r}{E_r} - \mu_{zt}\frac{\sigma_z}{E_z} \tag{2.4.5}$$

$$\varepsilon_z = \frac{\sigma_z}{E_z} - \mu_{rz}\frac{\sigma_r}{E_r} - \mu_{tz}\frac{\sigma_t}{E_t} \tag{2.4.6}$$

Where μ_{ij} is defined as the strain in the j direction divided by the strain in the i direction due to a direct stress in the i direction

or $$\varepsilon_j = -\mu_{ij} \times \frac{\sigma_i}{E_i}$$

The plane strain approximation $\varepsilon_z = 0$ is substituted into 2.4.6 which is then substituted into 2.4.4 and 2.4.5 to give

$$\varepsilon_r = \frac{\sigma_r}{E_r}\left(1 - \mu_{zr}\mu_{rz}\right) - \frac{\sigma_t}{E_t}\left(\mu_{tr} + \mu_{zr}\mu_{tz}\right) \tag{2.4.7}$$

$$\varepsilon_t = -\frac{\sigma_r}{E_r}\left(\mu_{rt} + \mu_{zt}\mu_{rz}\right) + \frac{\sigma_t}{E_t}\left(1 - \mu_{zt}\mu_{tz}\right) \tag{2.4.8}$$

Solving for the stresses we find:

$$\sigma_r = \frac{E_r}{-\left(\mu_{rt} + \mu_{zt}\mu_{rz}\right)\left(\mu_{tr} + \mu_{zr}\mu_{tz}\right) + \left(1 - \mu_{zr}\mu_{rz}\right)\left(1 - \mu_{zt}\mu_{tz}\right)}\left[\left(1 - \mu_{zt}\mu_{tz}\right)\varepsilon_r + \left(\mu_{tr} + \mu_{zr}\mu_{tz}\right)\varepsilon_t\right] \tag{2.4.9}$$

$$\sigma_t = \frac{E_t}{-\left(\mu_{rt} + \mu_{zt}\mu_{rz}\right)\left(\mu_{tr} + \mu_{zr}\mu_{tz}\right) + \left(1 - \mu_{zr}\mu_{rz}\right)\left(1 - \mu_{zt}\mu_{tz}\right)}\left[\left(\mu_{rt} + \mu_{zt}\mu_{rz}\right)\varepsilon_r + \left(1 - \mu_{zr}\mu_{rz}\right)\varepsilon_t\right] \tag{2.4.10}$$

These expressions are general for any linearly orthotropic cylindrically symmetric body.

2.4.1 Material Properties

Relative Stiffness

Timber from Tasmanian eucalypts, like most timbers, is approximately half as stiff in the tangential direction as it is in the radial direction. An explanation for this has been proposed by Ilic (1987). There are many more large thin walled vessels (rays) running in the radial direction than there are in the tangential direction (Ilic, 1991). Radially oriented vessels soften the wood tangentially in proportion to the longitudinal sections of the vessels, whereas the softening of the wood radially is only in proportion to the cross sectional area of the vessels. Thus the wood is softer in the tangential direction than in the radial direction.

The fibres being modelled lie longitudinally in the tree. The fibre cell secondary wall is composed of three layers, labelled the S1, S2, and S3 from the outside in, as described above. These layers are predominantly cellulose in the form of microfibrils. Microfibrils consist of long chain polymers called elementary fibrils, bundled together to form a structural unit which is typically 10nm to 30nm wide. The microfibrils are aggregated into macrofibrils, which are organised into lamellae within the different layers of the cell wall. In each of the secondary cell wall layers, the microfibrils are helically wound in a predominant direction. In the S1 and S3 layers, the microfibrils are close to perpendicular to the longitudinal axis of the fibre. In the S2 layer the microfibrils are close to parallel to the fibre axis (Siau, 1984).

The microfibrils are clearly stiffer along their length than across. Thus wood is much stiffer in the longitudinal direction than it is transversely, as the S2 layer, with predominantly longitudinal microfibrils, makes up the bulk of the fibre cell wall. The longitudinal cell wall stiffness is thus approximately equal to the longitudinal stiffness of the bulk wood, which in turn is about twenty times the bulk tangential stiffness or ten times the bulk radial stiffness. Similarly, the stiffness of the fibre wall in the transverse direction can be approximated by the radial stiffness of the bulk material, due to the tangential weakening effect described above, assuming that the ratio between longitudinal and transverse stiffnesses for bundles of microfibrils is similar to that for the bulk material.

An earlier investigation (Innes, 1992) into structural properties across the grain of Tasmanian Oak gave a tangential stiffness below the proportional limit at 22°C and MC>FSP of 310MPa. It is assumed that the radial modulus is approximately twice the tangential modulus, and that the longitudinal modulus is approximately twenty times the tangential modulus. Thus, for the cell wall, the values used are: $E_{rt} = 620$ MPa, and $E_z = 6.20$ GPa.

Poisson's ratios

Linearly elastic orthotropic analyses are based on the existence of a strain-energy function. If such a function does exist, it must be a quadratic function of the stresses, and therefore a quadratic function of the strains, because of the linear stress-strain relationship. Comparison of the function in terms of the stresses with that in terms of the strains leads to the general expression: $E_i\mu_{ji} = E_j\mu_{ij}$ (Love, 1944). There are three such equations in the orthotropic case; the Poisson's ratios and Young's moduli have been set up to ensure the satisfaction of these conditions.

The six Poisson's ratios below are taken from the US Forest Products Laboratory "Wood Handbook" (1974). These ratios are for the solid wood form of black walnut, which seems to behave structurally in a similar fashion to Tasmanian eucalypts.

$\mu_{tr} = 0.379$
$\mu_{zr} = 0.495$
$\mu_{rt} = 0.718$
$\mu_{zt} = 0.632$
$\mu_{rz} = 0.052$
$\mu_{tz} = 0.035$

Where the subscript r refers to the radial direction, t to tangential and z to longitudinal.

Note that the values of the Poisson's ratios are consistent with the relative stiffnesses as described above. That is, $\mu_{tr} < \mu_{rt}$, $\mu_{zt} < \mu_{zr}$, $\mu_{rz} < \mu_{tz}$.

The Poisson's ratios for the fibre wall components are inferred from the bulk material figures. Due to the near-longitudinal predominant direction of the microfibrils in the S2 layer it is assumed that: $\mu_{tr} = \mu_{rt}$, $\mu_{zt} = \mu_{zr}$, and $\mu_{tz} = \mu_{rz}$ in the S2 layer. That is, the radial stiffness is assumed to be equal to the tangential stiffness in this layer. This implies that the stiffness across a lamella is the same as the stiffness between lamellae.

Assuming that the fibre Poisson's ratios are similar to the bulk Poisson's ratios except for the tangential softening effect, we re-label the Poisson's ratios for the S2 layer and put: $\mu_{tr} = \mu_{rt} = \mu_{tra} = 0.38$, $\mu_{zt} = \mu_{zr} = \mu_{zrt} = 0.5$ and $\mu_{tz} = \mu_{rz} = \mu_{trz} = 0.05$. This assumes also that the bulk wood stiffness properties are due mainly to the S2 layer because of its relatively large thickness.

The S1 and S3 layers are assumed to consist of tangentially wound microfibrils. Thus, there is a 90° rotation in stiffness properties from the S2 to the S1 and S3 layers and there is also a 90° rotation in Poisson's ratios. Hence the radial and longitudinal stiffnesses are assumed to be equal, and hence we use: $\mu_{zr} = \mu_{rz} = 0.38$, $\mu_{tz} = \mu_{tr} = \mu_{tzr} = 0.5$, and $\mu_{zt} = \mu_{rt} = \mu_{zrt} = 0.05$ for the S1 and S3 layers.

2.4.2 Longitudinal symmetry - S2 layer

Substituting 2.4.9 and 2.4.10 into 2.4.1 using 2.4.2 and 2.4.3 and the simplifications introduced above we get:

$$\frac{d^2u}{dr^2} + \frac{1}{r}\frac{du}{dr} - \frac{u}{r^2} = 0 \qquad (2.4.11)$$

which is the same expression as derived for isotropic materials.
Thus the solution will again be

$$u = A_1 r + \frac{A_2}{r} \qquad (2.4.12)$$

where A_1 and A_2 are constants.

The expression for radial stress then simplifies to:

$$\sigma_r = \frac{E_y A_1}{\left(1 - \mu_{yy} - 2\mu_{xy}\mu_{yx}\right)} - \frac{E_y A_2}{r^2\left(1 + \mu_{yy}\right)} \qquad (2.4.13)$$

When we analyse firstly a single layer orthotropic cylinder based on the S2 layer, the boundary conditions will again be $\sigma_r|_{r_1} = -p_1$ and $\sigma_r|_{r_2} = -p_2$

so that we get

$$A_1 = \frac{\left(1 - \mu_{yy} - 2\mu_{xy}\mu_{yx}\right)}{E_y}\frac{\left(r_2^2 p_2 - r_1^2 p_1\right)}{\left(r_1^2 - r_2^2\right)}$$

$$A_2 = \frac{\left(1 + \mu_{yy}\right)}{E_y}\frac{\left(p_2 - p_1\right)r_1^2 r_2^2}{\left(r_1^2 - r_2^2\right)} \qquad (2.4.14)$$

Hence, as for the isotropic case, the deflection based analysis leads to a simple analytic solution for the stresses and strains through the S2 layer considered in isolation. The S2 layer can be treated as part of a multi layered cylinder by changing the boundary conditions to suit.

2.4.3 Tangential symmetry - S1 and S3 layers

The S1 and S3 layers consist of microfibrils which are wound around the fibre in a direction which is close to perpendicular to the longitudinal axis of the fibre. This analysis then assumes that the properties of the layer are the same in the radial and longitudinal directions, but different in the tangential direction.

Using a process similar to that above leads to the differential equation (d.e.) for radial deflection, u:

$$\frac{d^2u}{dr^2}+\frac{1}{r}\frac{du}{dr}-\frac{\mu_{xy}\left(1-\mu_{yy}^2\right)}{\mu_{yx}\left(1-\mu_{yx}\mu_{xy}\right)}\frac{u}{r^2}=0 \qquad (2.4.15)$$

The solution to this d.e. is not nearly so simple as the previous one. That is, the deflection based analysis does not lead to a simple solution. Another form of solution is used to simplify the problem.

Using the plane strain assumption gives the equation for static (planar) equilibrium of an element of a thick walled cylinder as

$$\frac{d\sigma_r}{dr}+\frac{\sigma_r-\sigma_t}{r}=0 \qquad (2.4.16)$$

This is used to solve for the stresses in a layer in an incremental fashion when we replace the derivative with finite differences and rearrange to give:

$$\delta\sigma_r=\delta r\left(\frac{\sigma_t-\sigma_r}{r}\right) \qquad (2.4.17)$$

To solve for the stresses using this approach, the layer is solved in steps from the inside (where initial conditions are known) to the outside, using a set value of δr to give $\delta\sigma_r$ and hence, the stress and strain conditions at the next step.

This approach was used in two Turbo Pascal programs implementing the model. One used the deflection based analytic solution for the S2 layer, while the other used the incremental solution for all layers. In this way, the incremental solution was

compared with the more definitive analytic solution. Boundary conditions between the layers were the same as those used in the multi layer isotropic model.

The result of this comparison was a verification of the incremental solution, which typically differed from the analytic solution by less than 1%. The comparison was made using 20 steps in radius through the S2 layer. This was taken as being sufficient support for the solution through the three layers using the incremental method. The incremental type of solution is used when the model is extended to non linear material behaviour as, in that case, equal increments of stress will not give equal increments of strain at different points on the loading curve.

2.5 Non-linear orthotropic analysis

The fibre wall is modelled as consisting of three layers, all with different non linear orthotropic material properties. This simulates the S1, S2 and S3 layers of the secondary fibre wall, each of which consists principally of helically wound cellulose microfibrils (Siau, 1984) as previously discussed. The primary wall is neglected due to its small thickness and random microfibril direction. The model was implemented as the Turbo Pascal program **Cyl_A**.pas (see Appendix D for a block diagram).

This model solves for the stress distribution through the cylinder wall from the inside to the outside. Increments of stress are used with the first solution being for low internal tension. The internal tension is then incremented toward its final value, and the stress and strain distributions determined for each increment. In this way, the non-linear material properties are accounted for by using a mean value for the (inelastic) modulus over the stress increment at each finite radius step within the cylinder wall. Each increment is iterated to arrive at the required radial stress at the outside of the fibre, corresponding to a specified external pressure.

2.5.1 Non linear, orthotropic material properties

Similar arguments are used for relative stiffness as those used in the linear orthotropic model, although in the non linear region, the conditions on ratios between moduli and Poisson's ratios clearly do not apply, as the strain energy will no longer be a quadratic function of the strains. The Poisson's ratios are assumed to be constant for all stresses, for want of better information.

Form of non-linear material properties

The form of the stress-strain curve used here, and its variation with temperature, is identical to that developed by Oliver (1991) to describe the bulk properties of Tasmanian Oak, a mixture consisting mainly of *E. regnans*, *E. delegatensis*, and *E. obliqua.* It consists of a linear portion up to a proportional limit, and then a non linear part leading asymptotically to failure. The form of his relationship is computationally simple, and agrees well with experimental data for Tasmanian Oak from Innes (1992). The computer model **KilnSched** (**Kiln Sched**uling program (Doe et al, 1994)) which uses this stress-strain relationship has been experimentally found to model timber behaviour to within approximately 10%. Wood properties in a batch of timber are expected to have approximately this much variation anyway. Properties for moisture content below FSP are irrelevant to this problem, as collapse occurs only when the fibre lumens are still saturated. It is possible that the cell wall material follows a different form of stress-strain relationship from that of the bulk material, but the relationships describing the bulk properties are thought to provide a realistic starting point.

Linear part

The form of the dependence of Young's modulus in the green state on temperature is taken from Innes (1992). The data is for Tasmanian Oak in the tangential direction from 21°C to 55°C.

Relationship from Innes (1992):

$$E_{green} = \exp(4.206 + 0.003265BD - 0.03029T) \quad (2.5.1)$$

or

$$E_{green} = \exp(6.403 - 0.03029T) \quad (2.5.2)$$

where E_{green} = Young' s Modulus of green material in the tangential direction

BD = Basic Density

T = Temperature

and the mean basic density of 673kg/m^3 from Innes (1992) is used to get equation 2.5.2 from equation 2.5.1.

The linear portion of the assumed stress-strain curve exists to a proportional limit strain e_y which is taken to be 0.005.

Non linear part

Above the proportional limit, the stress strain curve as defined by Oliver (1991) is given by

$$\sigma_u - \sigma = \left(\sigma_u - \sigma_y\right)\exp\left(-k \times \left|\varepsilon_i - \varepsilon_y\right|\right) \quad (2.5.3)$$

where:

σ_u = local ultimate stress

σ = local instantaneous stress

σ_y = local value of stress at proportional limit

ε_i = local instantaneous strain

ε_y = strain at proportional limit

k is fixed by the requirement that the curve be tangent to the linear part at the proportional limit

The criterion for failure was taken as ε_i=0.02.

From Oliver's assumption that the ultimate stress is directly proportional to the Young's modulus;

$$\sigma_u = KE \quad (2.5.4)$$

where K is a constant, we get

$$k = \left(\frac{1}{K - \varepsilon_y} \right) \tag{2.5.5}$$

Putting K=0.01, we get k=200 since ε_y=0.005.

Equation 2.5.3 leads to a relationship between the tangent modulus and the local stress of:

$$\frac{d\sigma}{d\varepsilon_i} = E^* = k \times \left(|\sigma_u| - |\sigma| \right) \tag{2.5.6}$$

A requirement of the program is that $|\sigma| < |\sigma_u|$ for all σ. Note that E^* refers to the local modulus at a given stress, not the Young's modulus of the linear part of the curve. The stress-strain curve is taken to be symmetrical in tension and compression.

2.5.2 Stress Analysis

The general three dimensional stress-strain relationships are:

$$\begin{aligned}
\varepsilon_r &= \frac{\sigma_r}{E_r} - \mu_{tr}\frac{\sigma_t}{E_t} - \mu_{zr}\frac{\sigma_z}{E_z} \\
\varepsilon_t &= \frac{\sigma_t}{E_t} - \mu_{rt}\frac{\sigma_r}{E_r} - \mu_{zt}\frac{\sigma_z}{E_z} \\
\varepsilon_z &= \frac{\sigma_z}{E_z} - \mu_{rz}\frac{\sigma_r}{E_r} - \mu_{tz}\frac{\sigma_t}{E_t} \\
\gamma_{tz} &= \frac{\tau_{tz}}{G_{tz}} \\
\gamma_{zr} &= \frac{\tau_{zr}}{G_{zr}} \\
\gamma_{rt} &= \frac{\tau_{rt}}{G_{rt}}
\end{aligned} \tag{2.5.7}$$

Where: γ = shear stress, τ = shear strain, G = bulk modulus, E = stiffness and the other symbols are as defined above.

Rewriting the equations 2.5.7 for increments of stress and strain, assuming that the shear stresses and strains are zero, gives:

$$\delta\varepsilon_r = \frac{\delta\sigma_r}{E^*_r} - \mu_{tr}\frac{\delta\sigma_t}{E^*_t} - \mu_{zr}\frac{\delta\sigma_z}{E^*_z}$$
$$\delta\varepsilon_t = -\mu_{rt}\frac{\delta\sigma_r}{E^*_r} + \frac{\delta\sigma_t}{E^*_t} - \mu_{zt}\frac{\delta\sigma_z}{E^*_z} \qquad (2.5.8)$$
$$\delta\varepsilon_z = -\mu_{rz}\frac{\delta\sigma_r}{E^*_r} - \mu_{tz}\frac{\delta\sigma_t}{E^*_t} + \frac{\delta\sigma_z}{E^*_z}$$

where δ signifies an increment and E^* represents ratios between incremental stress and strain, not the linear elastic modulus. The E^* values have to be obtained from equation 2.5.6.

We then let $\delta\varepsilon_Z = 0$ in the third of equations 2.5.8 and substitute the resulting expression for $\delta\sigma_Z/E^*_Z$ into the first two of the equations 2.5.8.

The strain equations thus become:

$$\delta\varepsilon_r = \left(1-\mu_{zr}\mu_{rz}\right)\frac{\delta\sigma_r}{E^*_r} - \left(\mu_{tr}+\mu_{zr}\mu_{tz}\right)\frac{\delta\sigma_t}{E^*_t}$$
$$\delta\varepsilon_t = -\left(\mu_{rt}+\mu_{zt}\mu_{rz}\right)\frac{\delta\sigma_r}{E^*_r} + \left(1-\mu_{zt}\mu_{tz}\right)\frac{\delta\sigma_t}{E^*_t} \qquad (2.5.9)$$

Hence, from the argument above regarding Poisson's ratios, for the S1 and S3 layers the strain equations become:

$$\delta\varepsilon_r = \left(1-\mu_{rz}^2\right)\frac{\delta\sigma_r}{E^*_r} - \mu_{tzr}\left(1+\mu_{rz}\right)\frac{\delta\sigma_t}{E^*_t}$$
$$\delta\varepsilon_t = -\mu_{zrt}\left(1+\mu_{rz}\right)\frac{\delta\sigma_r}{E^*_r} + \left(1-\mu_{zrt}\mu_{tzr}\right)\frac{\delta\sigma_t}{E^*_t} \qquad (2.5.10)$$

and for the S2 layer:

$$\delta\varepsilon_r = \left(1-\mu_{ztr}\mu_{trz}\right)\frac{\delta\sigma_r}{E^*_r} - \left(\mu_{tra}+\mu_{ztr}\mu_{trz}\right)\frac{\delta\sigma_t}{E^*_t}$$
$$\delta\varepsilon_t = -\left(\mu_{tra}+\mu_{ztr}\mu_{trz}\right)\frac{\delta\sigma_r}{E^*_r} + \left(1-\mu_{ztr}\mu_{trz}\right)\frac{\delta\sigma_t}{E^*_t} \qquad (2.5.11)$$

Rearranging, we can also get for the S1 and S3 layers:

$$\frac{\delta\sigma_t}{E^*_t} = \frac{\mu_{zrt}\delta\varepsilon_r + \left(1-\mu_{rz}\right)\delta\varepsilon_t}{\left(1-\mu_{rz}-2\mu_{tzr}\mu_{zrt}\right)} \qquad (2.5.12)$$

and for the S2 layer:

$$\frac{\delta\sigma_t}{E^*_t} = \frac{\left(\mu_{tra}+\mu_{ztr}\mu_{trz}\right)\delta\varepsilon_r + \left(1-\mu_{ztr}\mu_{trz}\right)\delta\varepsilon_t}{\left(1+\mu_{tra}\right)\left(1-\mu_{tra}-2\mu_{ztr}\mu_{trz}\right)} \qquad (2.5.13)$$

Static Equilibrium

Equation 2.2.5 is used to solve for the stresses in a layer in an incremental fashion by replacing the derivative with finite differences and rearranging to give:

$$\delta\sigma_r = \delta r\left(\frac{\sigma_t - \sigma_r}{r}\right) \tag{2.5.14}$$

To solve for the stresses using this approach, each layer is solved in steps from the inside to the outside. The radial stress on the inside of the cylinder is numerically equal to the negative of the internal pressure, and the tangential strain on the inside is guessed. A set value of δr is used to give $\delta\sigma_r$ and hence, the stress and strain conditions at the next step. This is done by an iterative process to ensure satisfaction of the static equilibrium equation. Equality of tangential strains and radial stresses across layer interfaces is used to solve the stress and strain distributions through the three layers. The correct value of internal tangential strain is found by iterating the whole procedure until the required value of radial stress on the outside of the fibre is returned. The radial stress on the outside of the fibre will be numerically equal to the negative of the external pressure. The internal tension is then incremented and the whole procedure repeated. A block diagram of **Cyl_A**.pas is presented in Appendix D.

Radial displacement is calculated from tangential strain by using $u = \varepsilon_t \times r$ (from equation 2.4.3).

2.6 Results from non-linear orthotropic three layer model

The main results from each run of the program **Cyl_A** are presented in the form of two sets of four graphs (Figs. 2.6.1 to 2.6.4 and Figs. 2.6.5 to 2.6.8): radial stress, tangential stress, radial strain and tangential strain distributions, all plotted against radial position in the fibre wall with centre of the fibre as origin. Compressive stresses and strains are shown as negative, and tensile stresses and strains are shown as positive. Each trace represents the respective stress or strain distribution for a value of internal tension. At the top of each graph, the S1, S2, and S3 layers are labelled, with solid vertical lines indicating the interfaces between layers. Below this, P_0, P_2 and T are given. As before, P_0 is the initial pressure of the system, P_2 is the external

pressure, and T is the temperature. The legend shows P_1, the internal pressure for each trace. Note that, although only four traces are shown, typically forty stress increments are used in the calculations.

The radial stress and tangential strain curves are continuous (but not smooth), whilst the tangential stress and radial strain curves are discontinuous. The continuity of radial stress and tangential strain curves specify the boundary conditions: continuity of tangential strain is mathematically equivalent to continuity of radial displacement by 2.5.14, which is obviously required in order to maintain the integrity of the material at the layer interfaces. Radial stresses at the inner and outer surfaces must be equal to the internal and external tensions respectively. It follows that the radial stresses are continuous at interfaces, so long as the material is continuous. The tangential stress and radial strain distributions are discontinuous due to the different material properties on either side of each interface.

Representative values of fibre external and lumen diameters for Tasmanian regrowth *E. globulus* were found by examination of macerated fibres under a light microscope with a digital camera and image analysis software (Hasan, 1994). Dimensions used were for earlywood as this is usually observed to collapse much more than latewood (Bisset and Ellwood, 1951). Thickness of the S1, S2 and S3 layers were calculated from proportions of averages of values given by Siau (1984).

The first set of four graphs below are for a fibre with internal diameter 5.2 micron, external diameter 7.5 micron, with internal tension of 6.2 MPa and temperature 20°C. The second set of graphs are for the same fibre with an internal tension of 5.33 MPa at 25°C. These conditions both result in a radial strain on the inside fibre wall of approximately 19000 microstrain, 95% of the nominal failure strain of 0.02.

Further complications to the model were not pursued, as they involve modelling of the fibre after it loses the circular shape assumed here. This becomes a complex two-dimensional problem which does not appear to add much to this discussion, as the present aim is to prevent the occurrence of collapse in the first place.

The S2 layer from 5.37 micron to 7.10 micron is the thickest layer. Its tangential stiffness is much lower than the S1 or S3 layers. Hence, we see that although the tangential stress distribution is almost flat, the tangential strain increases quite steeply from the inside to the outside of the layer. The S1 and S3 layers have much higher

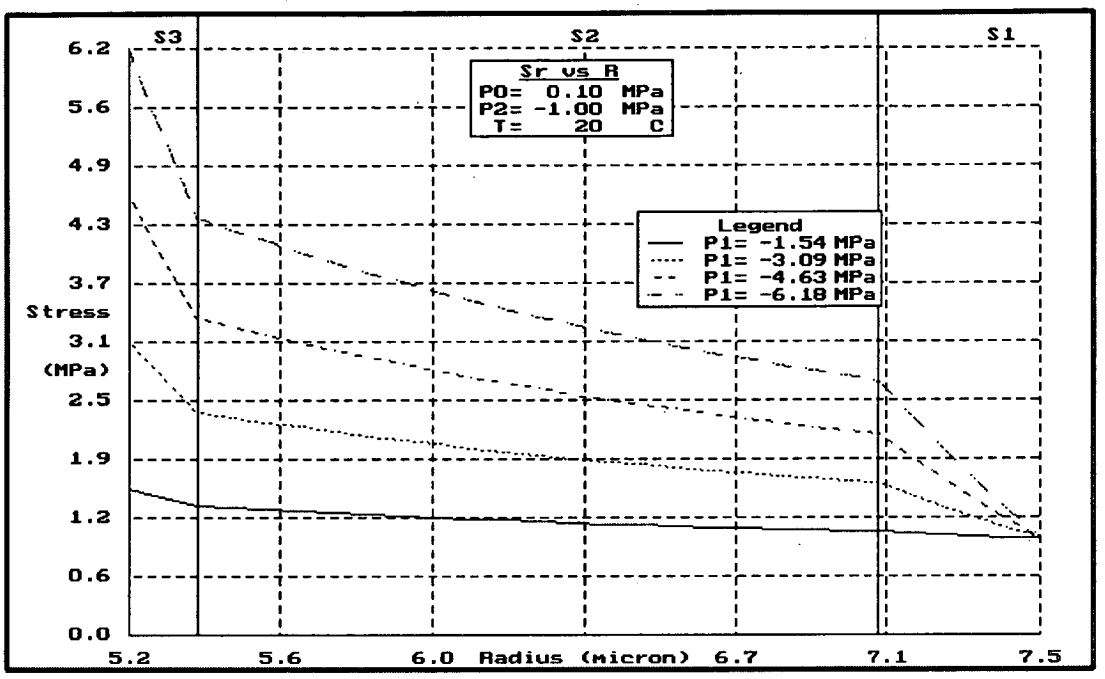

Figure 2.6.1 Radial stress vs radial position in fibre wall at 20°C.

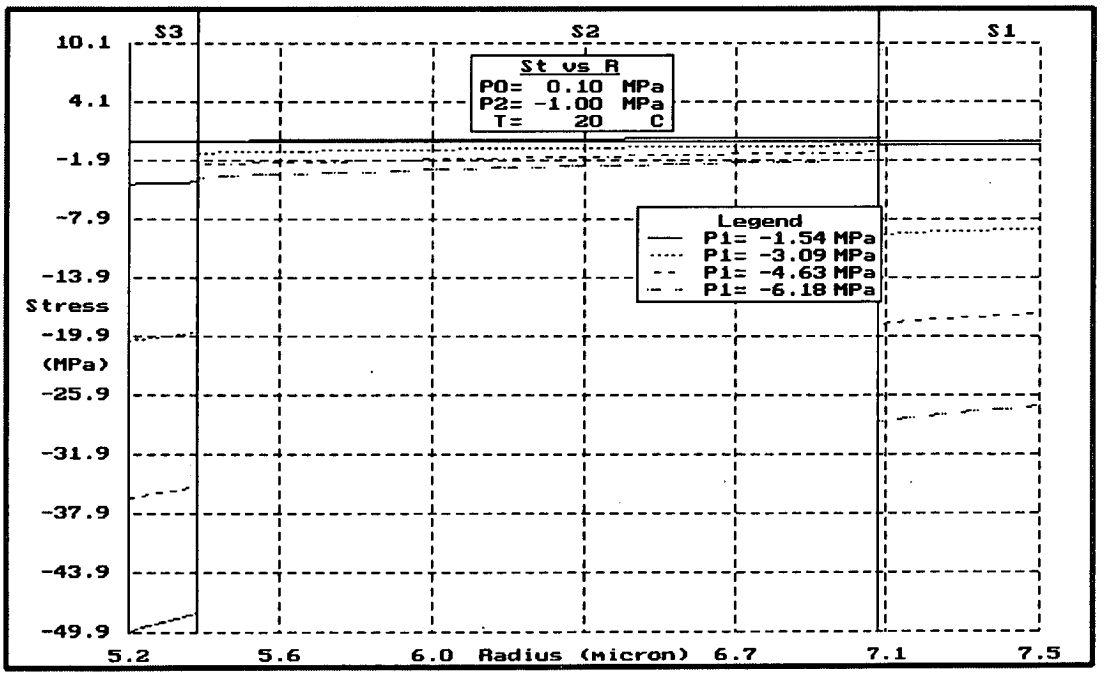

Figure 2.6.2 Tangential stress vs radial position in fibre wall at 20°C.

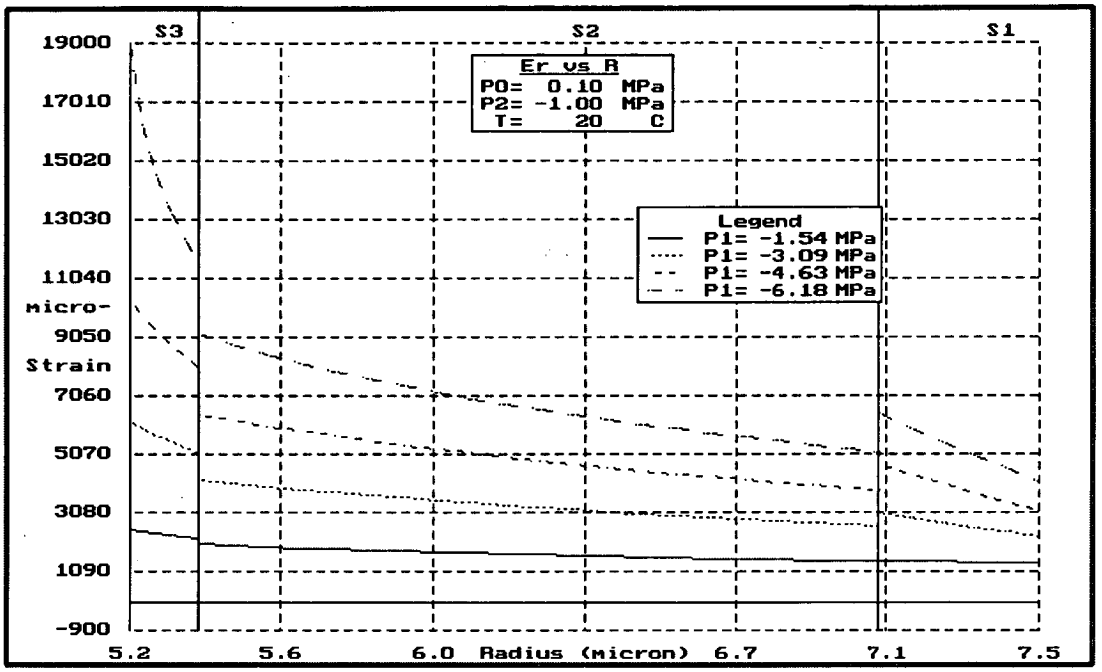

Figure 2.6.3 Radial strain vs radial position in fibre wall at 20°C.

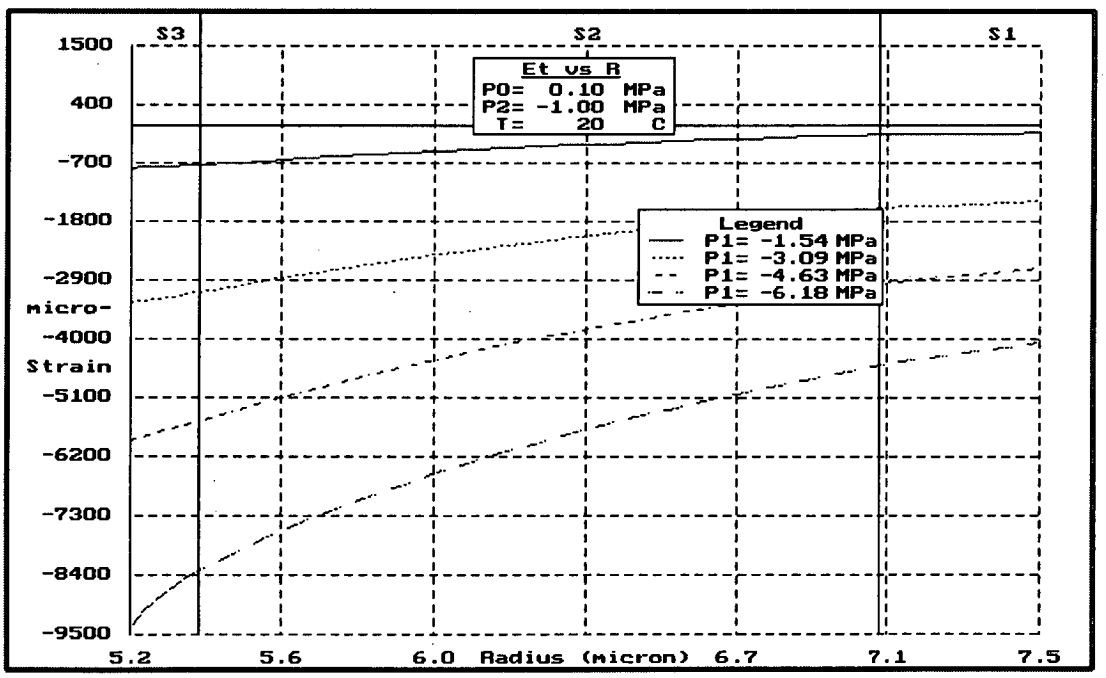

Figure 2.6.4 Tangential strain vs radial position in fibre wall at 20°C.

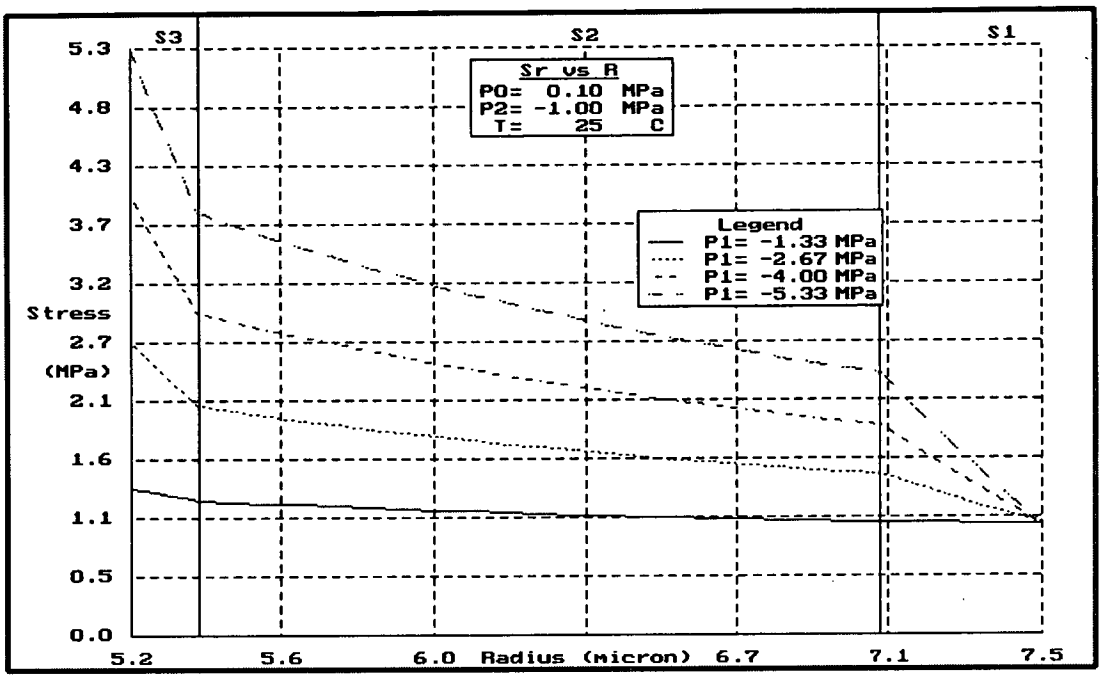

Figure 2.6.5 Radial stress vs radial position in fibre wall at 25°C.

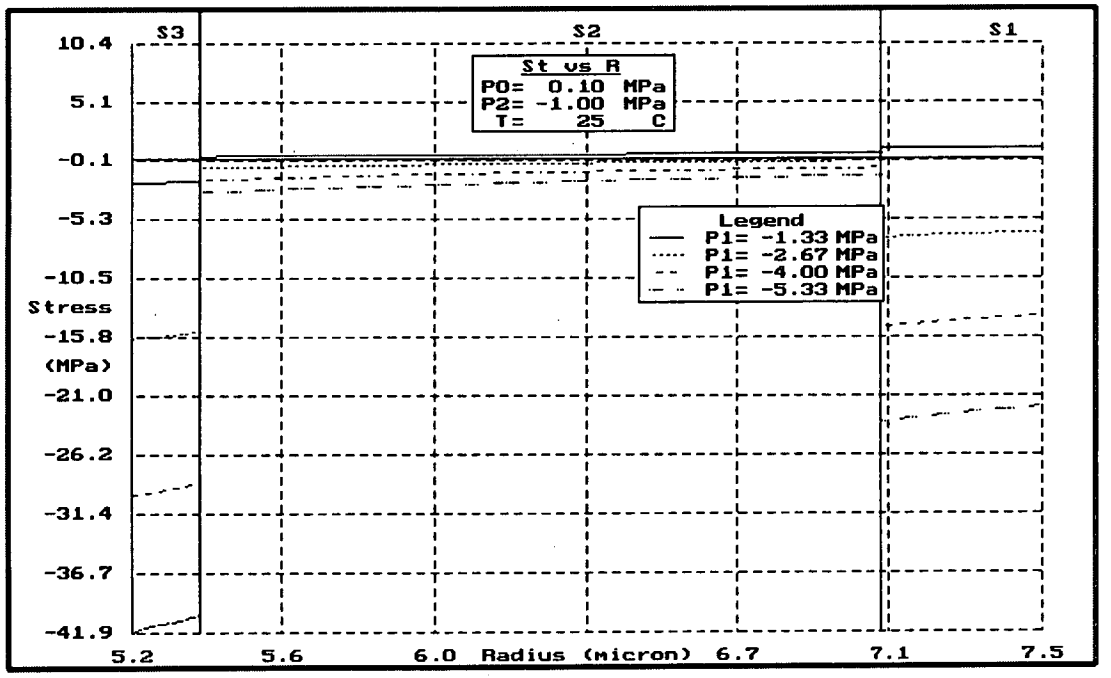

Figure 2.6.6 Tangential stress vs radial position in fibre wall at 25°C.

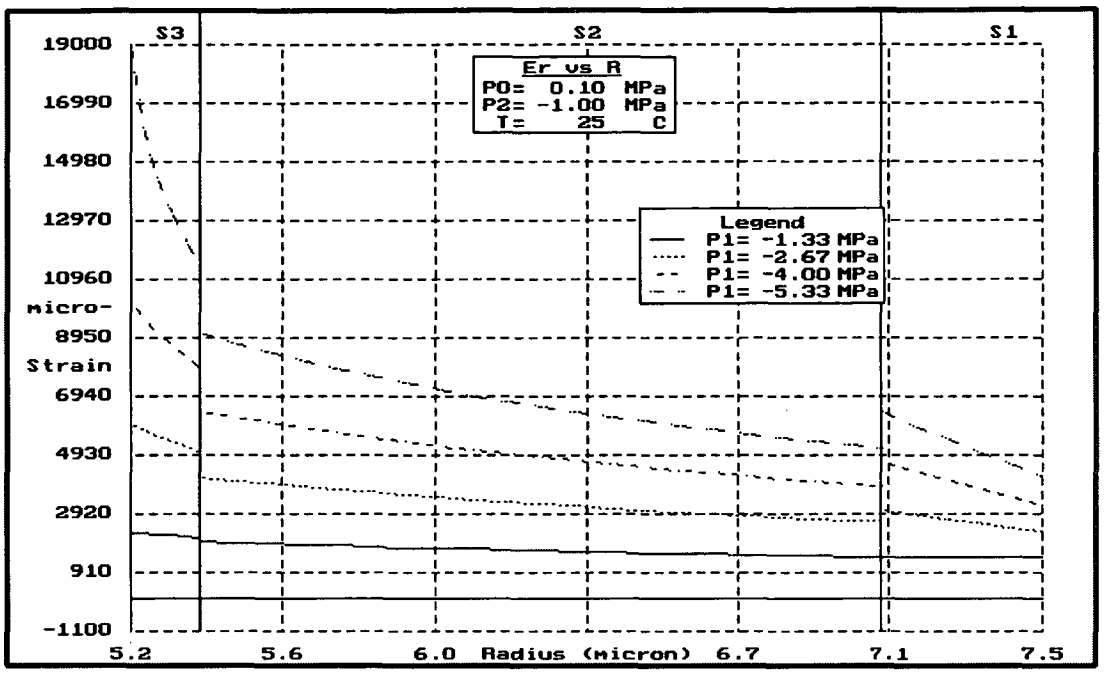

Figure 2.6.7 Radial strain vs radial position in fibre wall at 25°C.

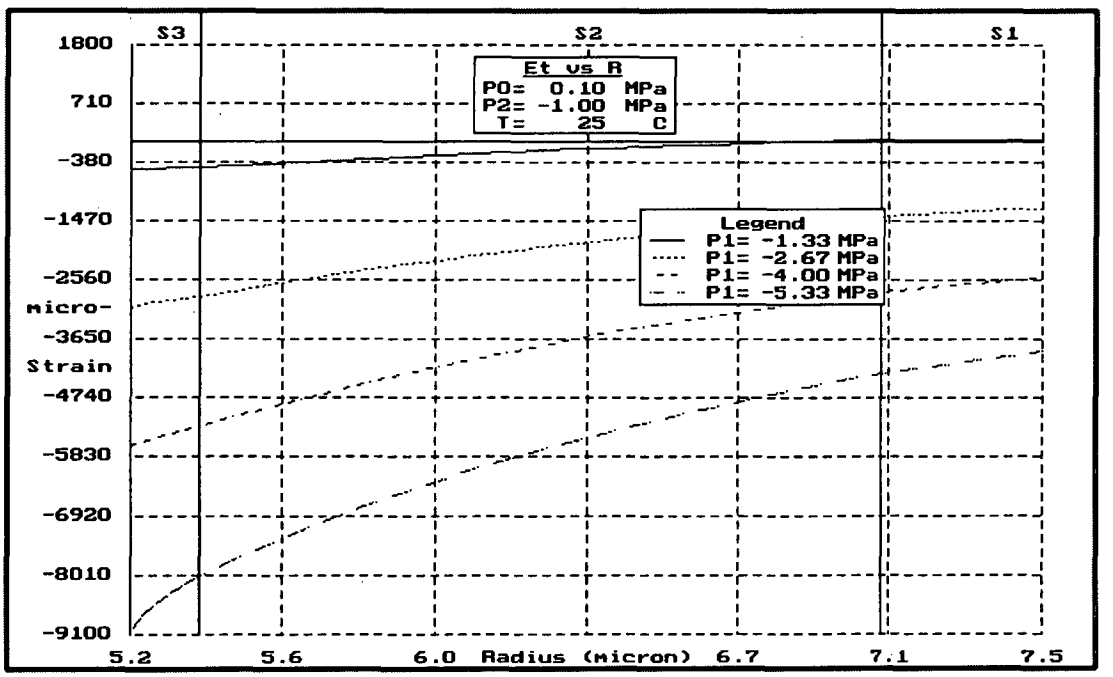

Figure 2.6.8 Tangential strain vs radial position in fibre wall at 25°C.

magnitude tangential stresses than the S2 layer because of their relatively high tangential stiffnesses.

It must be kept in mind that the actual fibre cell wall is not uniform as assumed, but has pits and other irregularities. Physical collapse will thus start at a point where the local stiffness is relatively low. Therefore, since the start of collapse is a local effect, it may occur before the rest of the fibre wall reaches the ultimate stress or strain in any direction. Collapse may also start preferentially in fibres near vessels or rays where they may be deformed.

2.6.1 Sensitivity to temperature

The model was run at 25°C and 20°C for otherwise identical conditions. Internal tensions were chosen so that the maximum strain in both cases was approximately equal to 95% of the nominal failure strain. The tension at 20°C was 6.18 MPa, and the tension at 25°C was 5.33 MPa. Thus the fibre modelled could sustain approximately 850 kPa higher internal tension at 20°C than it could at 25°C.

The radial strain distributions Figs. 2.6.3 and 2.6.7 were virtually identical (to within 2%). The tangential strain plots Figs. 2.6.4 and 2.6.8 were also very similar, to within approximately 5%.

The radial stress profiles Figs. 2.6.1 and 2.6.5 were different due to the higher internal tension at 20°C. The difference between the two curves decreased towards the outside of the fibre, where both curves reached the negative of the value of external pressure specified. The compressive tangential stresses were higher at 20°C due to the higher internal tension. This effect was more pronounced towards the outside of the fibre, with the difference approximately 20%.

The program was run a third time, with the conditions being identical to the 25°C run shown in Figs. 2.6.5 to 2.6.8, but with a temperature of 20°C. The aim was to find the difference in strains due to temperature, and hence how much closer to failure the fibre is at 25°C than at 20°C with the same internal and external pressure. Results are not shown as they were all very similar in shape to the plots shown above.

As expected, the stress profiles were all very similar, with less than 3% difference anywhere in either the radial or tangential stress profiles. The radial strain on the inside of the fibre wall at 20°C was only 66% of the nominal ultimate value of 0.02, whereas at 25°C the corresponding strain was 95% of ultimate. The difference between the radial strains at 20°C and 25°C ranged from 37% at the inside of the fibre wall, to 16% on the outside. Similarly, the compressive tangential strain ranged from 20% higher on the inside to 16% higher on the outside at 25°C than at 20°C.

These results indicate that when the internal tension was close to a value which would cause failure, a small increase in temperature could be enough to precipitate collapse. This agrees with Booker's (1994a) observation reported in Section 1.6.

Over a wide range of temperatures (10°C to 40°C) and external pressures (-4 to +0.1 MPa), the radial strain on the inside of the fibre was always found to approach the nominal failure value before the strain anywhere else in the material. Thus, it appears likely that fibre collapse is precipitated by failure of the S3 layer. This pattern of failure does not change with temperature, although, as shown above, the process of collapse is sensitive to temperature.

2.6.2 Sensitivity to Poisson's ratios

It is possible that the Poisson's ratios for the fibre wall material are significantly different from the bulk material values used here. To ascertain the effect of changing Poisson's ratios, a second set of results was calculated for Poisson's ratios of 0.3, 0.3, and 0.03, corresponding to the values used above of 0.38, 0.5, 0.05 respectively. The conditions used were T=20°C, P_0=0.1 MPa, P_1=-6.2 MPa, P_2=-1.0 MPa. The radial strain on the inside of the fibre was 95% of the ultimate value.

The stress profiles for the two sets of Poisson's ratios did not differ by more than 2%. However, the radial strain on the inside of the fibre decreased by 10% with the second set of Poisson's ratios, relative to the first set. The steps in radial strain at the S1-S2 interface, and at the S2-S3 interface, were decreased by a factor of approximately 3.5 with the second set of Poisson's ratios. The magnitude of tangential strain was decreased by between 1 and 5% by using the second set of Poisson's ratios. This potential source of inaccuracy is not thought to be particularly significant, as the real

Poisson's ratios are unlikely to be any further removed from the original set than are the second set.

2.7 Conclusions

A mathematical model to analyse the stress and strain in the walls of hardwood fibre cells was implemented in a computer program with the aim of predicting the onset of collapse and identifying its mechanism. The model confirmed that the stresses and strains in the fibre cell wall are sensitive to small changes in temperature. It showed that, when the internal tension was close to a value which would cause failure, a small increase in temperature could be enough to precipitate collapse due to failure of the S3 layer. It also showed that the shrinkage of a fibre due to removal of free water from the lumen is very small, while the fibre retains its assumed axial symmetry.

Chapter 3. The collapse threshold temperature

The single fibre stress model described in Chapter 2 predicted that the onset of collapse is highly sensitive to temperature. Practical experience of drying timber supports this prediction. This research established that for each sample of wood examined there existed a *collapse threshold temperature*. If wood at MC greater than FSP is dried at temperatures above its collapse threshold temperature, then collapse will occur. If it is dried at temperatures below its collapse threshold temperature, then collapse will not occur. Different collapse threshold temperatures exist for the earlywood and latewood of a sample of wood. Two different methods of determining the collapse threshold temperature were compared, and found to agree closely. Collapse threshold temperature tests were conducted on *E. regnans*, and a subsequent kiln trial during which the temperature was restricted to remain below the collapse threshold temperature, dried a charge of timber free of collapse.

3.1 Materials

Collapse threshold temperature tests were performed in October 1994 at the Hobart laboratory on samples of naturally regenerated *E. regnans* from the Western Tiers region of Tasmania. The last recorded major fire in this area occurred in 1881. Collapse threshold temperature tests and a $20m^3$ kiln trial were also carried out in September 1994 at the Victorian Timber Industry Training Centre at Creswick, Victoria, on 1939 regrowth *E. regnans* (alpine mountain ash) from the Powell Town region of Victoria.

Basic density of the Tasmanian *E. regnans* was 580±30 kg/m^3, green to dry normal tangential shrinkage was approximately 9%, with 0.5% shrinkage at 30% MC (FSP) and 5.5% shrinkage at 10% MC (equilibrium moisture content, EMC).

Basic density of the Victorian *E. regnans* was 484±25 kg/m^3 and normal tangential shrinkage (green to dry) measured on 0.6mm thick transverse slices was approximately 7% with 0.5% shrinkage at an FSP of 30%, and 4.5% shrinkage at an EMC of 10%.

3.2 Collapse threshold temperature determination

3.2.1 Slicing technique

A cube of timber of approximately 20mm side length was cut from a green board at least 30mm clear of the end and edges, to ensure that as little drying as possible had occurred (Fig. 3.2.1). It was then trimmed so that its faces were exactly radial and tangential, and then sliced into longitudinal-tangential (L-T) slices (Fig. 3.2.2) between 0.8mm and 1.5mm thick, separating earlywood (EW) and latewood (LW). Each slice was placed in a wire bridle to prevent out-of-plane deformation (Fig. 3.2.5). Two marks were made on the slice separated tangentially by approximately 20mm. The slice was then allowed to dry at the selected temperature without forced air flow. The slice was periodically weighed and the distance between the two marks recorded (Fig. 3.2.4). After attainment of EMC, slices were oven dried then cooled in a desiccator, and final measurements taken. The same procedure was followed to measure tangential shrinkage of radial-tangential (R-T) slices (Fig. 3.2.3), which were tested simultaneously to ensure the same drying conditions. Shrinkage measured by this technique is generally termed "unconfined shrinkage", that is, free shrinkage of a small section of wood, not restricted by surrounding material as it is whilst still in the form of a block. Obviously, EW and LW cannot be physically separated in an R-T slice, so that there may have been some interaction between the shrinkage of the EW and LW in R-T slices (see Section 4.2.2).

For each slice the data was plotted as MC vs shrinkage. Virtually all of the fibres in the R-T slices were severed by slicing and hence could not be subject to collapse, so that the R-T slices were assumed to undergo normal shrinkage only. Most of the fibres in the L-T slices were undamaged by slicing since they lie in the same direction as the slicing blade, and thus were prone to collapse, so that the L-T slices were assumed to undergo both normal and collapse shrinkage. Thus, the difference between the two curves was collapse shrinkage. The difference between normal shrinkage observed in earlywood and latewood of R-T slices was negligible (see Section 4.2.2). The temperature at which successive slices were dried was progressively decreased until the amount of collapse shrinkage measured was negligible. The temperature at which this occurred was the collapse threshold temperature.

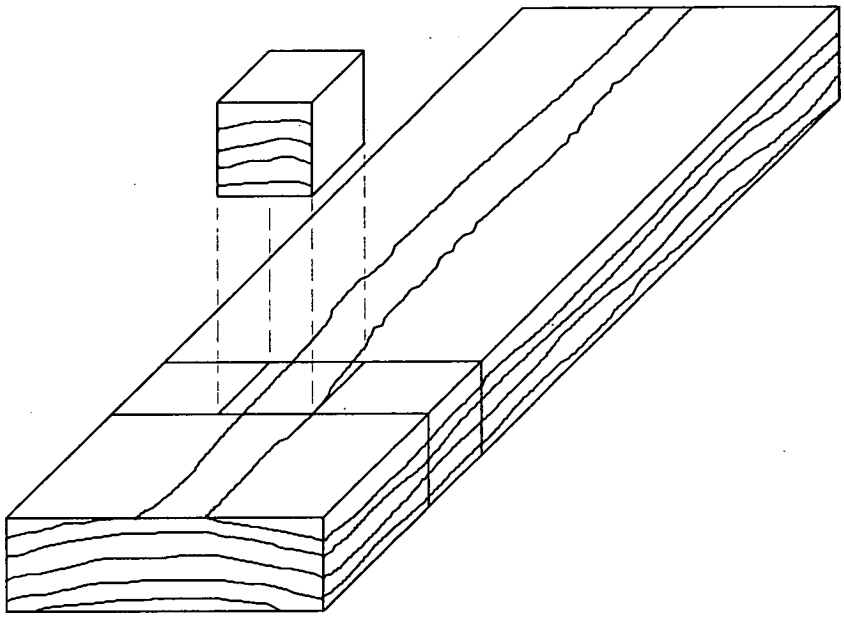

Figure 3.2.1 Cube for slicing

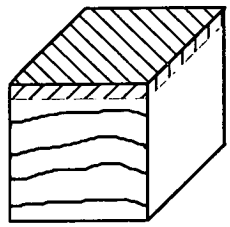

Figure 3.2.2
L-T slice

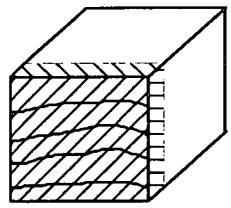

Figure 3.2.3
R-T slice

3.2.2 Board technique

For the Creswick experiments, 200mm long sections of 100×25mm board were rapidly dried in a laboratory oven (with no humidity control) at various temperatures. They were not end-coated. The first two sections (cut from two different boards randomly selected from the stack and cut 100mm clear of the log end) were dried at 40°C for approximately 24 hours. After this, the ends were docked approximately 50mm and the freshly cut surfaces examined for internal checking. They were both found to have small checks in several earlywood bands. The board surfaces exhibited some "washboarding". This is the rippled surface characteristic of timber in which some growth bands have collapsed (see Fig. 3.4.1). The collapse threshold temperature was thus known to be less than 40°C. The test was then repeated at progressively lower temperatures until the samples were found to be free of visible collapse, with no internal checks at all. The highest temperature at which the samples were free of collapse was chosen as the collapse threshold temperature.

A similar procedure was followed for the Tasmanian timber in the Hobart laboratory. The timber was dried in a controlled temperature chamber of $0.25m^3$ with a small 12V fan blowing along the boards. The procedure was refined slightly in that the

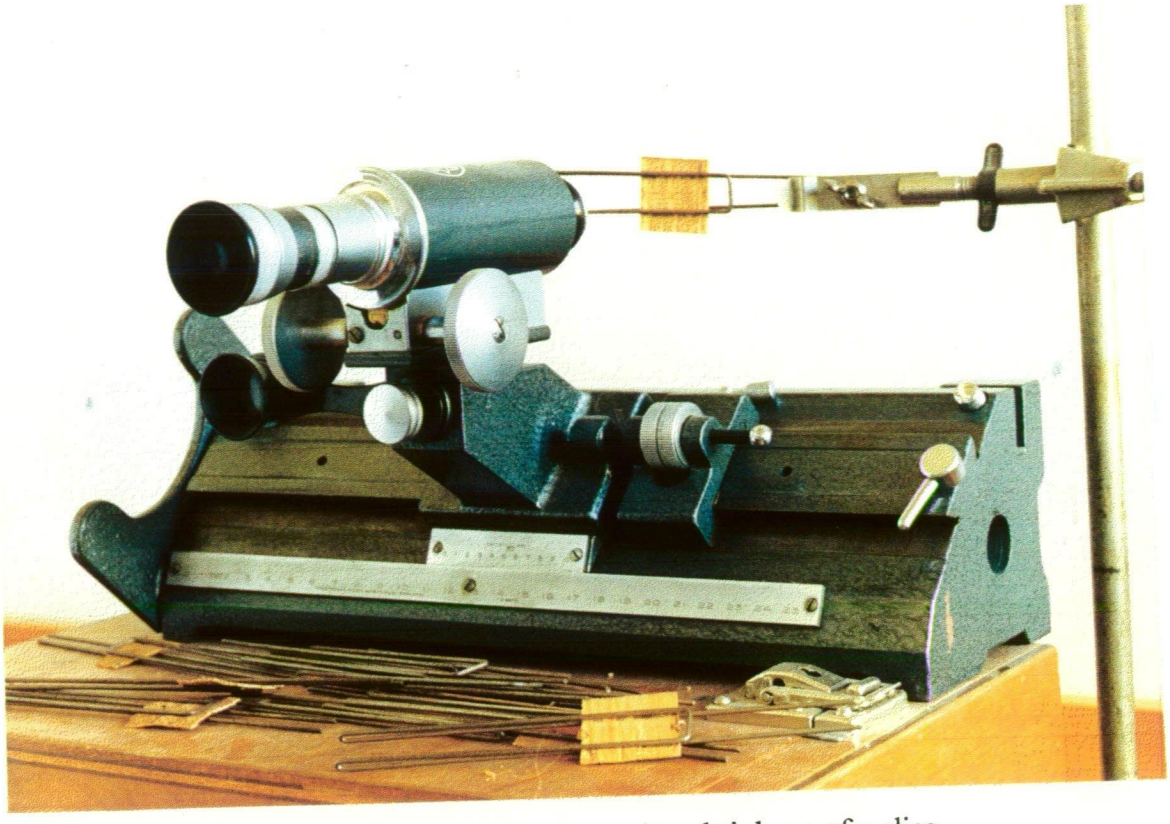

Figure 3.2.4 Travelling microscope for measuring shrinkage of a slice.

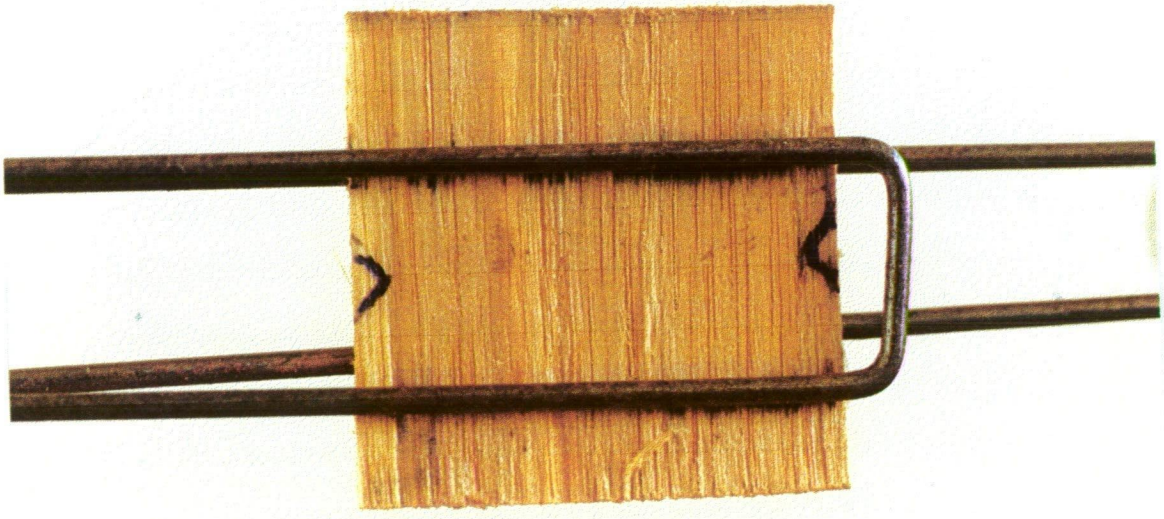

Figure 3.2.5 L-T slice marked for shrinkage measurement, restrained against warping by wire bridle.

board sections for the Hobart trials were end-coated to ensure that end-drying could not interfere with the experiments. Length of the board section used for these tests is irrelevant provided that end-drying is prevented.

3.3 Experimental results

3.3.1 Tasmanian *E. regnans*

Fig. 3.3.1 shows a selection of the measured shrinkage curves. Each curve represents at least two shrinkage measurements. These measurements show that the collapse threshold temperature of this timber is between 24°C and 28°C since collapse shrinkage is evident in the L-T slices dried at 28°C but not in those dried at 24°C. The transverse (R-T) slices do not undergo collapse as all of the fibres have been damaged in slicing.

The board sections that were dried using the technique described in Section 3.2.2 predicted a collapse threshold temperature of approximately 24°C using 2°C increments. The board technique tests were carried out on two 2.4m boards randomly selected from the stack and docked into 300mm sections. One of these boards was also used for the slicing technique tests. Final centre MCs were typically around 60% - if internal checking was going to form, it had usually occurred by this stage, particularly closer to the surface, where the MC was substantially lower.

3.3.2 Victorian *E. regnans*

The board technique yielded a value for the collapse threshold temperature of 30°C. Some of the shrinkage measurements taken on slices are shown in Fig. 3.3.2. Each trace represents at least two individual shrinkage measurements. It is not possible to define a collapse threshold temperature from Fig. 3.3.2 as all of the L-T slices exhibit collapse shrinkage.

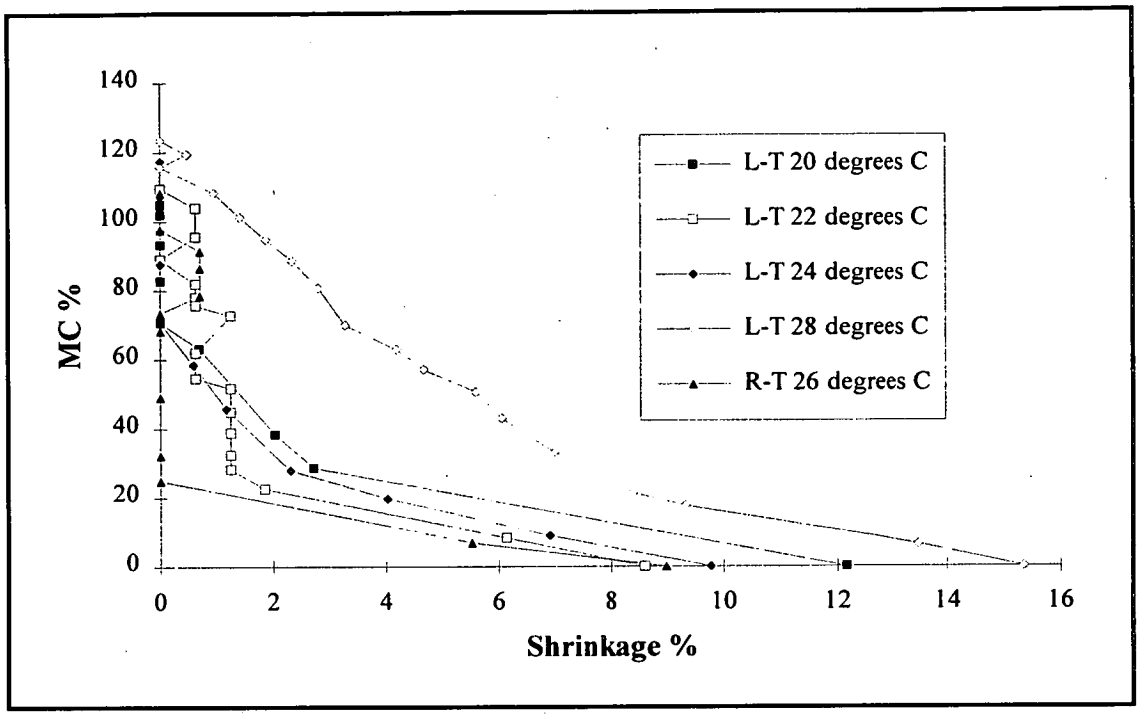

Figure 3.3.1 Shrinkage curves, Tasmanian *E. regnans*. L-T: longitudinal-tangential section, R-T: radial-tangential section.

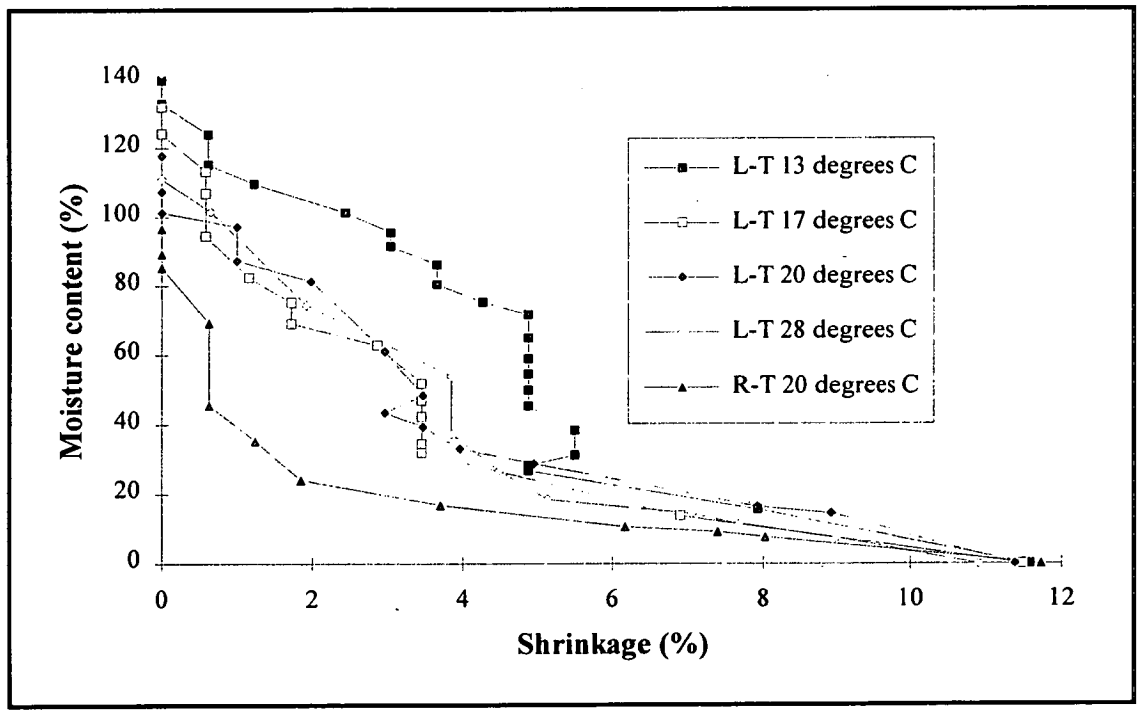

Figure 3.3.2 Shrinkage curves, Victorian *E. regnans*. L-T: longitudinal-tangential section, R-T: radial-tangential section.

3.3.3 Creswick kiln trial

A full charge of the Victorian *E. regnans* was dried in the Victorian Timber Industry Training Centre's 20m^3 "Vanicek" kiln at Creswick in Victoria over a three week period. The charge was of 25mm boards of width between 50mm and 150mm, and predominantly quartersawn. The trial was run as part of the commercialisation program of the Clever Kiln Controller (CKC, Chapter 6). Unfortunately, the trial was marred by several software crashes of the CKC, and repeated failures of the boiler which provided the kiln heating. Despite this, the timber was dried from an initial MC of 120% to an average of approximately 40%, at temperatures below 30°C. At the end of this period, there was no visible collapse. The timber was then left under cover in the open air for another month. Some of the timber displayed collapse after this (see Fig 3.4.2). The collapse was almost certainly caused by high ambient temperatures of up to 40°C which occurred at Creswick during the drying from 40% MC to FSP outside the kiln.

3.4 Discussion

The aim of this investigation was to determine a simple procedure to enable a charge of timber to be dried largely free of collapse. The experimental results presented in Section 3.3 provide evidence which supports the use of the board section technique described in Section 3.2.2 to determine the collapse threshold temperature, and subsequently drying the charge below the collapse threshold temperature, as such a procedure.

Kollmann (1950; cited in Kollmann and Côté 1984) presents a graph showing a linear relationship between relative portion of internal checks and dry bulb temperature between approximately 60°C and 145°C for oak. It appears that "relative portion of internal checks" is a measure of the area of a cross section occupied by internal checks. Kollmann's work provides a measure of damage caused by internal checking, whereas the work presented here demonstrates how such damage may be avoided altogether.

An examination of the collapse in Victorian *E. regnans* shown in Fig. 3.4.2 reveals bulk collapse in the right hand half of the board, without any associated internal

checking. The other half of the board exhibits minimal visible collapse, but several internal checks are seen. This indicates that the checks form as a result of differential shrinkage. We see that the checks are formed in a relatively wide earlywood band flanked by two narrower earlywood bands (separated by latewood bands). It seems that the wide earlywood band is more likely to collapse, as observed by Amos (1954), presumably because it consists of faster grown, thinner walled and larger diameter fibres. When the adjacent earlywood bands do not collapse, there appears to be sufficient differential shrinkage to cause checking. When, however, several adjacent earlywood bands collapse, then there is little differential shrinkage and so no check formation, as seen in the right hand side of Fig. 3.4.2. Thus internal checking can often be found in boards which display minimal externally visible collapse, whilst boards which do show obvious collapse shrinkage may not be internally checked.

Most eucalypt timber is approximately twice as stiff in the radial direction as it is in the tangential direction. This indicates that the latewood bands do not control the bulk stiffness; this seems to be controlled by the ray cells which are thin walled and hence have low stiffness, and pass through earlywood and latewood bands (this is discussed further in Section 4.2.1). Thus the difference in tangential stiffness between earlywood and latewood is much lower than might otherwise be expected. Shrinkage measurements were made on slices of latewood of the Victorian *E. regnans* in this study which did not collapse. The right hand side of Fig. 3.4.2 shows bulk collapse but no internal checking as has been discussed above; clearly the latewood had insufficient stiffness to induce enough differential shrinkage to result in internal checking. Thus, large differential shrinkages between neighbouring earlywood bands are necessary if checking is to occur, irrespective of the shrinkage behaviour of the latewood band between them.

Use of the board section procedure implicitly assumes that the wood temperature remains close to the dry bulb temperature during the board section drying. In fact, the wood temperature at the start of drying is close to the wet bulb temperature of the air stream, rising to be close to the dry bulb temperature of the air stream as the board approaches EMC. This effect has been demonstrated by the model **KilnSched** (verified by wood temperature measurements performed by Schaffner 1981). Since the timber stack would normally be dried at a slower rate than the samples for collapse threshold temperature determination (that is, in an air stream with a higher wet bulb temperature than that during the collapse threshold temperature determination tests, with the same dry bulb temperature), the wood temperature is actually higher during drying than it was during the board section test, and thus more

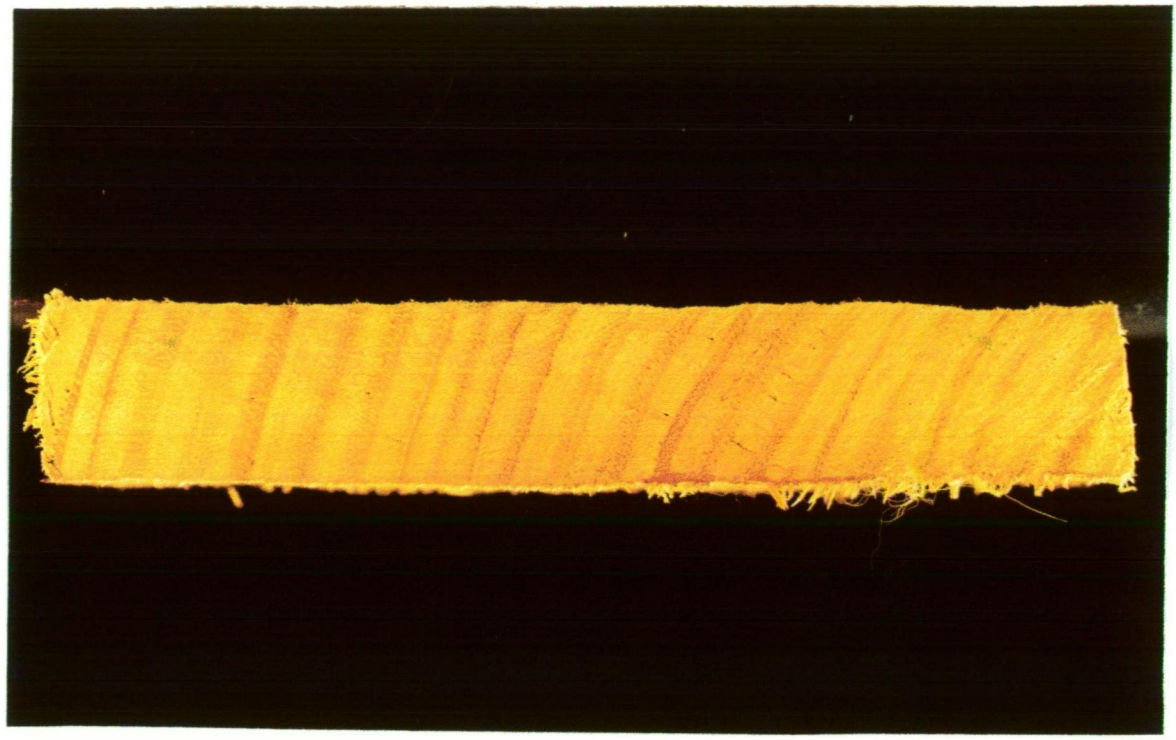

Figure 3.4.1 Section of Victorian *E. regnans* showing "washboarding" and internal checking.

Figure 3.4.2 Section of Victorian *E. regnans* showing collapse with associated internal checking (circled), and collapse with no associated internal checking.

likely to collapse. This is a problem intrinsic to the use of this test, and can be avoided by use of a "safety factor"; drying the timber at a dry bulb temperature lower than the collapse threshold temperature predicted by the board section tests. The use of more sophisticated equipment to control wet bulb temperature during the collapse threshold temperature determination tests, and to thus maintain wood temperature at a constant level during the test (either measured directly or predicted by a drying simulation program such as **KilnSched**) would perhaps allow such a safety factor to be dispensed with, and thus allow more rapid drying of the stack. However, some account must still be taken of variation within the wood in the stack. This, coupled with the extra hardware required to perform the more complex tests results in a problem which can only be solved with an extensive economic analysis. The board section test was first used at Creswick for the experimental work described in Sections 3.3.2 and 3.3.3, so that equipment was limited to that typically available at commercial kilns in Australia.

An important source of variation in collapse threshold temperature between the slice and board techniques specified above is the growth ring selected for the slice. The collapse threshold temperature for a board will be determined by the most collapse susceptible growth ring within the board. In the tests on the Tasmanian timber the slice technique gave a collapse threshold temperature higher than the board test, probably because the most susceptible growth ring had not been selected. Hence, although the slice technique is clearly faster, the board technique is more appropriate for the determination of the collapse threshold temperature for a charge of timber prior to the commencement of drying. It seems that the widest earlywood band is likely to be the most collapse susceptible, so the board sections selected for these tests should have the widest growth rings within them.

The tests on Tasmanian *E. regnans* demonstrated the existence of the collapse threshold temperature with close agreement between the slice and board section measurements. The board section tests carried out prior to the Creswick kiln trial were successful in allowing the kiln charge to be pre-dried free of collapse. The slice tests on the Victorian timber shown in Fig. 3.3.2 do not appear to have been as successful. Unfortunately, shrinkage measurements were not made above 28°C.

Fig. 3.3.2 indicates unusual shrinkage behaviour. We see large shrinkage in all of the L-T sections to approximately 60% MC and 3.5% shrinkage and then a vertical drop of no shrinkage for a MC change of approximately 20%, after which the total shrinkage curves follow the normal shrinkage curve. There are several possible

explanations for this behaviour. It is possible that the slice is behaving like a board, that is, there are significantly non uniform MC and stress profiles within the slice. Alternatively, it seems feasible that only some proportion of the fibres undergo collapse shrinkage because of the density distribution within the earlywood band. A third possible explanation is that the slice initially starts to behave like a collapsing slice, but at some point the water tension in the fibres causing the collapse is lost. It seems possible that the tension could reach a point where cavitation could occur. The fibre would then stop shrinking until the MC reached FSP at which point normal shrinkage would begin.

This type of shrinkage has also been observed in 2.0mm thick R-T slices. This indicates that the shrinkage behaviour is unlikely to be due to the development of moisture profiles through the slice, as the MC distribution could be expected to be approximately uniform since transverse slices dry very rapidly through the exposed end grain.

3.5 Conclusions

A temperature called the collapse threshold temperature is defined as being the highest temperature at which a charge of wood can be dried to FSP without resulting in collapse. The collapse threshold temperatures were found for timber from two trees of *E. regnans* by rapidly drying small samples and also by taking shrinkage measurements on slices. A kiln charge of timber was then successfully dried to 40% average MC free of collapse by drying at temperatures below the collapse threshold temperature.

Chapter 4. Modelling of wood as a heterogeneous material.

Until now, most of the stress-strain and drying modelling of the timber seasoning process has assumed wood to be a homogeneous material. Some models consider the location of pith, heartwood or sapwood (for example, Ranta-Maunus, 1994). Modelling of a board drying with discrete growth bands undergoing collapse requires acknowledgement of the heterogeneous properties of wood with respect to earlywood and latewood. The discussion and modelling below is based on observations of Tasmanian and Victorian eucalypts only.

Trees are roughly cylindrically symmetric structures. Wood essentially consists of alternate bands of earlywood (EW) and latewood (LW) corresponding to the rapid and the slow growth phases of an annual increment respectively. The demarcation between EW and LW is not necessarily abrupt; there may be a gradual change in properties. For instance the distribution of density between the maximum in LW and the minimum in EW is nearly linear (Yang, 1994).

Nearly all of the modelling performed to date has ignored this banded structure and considered wood as a homogeneous material; that is, a material which has the same properties at all points within its structure (given, of course, that the MC and temperature are uniform). This has been appropriate for modelling the stress-strain and drying behaviour of boards which are not subject to collapse. The problem of collapse presents fresh challenges in modelling. Since collapse behaviour of EW and LW is different, it is necessary to treat them differently when modelling wood subjected to collapse inducing conditions. A heterogeneous model for investigation of collapse will thus acknowledge the different properties of EW and LW with respect to shrinkage and moisture movement. The nature of the one-dimensional model used as the basis for this work (**LabS**; Oliver, 1993b; a later version of **KilnSched**) means that only backsawn (slabsawn, or tangential) boards can be simulated by the heterogeneous model.

4.1 KilnSched

KilnSched (Oliver, 1991; Doe et al, 1994; Booker, 1994b) is a one-dimensional drying model which assumes that the wood is homogeneous and orthotropic. The stress-strain behaviour of the board is modelled beyond the proportional limit (ie material properties are non-linear), and it includes creep and mechano-sorptive effect.

The heat-mass-momentum transfer analogy (Rohsenow and Choi, 1961) is used to infer surface heat and mass transfer from a measured friction factor, following measurements from Wu (1989). Above FSP, the board surface is assumed to act as a free water surface; below FSP Nelson's (1983) formula is used. This provides the boundary conditions at the surface of the board for calculation of temperature and MC changes within the board.

Mass transfer within the board is modelled by Fick's law:

$$\frac{\partial q}{\partial t} = D\frac{\partial^2 q}{\partial y^2} \qquad (4.1.1)$$

where q is moisture concentration (kg/m^3), and D is diffusion coefficient (m^2/hour). The diffusion coefficient is assumed to vary with temperature only, according to equation 4.1.2.

$$D = D_0 \exp\frac{-3800}{T_k} \qquad (4.1.2)$$

where D_0 is a constant, and T_K is temperature in Kelvin. D_0 is calculated from a reference diffusion coefficient and the temperature at which it was measured.

The strain is assumed to consist of four separate components. These are necessarily linearly additive, since strain is a purely geometrical concept. Thus the net strain, e_n is given by:

$$e_n = e_u + e_i + e_m + e_c \qquad (4.1.3)$$

where:

e_u = unconfined shrinkage strain

e_i = instantaneous strain

e_m = mechano-sorptive strain

e_c = creep strain

The stress is calculated by assuming that plane sections normal to the surface of the board remain plane (Navier hypothesis), so that the net strain is the same at all depths within the board, and that there is no net force across a board section. **LabS**, the basis

for the heterogeneous model, is a later version of **KilnSched** and can use non-uniform grid spacings. This allows the input of arbitrary grid spacings to correspond to the location of latewood and earlywood growth bands. However, since the internal moisture concentration distributions are calculated in **LabS** by fitting parabolas to logarithms of moisture concentration, a wide grid spacing followed by a narrow one can cause the predicted moisture concentration to overshoot. To avoid this problem, each grid spacing was set to be greater than approximately 50% of the previous grid spacing.

4.2 Modifications to consider wood as a heterogeneous material

4.2.1 Strength properties

Since the latewood is denser than the earlywood, it would initially appear that it should be modelled as being stiffer. Consider a section of wood, far from the centre of the tree so that the growth rings can be approximated as being straight (see Fig. 4.2.1). If the wood were loaded in the tangential direction, then the stiffness would be determined by the stiffer latewood. If the wood were loaded radially, across the layers, then the stiffness would be determined by the softer earlywood. That is, if the bulk stiffness of the timber were controlled by the latewood being stiffer than the earlywood, then it follows that wood should be stiffer tangentially than radially.

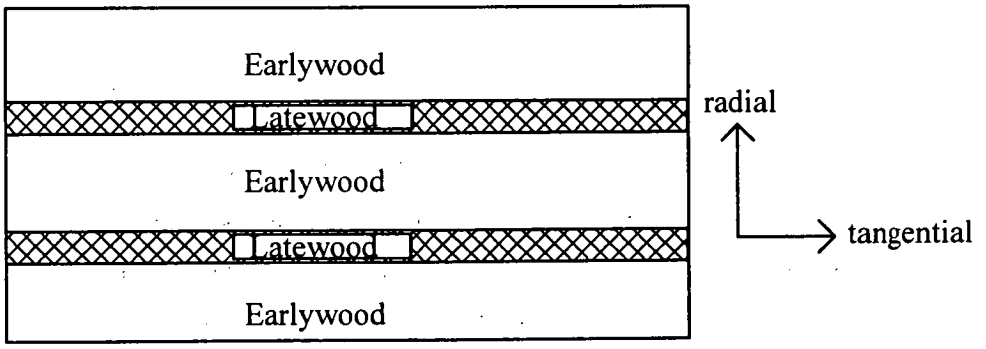

Figure 4.2.1 Idealised section of wood

In fact, the opposite is true for eucalypt timbers, the radial stiffness is approximately twice the tangential stiffness. An explanation has been proposed for this by Ilic (1987). Consider a block of isotropic material with many holes in one direction (see Fig. 4.2.2). The area reduction effect in the z direction of Fig. 4.2.2 is much less than that in the x or y directions, so that the block is much stiffer when stressed in the z direction than when stressed in the x or y directions.

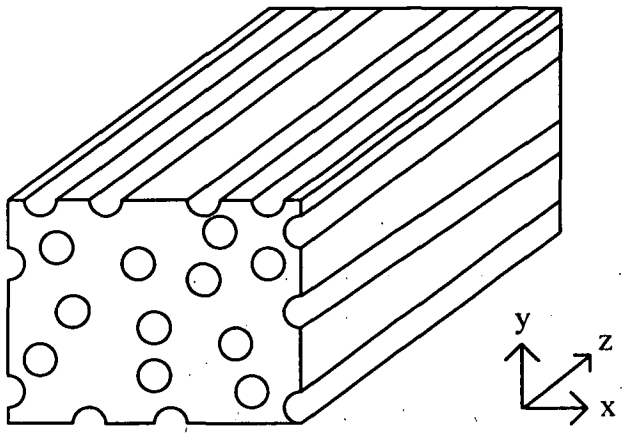

Figure 4.2.2 Block of isotropic material with holes in one direction

Eucalypt timber has a large number of vessels in the radial direction as compared to those in the tangential direction (Ilic, 1991). The rays in the tangential direction soften the timber more radially; those in the radial direction soften the timber more tangentially, by the argument above. Thus the timber is overall stiffer radially than tangentially, by a factor of approximately two. The softening effect of the rays is a bulk effect, since the rays pass through EW and LW. Thus tangential stiffnesses of the EW and LW are assumed to be the same, but subject to the effects of variation in temperature and MC. Similarly, radial stiffness is assumed to be uniform through the wood, subject to the effects of variation in temperature and MC.

4.2.2 Shrinkage properties

Due to the higher content of cell wall material per unit volume in LW, it probably undergoes slightly greater normal shrinkage than EW. In fact, Pentoney (1953) measured radial and tangential shrinkage on isolated springwood (EW) and summerwood (LW) of Douglas fir (*Pseudotsuga taxifolia*). He found that LW shrinkage was greater than EW shrinkage by factors of 1.5 and 3.7 in the tangential and radial directions respectively. His samples were approximately 1.5mm radially by 5mm tangentially by 1mm longitudinally. Thus, collapse shrinkage could not occur as all of the tracheids would have been cross cut (Pentoney states that the

average tracheid length in Douglas fir is approximately 3mm). The shrinkage measurements Pentoney presents consist only of dry shrinkage values, not complete shrinkage curves so that it is not possible to determine if any shrinkage occurred at MC above FSP. Measurements were made directly by a travelling microscope capable of 5μm resolution. Unfortunately, Pentoney does not state how the samples were marked for measurement, or restrained from out-of-plane deformations; an error in tangential shrinkage of 1% would have resulted from a linear measurement error of only 25μm at each of the two measurement points for each shrinkage value given. The samples were cut with a saw, so that physical damage to the tracheids may have affected the results.

Comparable measurements were not carried out for the eucalypt timbers examined in this study because the technical difficulties inherent in measuring shrinkage on samples less than 1mm radially and longitudinally (fibre length and LW width are much smaller in eucalypts than in softwoods such as Douglas fir) were considered to be sufficiently large as to make such measurements unreliable. Thus, the normal shrinkage measurements of EW and LW were made on R-T (cross-sectional) slices approximately 20mm radially and tangentially by approximately 0.8mm longitudinally, so that some interaction between shrinkage of the attached EW and LW was expected. In fact, no measurable difference between the normal shrinkage of attached EW and LW was detected. The physical differences between Douglas fir and eucalypt timbers precluded the use of Pentoney's measurements in this investigation. Thus for the purposes of the modelling performed, the same normal shrinkage curve was used for both earlywood and latewood.

Total shrinkage of EW and LW were measured on separate L-T slices at various temperatures; shrinkage of EW and LW is clearly different if either is undergoing collapse. These shrinkage curves were then fitted with hyperbolas for use in the model.

4.2.3 Moisture properties

EW and LW have different properties with respect to moisture absorption and desorption, due to their different structures. The strategy to cope with this in the model is outlined below.

EW fibres have thinner walls and larger lumens than LW fibres. There is thus a larger proportion of void volume in EW than in LW. Correspondingly, EW generally has a higher initial MC (IMC) than LW, typically 140% as compared to 80% for LW for Tasmanian eucalypt timbers. EW typically also has a larger proportion of vessels than LW, but it is assumed that most of the water in these has drained out soon after sawing.

It is important to note that the models work on absolute moisture concentration (AMC, kg water/m^3 wet wood) and not moisture content (MC, kg water/kg dry wood). It is easy to approximately convert from one to the other by using the relation;

$$AMC = MC \times BD \qquad (4.2.1)$$

where BD = Basic density (dry mass of wood/green volume of wood).
Note that this is not exact, since the green volume of wood is greater than the volume at any lower MC.

EW and LW have different IMC as explained above. The simple diffusion model for a homogeneous material based on moisture concentration would then predict moisture movement from the EW to the LW. This clearly does not happen, as otherwise the IMCs of EW and LW would have reached equilibrium at the same point. It appears that it is the concentration of free water in the void volume that provides the gradient for moisture movement above FSP. Thus, free water can diffuse from LW to EW, even though the actual AMC of the LW is lower. Below FSP, the driving potential for moisture movement is assumed to be moisture concentration in the fibre wall material. Fibre walls are assumed to be fully saturated at moisture concentrations above FSP.

Assuming that the cell wall materials in EW and LW have a similar affinity for water, then FSP will occur at the same MC (and thus different AMC) in EW and LW. Hence, on the basis of this argument, separate FSP points need to be defined in the model for EW and LW.

To provide for this heterogeneity, an adjusted moisture concentration for the latewood is defined, LWAMC. LWAMC is defined such that it is equal to the AMC in the EW under conditions which do not cause diffusion between EW and LW. One such condition is the saturation condition. That is, LWAMC = AMC of EW at their respective IMCs. Another condition is the FSP condition. When all of the free water has been removed, but the cell walls are fully saturated, no diffusion between EW and

LW is expected. A third condition is that LWAMC = 0 when AMC of the latewood = 0. The adjustments are outlined below.

Above FSP;

$$LWAMC = \frac{MC0LW - FSPLW}{MC0EW - FSPEW} MC + FSPLW - \frac{MC0LW - FSPLW}{MC0EW - FSPEW} FSPEW \quad (4.2.2)$$

Below FSP;

$$LWAMC = \frac{FSPLW}{FSPEW} MC \quad (4.2.3)$$

where:

MC0 Refers to initial moisture concentration

FSP Refers to fibre saturation point

LW Refers to latewood

EW Refers to earlywood

These modifications were included by the author in a computer program called **HetLabS** (**Het**erogeneous **Lab**oratory kiln **S**cheduling program). See Appendix D for a block diagram of **HetLabS**.

4.3 Experimental Results

Experimental tests were performed on wood from one board of *E. regnans*. The tree came from the Western Tiers region of Tasmania, and was naturally regenerated; the last major fire in this area occurred in 1881. Basic density of the wood was 580±30 kg/m^3.

4.3.1 Shrinkage measurement

Tangential shrinkage was measured on L-T and R-T slices using the technique described in Section 3.2.1.

For each slice the data was plotted as MC vs shrinkage. The R-T slices were assumed to undergo normal shrinkage, as nearly all of the fibres would have been damaged in

cutting. The L-T slices were assumed to undergo total shrinkage (both normal and collapse shrinkage) since most of the fibres were undamaged by slicing. Shrinkage measurements were carried out at 20°C, 22°C, 24°C and 28°C. Results are shown below in Figs. 4.3.1 to 4.3.4. Each trace is representative of two separate measurements, which generally did not differ by more than 1.5% shrinkage anywhere on the curve. Normal shrinkage measured on R-T slices (not shown) was not dependent on temperature, and consisted of 0% to 0.5% shrinkage to FSP, and approximately 9% shrinkage oven dry. There was no measurable difference between normal shrinkage measured on an earlywood part of the R-T slice and that measured on the latewood part of the slice.

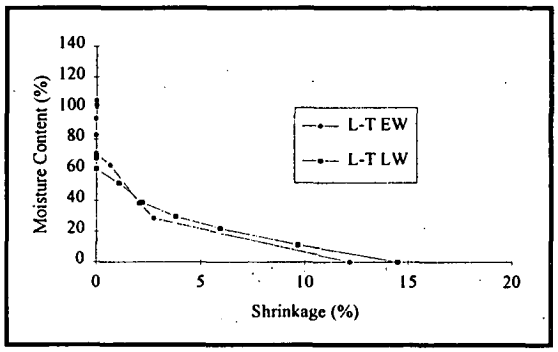

Figure 4.3.1 Shrinkage measured on slices at 20°C

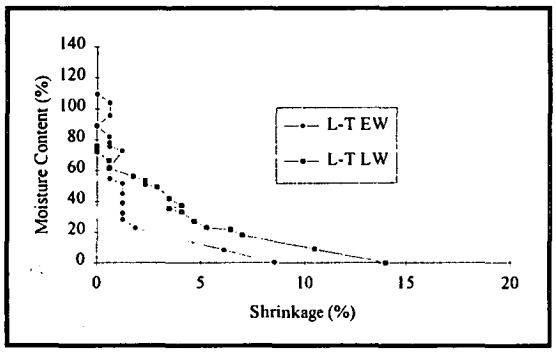

Figure 4.3.2 Shrinkage measured on slices at 22°C

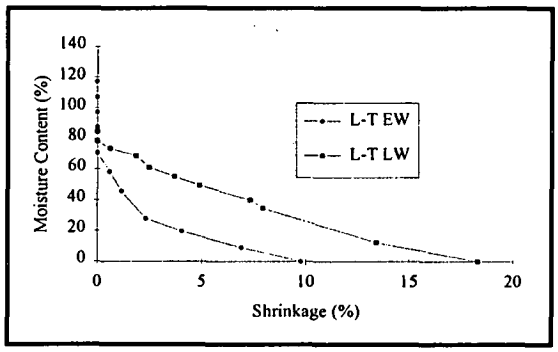

Figure 4.3.3 Shrinkage measured on slices at 24°C

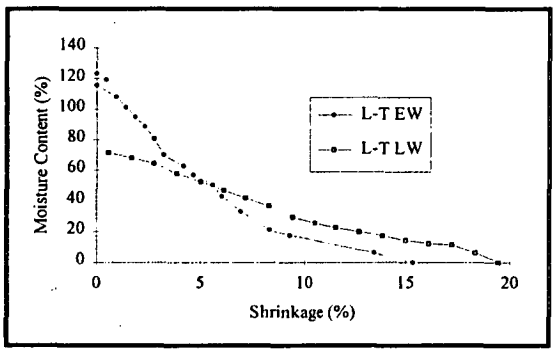

Figure 4.3.4 Shrinkage measured on slices at 28°C

Examination of Figs. 4.3.1 to 4.3.4 reveals collapse shrinkage in the latewood at all of the temperatures at which measurements were taken; in contrast, the earlywood only demonstrates substantial collapse shrinkage in the measurements taken at 28°C. Note that this designation of the shrinkage as being due to collapse follows the definition of collapse shrinkage as that shrinkage which occurs at MC *above* FSP. If the normal shrinkage of unconfined LW were indeed greater than that of unconfined EW, this would only affect the results at MC *below* FSP.

Examination of boards at the mill has shown that earlywood normally collapses more readily than latewood, this is seen as rippled or "washboarded" board surfaces. Shrinkage tests on earlywood and latewood slices of other samples of wood support these observations. The timber under study here is thus unusual in having latewood more prone to collapse than earlywood.

Usually, internal checks start in discrete earlywood bands, presumably as a result of the collapse shrinkage occurring in those bands but not in others. It would thus be reasonable to expect that, if the latewood were collapsing, then internal checks would start in the latewood. This was in fact observed; see Figs. 4.3.5 and 4.3.6 . These are photographs of cross sections of the Tasmanian *E. regnans* boards dried at temperatures below 26°C. In general, internal checks appeared in the earlywood of this timber sample only when it was dried at temperatures above 26°C; at temperatures below this, most internal checks were seen to start in bands of latewood. The collapse threshold temperature of the latewood of this timber is less than 20°C (assuming that one exists).

4.3.2 Collapse threshold temperature trials

Rapid drying trials using the board technique described in Section 3.2.2 were conducted to confirm the collapse threshold temperature for earlywood shown in the shrinkage trials to be between 24°C and 28°C. End-coated backsawn board sections of 150×30mm approximately 200mm long were dried in an insulated chamber of $0.25m^3$ with a small fan blowing along the boards. Dry bulb temperature was controlled to within ±0.4°C, and humidity maintained at a similar level to that of the laboratory by venting. The collapse threshold temperature for earlywood was determined by drying board sections at progressively lower temperatures until no collapse or internal checking was visible in the earlywood. Note that accurate control of drying conditions other than dry bulb temperature is not required for collapse threshold temperature determination as it is assumed that drying rate does not significantly affect propensity to collapse (see Sections 5.1 and 5.2 for an examination of the possible effect of creep and mechano-sorptive strains on fibre collapse). Tests were run at temperatures of 35°C, 28°C, 26°C and 24°C.

Figure 4.3.5 Photograph of a section of Tasmanian *E. regnans* showing an internal check in a latewood band.

Figure 4.3.6 Photograph of a section of Tasmanian *E. regnans* showing three internal checks in two latewood bands.

The board section tests showed visible collapse accompanied by some internal checking. Many of the internal checks appear to have formed initially in the latewood (see Figs. 4.3.5 and 4.3.6). Internal checks generally did not form in the earlywood when the timber was dried at temperatures below approximately 26°C. Usually, collapse occurs only in the earlywood, producing a "washboarded" appearance. The collapsed boards did not have this "washboarded" appearance since the collapse occurred predominantly in the latewood bands, which are usually much narrower than the earlywood bands. It is not clear as to why collapse occurred first in the latewood bands in this wood. The lumens of latewood fibres are smaller than those of earlywood fibres, so that the internal tension which can be sustained in the latewood fibres before the occurrence of cavitation is higher than that which can be sustained in earlywood fibre lumens. Hence, although the latewood fibre walls are obviously stiffer than the earlywood fibre walls, it appears possible that the walls of the latewood fibres were not sufficiently stiffer than those of the earlywood fibres to withstand the greater tension generated in the latewood fibre lumens.

4.4 Results from mathematical modelling

The properties of the timber measured above were used as input data for the model, and a uniform initial moisture concentration of 696 kg/m^3 (moisture content of 120%) assumed. The model was then run for various drying conditions, first to qualitatively validate the output from the model, and then to predict the response of the timber to other drying conditions. Three drying strategies were compared:

- Drying at temperatures which caused collapse in the latewood but not in the earlywood.
- Drying at temperatures which caused collapse in both the latewood and the earlywood.
- Drying at higher temperature to determine if the resultant softening of the wood was sufficient to allow the differential shrinkages imposed by collapse without internal check formation.

The shrinkage tests on slices indicated that the latewood collapsed at temperatures between 20°C and 28°C. It is assumed that it would also collapse at higher

temperatures. That is, it is assumed that there is a collapse threshold temperature for the latewood which is less than 20°C.

The experimental board tests described in section 4.3.2 showed the appearance of incipient internal checks in the collapsing latewood bands (see Figs. 4.3.5 and 4.3.6). These were rapid drying tests which also surface checked the wood. The aim of the tests was to provide a connection between the shrinkage curves measured at specific temperatures, and formation of collapse-related internal checking when boards were dried at these temperatures. The aim of modelling the drying was to ascertain whether the timber could be dried free of surface and internal checks in a reasonable time. The rapid drying tests themselves could not be modelled, as surface checking formed early in the drying, and the model clearly cannot simulate the stress-strain or moisture movement behaviour of surface checked boards.

To carry out the modelling, the reference diffusion coefficient used was 1.7e-7 m^2/hr at 25°C, a typical value for Tasmanian eucalypts. EW and LW ring widths and positions of the modelled timber are shown in table 4.4.1. When simulating drying at temperatures above the collapse threshold temperature, all of the earlywood bands were assumed to undergo collapse shrinkage. Latewood was assumed to collapse at all simulation temperatures. The first simulation was carried out for constant kiln conditions of 20°C dry bulb temperature, 18°C wet bulb temperature, and air velocity of 1m/s. Figs. 4.4.1 to 4.4.6 show the results from the model. Legends indicate simulated drying time.

Note that the surface stress increases for the first 150 hours drying, then starts to decrease; the simulated board was about to go into stress reversal. The moisture concentration profiles show slightly higher moisture concentration in the latewood than the earlywood. The basic density difference between early and latewood means that the predicted MC of latewood is significantly lower than that of earlywood at moisture concentrations above FSP. The unconfined shrinkage strain profiles show peaks in the latewood bands since they are presumed to undergo collapse. Fig. 4.4.4 shows that the instantaneous strain in the first latewood band reaches the ultimate value of 0.02 before the instantaneous strain at the surface does. Note that the failure criterion used here is instantaneous strain. Thus, even if this timber is dried surface check free, it will probably form internal checks in the collapsing latewood bands. The internal checks form even though the stress in the first latewood band is lower than the stress at the surface. Figs. 4.3.5 and 4.3.6 support the use of this failure criterion. The collapse in these boards tended not to be very visible on the surfaces,

so that there would be no indication of drying induced defects until the wood was machined.

Dimension	EW	LW	EW	LW	EW	LW	EW	LW
Width (mm)	2.0	1.6	2.7	1.8	3.2	0.6	1.8	1.4
Distance from surface (mm)	2.0	3.6	6.3	8.1	11.3	11.9	13.7	15.1

Table 4.4.1 Earlywood and latewood ring widths and positions.

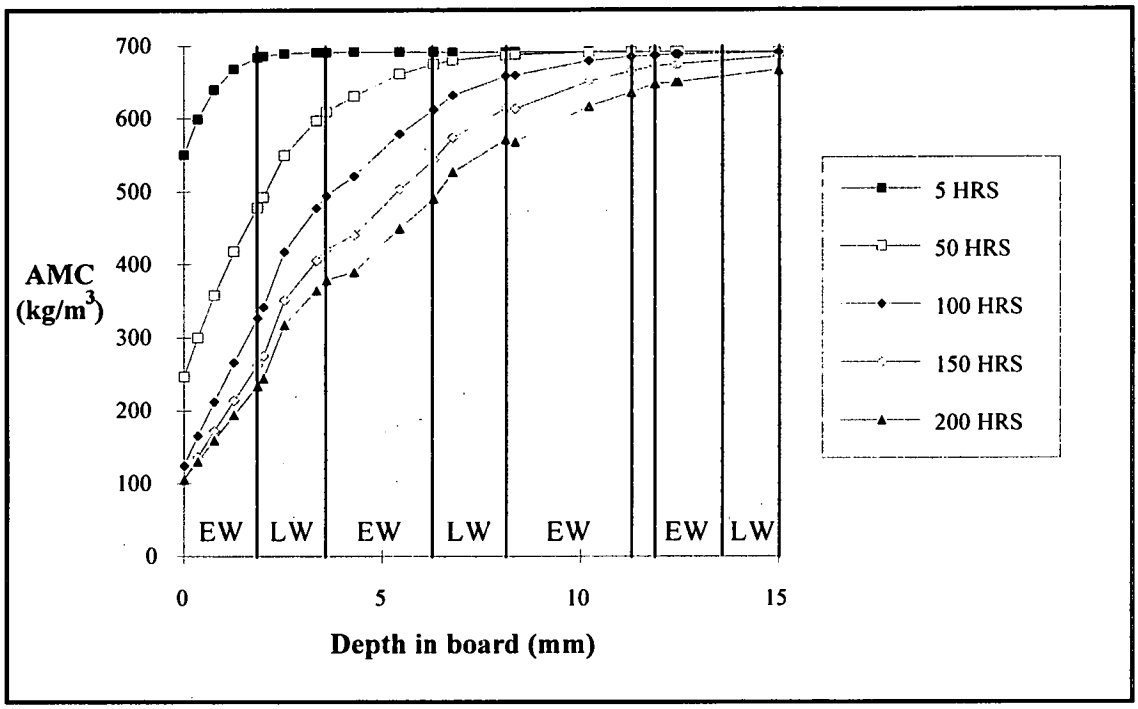

Figure 4.4.1 Moisture concentration profiles in board predicted by mathematical model. Drying conditions: 20°C dry bulb, 18°C wet bulb, 1m/s velocity.

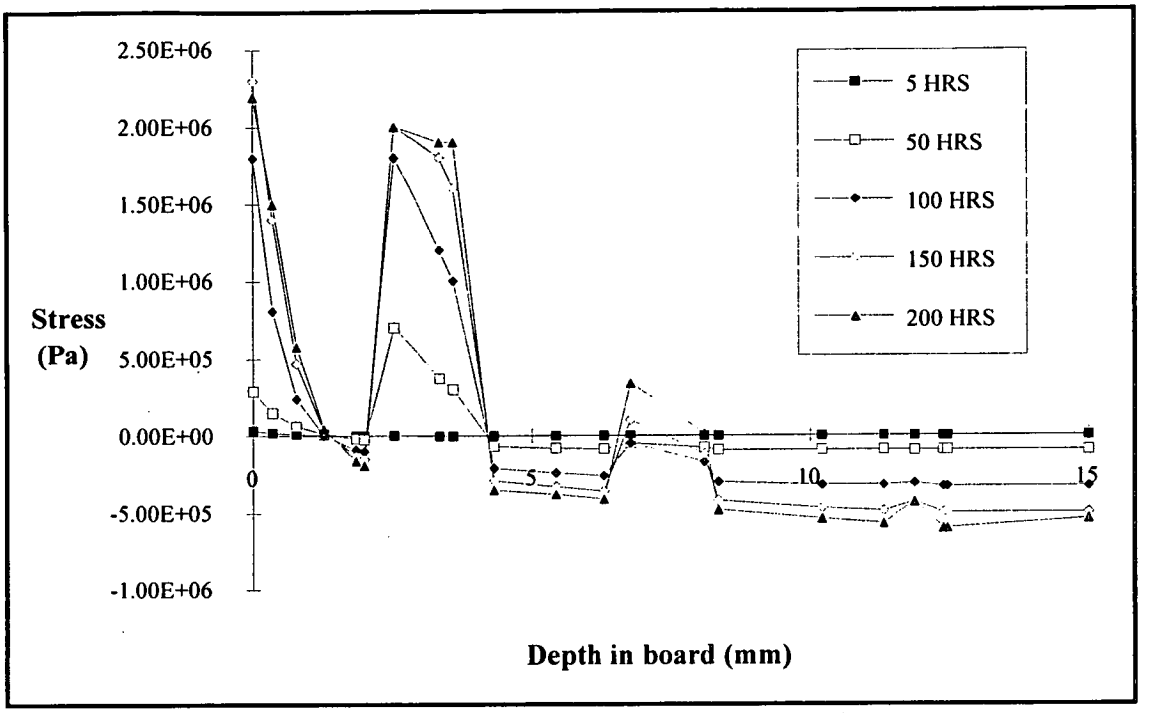

Figure 4.4.2 Stress vs depth in board predicted by mathematical model. Drying conditions: 20°C dry bulb, 18°C wet bulb, 1m/s velocity.

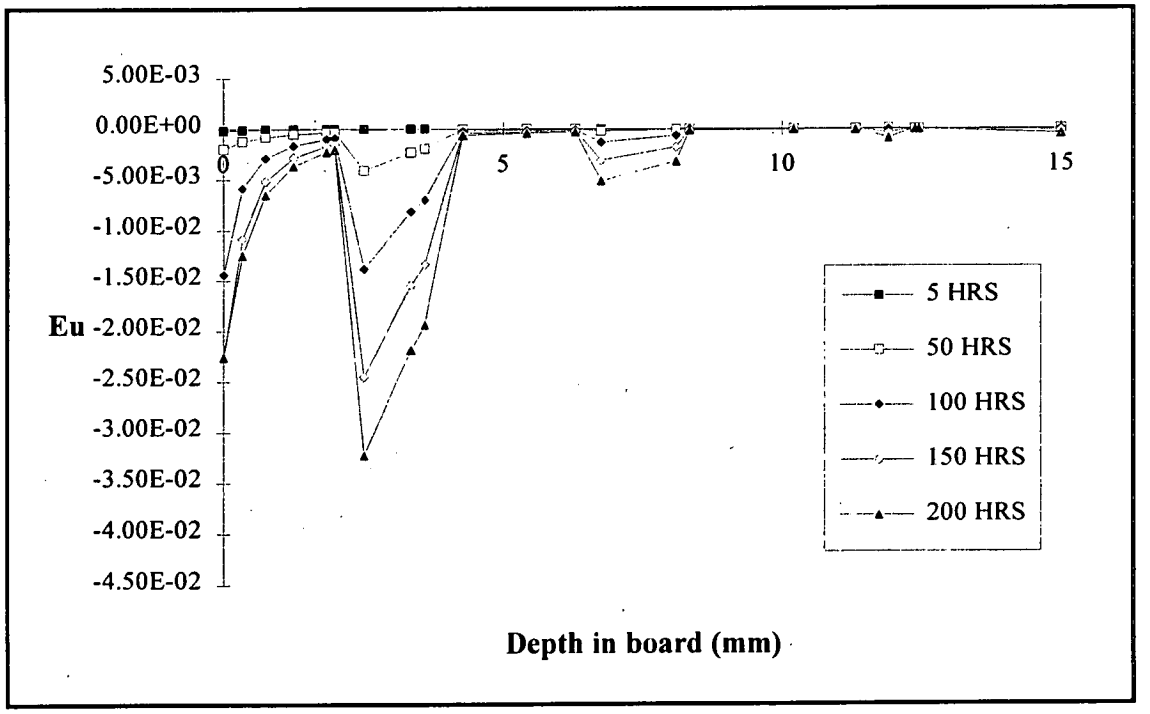

Figure 4.4.3 Unconfined shrinkage vs depth in board predicted by mathematical model. Drying conditions: 20°C dry bulb, 18°C wet bulb, 1m/s velocity.

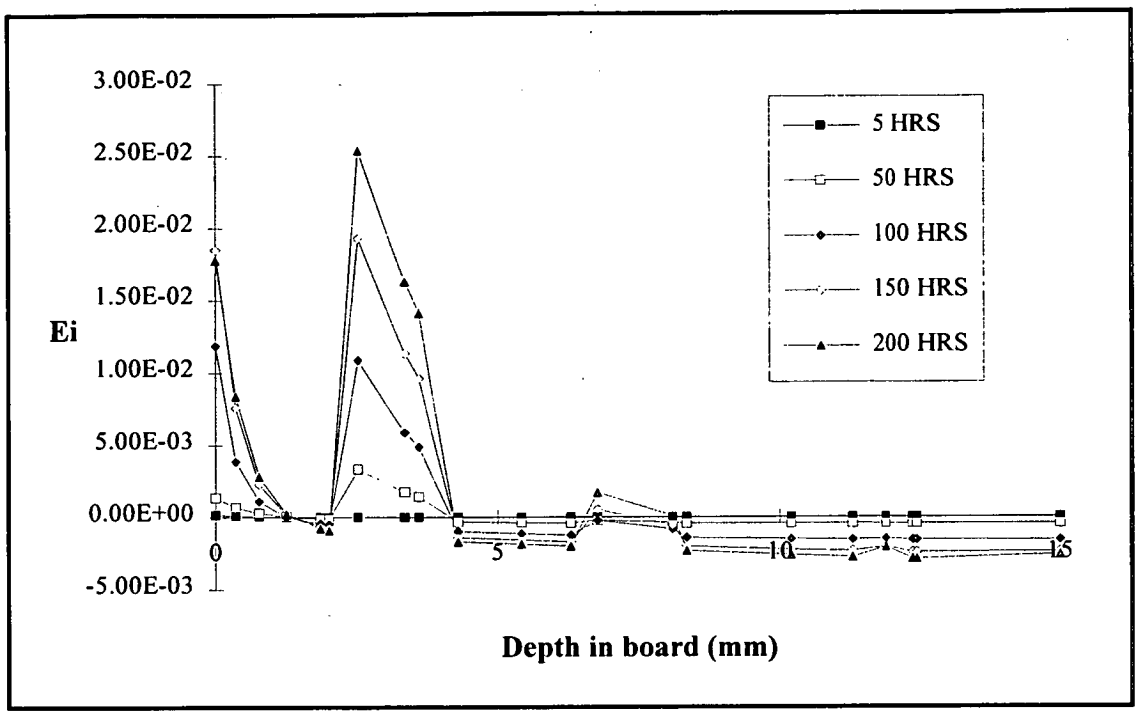

Figure 4.4.4 Instantaneous strain vs depth in board predicted by mathematical model. Drying conditions: 20°C dry bulb, 18°C wet bulb, 1m/s velocity.

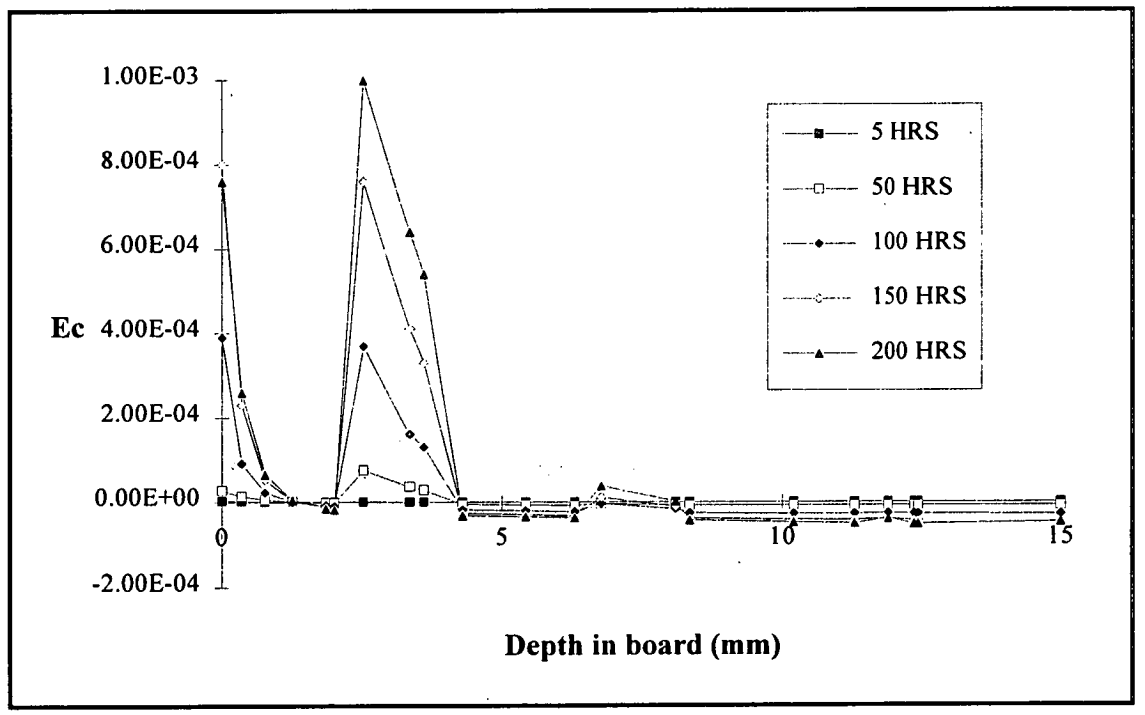

Figure 4.4.5 Creep strain vs depth in board predicted by mathematical model. Drying conditions: 20°C dry bulb, 18°C wet bulb, 1m/s velocity.

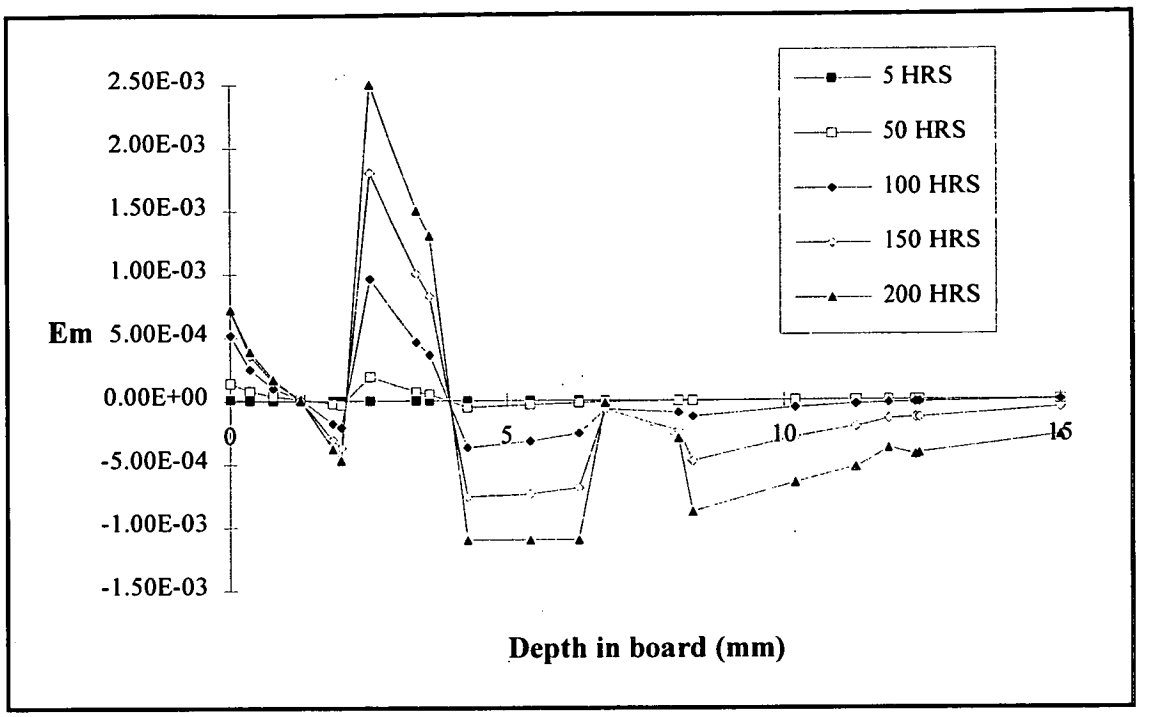

Figure 4.4.6 Mechano-sorptive strain vs depth in board predicted by mathematical model. Drying conditions: 20°C dry bulb, 18°C wet bulb, 1m/s velocity.

The program predicted that even if the board were dried under a very mild schedule which would not produce any surface checking, internal checks would form in the bands of collapsing latewood. The program's predictions for location of internal checking agreed qualitatively with the observed results from board tests on the *E. regnans* being modelled, with internal checking forming initially in collapsing latewood bands near the surface.

The program was run again for much milder conditions to see if the timber could be dried free from internal checks. Results are shown in Figs. 4.4.7 to 4.4.12.

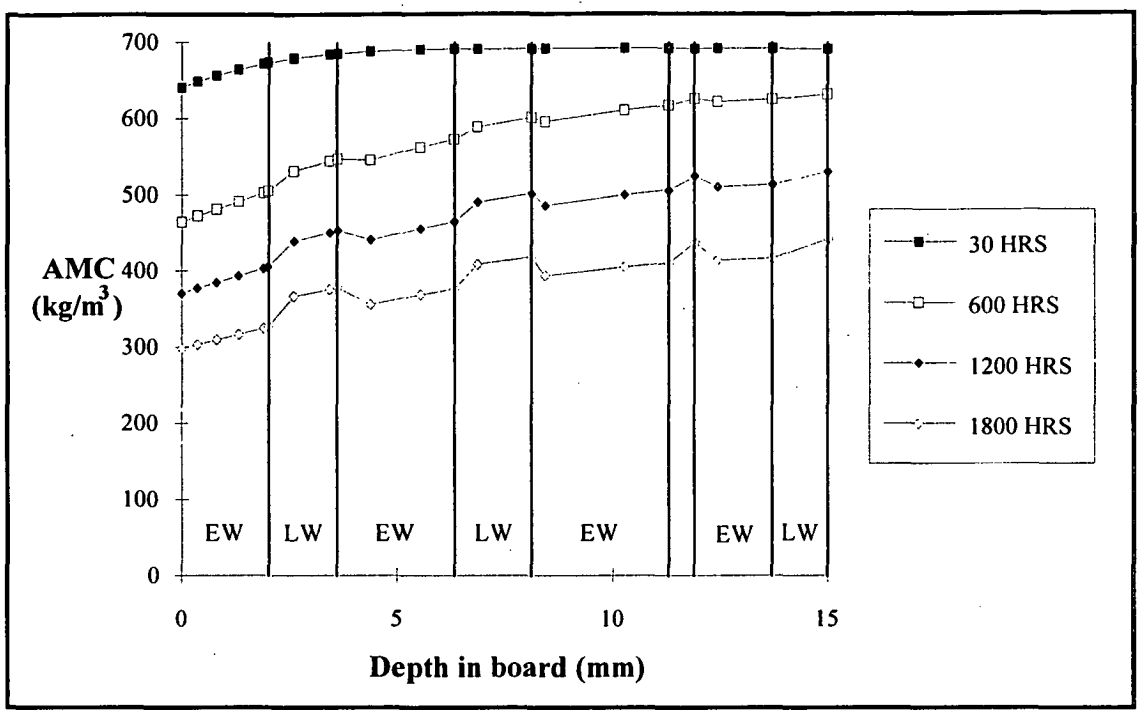

Figure 4.4.7 Moisture concentration profiles predicted by mathematical model. Drying conditions: 20°C dry bulb, 19.4°C wet bulb, 0.5m/s velocity.

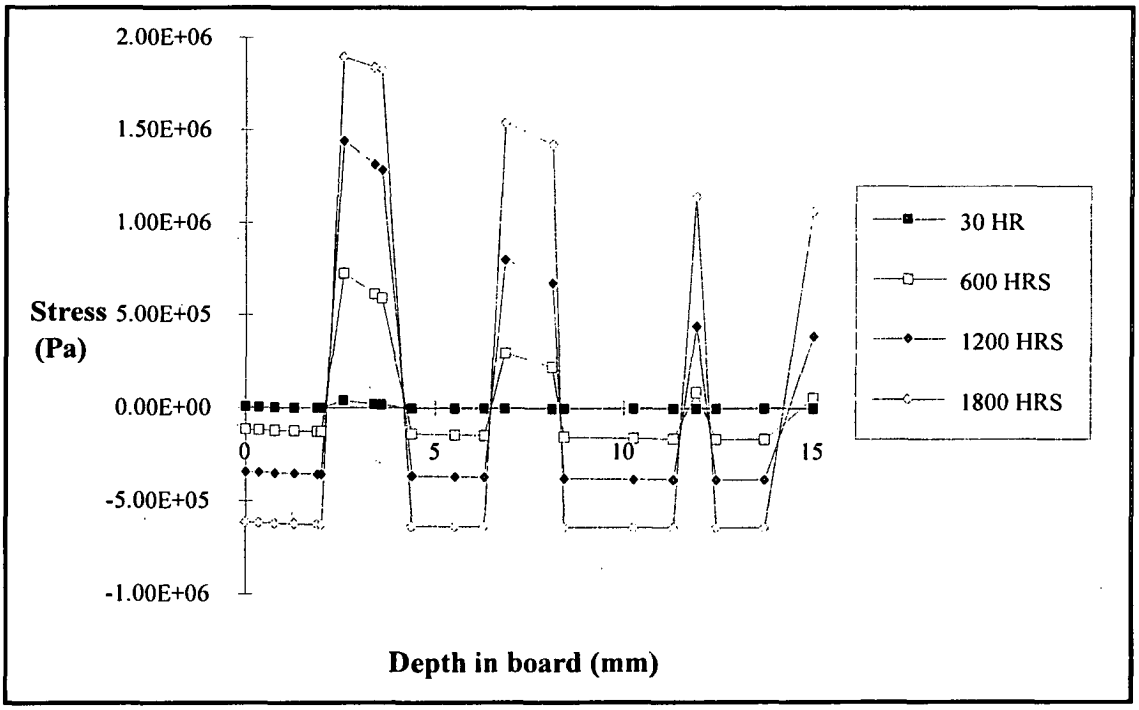

Figure 4.4.8 Stress vs depth in board predicted by mathematical model. Drying conditions: 20°C dry bulb, 19.4°C wet bulb, 0.5m/s velocity.

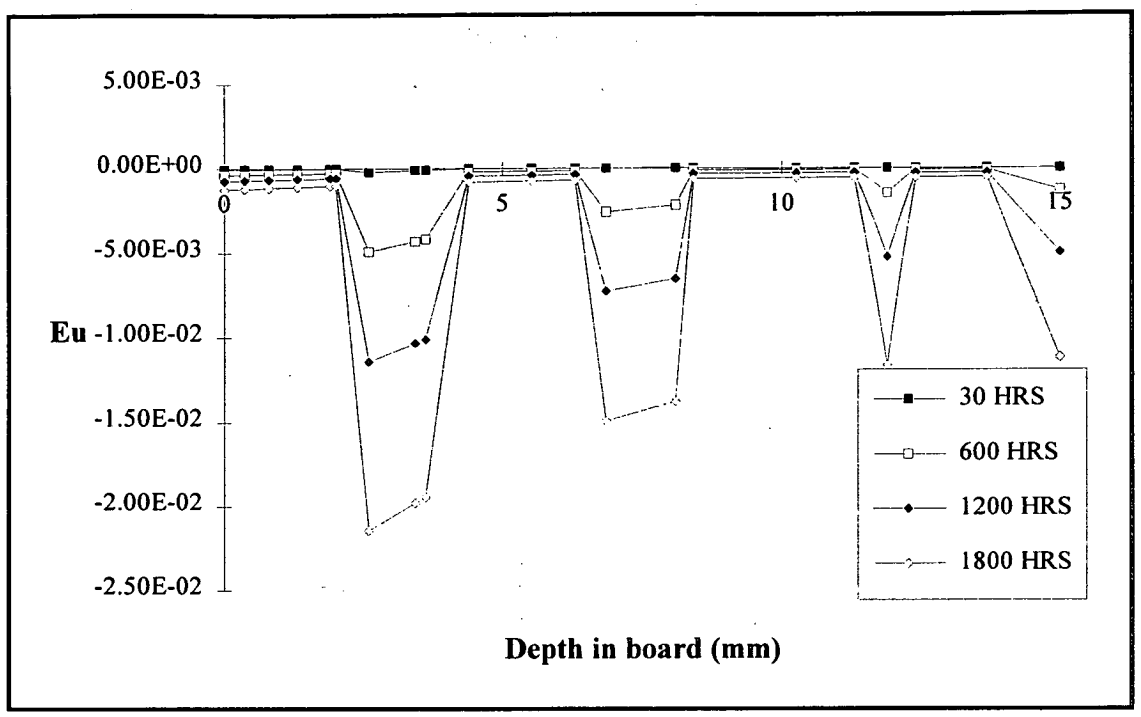

Figure 4.4.9 Unconfined shrinkage strain vs depth in board predicted by mathematical model. Drying conditions: 20°C dry bulb, 19.4°C wet bulb, 0.5m/s velocity.

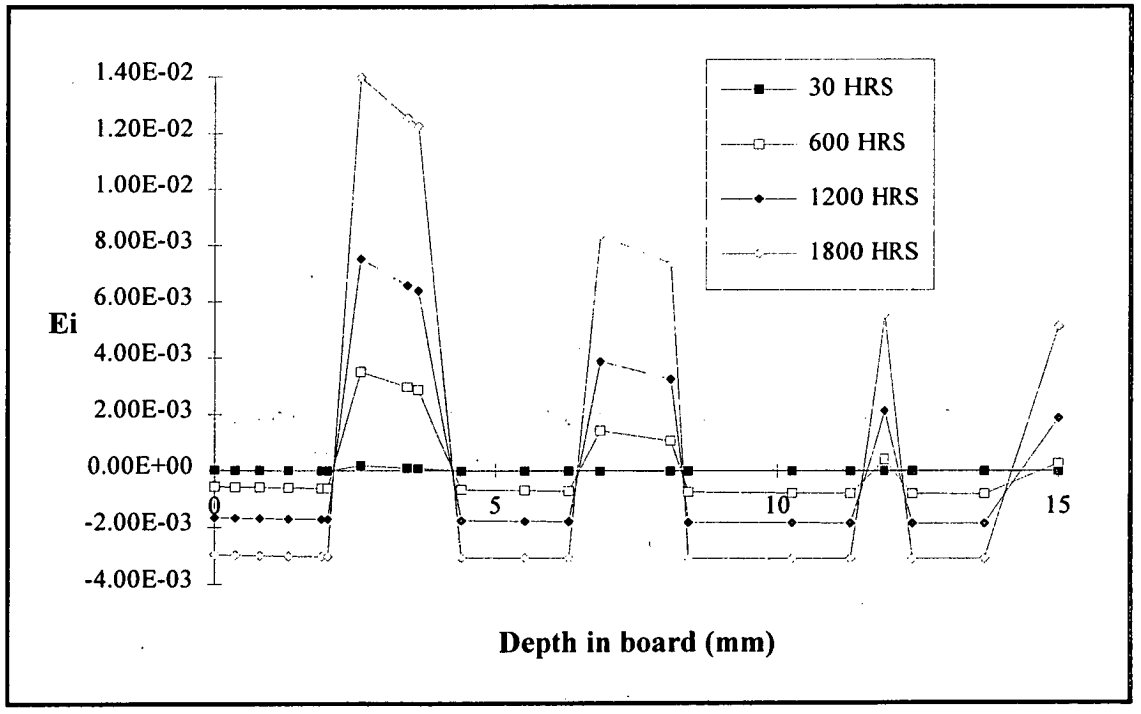

Figure 4.4.10 Instantaneous strain vs depth in board predicted by mathematical model. Drying conditions: 20°C dry bulb, 19.4°C wet bulb, 0.5m/s velocity.

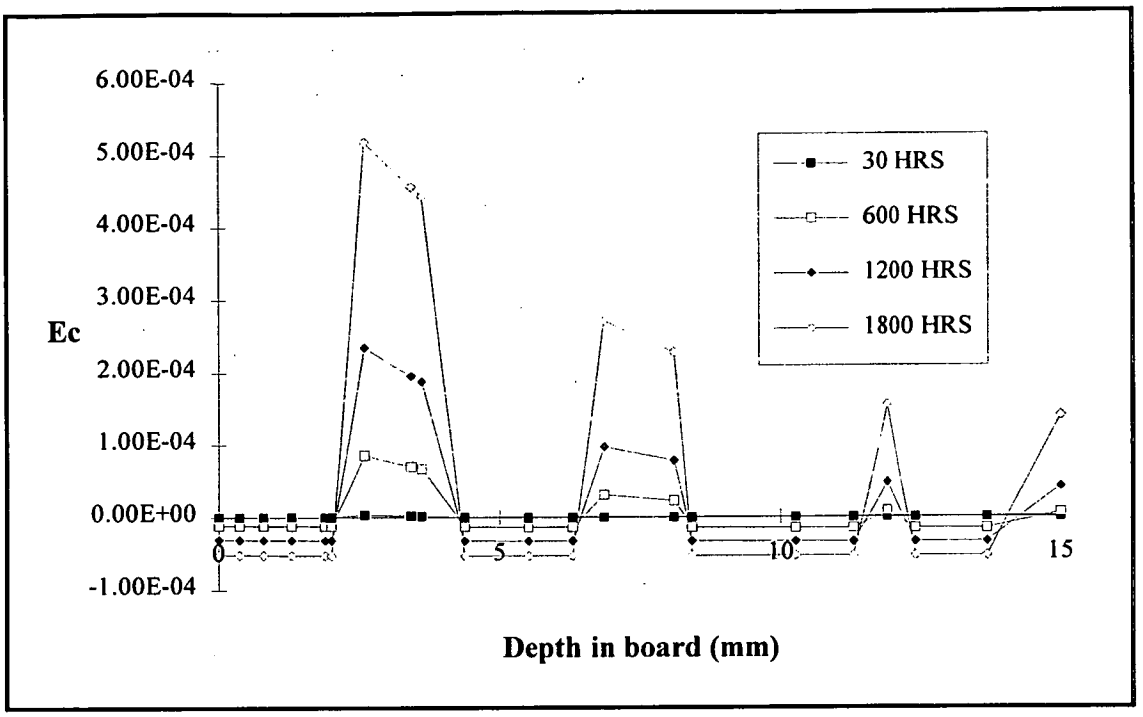

Figure 4.4.11 Creep strain vs depth in board predicted by mathematical model. Drying conditions: 20°C dry bulb, 19.4°C wet bulb, 0.5m/s velocity.

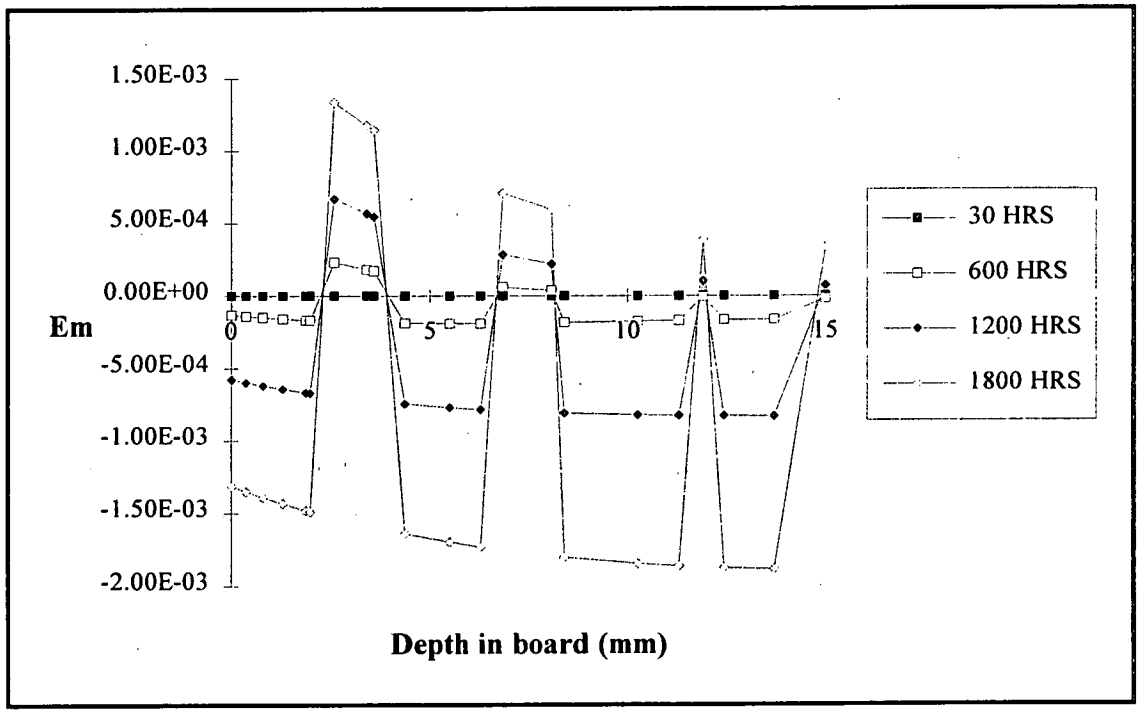

Figure 4.4.12 Mechano-sorptive strain vs depth in board predicted by mathematical model. Drying conditions: 20°C dry bulb, 19.4°C wet bulb, 0.5m/s velocity.

The simulation results show that to reduce the drying rate sufficiently to avoid internal check formation requires an absurdly low drying rate - after 1800 hours drying the surface moisture content is of the order of 56%. The drying atmosphere is so moist

that the surface of the board never goes into tension at all. Note the much more uniform stress and strain profiles due to the slower rate of drying and much longer drying time. The instantaneous strain at the first latewood band in from the surface actually reached 1.61E-2 at 1950 hours simulation, and was still increasing. The model was run again with a (collapsing) latewood band at the board surface, to find whether this would require slower drying or not. Results are shown in Figs. 4.4.13 to 4.4.18.

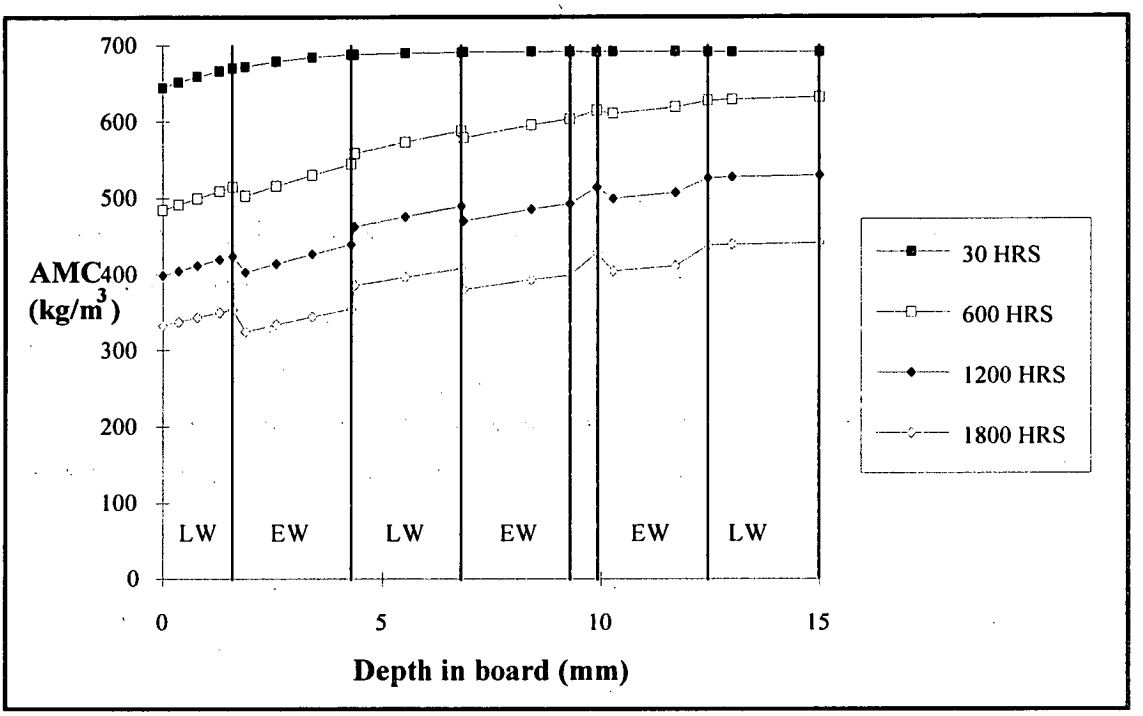

Figure 4.4.13 Moisture concentration profiles predicted by mathematical model. Drying conditions 20°C dry bulb, 19.4°C wet bulb, 0.5m/s. Surface is latewood.

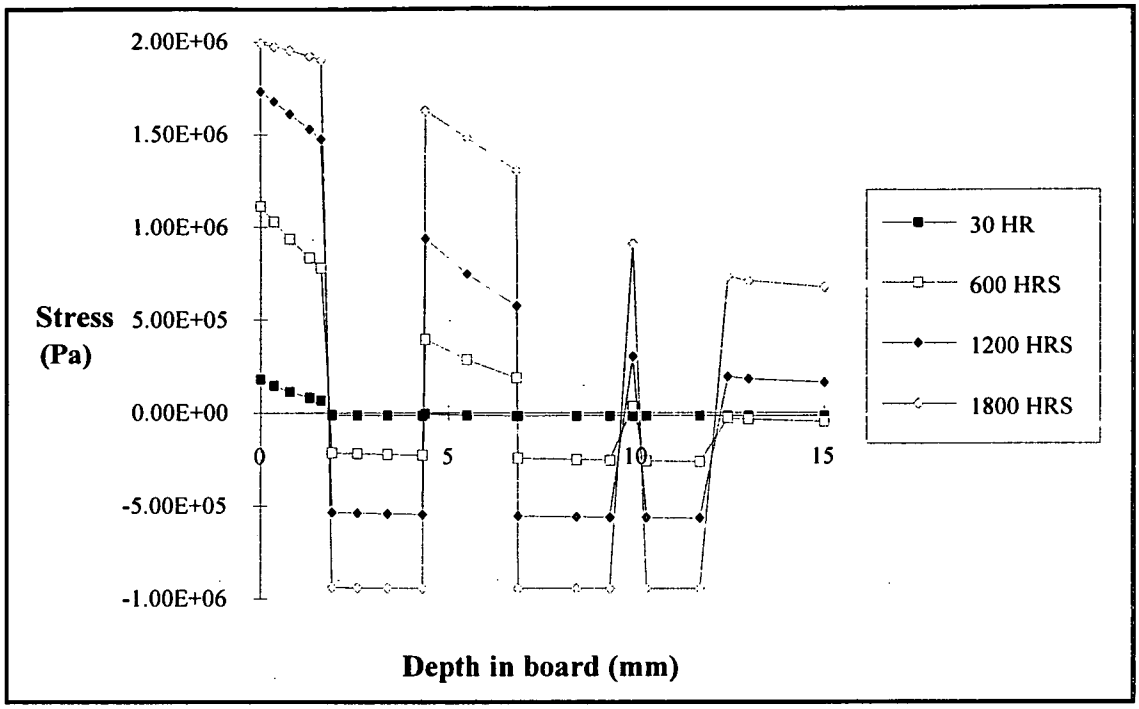

Figure 4.4.14 Stress vs depth in board predicted by mathematical model. Drying conditions 20°C dry bulb, 19.4°C wet bulb, 0.5m/s. Surface is latewood.

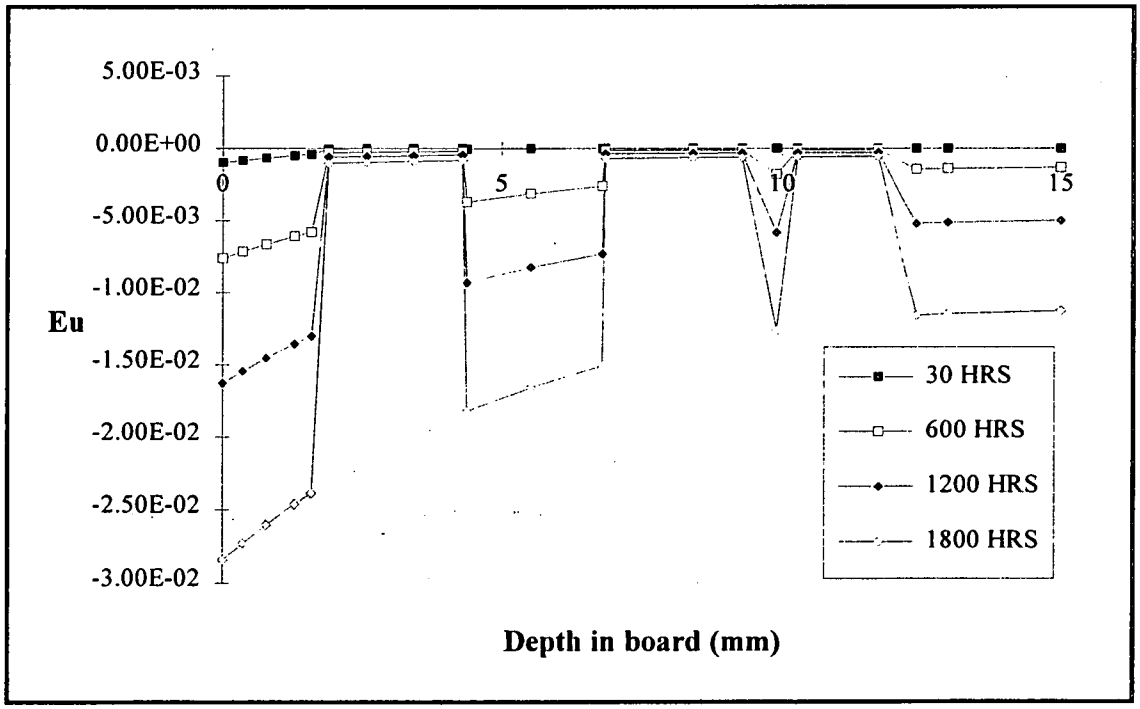

Figure 4.4.15 Unconfined shrinkage strain vs depth in board predicted by mathematical model. Drying conditions 20°C dry bulb, 19.4°C wet bulb, 0.5m/s. Surface is latewood.

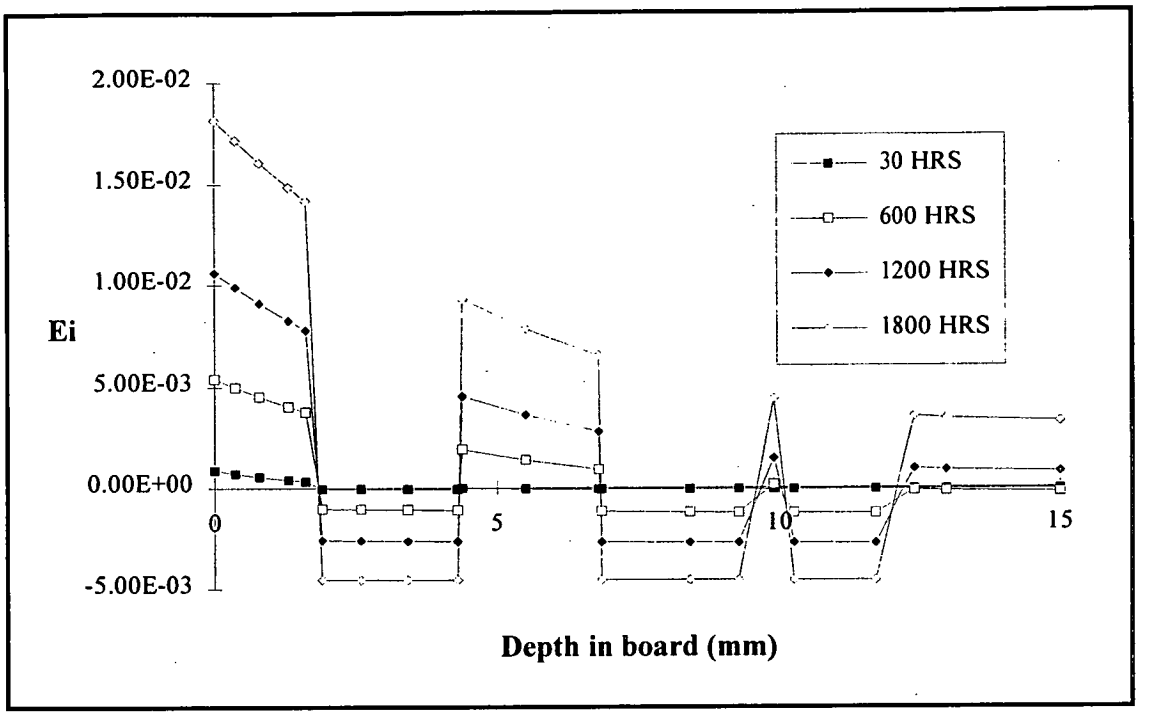

Figure 4.4.16 Instantaneous strain vs depth in board predicted by mathematical model. Drying conditions 20°C dry bulb, 19.4°C wet bulb, 0.5m/s. Surface is latewood.

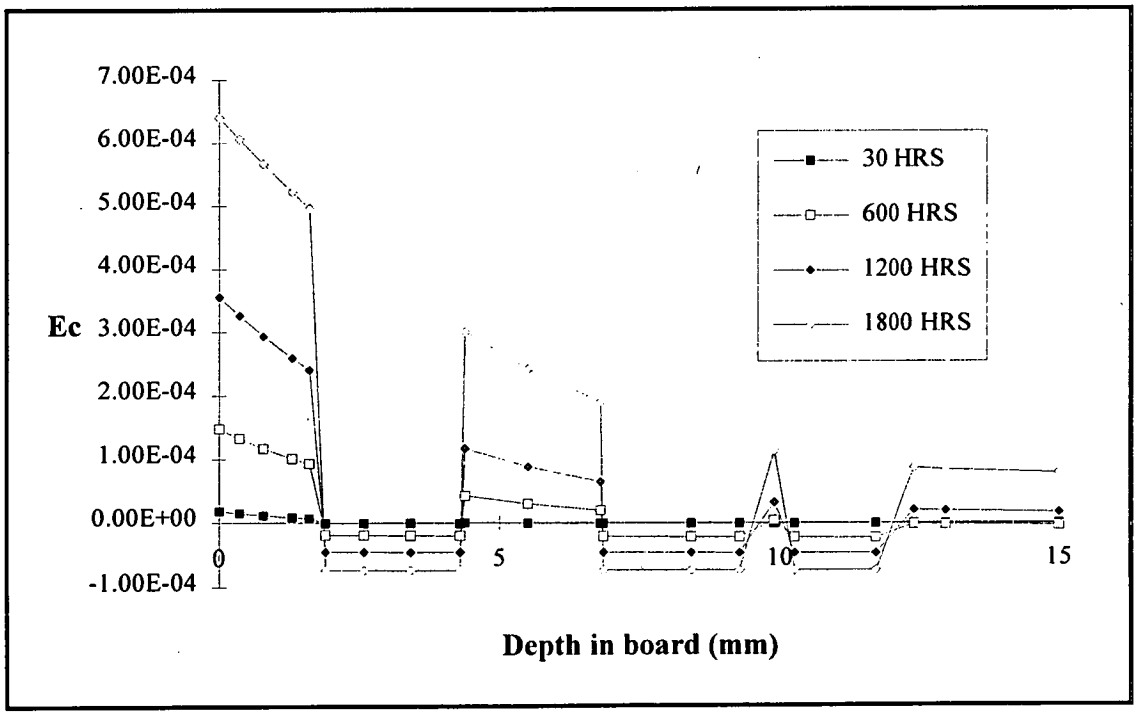

Figure 4.4.17 Creep strain vs depth in board predicted by mathematical model. Drying conditions 20°C dry bulb, 19.4°C wet bulb, 0.5m/s. Surface is latewood.

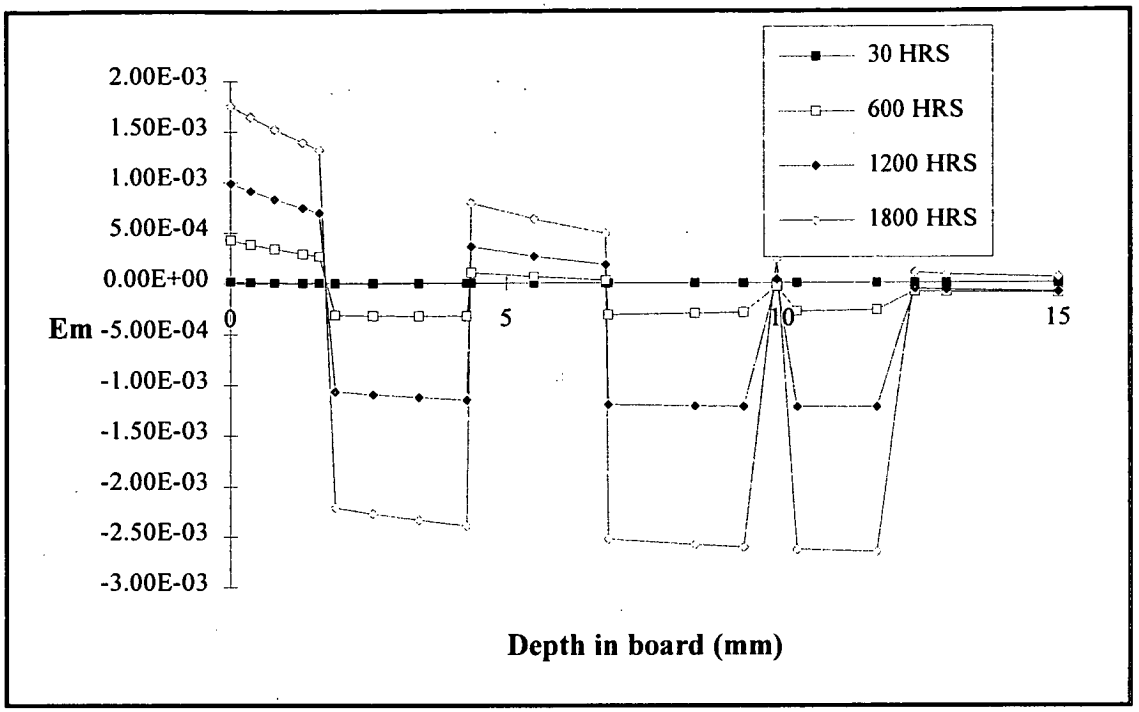

Figure 4.4.18 Mechano-sorptive strain vs depth in board predicted by mathematical model. Drying conditions 20°C dry bulb, 19.4°C wet bulb, 0.5m/s. Surface is latewood.

The simulation showed that the simulated board formed surface checks at 1932 hours. Average MC was similar to the previous simulation with the same drying conditions. Comparison of the two simulations shows that the limiting case for drying rate is having the growth band at the surface collapsing. It appears that drying this timber at 20°C with the latewood collapsing is not economically feasible, due to the large amount of time required. Very precise kiln control would be required to season this timber without inducing unacceptable degrade.

It would initially appear possible to dry this timber successfully at temperatures above 28°C since the early and latewood shrinkage behaviour at this temperature seem similar. To test this hypothesis, simulations were run for conditions of 30°C dry bulb temperature and 0.7m/s air velocity. Wet bulb temperature was adjusted to a value which did not induce surface or internal check formation. The final value chosen for wet bulb temperature was 29.2°C. Results are shown in Figs. 4.4.19 to 4.4.24.

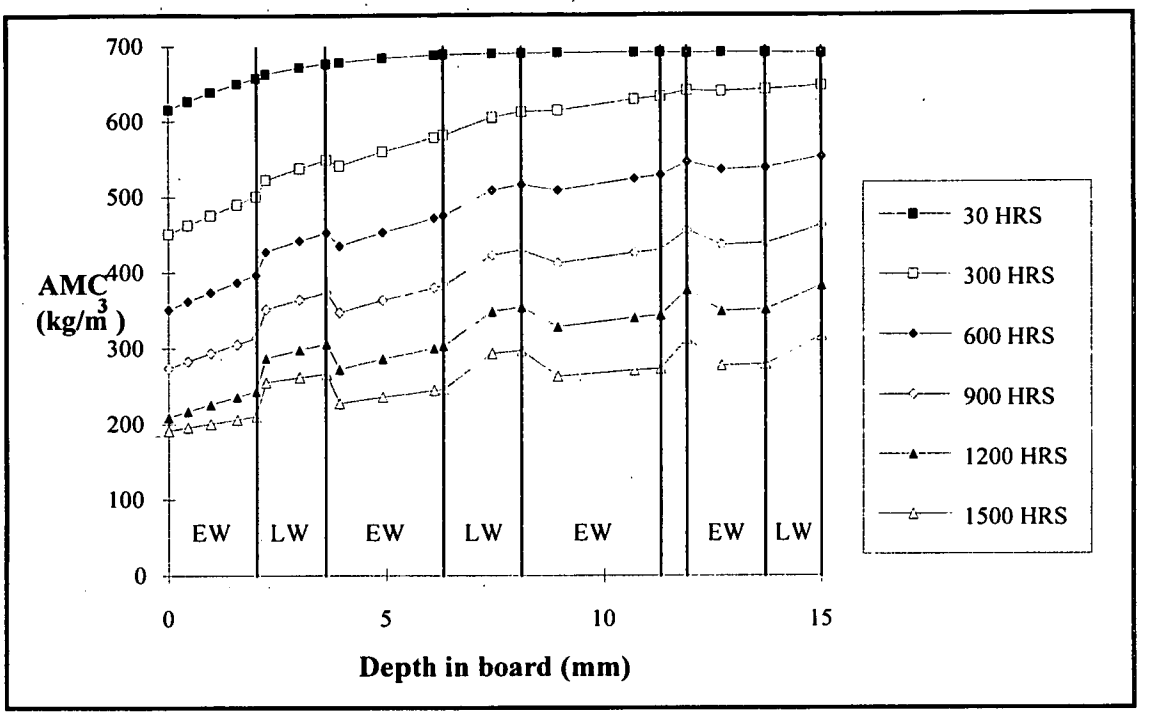

Figure 4.4.19 Moisture concentration profiles predicted by mathematical model. Drying conditions: 30°C dry bulb, 29.2°C wet bulb, 0.7m/s velocity.

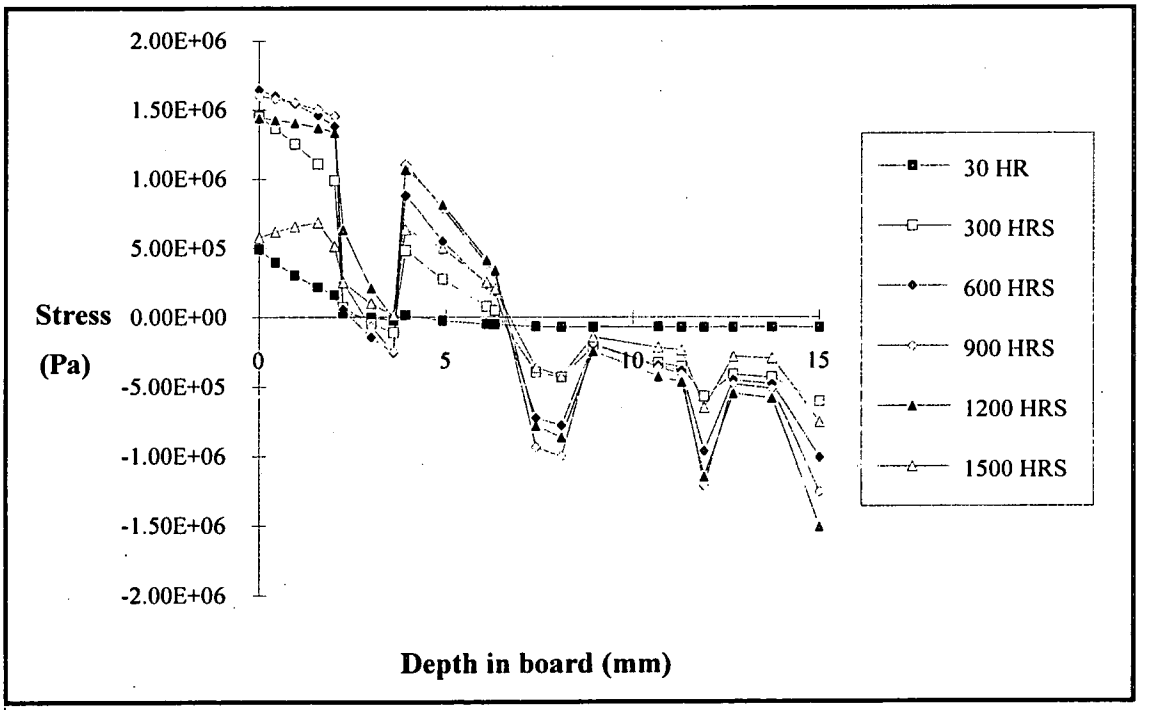

Figure 4.4.20 Stress vs depth in board predicted by mathematical model. Drying conditions: 30°C dry bulb, 29.2°C wet bulb, 0.7m/s velocity.

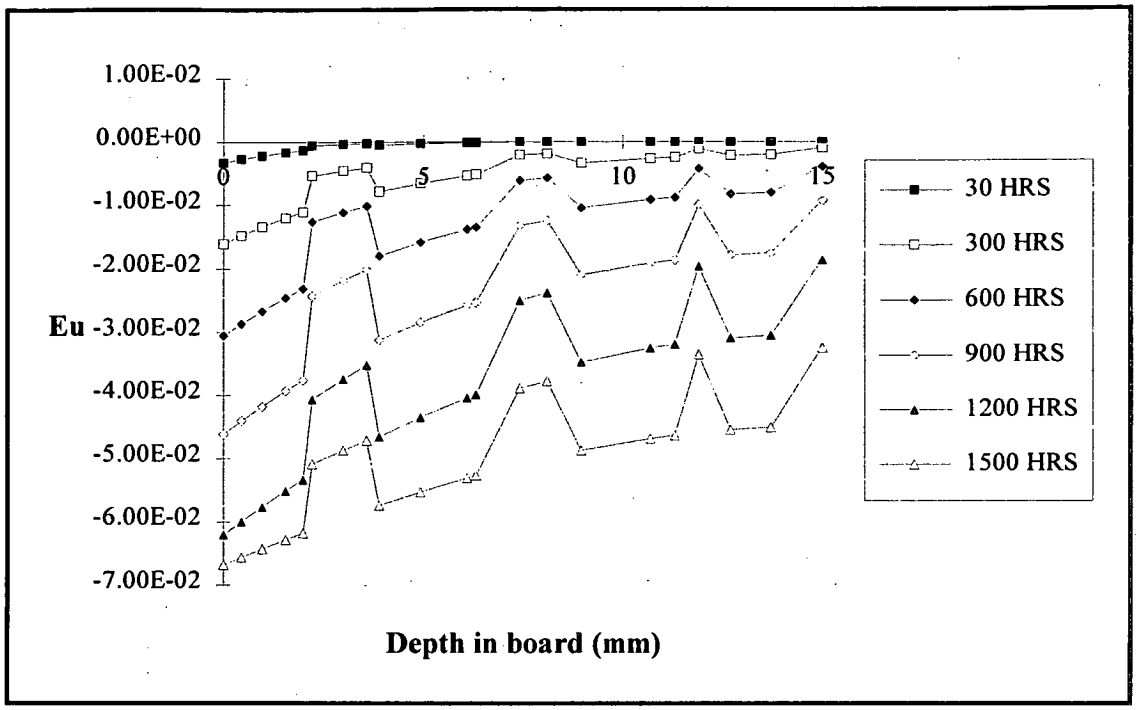

Figure 4.4.21 Unconfined shrinkage strain vs depth in board predicted by mathematical model. Drying conditions: 30°C dry bulb, 29.2°C wet bulb, 0.7m/s velocity.

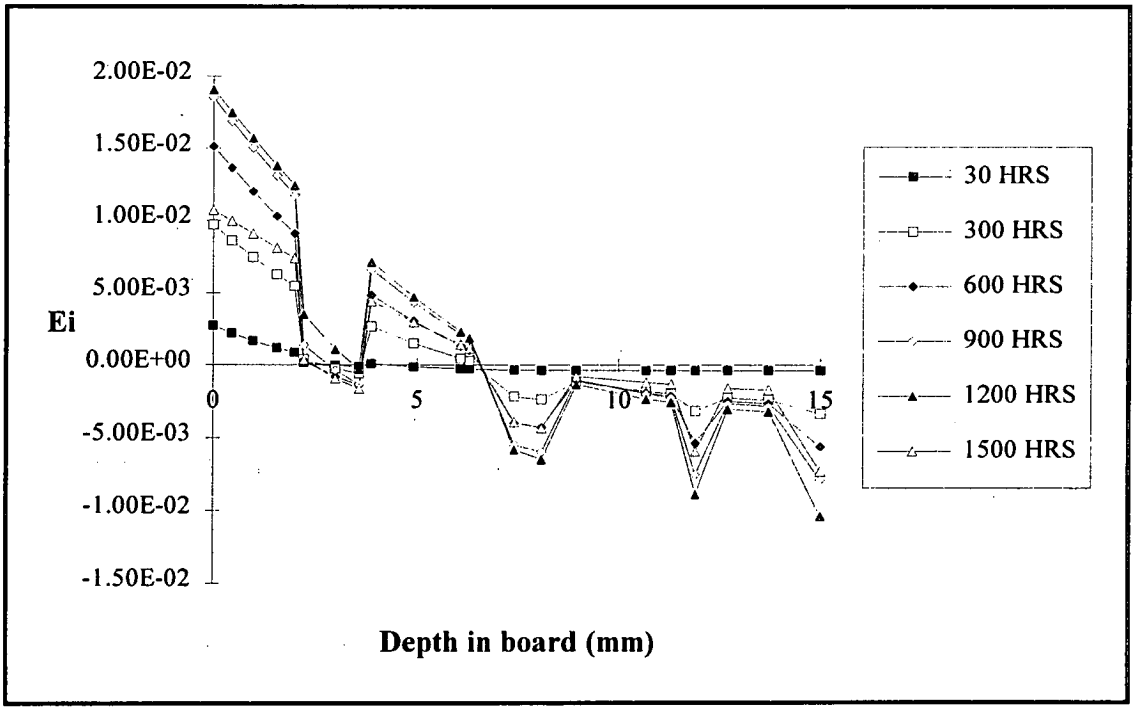

Figure 4.4.22 Instantaneous strain vs depth in board predicted by mathematical model. Drying conditions: 30°C dry bulb, 29.2°C wet bulb, 0.7m/s velocity.

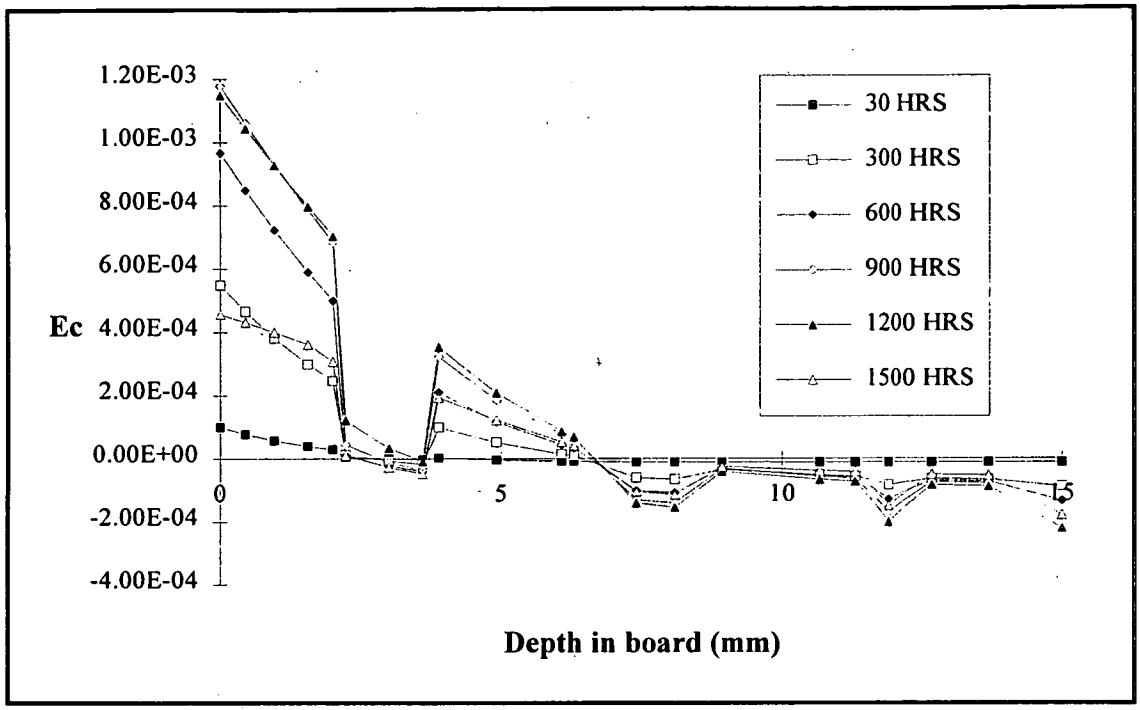

Figure 4.4.23 Creep strain vs depth in board predicted by mathematical model. Drying conditions: 30°C dry bulb, 29.2°C wet bulb, 0.7m/s velocity.

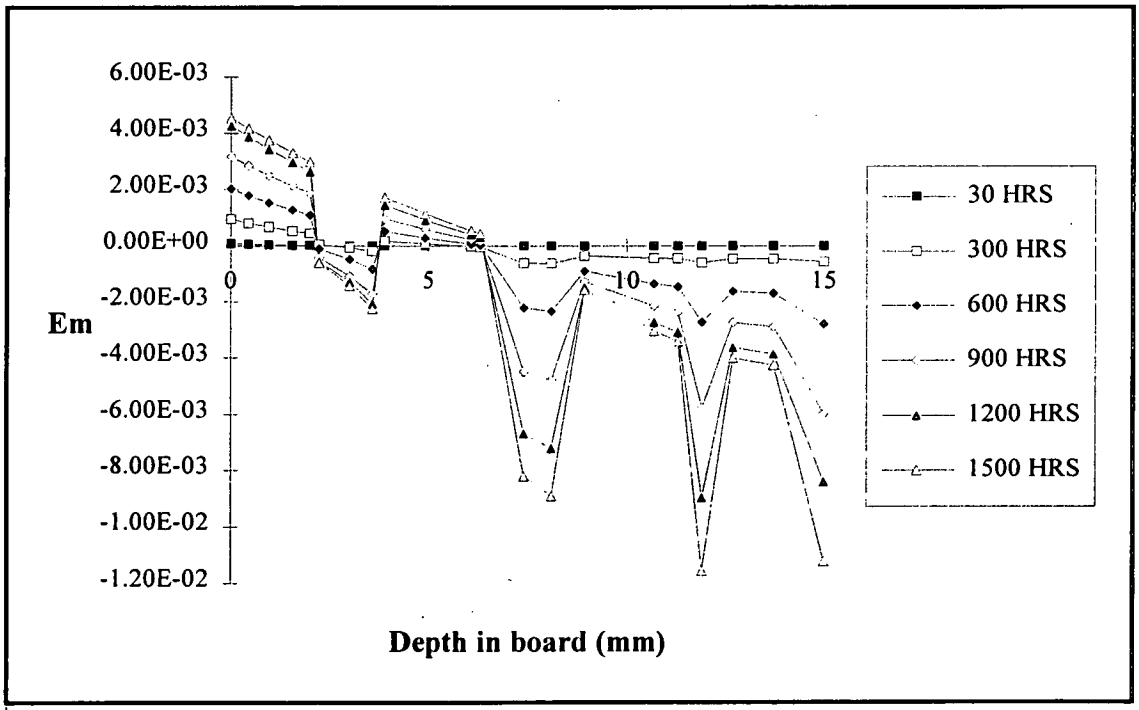

Figure 4.4.24 Mechano-sorptive strain vs depth in board predicted by mathematical model. Drying conditions: 30°C dry bulb, 29.2°C wet bulb, 0.7m/s velocity.

The simulation results indicate that it may be possible to dry this timber under conditions which cause collapse in both the earlywood and the latewood. Note that after 600 hours in Fig. 4.4.20, the board has begun to approach stress reversal; the

stress and the instantaneous strain at the surface have started to fall. The peak surface instantaneous strain was less than 0.02, indicating the absence of surface checks.

Although the simulation indicates that this timber could be successfully dried free of surface checking at temperatures above the collapse threshold temperature for earlywood (and, of course, latewood), variation in the timber is likely to preclude this possibility. A small amount of extra shrinkage in the growth band at the surface would cause surface checking. The constant schedule simulated above of 30°C dry bulb, 29.2°C wet bulb, 0.7m/s air speed is already very mild (and hence the timber dried very slowly), so that a small amount of variation in the timber could make this strategy unworkable. Conditions of 30°C dry bulb, 29°C wet bulb and 0.7m/s air speed caused the wood to form surface checks in approximately 1000 hours of simulated drying. The timber is thus particularly sensitive to drying conditions at these temperatures.

It was hypothesised that drying at higher temperature may soften the wood sufficiently for it to withstand the differential shrinkages due to collapse. To test this, the model was run with a dry bulb temperature of 55°C; results are shown in Figs. 4.4.25 to 4.4.30. This temperature was selected as it is the maximum temperature for which the strength relations used in **KilnSched** have been tested against Tasmanian Oak (Innes, 1992). Note that this simulation assumes that shrinkage at 55°C is the same as that at 28°C. This is probably true for normal shrinkage, but it is expected that collapse shrinkage will increase with temperature since the timber stiffness is inversely proportional to temperature. Indeed, Figs 4.3.1 to 4.3.4 show that the total shrinkage of the latewood does generally increase with increase in temperature between 20°C and 28°C. Allowance for this effect has been made in the model, but it has not been extrapolated beyond the measured temperature range. The diffusion coefficient may not be precise as the measurements on which equation 4.1.2 were based were carried out between 18°C and 40°C (Schaffner, 1981).

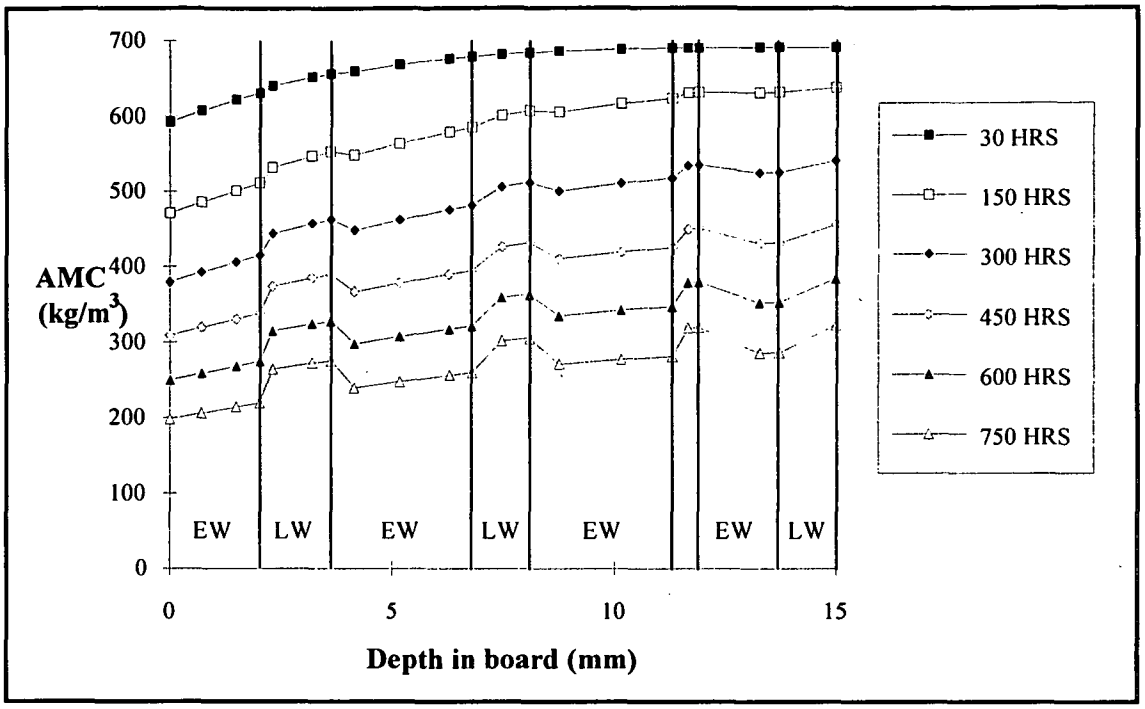

Figure 4.4.25 Moisture concentration profiles predicted by mathematical model. Drying conditions: 55°C dry bulb, 52.8°C wet bulb, 0.5m/s velocity.

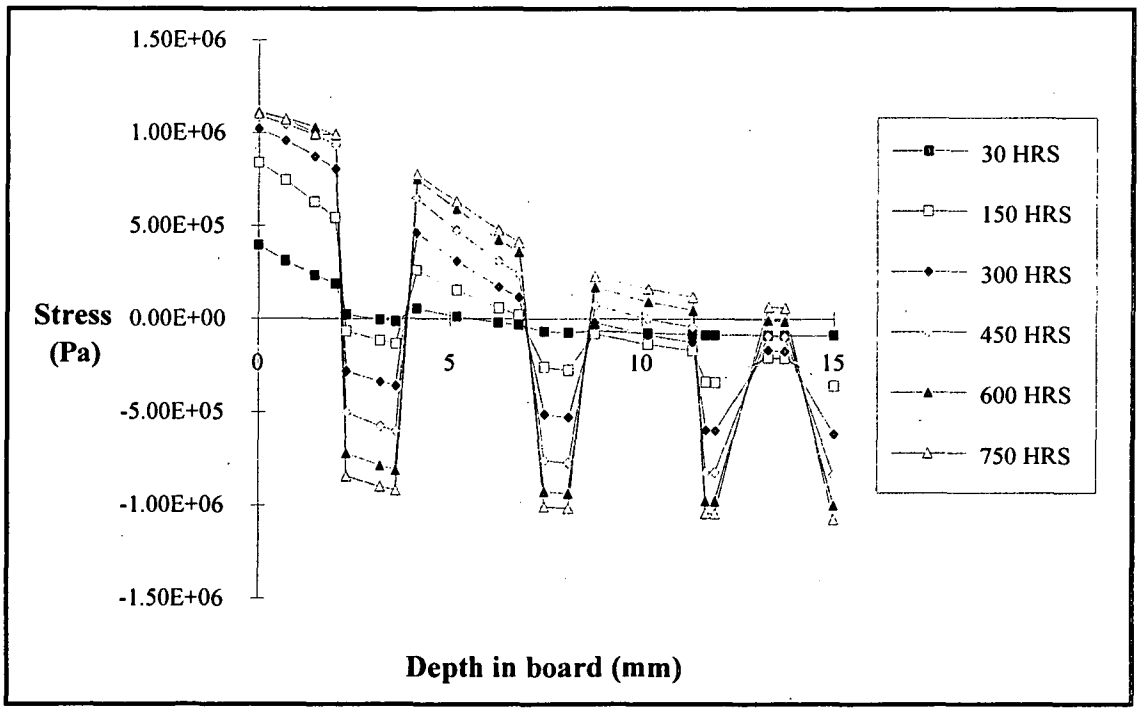

Figure 4.4.26 Stress vs depth in board predicted by mathematical model. Drying conditions: 55°C dry bulb, 52.8°C wet bulb, 0.5m/s velocity.

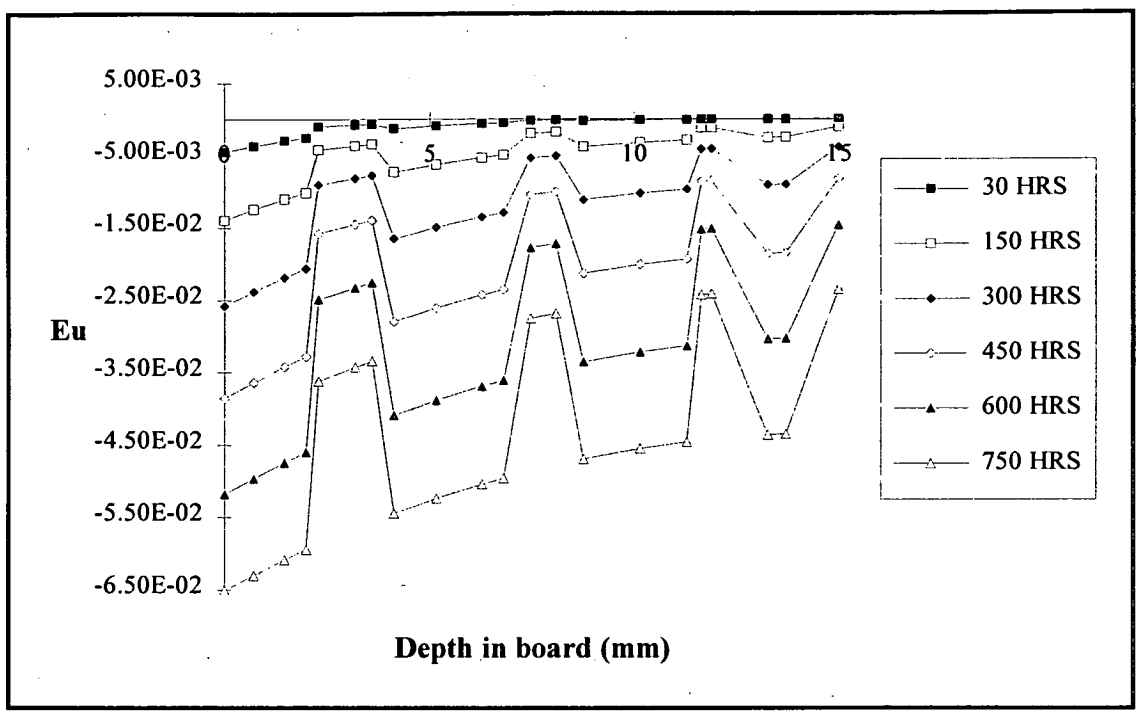

Figure 4.4.27 Unconfined shrinkage strain vs depth in board predicted by mathematical model. Drying conditions: 55°C dry bulb, 52.8°C wet bulb, 0.5m/s velocity.

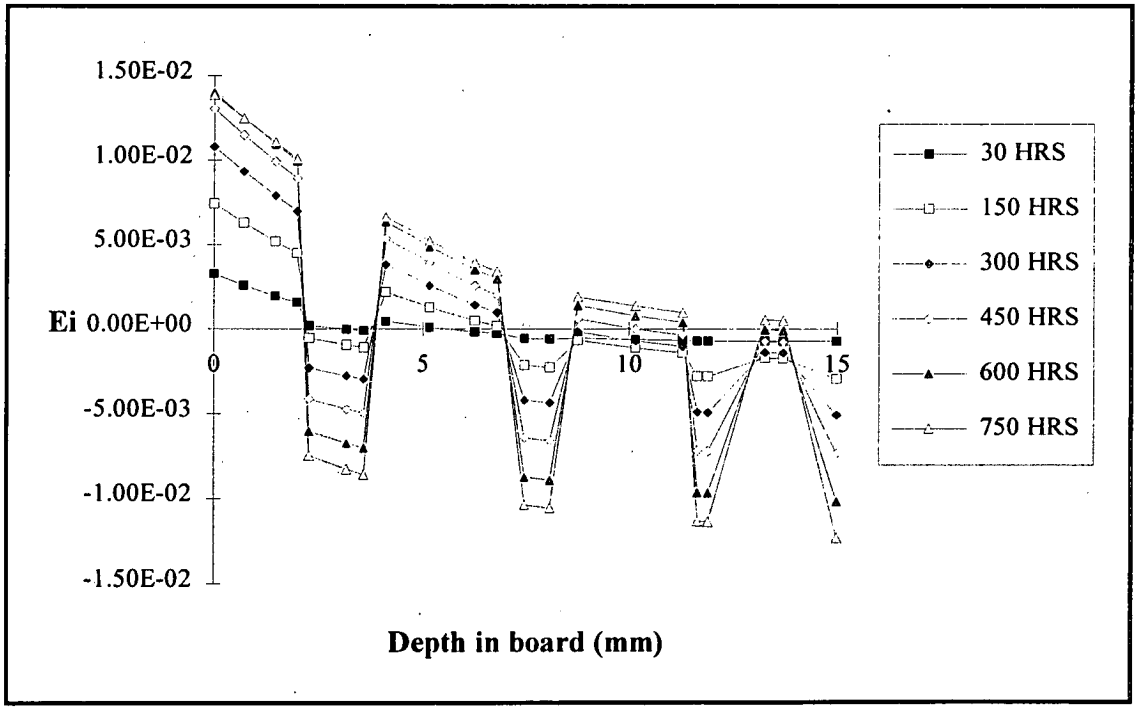

Figure 4.4.28 Instantaneous strain vs depth in board predicted by mathematical model. Drying conditions: 55°C dry bulb, 52.8°C wet bulb, 0.5m/s velocity.

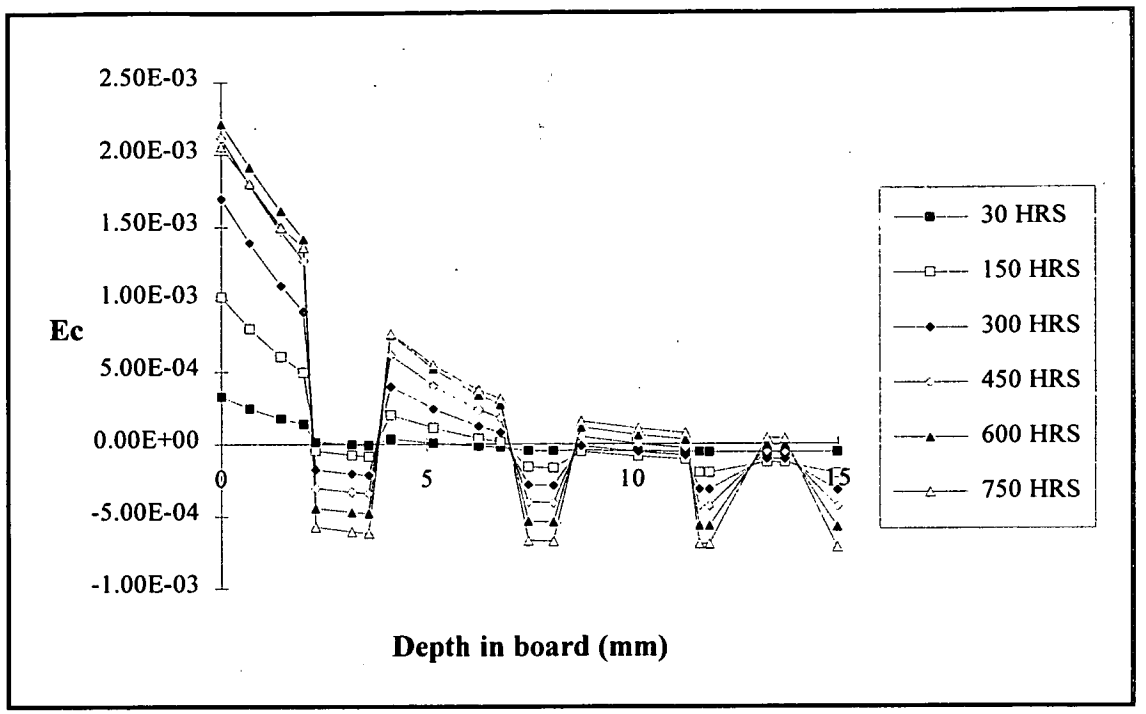

Figure 4.4.29 Creep strain vs depth in board predicted by mathematical model. Drying conditions: 55°C dry bulb, 52.8°C wet bulb, 0.5m/s velocity.

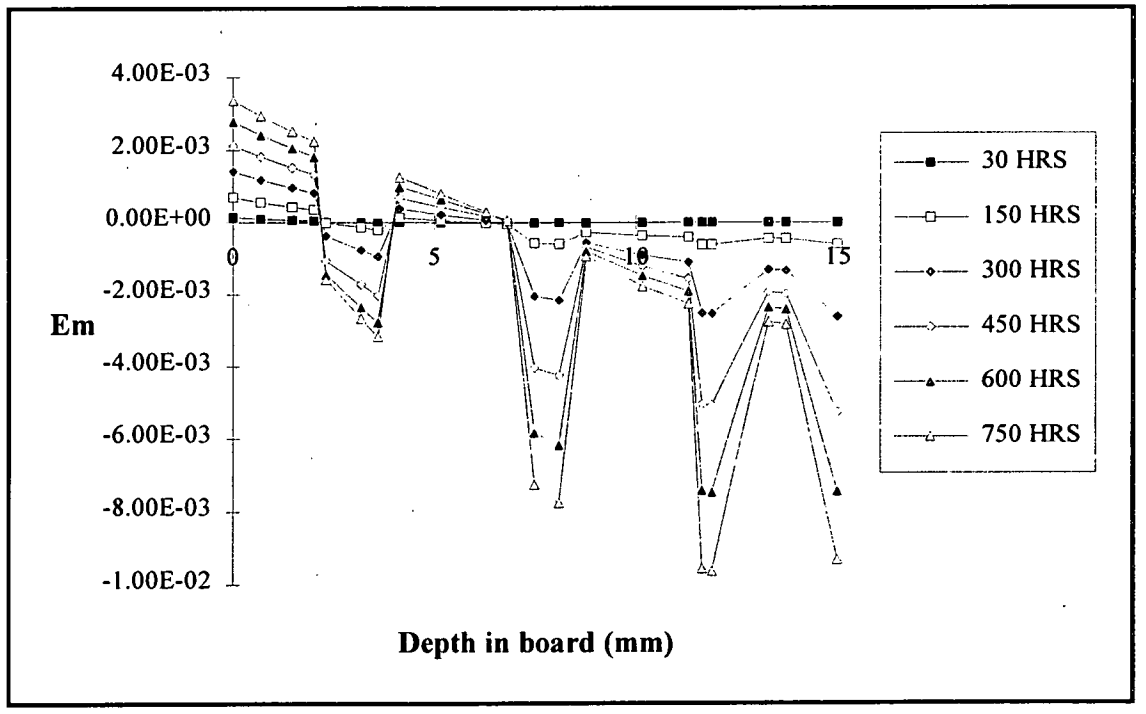

Figure 4.4.30 Mechano-sorptive strain vs depth in board predicted by mathematical model. Drying conditions: 55°C dry bulb, 52.8°C wet bulb, 0.5m/s velocity.

The simulations show that after 750 hours drying, the surface is at a moisture concentration of approximately 200 kg/m^3 or 38% (Fig. 4.4.25). The surface strain has just started to decrease, after attaining a maximum of approximately 1.30E-2 at

about 660 hours. The limiting factor on drying rate in this case (as at 30°C) is the surface instantaneous strain (as distinct from drying at temperatures below 28°C where the limiting factor was instantaneous strain in the first latewood band).

To provide a comparison with the above predictions, simulations were carried out for drying conditions of 15°C dry bulb temperature, 11.6°C wet bulb temperature and 0.5m/s velocity, assuming that the collapse threshold temperature of the latewood was above 15°C. That is, no collapse shrinkage was applied. Results are shown below in Figs. 4.4.31 to 4.4.36.

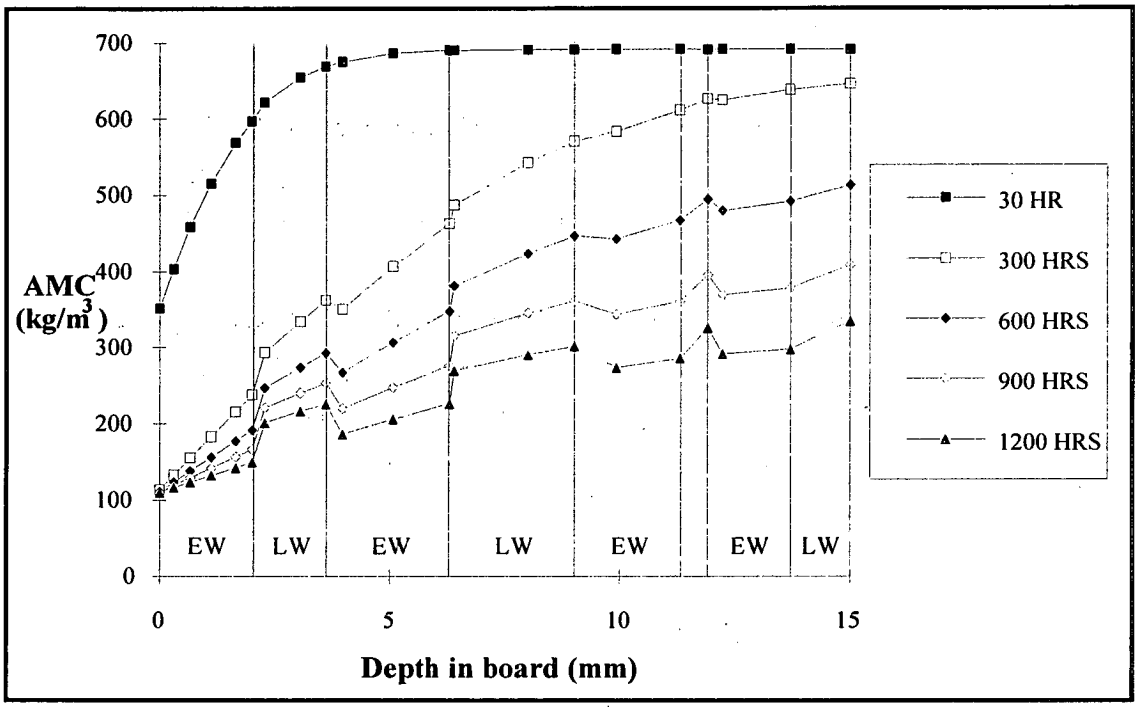

Figure 4.4.31 Moisture concentration profiles predicted by mathematical model. Collapse free drying conditions: 15°C dry bulb, 11.6°C wet bulb, 0.5m/s velocity.

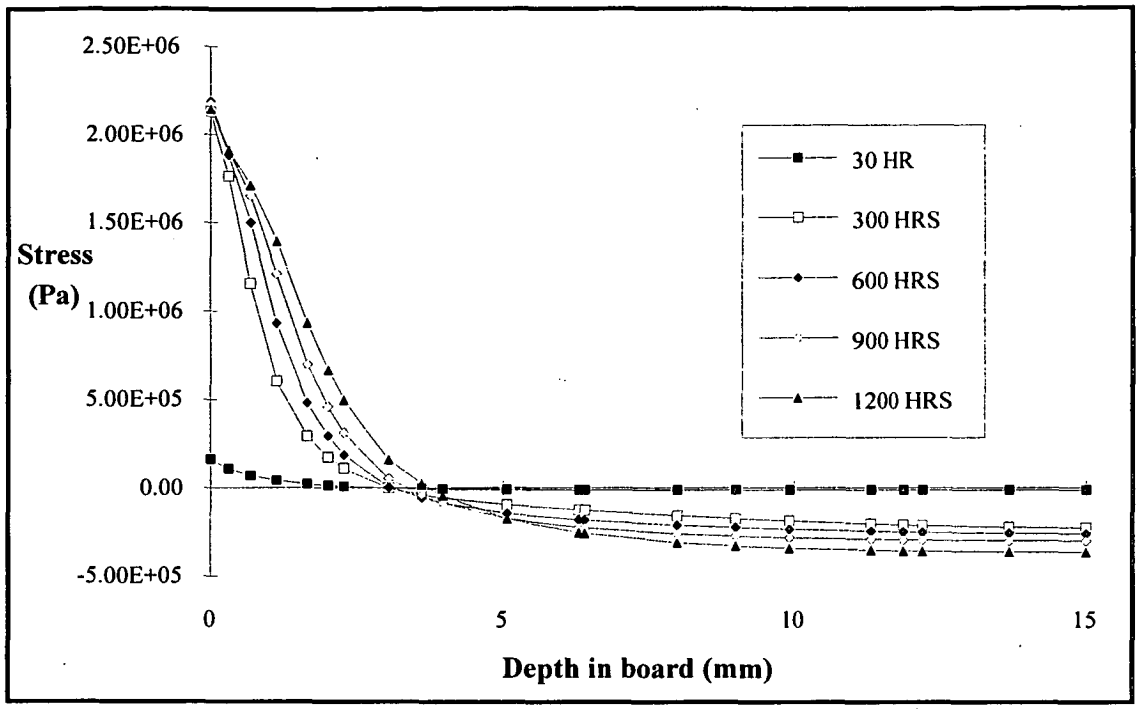

Figure 4.4.32 Stress vs depth in board predicted by mathematical model. Collapse free drying conditions: 15°C dry bulb, 11.6°C wet bulb, 0.5m/s velocity.

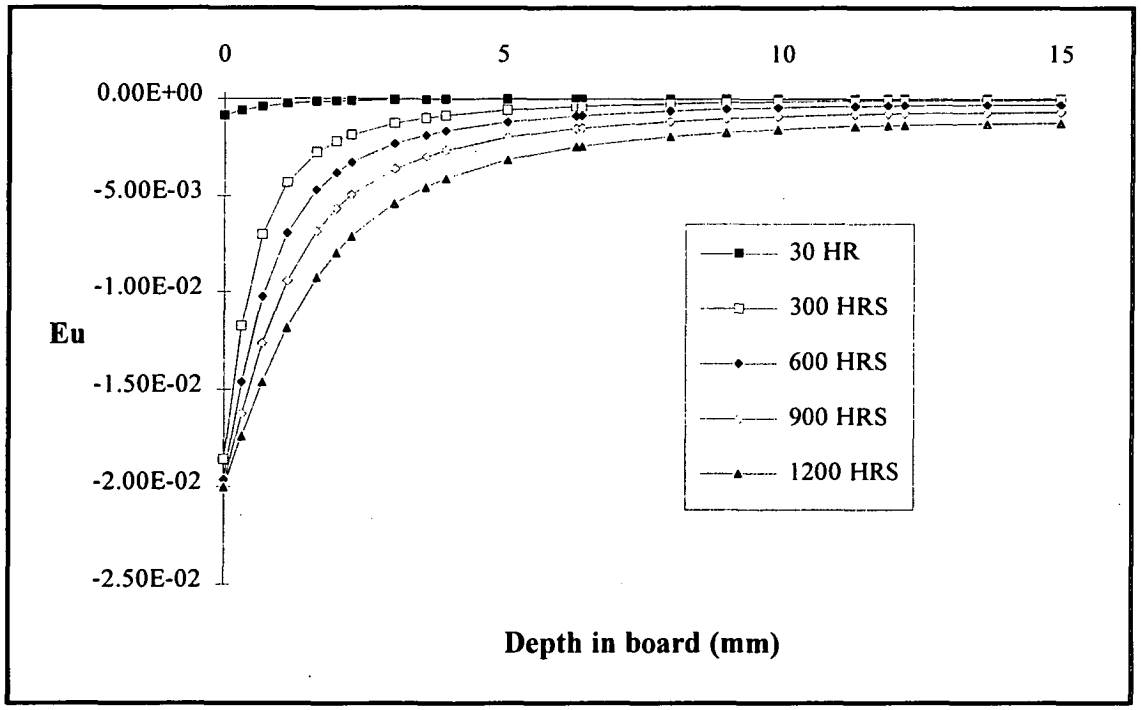

Figure 4.4.33 Unconfined shrinkage strain vs depth in board predicted by mathematical model. Collapse free drying conditions: 15°C dry bulb, 11.6°C wet bulb, 0.5m/s velocity.

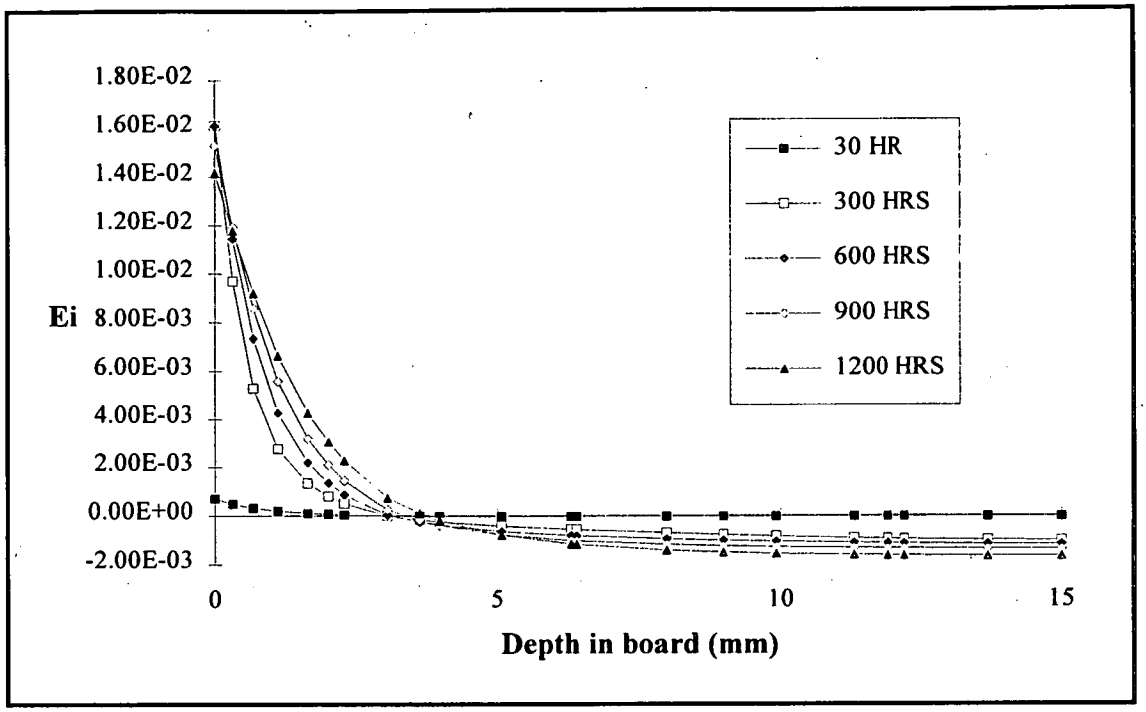

Figure 4.4.34 Instantaneous strain vs depth in board predicted by mathematical model. Collapse free drying conditions: 15°C dry bulb, 11.6°C wet bulb, 0.5m/s velocity.

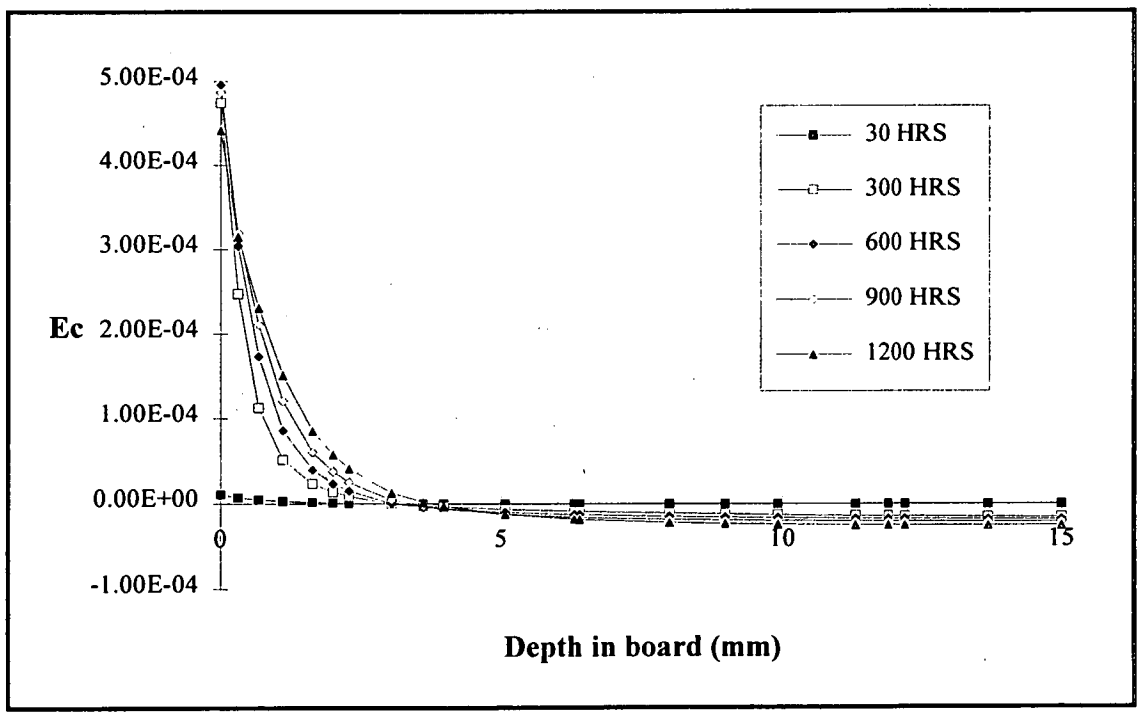

Figure 4.4.35 Creep strain vs depth in board predicted by mathematical model. Collapse free drying conditions: 15°C dry bulb, 11.6°C wet bulb, 0.5m/s velocity.

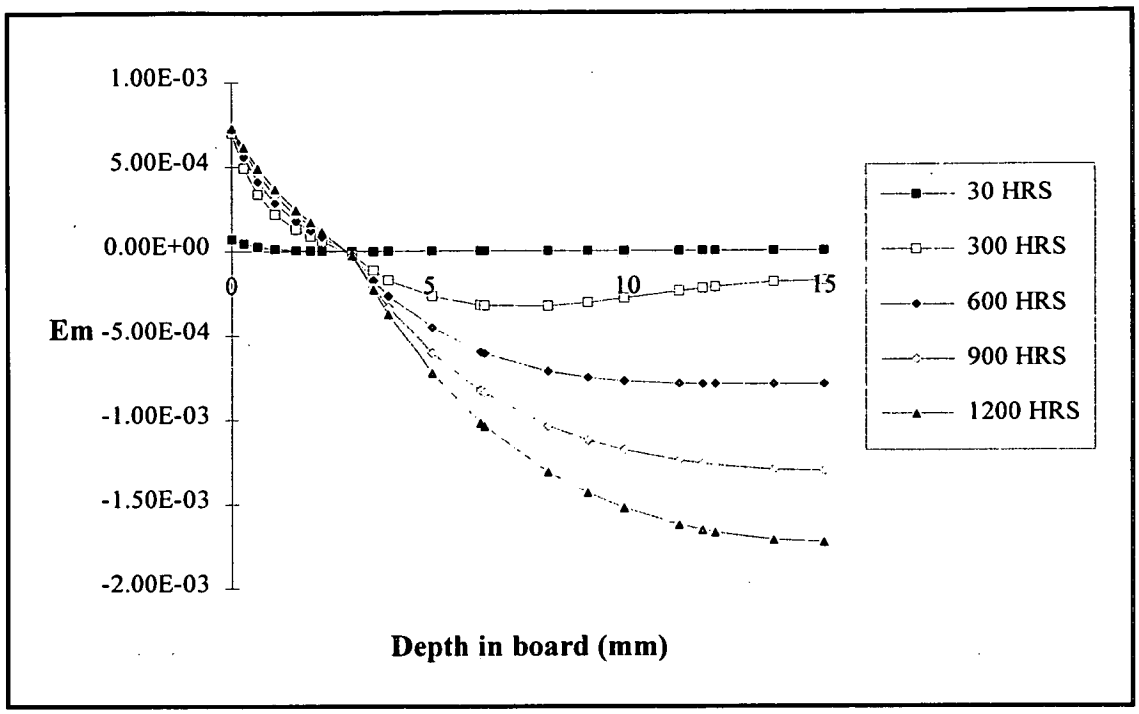

Figure 4.4.36 Mechano-sorptive strain vs depth in board predicted by mathematical model. Collapse free drying conditions: 15°C dry bulb, 11.6°C wet bulb, 0.5m/s velocity.

Figs. 4.4.31 to 4.4.36 show that drying at temperatures below the collapse threshold temperatures of the wood allows much faster drying without inducing checking than the lower temperature schedules.

4.5 Conclusions from mathematical modelling

The wood under study in this case was unusual in that both the earlywood and latewood underwent collapse shrinkage. Indeed, the latewood demonstrated more shrinkage at all measured temperatures (20°C to 28°C) than the earlywood. Most of the extra shrinkage in LW occurred at MC above FSP, and so must have been due to collapse. The collapse threshold temperature for the earlywood was found to be approximately 26°C, whereas that for the latewood was less than 20°C (assuming that one existed). Modelling of the drying of this timber at temperatures below the collapse threshold temperature of the earlywood indicated that it would need to be dried very slowly under such conditions to avoid internal check formation. The drying rate required was so slow that the internal checks formed even when the timber

had not formed any surface checks. It is unlikely that such a slow drying rate would allow the check-free seasoning of this timber for worthwhile economic advantage.

To boost the drying rate, simulations were performed for temperatures just above the collapse threshold temperature for the earlywood. It was found then that the timber was very susceptible to surface checking; this is probably because of the very large shrinkage at the surface (which was collapsing). To avoid this surface checking, it was found that the drying rate would need to be slowed down to a rate which would probably not be economically viable either. Variation in the timber make this method risky. The very slow drying rate required a very high humidity, which would be difficult to control adequately in an industrial kiln.

In an attempt to increase the drying rate, simulations were performed at a dry bulb temperature of 55°C. It was postulated that the high temperature may soften the wood sufficiently to allow it to better withstand the differential shrinkages induced by drying at collapse inducing temperatures. It was again found that a drying rate much slower than usual was required to prevent the formation of surface checks.

Simulations of drying at higher temperatures showed that the wood generally has flatter moisture gradients. This is due to two effects. The first is that the timber has a higher diffusion coefficient at higher temperature, so that moisture movement within the board is freer. The second is that the surface drying rate was slower to keep the surface e_i below ultimate. The higher temperature simulations also showed much higher mechano-sorptive and creep strains, as expected. The simulations showed that when the surface growth band collapses, surface checking becomes difficult to prevent, and is the controlling variable limiting drying rate. It is likely that a significant portion of a charge of timber will have a collapsing growth band intersecting the surface, so that simulations at temperatures above the collapse threshold temperature should always be carried out for a board with a collapsing surface growth band. Thus it currently appears that the best way to dry timber free of surface and internal checks is to dry at temperatures below the collapse threshold temperatures for earlywood and latewood. Usually it is assumed that the collapse threshold temperature for earlywood is lower than that for latewood.

Large differential normal shrinkages such as those which appear to have been observed by Pentoney (1953) could conceivably lead to formation of internal checking in the latewood, but this is not believed to have been the cause here for the following reasons:

- the checking was observed in parts of the wood at MC above FSP, when virtually no normal shrinkage had occurred
- had the differential normal shrinkage been sufficiently large to cause checking in the latewood, such checking would have been observed in the R-T slices used for shrinkage measurement; no such checking was observed

It is possible that the model is not adequately simulating the actual situation, due to a few complications. It seems possible that saw damage may prevent collapse right at the surface, although Wilkins and Wilkes (1987) show that the first undamaged fibres beneath the surface are prone to collapse. It is also possible, as mentioned above, that the shrinkage at higher temperatures is greater than that measured near ambient temperatures. The temperature dependence of the diffusion coefficient may not be precise for temperatures greater than approximately 40°C. It appears likely that the latewood has a collapse threshold temperature, but shrinkage trials could not be carried out below ambient temperature. An implicit assumption that the model makes in the simulations above is that all latewood follows one shrinkage curve and all earlywood follows another. This is clearly not the case in all wood, as internal checks are usually seen to occur in one or more discrete growth bands before they appear anywhere else.

The idea of drying wood at temperatures high enough to allow it to withstand differential shrinkages from collapse may work at higher temperatures than those modelled here. However, it seems likely that when the timber is pre-dried at temperatures above its softening temperature (Hillis and Rozsa, 1978), collapse is not reversible by reconditioning. Such simulations cannot be performed until better information on the high temperature properties of the wood under study are determined.

The concept of drying at fully collapsing high temperatures holds some promise, but much experimental and theoretical work is needed to test its practicality. At present, the safest way to avoid internal checking seems to be to determine the collapse threshold temperature for the timber, and ensure that the timber temperature does not become higher than the collapse threshold temperature in those parts of the wood at MC above FSP.

It appears that with the present state of our knowledge, the best way to dry this timber would be at temperatures below the collapse threshold temperature for the latewood. To find the collapse threshold temperature of the latewood requires further shrinkage

measurements at lower temperatures. The simulations suggest that even if the collapse threshold temperature were very low, the drying rate possible without causing checking would still be much greater than if collapse shrinkage were to occur. If the collapse threshold temperature for latewood turns out to be unreasonably low, this timber could probably not be practically seasoned for economic advantage. Indeed, given the present state of our knowledge of collapse, the best way to dry any collapse prone timber seems to be to determine the collapse threshold temperatures, and dry at temperatures below them. The limiting factor for seasoning time is then the tendency of the wood to form surface checks.

Chapter 5. Optimisation of dry bulb temperature during drying to FSP

Drying trials using the Clever Kiln Controller have usually been run at a constant dry bulb temperature until all parts of the wood are at MCs below FSP. This temperature was determined for later CKC trials by the collapse threshold temperature tests described earlier. However, it is common practice in industry to progressively increase the temperature of the wood from the very start of drying. Clearly, raising the dry bulb temperature will increase the diffusion coefficient, and increase the rate of drying. Unfortunately, the improvement in drying rate may well come at the expense of timber quality, as the higher temperatures may lead to more collapse, and collapse induced internal and surface checking. The work detailed in this chapter was performed to determine if there is a theoretical basis to support this practise.

One factor which could make the raising of dry bulb temperature (DBT) during pre-drying acceptable is creep and mechano-sorptive relaxation of the internal stresses in collapse prone fibres. To investigate this possibility, creep and mechano-sorptive strains were added to the single fibre stress-strain model presented in Chapter 2. Following this, the effect of the decrease in surface tension with an increase in temperature was investigated. Finally, an approximate measure of the effect of board stresses due to drying on the single fibre stresses was formulated.

5.1 Creep strain in the single-fibre stress model

The creep formulation used here was that developed by Oliver (1991) to fit the data of Kingston and Clarke (1961). These data were for *E. regnans* grown in Victoria, and appear to be the most complete set of creep tests performed on this species to date. The timber was tested at 21.5, 41.5, and 56.5°C, at EMC (MC of approximately 10 - 12%). Previous work (Armstrong and Kingston, 1960) had shown that creep was not strongly dependant on MC as long as it was held constant. The timber was tested in bending along the grain.

Oliver's model consists of a spring in series with a spring and dashpot in parallel. Both springs are non-linear. The stiffness of the first spring (E) is defined by the instantaneous strain. The stiffness of the spring in parallel with the dashpot (E_2) is

defined by Kingston and Clarke's (1961) measured values of the creep ratio ($\varepsilon_i/\varepsilon_c$). The relationship between creep ratio and stress ratio (s/s_u) is taken to be linear. Oliver shifted the reference stress from the ultimate value at 21.5°C and 11% MC to the ultimate value for green timber at 21.5°C. To do this he assumed that the ultimate strength of the green timber is equal to half the ultimate strength of the timber at 11% MC. This assumption was supported by the data of Innes (1992). The fits to Kingston and Clarke's (1961) data were then

$$R = \frac{E_2}{E} = R_0 - R_s\left|\frac{s}{s_u}\right| \tag{5.1.1}$$

where $R_0 = 105.6 - 3.46T + 0.0319T^2$ (5.1.2)

and $R_s = 60 - 1.99T + 0.019T^2$ (5.1.3)

T is temperature in °C.

To avoid problems at high stress, a lower limit of $a_2 = 0.04R_0$ has been applied to R.

Oliver replaced the two straight lines defined by 5.1.1 and $R = a_2$ by the hyperbola

$$\left(R - a_2\right)\frac{R - R_0 + R_s\left|\frac{s}{s_u}\right|}{\frac{s-f}{s}} = k_2^2 \tag{5.1.4}$$

to avoid computational difficulties near the intersection of the lines. The term (s-f)/s is the proportion of stress carried by the spring E_2 in parallel with the dashpot. Thus f is the stress carried by the dashpot, and is hence a function of time. k_2 specifies how closely the hyperbola follows the asymptotes, and is given the value of 5.

Solving equation 5.1.4 for R gives

$$R = b_2 + \sqrt{k_2^2 - a_2 R_1 + b_2^2} \tag{5.1.5}$$

where $b_2 = 0.5\left(a_2 + R_1\right)$ (5.1.6)

and $$R_1 = \frac{R_0 - R_s\left|\frac{s}{s_u}\right|}{\frac{s-f}{s}} \tag{5.1.7}$$

The curves of creep ratio against time presented by Kingston and Clarke (1961) have nearly the same shape when divided by the final ordinate. Oliver approximated this shape with the Kelvin model, giving the creep ratio e

$$e = \frac{\varepsilon_c}{\varepsilon_i} = A\left(1 - \exp\left(-k_1 t\right)\right) \tag{5.1.8}$$

and differentiating gives

$$\frac{de}{dt} = k_1 A \exp(-k_1 t) \tag{5.1.9}$$

Eliminating the term in t from equations 5.1.8 and 5.1.9 yields

$$\frac{de}{dt} = k(A - e) \tag{5.1.10}$$

The value of A in equation 5.1.8 is clearly the ultimate value of e obtained when the stress carried by the dashpot is zero (ie. all of the applied stress is taken by the spring E_2). Thus A is the inverse of R from equation 5.1.4 with f = 0;

$$A = \frac{1}{b_1 + \sqrt{k_2 - a_2\left(R_0 - R_s\left|\frac{s}{s_u}\right|\right) + b_1^2}} \tag{5.1.11}$$

where $b_1 = \frac{1}{2}\left(a_2 + R_0 - R_s\left|\frac{s}{s_u}\right|\right)$ (5.1.12)

The creep strain calculated using this formulation was added to the instantaneous strain calculated by the single fibre stress model of Chapter 2 for each of the radial and tangential directions, at each radius step, to give the net strain. A time step was introduced, which coincided with the increments of internal stress used in the stress-strain model during increase in internal tension. The behaviour of the stress and strain under relaxation was then calculated. Note that this solution is only approximate; a more exact solution would require an extra iterative loop to achieve static equilibrium to higher accuracy. The creep strain does not reach high enough values to warrant the extra calculations in this study.

Figures 5.1.1 to 5.1.3 show the behaviour of the calculated stress, net strain, and creep strain at the fibre inner wall with time. Figures 5.2.3 and 5.1.5 show the calculated profiles of the radial and tangential creep strains through the fibre wall at various times. The temperature was 20°C.

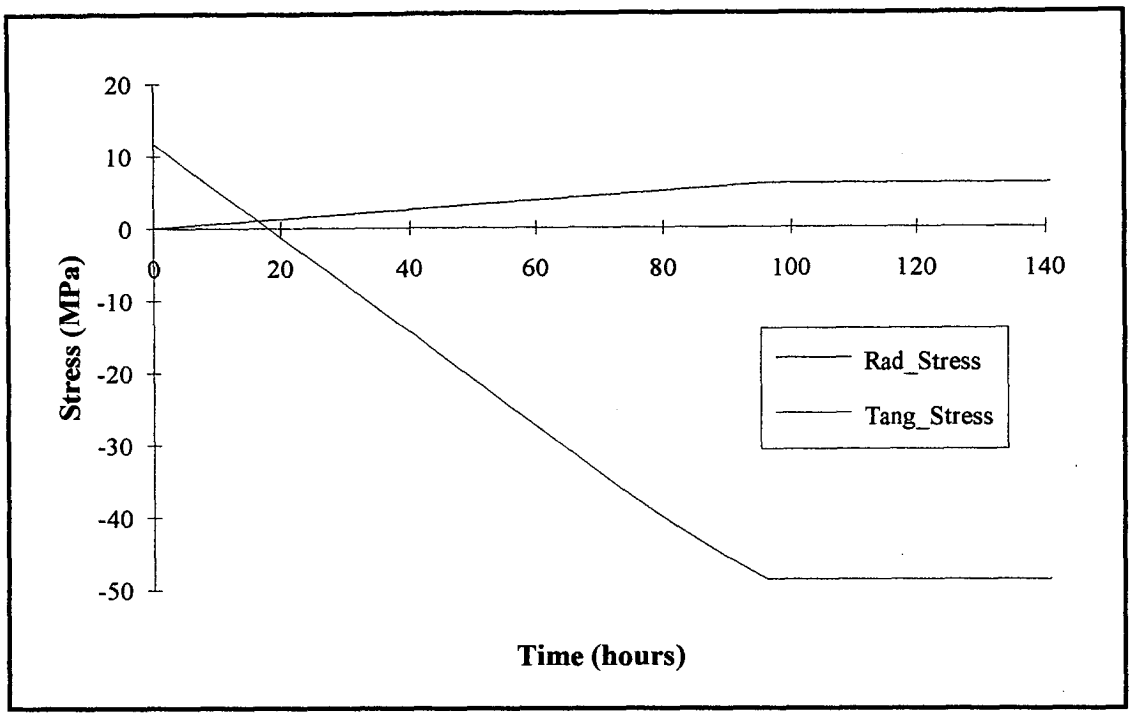

Figure 5.1.1 Stresses at fibre inner wall calculated by the model

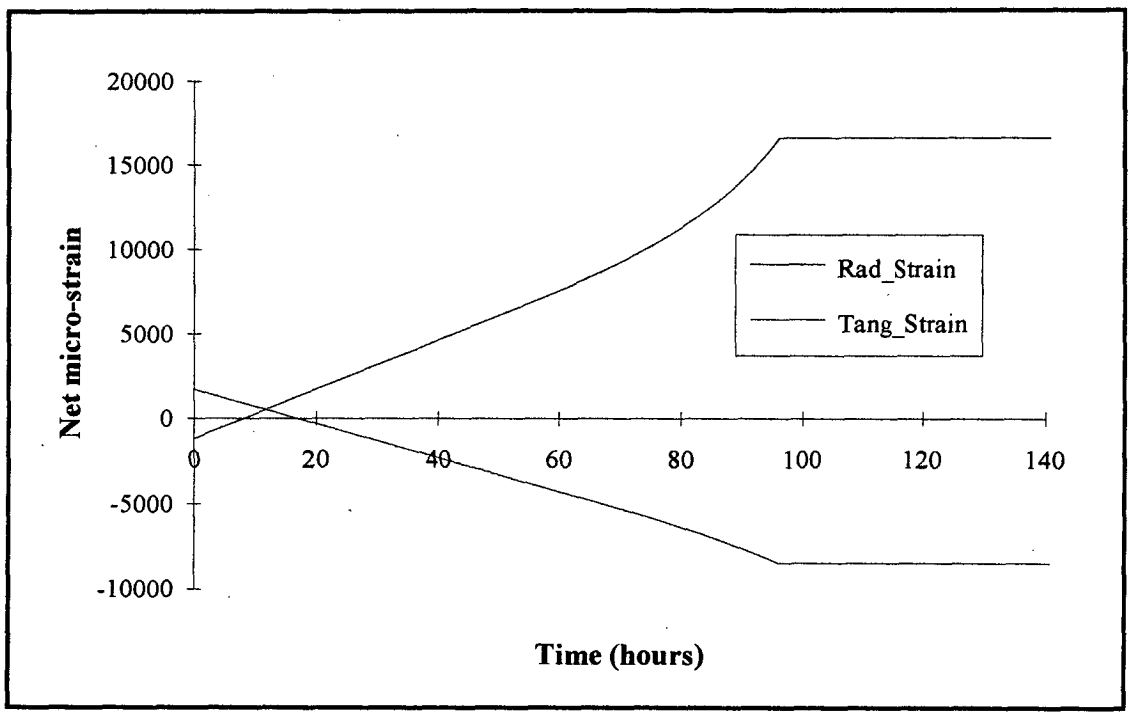

Figure 5.1.2 Net strains at fibre inner wall calculated by the model

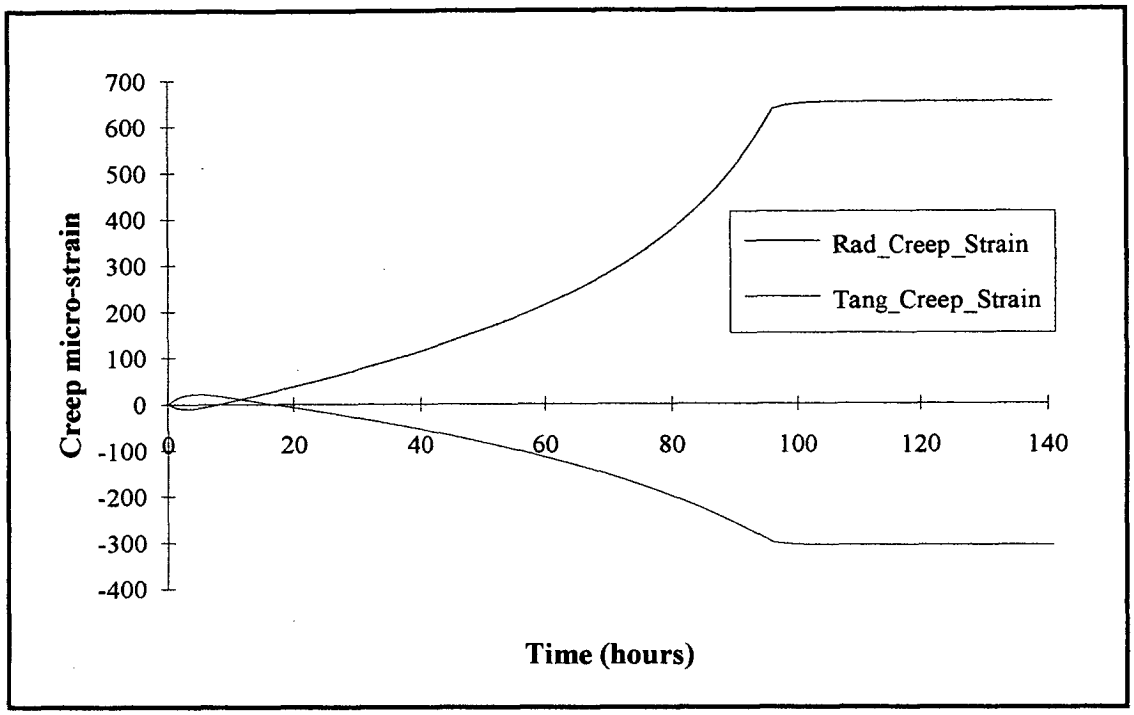

Figure 5.1.3 Creep strains at fibre inner wall calculated by the model

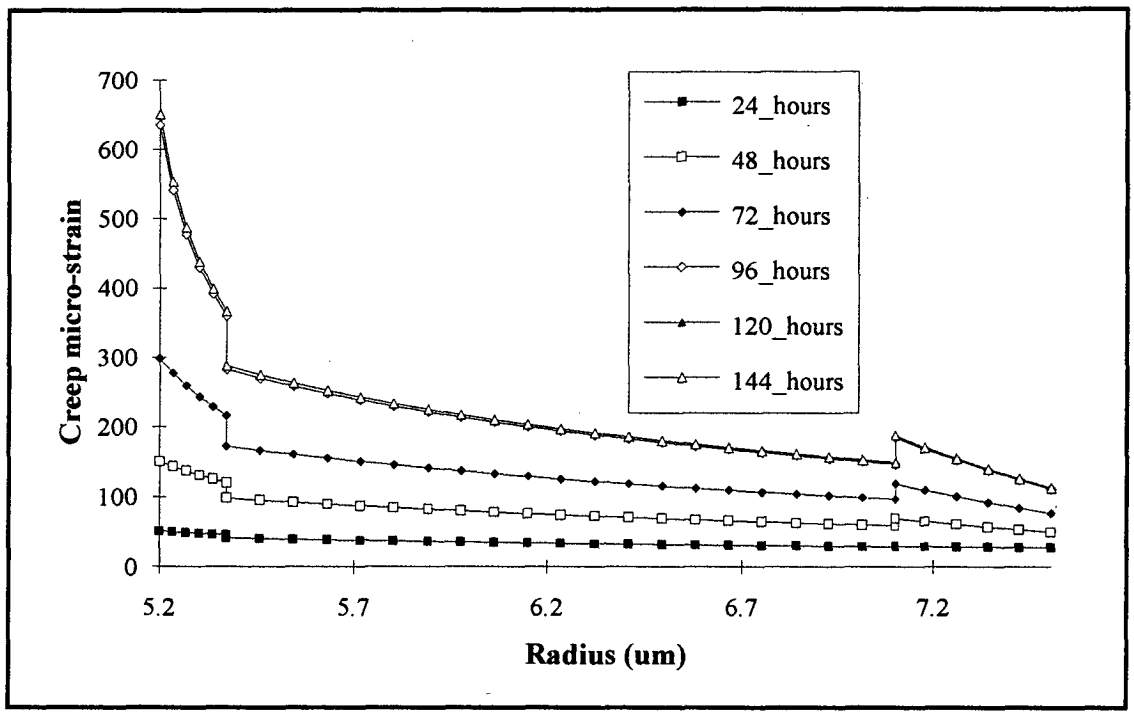

Figure 5.1.4 Radial creep strain profiles

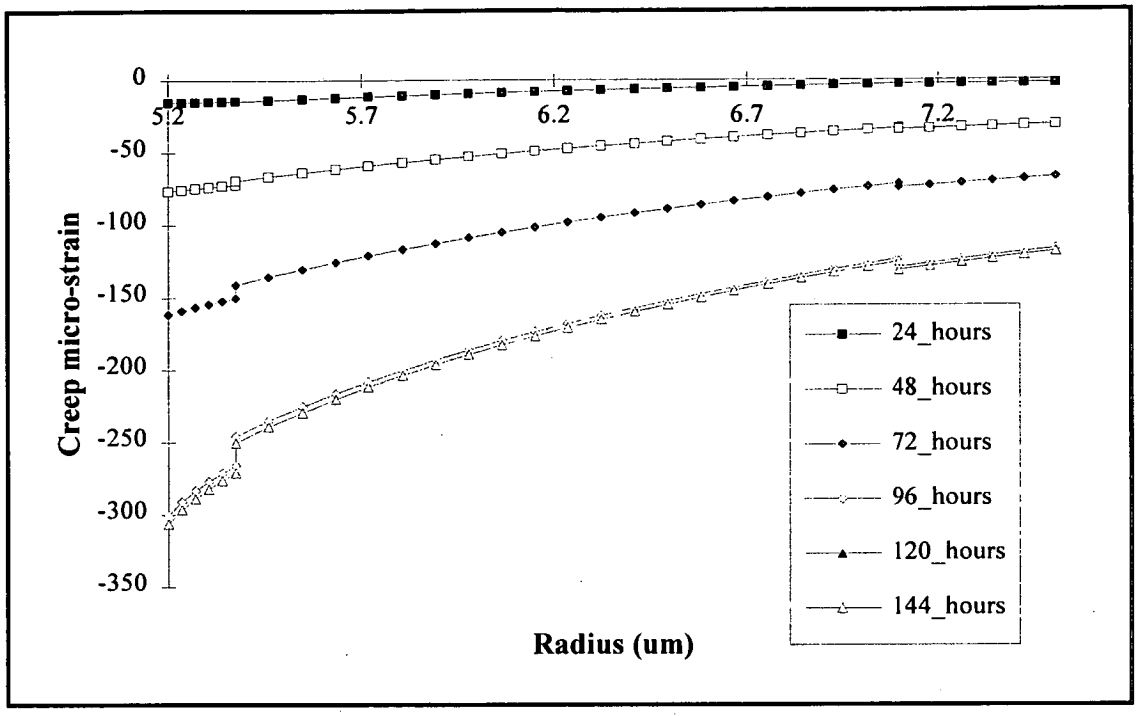

Figure 5.1.5 Tangential creep strain profiles

Note that in Figs. 5.1.4 and 5.1.5 the plots for 120 hours are obscured beneath the plots for 144 hours. The internal stress is incremented to its maximum value of 6MPa at 96 hours. Following this, the creep relieves some of the internal stress. The creep strains reach a maximum of approximately 5% of the instantaneous strains. Creep in the fibre wall under these conditions does not permit a worthwhile increase in the dry bulb temperature during pre-drying without causing collapse.

5.2 Mechano-sorptive strain in the single-fibre stress model

It is here hypothesised that a mechano-sorptive strain results from a movement of water within the wood cell wall combined with an applied external stress. Thus a mechano-sorptive effect occurs above FSP in timbers which have occluded pits so that free water must undergo molecular diffusion through the fibre walls to escape the lumens. Species of wood which have open pits do not exhibit a mechano-sorptive effect above FSP as the free water within the cell lumens can then permeate through the pits instead of passing through the cell wall by molecular diffusion. A mechano-sorptive effect will occur below FSP in all timbers, as bound water is removed from

the cell walls. It appears that the effects above and below FSP may not necessarily be quantitatively similar.

This hypothesis follows the work of Gibson (1965) who postulated that mechano-sorptive strains "..could result from the continual making and breaking of hydrogen bonds through the movement of water during the approach to a new equilibrium moisture content." Gibson firstly suggests that wood be considered as a hydrogen bonded structure. He next states that hydrogen bonds between adjacent cellulose chains involving water as a bridging molecule are weaker than hydrogen bonds directly between adjacent cellulose chains. He then suggests the concept of "a physical or spatial redistribution of hydrogen bonds rather than a difference in the number of bonds existing at the same moisture content before and after [moisture content] cycling" since the elastic modulus is unchanged by cycling (Hearmon and Paton, 1964). Gibson explains how "every temporary break of a hydrogen bond will give rise to a temporary weakening of the piece of wood and a slightly increased strain in response to a fixed applied stress", providing an explanation for the mechano-sorptive effect during desorption. He suggests that the energy for deflection recovery during cycling may come from the exothermic heat of adsorption from the vapour phase.

Armstrong (1972) performed experiments on bunya pine (*Araucaria bidwillii* Hook.) to determine if mechano-sorptive strains occurred in each of three situations;

- Constant and uniform moisture content
- Constant moisture content in samples subjected to moisture flux
- Changing moisture content.

Armstrong's (1972) experiments consisted of subjecting blocks of wood to longitudinal compression in constant humidity atmospheres. The blocks each had a hole in the middle, to which a vacuum pump could be connected, thus drawing air and moisture through the wood from the outside atmosphere. In this way, he could subject the wood to moisture movement, but at unchanging moisture content. Of the moisture movement, he states that "Some of this water may have been carried through the wood in the air stream, but an amount must have been transported through the wood cell walls in response to the steady-state moisture gradient." Unfortunately, he had no quantitative measure of this moisture gradient. It seems likely that most of the water which moved through the wood would have moved via the rays. Water which moved through the cell walls in response to any moisture concentration gradient would probably have moved via the open pit structure of this timber. That is, most of the moisture movement through the cell walls would have occurred by permeation in

the liquid or vapour state, rather than the molecular diffusion which appears to dominate moisture movement in Tasmanian eucalypts. The mechano-sorptive deformations undergone by the specimens subject to MC change was up to an order of magnitude larger than those undergone by the constant MC specimens. Armstrong concluded that "the movement of water through wood in the absence of moisture content change has little or no effect on the deformation of wood in compression parallel to the grain". This conclusion could perhaps be qualified by noting that the movement of water through wood did not necessarily include diffusion through the fibre wall material.

Following the work of Armstrong and Kingston (1960; 1962) and Armstrong (1972), Armstrong (1983) tested the hypothesis that mechano-sorptive strains could be explained in terms of "displacements between the cellulose chains of the wood substance, under the bias of an external force, following changes in the macromolecular configurations initially motivated by volume changes in the wood during sorption of water. Without this motivation no relative displacement occurs between units of the molecular system, even though water molecules move through the system and exchange with those present between hydroxyl groups of adjacent cellulose chains". Armstrong's (1983) experiments consisted of bending tests on seven species of wood. The species were separated into three groups:

- Collapse prone eucalypts (*E. delegatensis*, *E. regnans*, *E. pilularis*, *E. saligna* Sm.)
- A non-collapsing hardwood, Merbau (*Intsia palembanica* Miq.)
- Non-collapsing softwoods (*Araucaria cunninghamii* Ait. ex D.Don, *Pinus radiata* D.Don)

Armstrong's (1983) hypothesis was that the fibre walls of the collapsing timbers would undergo volume change during MC change above FSP, and thus, following his earlier hypothesis, be subject to mechano-sorptive deformations. The other species, not being prone to collapse and hence having no cell wall volume change above FSP, should not experience mechano-sorptive deformations. His experiments provided results which supported his hypotheses.

However, the results of Armstrong (1972, 1983) and Armstrong and Kingston (1962) also provide support for the hypothesis stated above, that the mechano-sorptive effect results from the diffusion of water through wood cell wall material under the bias of an external force. Armstrong and Kingston (1962) performed tests on radiata pine (*Pinus radiata*), hoop pine (*Araucaria cuninghamii*), *E. regnans*, *E. pilularis*, and *E. delegatensis*. They measured a mechano-sorptive effect from green to dry on the

eucalypts, but could only find a mechano-sorptive effect below FSP in the pines. Armstrong (1983) similarly found a mechano-sorptive effect above FSP only in the eucalypts he studied, but not for Merbau or the softwoods. He associated this with the collapse prone nature of the eucalypts. It appears possible, however, that the eucalypts were the only species he studied which had occluded pits so that the moisture moving out of the cell lumens above FSP had to diffuse through the fibre wall. Wu (1989) in studies on peppermint eucalypt (either *E. pulchella* or *E. tendiramis*) found that the mechano-sorptive effect above FSP was nearly linearly dependant on temperature over the range of measurements (30°C to 70°C). Oliver (1996) stated that there was no collapse in the timber used for Wu's study. Armstrong and Kingston (1962) found a larger mechano-sorptive effect in blackbutt (*E. pilularis*) than in mountain ash (*E. regnans*) despite the fact that blackbutt generally suffers less from collapse than mountain ash (Bootle, 1983).

Most of the investigations mentioned above involved beam tests. These are inherently more difficult to interpret than direct tension or compression tests. In particular, sections greater than approximately 1mm thick are subject to moisture and stress gradients during drying. This leaves open the possibility for explanations of measured phenomena by effects other than that under study.

It appears that further experimental work is required to determine whether Armstrong's (1983) hypothesis is more or less satisfactory than the hypothesis posed here explaining the mechano-sorptive effect as a result of water movement in the wood cell walls combined with an external stress. None of the above investigations involved measurement of shrinkage on slices under the same conditions as those of the test, so that whether or not collapse occurred cannot be categorically stated. To directly test whether the mechano-sorptive effect is dependant upon molecular diffusion through the wood cell walls seems rather more difficult. Such investigations are beyond the scope of this thesis. The explanation behind the mechano-sorptive effect makes little difference to the implementation used here. Either hypothesis permits the calculations performed.

The mechano-sorptive strain calculations were performed using Oliver's (1991) fits to the data of Armstrong and Kingston (1962) for bending tests on beams of *E. regnans*, *E. pilularis*, and *E. delegatensis* loaded in the longitudinal direction. The formulation seems likely to be a gross simplification of the real situation, but has been used here on the basis of the success of the program **KilnSched** in predicting surface checking; **KilnSched** depends on this formulation. Future investigations into the mechano-

sorptive effect will undoubtedly yield much better mathematical descriptions of the effect. The expression used was:

$$\Delta\varepsilon_m = \frac{u.\Delta m.s}{E_g} \qquad (5.2.1)$$

$$u = \begin{cases} 3.3 \text{ when } e_u \text{ has the same sign as s} \\ 0.6 \text{ when } e_u \text{ has the opposite sign to s} \end{cases}$$

where: Δm = non-dimensional change in moisture content

s = stress

E_g = Young's Modulus of green timber

The value of u = 0.6 when e_u and s have the same sign appears likely to require modification; Gibson (1965) suggests that in the case of absorption some recovery results from the exothermic heat of adsorption. This implies that in some cases, the value of u may need to be negative. Direct tests in tension and compression across the grain are needed to resolve this question. Figures 5.2.1 to 5.2.3 show the predicted mechano-sorptive strains from the modelling. The temperature was again 20°C.

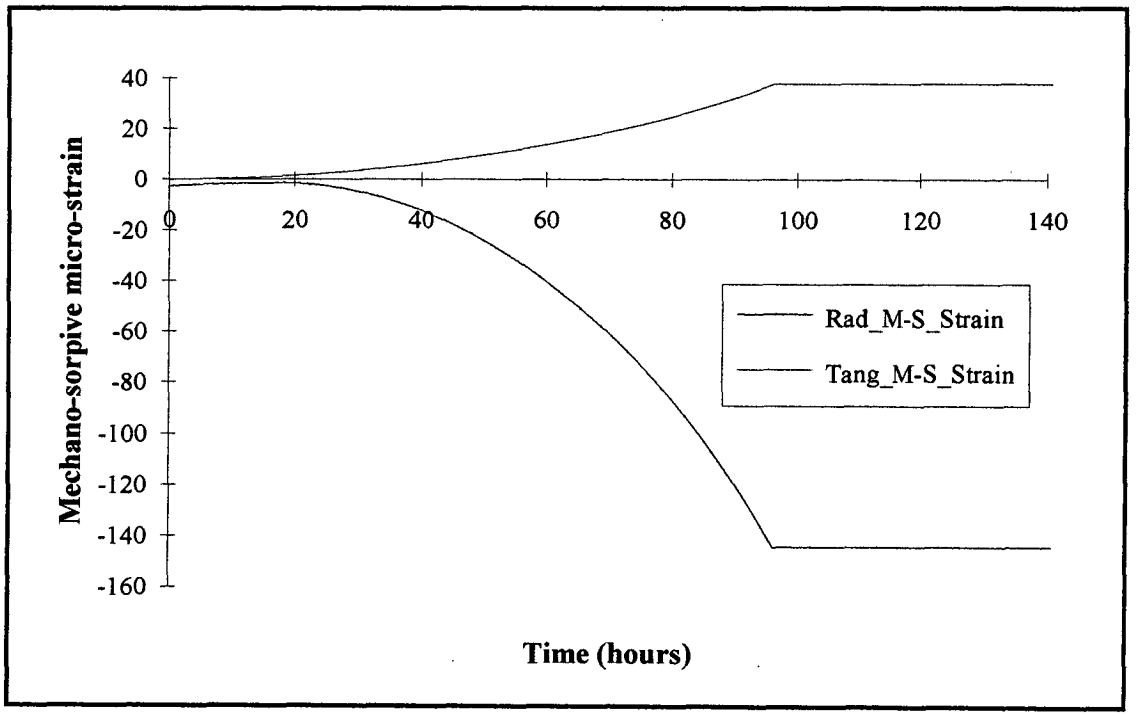

Figure 5.2.1 Mechano-sorptive strains at fibre inner wall calculated by the model.

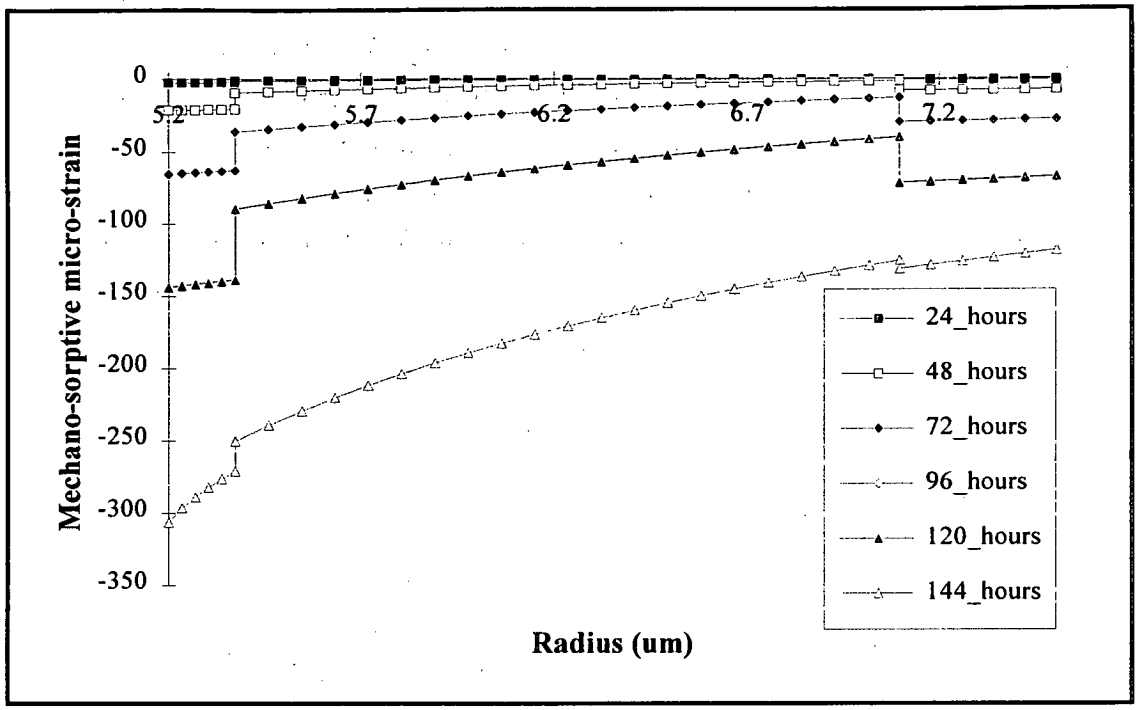

Figure 5.2.2 Radial mechano-sorptive strain profiles

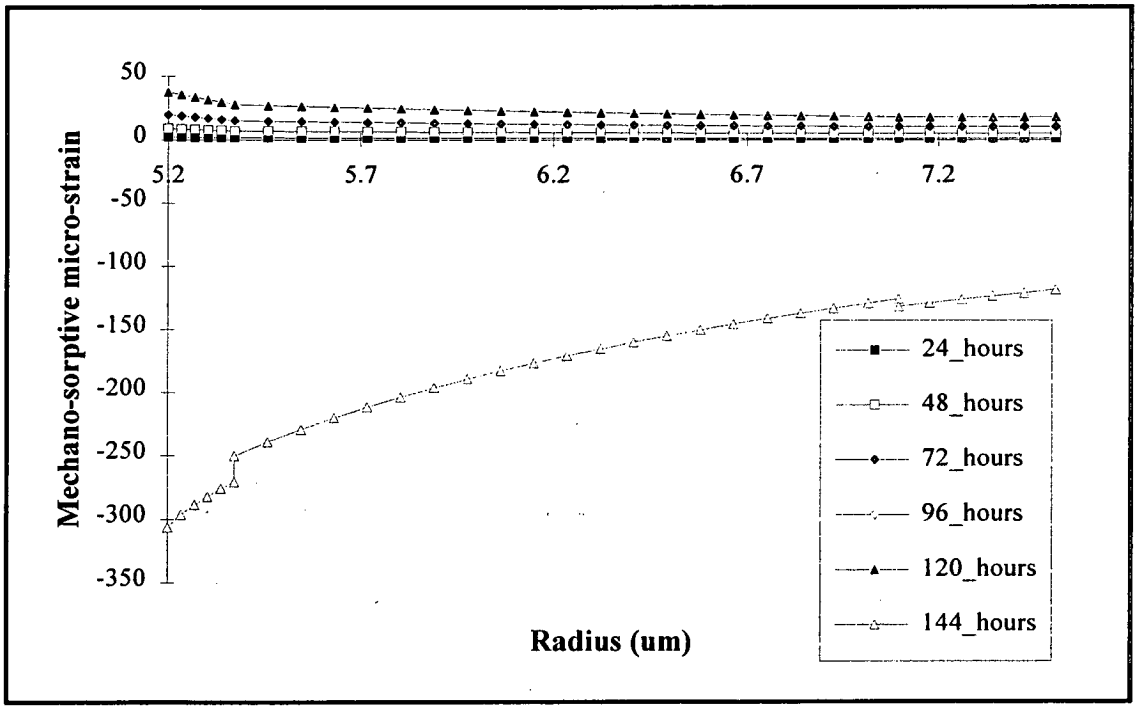

Figure 5.2.3 Tangential mechano-sorptive strain profiles

The change in MC used for these predictions was calculated from two sources. The first was loss of free water from the fibre lumen, based on the new internal fibre radius due to the internal tension, as calculated by the model. The second was the gain of a small amount of bound water, due to a very small increase (of the order of 0.2%) in volume of the fibre wall. This was based on the calculations of fibre wall dimensions

by the model when the fibre was subjected to internal tension, and on the assumption that 50% by volume of the fibre wall was water (Slatyer 1967). This assumption implies a green moisture concentration of approximately 740kg/m^3 assuming that the fibre lumens are full of free water.

The mechano-sorptive strains, like the creep strains, were added to the instantaneous strain to give the net strain. The mechano-sorptive strains predicted by the model are insignificant in comparison to the instantaneous strains. They do not provide sufficient stress relief to allow the dry bulb temperature to be increased during pre-drying, according to these calculations.

5.3 Temperature effect on internal tension

An increase in temperature leads to a decrease in the surface tension of water. This leads to a decrease in the internal tension within the fibre cell. However, the increase in temperature also leads to a decrease in strength of the fibre wall. To examine this effect, the model was run with a linear increase of temperature with time during the relaxation phase. The internal tension was decreased linearly with temperature at 0.2%/°C. This value was obtained from surface tension data of Vennard and Street (1982).

The internal tension was stepped up to 6MPa, as for previous runs of the program. The temperature was started at 23°C, as the ultimate tensile strength of the inner fibre wall at this temperature is slightly greater than 6MPa. The temperature could not be increased during the stress relaxation period without the internal tension exceeding the ultimate radial tensile stress at the inner fibre wall. This indicates that an increase in temperature decreases the tensile strength of the wood faster than it decreases the surface tension of water. Thus the decrease of surface tension with temperature is not sufficient to allow the temperature to be raised during pre-drying.

5.4 Effect of board stress distribution on single fibre stress

During the process of drying a board to FSP, the internal parts of the board are subjected to compression in response to the tension from the outer layers which dry more quickly. This compression has been thought by many to contribute to collapse (Greenhill, 1938; Kauman, 1960) or indeed to be the sole cause (Stamm and Loughborough, 1942).

This effect has been studied here, using values predicted by **SmartKiln** (see Section 6.4.3) for the compression stress in the centre of the board. This stress is then used as the external stress in the single fibre stress model. Note that this implies a uniform two-dimensional compression stress in the board, which is not generally the case. These calculations were performed in the hope of providing some qualitative understanding, rather than meaningful quantitative modelling.

Typical input data for a Tasmanian eucalypt was used in **SmartKiln**, with density = 700 kg/m^3, initial MC = 100%, board thickness 38mm, racking stick thickness 18mm, and reference diffusion coefficient 1.5E-7 m^2/hr at 20°C. Shrinkage at FSP (30% MC) was 1%, with 8% shrinkage at an EMC of 12% MC. The board simulated was backsawn. Dry bulb temperature was increased from 20°C when green to 35°C when the centre of the board reached FSP. Graphical output of the simulation is shown below in Fig. 5.4.1. The variation of stress in the centre of the board with time predicted by **SmartKiln** is shown in Fig. 5.4.2. **SmartKiln** was run for 2000 hours, long enough to dry the centre of the simulated board to FSP.

The stress at the centre of the board as predicted by **SmartKiln** was used as the external stress for the single fibre stress model (including mechano-sorptive and creep strains). The time of increasing stress was 400 hours, during which time the internal tension was increased to 5MPa, the temperature constant at 23°C. Over the following 1592 hours, the temperature was increased linearly with time to 32°C. Variation of stresses and strains at the inner fibre wall with time are shown in Figs. 5.4.3 to 5.4.5. Mechano-sorptive strain has not been plotted as it was insignificant. Fig. 5.4.6 shows the predicted stress profiles through the fibre wall at various times.

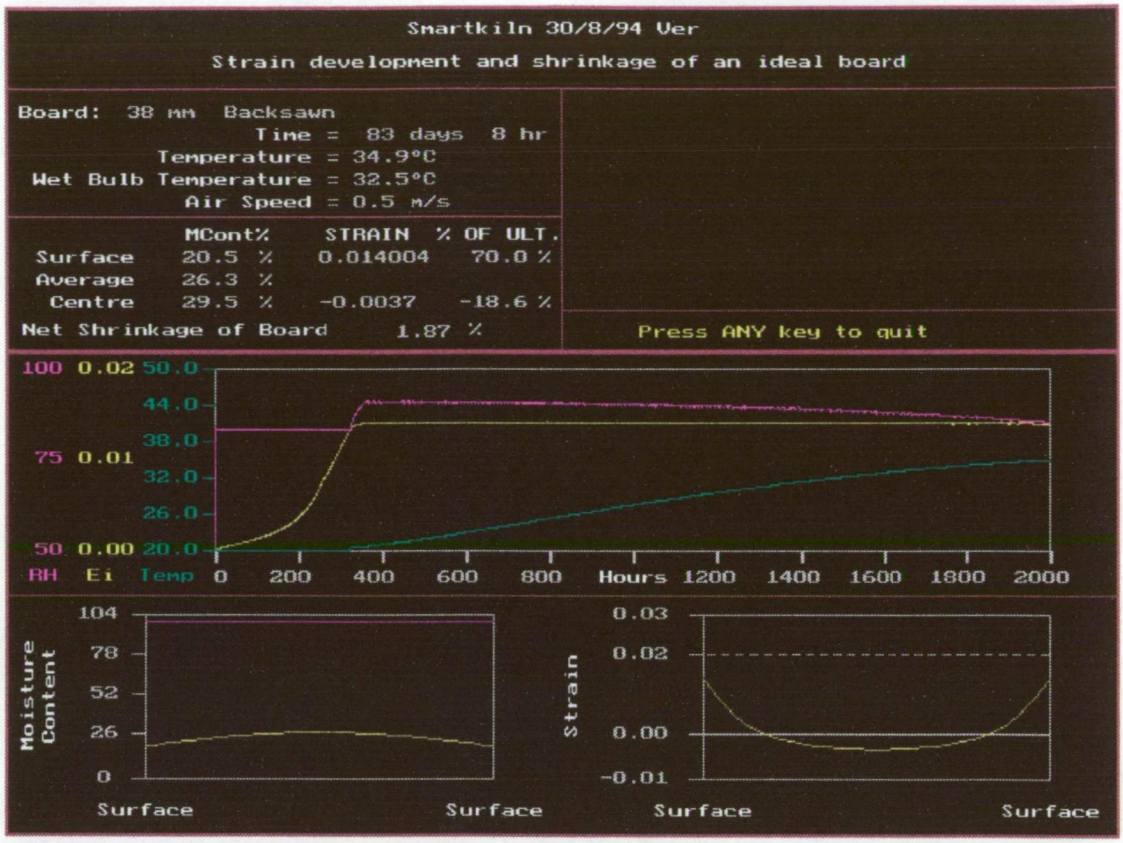

Figure 5.4.1 Graphical output of **SmartKiln** simulation results

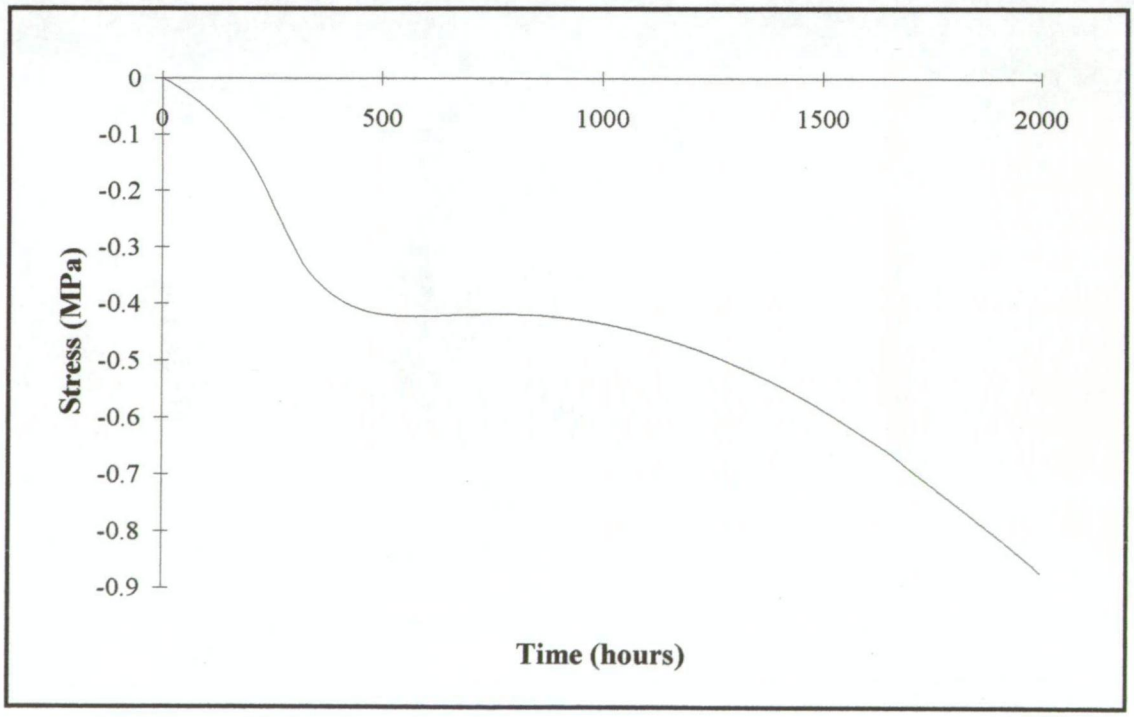

Figure 5.4.2 Stress in the middle of the board predicted by **SmartKiln** simulation

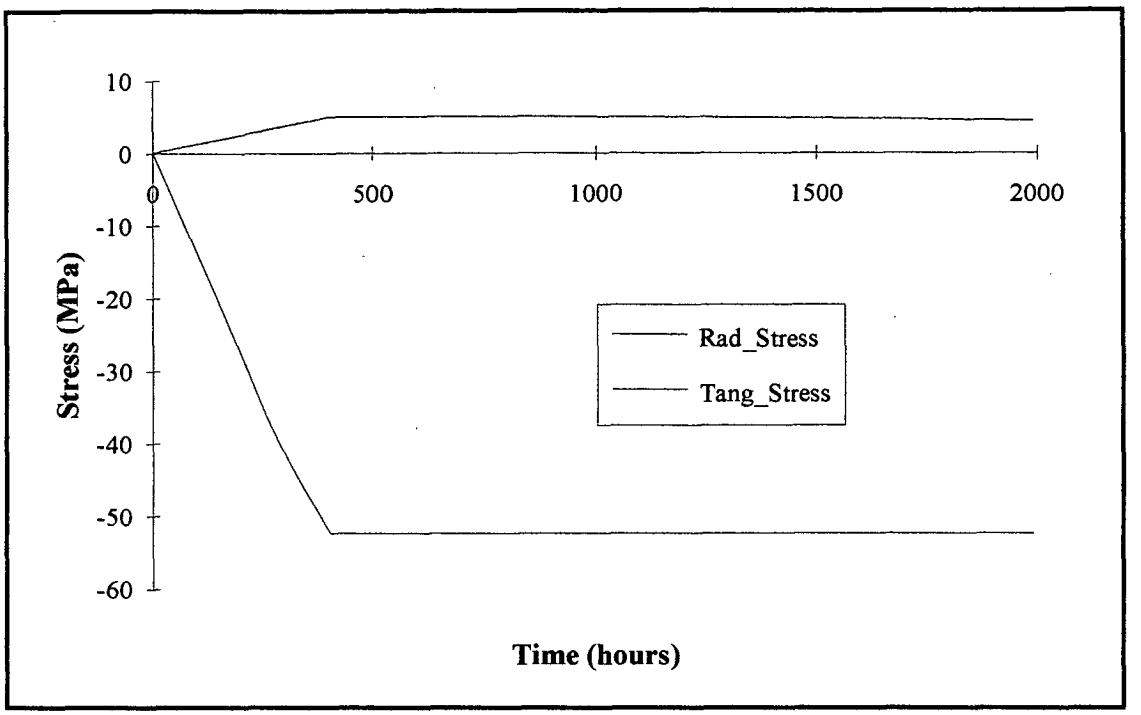

Figure 5.4.3 Stresses at fibre inner wall predicted by model

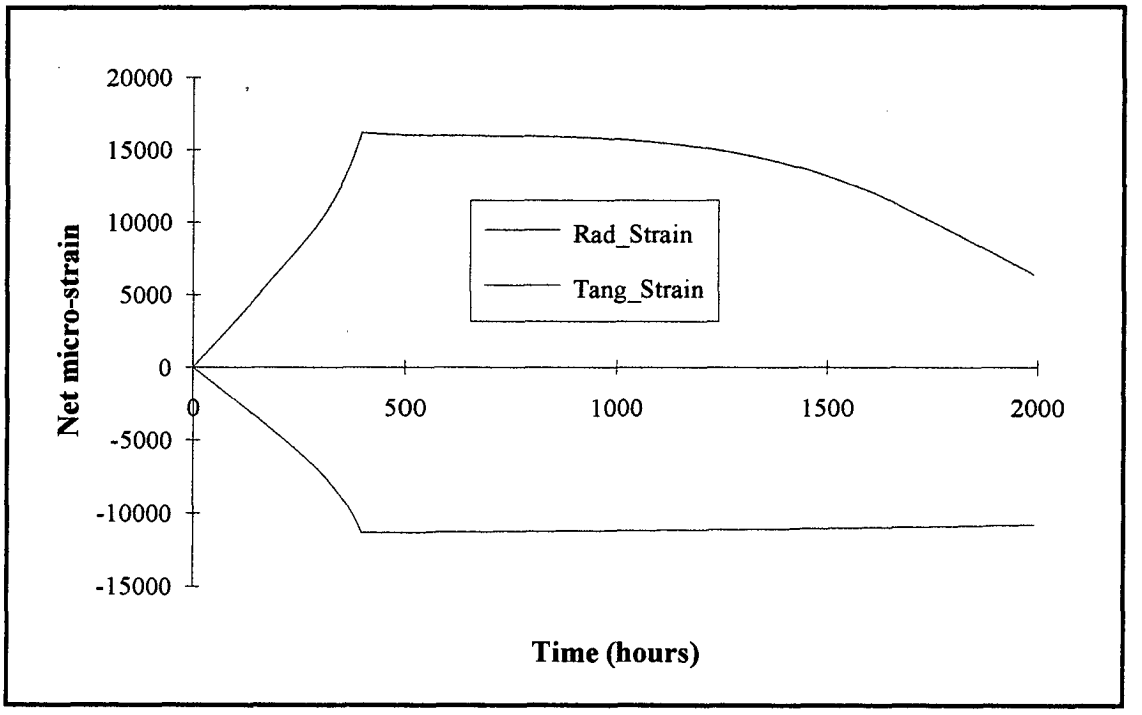

Figure 5.4.4 Net strains at fibre inner wall predicted by model

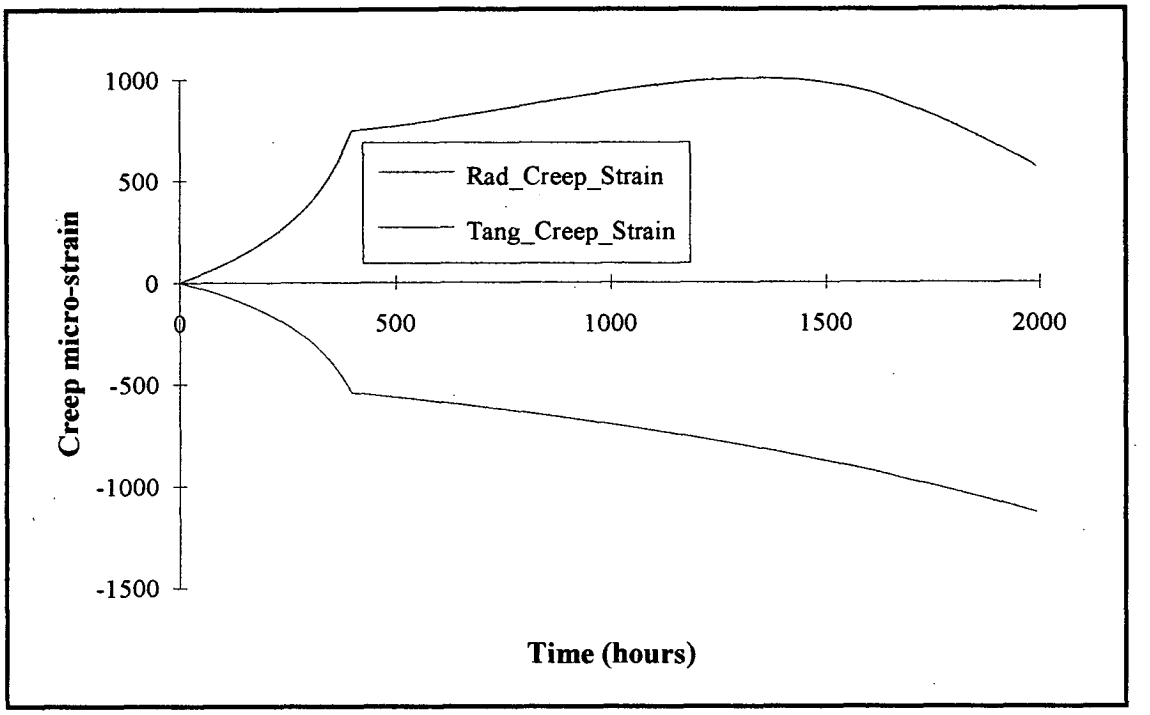

Figure 5.4.5 Creep strains at fibre inner wall predicted by model

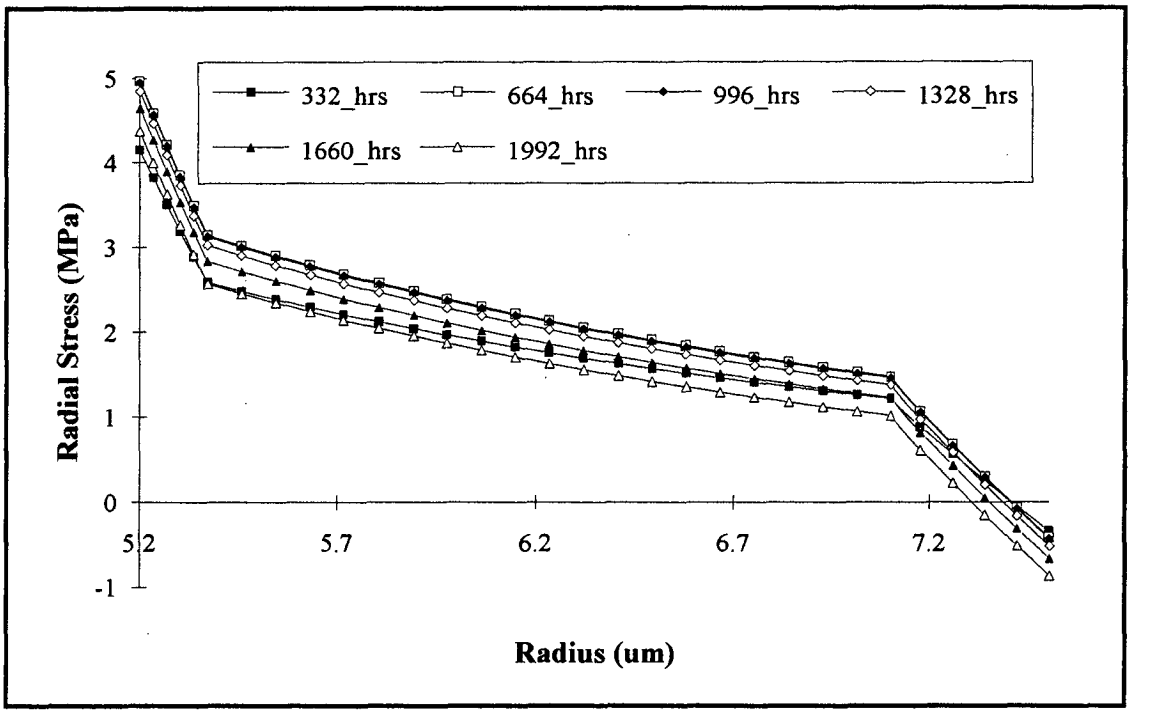

Figure 5.4.6 Stress profiles predicted by model

A second run of the single fibre model was performed with conditions identical to those described above, except that the temperature was maintained constant at 23°C. The radial stress at the inner fibre wall dropped from 5 MPa to 4.42MPa over the 1592 hour relaxation period.

The single fibre stress model predicts that under these conditions the temperature during pre-drying can be increased by several degrees without inducing collapse. Increasing the compressive stress on the outside of the fibre decreases the internal radial stress (see Fig. 5.4.6). Since failure is initiated at the inner fibre wall, a decrease in radial stress there allows temperature to be increased without exceeding the ultimate stress.

The calculations performed here serve only to demonstrate that compressive stresses on the inner parts of boards due to drying may decrease the tendency for fibres to collapse. The stresses calculated by **SmartKiln** are parallel to the surface of the board; the single fibre model uses a uniform external stress. An accurate quantitative solution to the problem requires a full two dimensional stress and drying model of timber seasoning; such a model is not currently available to this author. A two dimensional stress model of a single fibre would then be required, and could be combined with the 2-D drying model at several depths within the board to fully optimise the dry bulb temperature during pre-drying. Such a comprehensive model would require more computing power than can currently be practically supplied in most timber seasoning installations. It is likely that the most profitable approach would be to use such a model to predict likely "safe" schedules for dry bulb temperature during pre-drying for the Clever Kiln Controller, and then use the modelling and AE monitoring capabilities of the CKC to control kiln humidity.

5.5 Conclusions

These calculations demonstrate that the bulk stresses in the drying board may decrease the tendency to collapse. This may allow an increase of dry bulb temperature during pre-drying without inducing collapse. Creep and mechano-sorptive strains appear unlikely to cause sufficient relaxation of fibre wall stresses to allow an increase of dry bulb temperature during pre-drying.

Numerical modelling to predict optimum dry bulb temperature pre-drying schedules seems some way off. The most practical approach at present is to run drying trials aimed at empirically producing the required information to control dry bulb temperature during pre-drying for minimum drying time and degrade. Time constraints prevented such drying trials being carried out as part of this project.

Chapter 6 The Clever Kiln Controller®

The Clever Kiln Controller® (CKC) is an automatic kiln controller which utilises sensed AE feedback in conjunction with on line simulation of the drying process to dry eucalypt timber free of surface checks in the minimum practicable time. It was developed at the University of Tasmania over the last three years by several workers, based on research spanning approximately fifteen years. An overview of the controller is presented here as the author modified the CKC as part of this project.

6.1 Introduction to the CKC

The CKC is a timber kiln controller aimed at small to medium sized batch kilns. It is designed to dry eucalypt timbers from green to FSP free of surface checking. Further research is required to optimise the final drying and stress relieving processes. The CKC is a Windows package run on an IBM PC or compatible. It is written in C++.

The CKC brings together work on the simulation of timber drying (Schaffner and Doe, 1981; Oliver et al, 1986; Wu, 1989; Oliver, 1991; Doe et al, 1994) with advances in the application of sensed AE (Booker, 1994a; 1994b; 1994c; 1995). The modelling work is used to predict an optimum schedule with which to dry a batch of timber, and the sensed AE is used as an override in case of inaccurate modelling or poor kiln control.

The CKC is close to commercialisation. Semi commercial scale trials have been conducted at the VTITC[1] 20m^3 timber capacity kiln at Creswick in Victoria, at the AFRDI[2] 0.5m^3 kiln in Launceston, and two trials at the CALM[3] 1m^3 kiln at Harvey in Western Australia. Most of the CKC development was carried out at the Hobart laboratory, using a 0.125m^3 tunnel kiln described by Booker (1994b).

[1]Victorian Timber Industry Training Centre

[2]Australasian Furnishing Research and Development Institute Ltd.

[3]Western Australian Department of Conservation and Land Management

6.2 Hardware

The CKC runs on an IBM PC or compatible with 80386 or higher processor, under Microsoft Windows 3.1. It uses a Boston Technology PC30B analogue to digital (A/D) board. Also required is a hardware interface box ("relay box") between the A/D board and the kiln, three Physical Acoustics Corp. R6I AE sensors and associated processing circuitry (described by Booker 1994b). Temperature is measured by either one or two pairs of wet and dry bulb transducers, usually either Analogue Devices semiconductor AD590 or 100Ω platinum resistance probes. Air velocity is measured manually and input to the controller for modelling purposes. The kiln must have heaters, vents and humidification (preferably cold water spray), all with either on/off (digital) or 0-10V analogue control. Fan speed can be controlled by a 0-10V analogue output, and is usually kept constant. The relay box is customised to the kiln. The time period of pulse width modulated (digital) output signals from the CKC can be altered in the software. Currently under development is a serial link to control via commercial Programmable Logic Controllers (PLCs). This will simplify installation to existing kilns, and provide kilns with the robustness of industrial PLCs.

6.3 Input data for the CKC

To accurately model the drying behaviour requires precise knowledge of the timber properties. Shrinkage, initial MC profile and basic density are measured in the usual (direct) ways before the drying run begins. Several days drying are then needed under schedule setpoint control to determine the diffusion coefficient. MC profiles of a reference board in the stack are measured every day or two from the start of the drying run. The diffusion coefficient is found using **MCProfiles**, a cut-down version of **KilnSched** which does not include any stress-strain analysis. The drying of the reference board is modelled by **MCProfiles** using an estimated diffusion coefficient, and the predicted moisture profiles compared with the measured ones. The diffusion coefficient is then adjusted, and the procedure repeated until there is close agreement between the calculated and measured values. To obtain an accurate value of diffusion coefficient requires an initial MC profile very close to uniform through the board, and sufficient drying for there to be a substantial decrease in surface MC. This process will obviously take longer for lower diffusion coefficient timbers, as the timber needs

to be dried slowly enough to avoid surface checking. Note that in **KilnSched**, **MCProfiles** and **SmartKiln** the diffusion coefficient is assumed to vary with temperature only. The literature shows the diffusion coefficient of some timbers to be dependent on the moisture concentration, but Wu (1989) found that, for Tasmanian eucalypts at temperatures near 20°C, the diffusion coefficient is independent of moisture concentration.

There is also required an input value for a variable labelled collapse temperature. The controller under AE/**SmartKiln** mode ramps up the dry bulb temperature from the initial temperature specified in the schedule to reach the collapse temperature when the centre MC is reduced to FSP. Usually, however, the controller is run with the dry bulb temperature equal to the collapse temperature from the start of drying, as this gives the highest diffusion coefficient without causing collapse. See Chapter 5 for an examination of the problem of dry bulb temperature optimisation during drying to FSP.

6.4 Control modes

The CKC operates in one of three modes. It either acts as a setpoint controller, controlling the kiln to a predetermined schedule; it controls solely on the sensed AE; or it predicts an optimum continuously varying schedule, and controls to that unless the AE exceeds a safe level.

The heater and humidification settings are controlled by tunable PID (Proportional, Integral, Differential) control algorithms using the DBT and relative humidity (RH) errors respectively. The CKC originally used the DBT and wet bulb temperature (WBT) errors (Booker 1994a). Use of RH as the controlled variable rather than WBT leads to better kiln control, as drift in DBT directly gives drift in WBT, but not in RH. Control of WBT led to poor control, with all of the outputs often increasing together. Changing to RH control significantly improved the CKC's performance. The vents are usually controlled proportionally in response to error in RH, except that if the kiln DBT rises more than 1°C above setpoint the vents open rapidly. The vents then close rapidly when the DBT returns to setpoint, and vent control returns to error in RH. This reduces overshoot in DBT when the kiln is heating up at the start of a kiln trial.

6.4.1 Schedule setpoint control

In this control mode, the CKC controls the kiln to a schedule input by the user. The schedule consists of a series of logical commands for WBT and DBT changes at specified kiln times. In this mode, the CKC acts just like a normal kiln control system.

6.4.2 AE control

This control mode uses sensed AE as feedback to determine appropriate kiln conditions to avoid surface checking. The time constants and threshold AE levels can be changed in software. Figs. 6.4.1 and 6.4.2 show detail of the CKC behaviour from part of the kiln trial run at Harvey in September 1995. Fig. 6.4.3 shows the entire logged temperatures and AE from the Harvey trial. The zero data recorded from approximately 1000 hours is the result of a power failure to the transducers.

Fig. 6.4.1 shows the sawtooth behaviour of the control AE level, and Fig. 6.4.2 shows the resultant kiln setpoint response. This control strategy is necessary to prevent the sensed AE from significantly exceeding the upper control AE level (60% of failure in this case) as there is a lag between setpoint changes and kiln conditions (see Fig. 6.4.2, WBT and setpoint). Note that the DBT is maintained constant so that the drying rate is controlled only by the humidity.

Booker (1994b) found that the peaks of AE correlate with average surface instantaneous strain (ε_i) calculated by the **KilnSched** drying model to within approximately 15%, when both have been normalised to the failure levels. It appears that under increasing stress, the AE peaks rise similarly to the ε_i. Under conditions of decreasing stress, however, the AE drops off rapidly, and the AE peaks are no longer representative of the average surface ε_i. If the stress starts to increase again, the AE rises very rapidly, to again be indicative of surface ε_i. Under these conditions, the drying rate in the kiln needs to be rapidly reduced to avoid exceeding the checking threshold. This is the motivation behind the seemingly complex saw-tooth control AE behaviour.

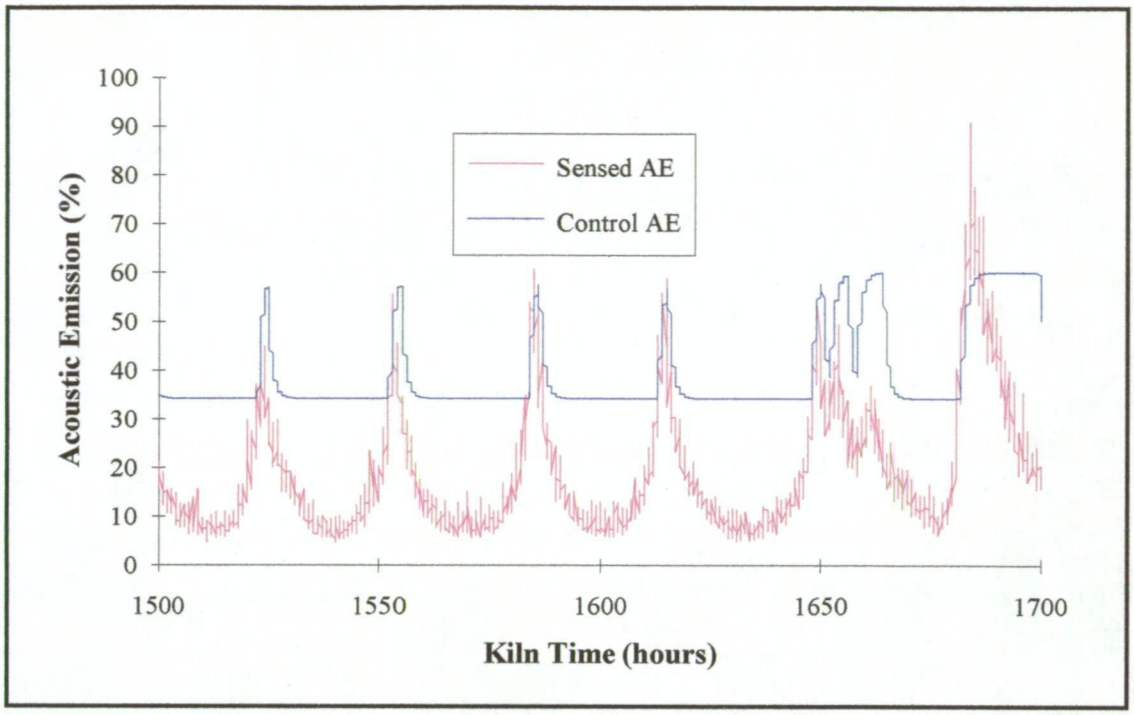

Figure 6.4.1 AE response in AE control mode

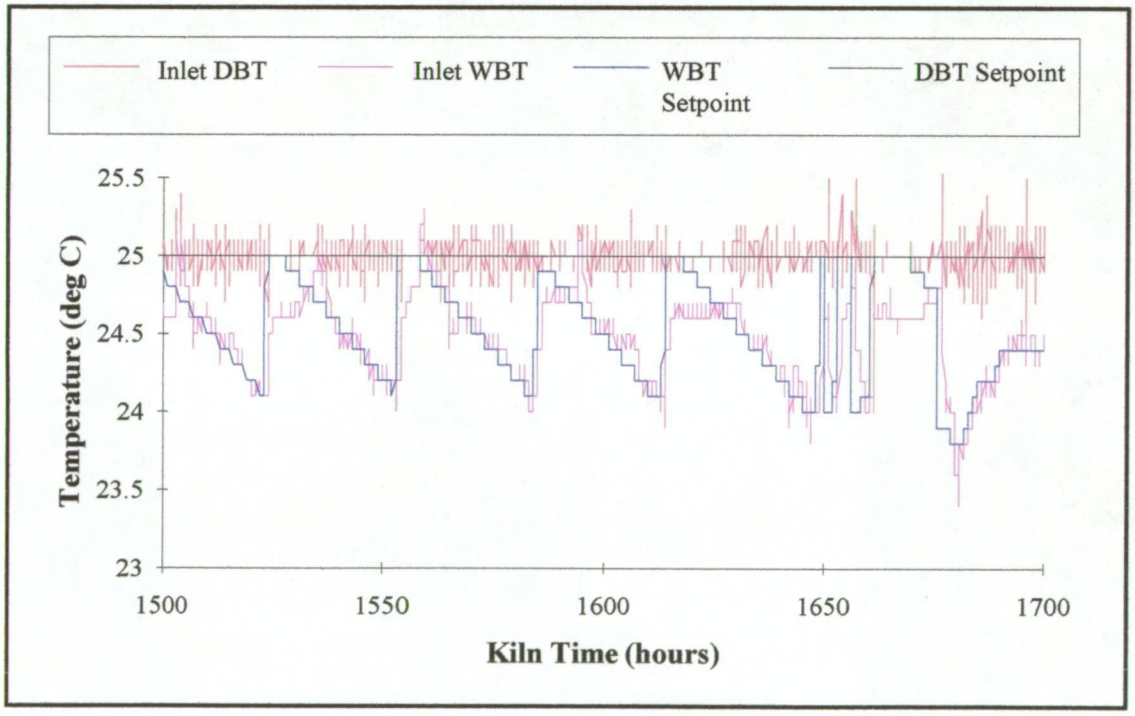

Figure 6.4.2 Temperature response in AE control mode

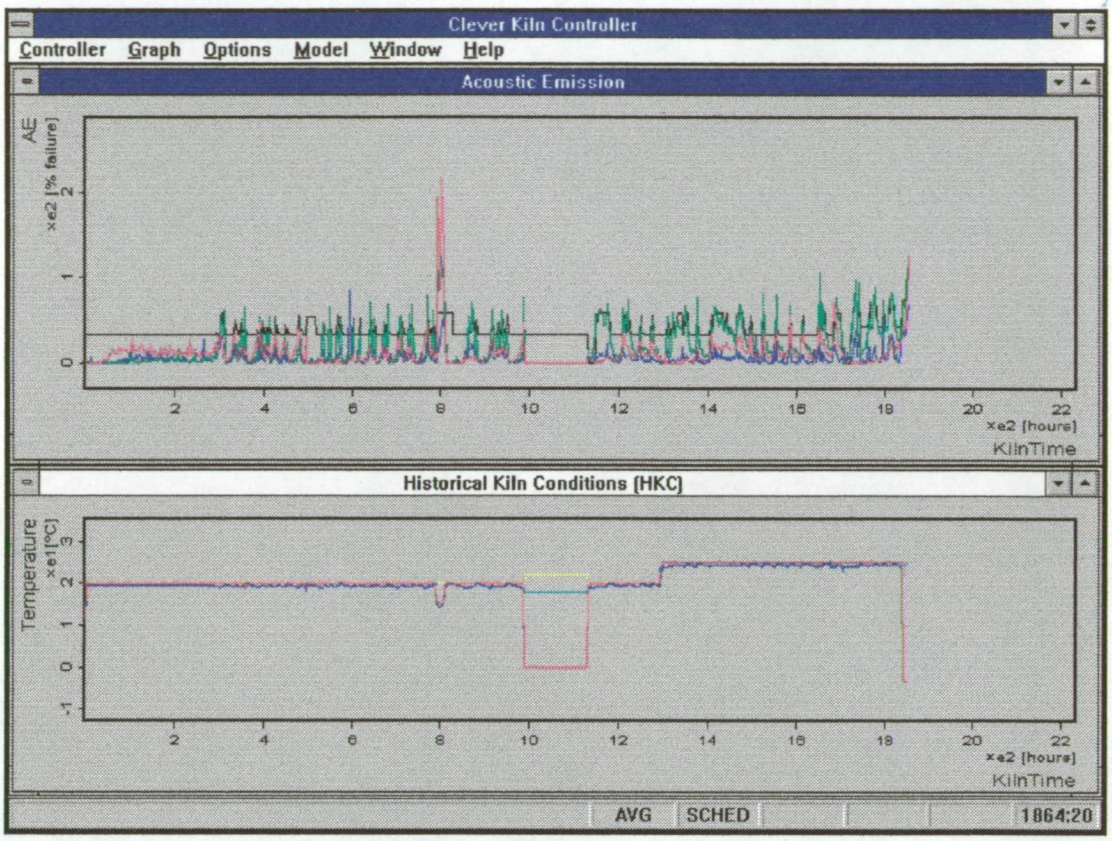

Figure 6.4.3 Typical display screen of the CKC

6.4.3 AE / SmartKiln control

SmartKiln is a derivative of the **KilnSched** model (Oliver, 1991). Booker (1994a) modified **KilnSched** to predict future kiln conditions which would dry the wood as quickly as possible without exceeding a preset surface instantaneous strain. The most sophisticated control mode of the CKC combines the predictive modelling capacity of **SmartKiln** with AE feedback. The model simulates the drying that has occurred based on measured temperatures and air velocity, and then arrives at future drying conditions to maintain the surface instantaneous strain at some safe proportion of the failure strain. The modelling is continuously updated based on measured data, and the optimum schedule revised.

This mode of operation provides faster drying than controlling on AE alone, as the AE control mode tends to produce cyclical drying conditions as shown in Fig. 6.4.2. Given accurate input data, the AE/**SmartKiln** control mode will dry the timber with the average surface stress staying very close to a fixed proportion of the failure level.

An error in modelling will not usually be very large, so that the AE override will be able to ameliorate the drying conditions quickly enough to avoid surface check formation. A conservative error in modelling will result in longer drying times; this could be detected by manually changing kiln conditions to increase the surface drying rate and thus increase the AE. This control mode is relatively new, and thus subject to change with experience. The controller is usually run at only 60-70% of failure levels, partly because of lack of experience, and partly to allow for variation in the wood.

6.5 Over-temperature control

Most timber kilns are not equipped with the capability to provide cooling. The work on collapse described in this thesis showed that restricting the DBT during drying to FSP was necessary to prevent collapse checking. The CKC was thus modified to restrict the drying rate when the ambient temperature rose to become higher than the DBT setpoint. This was achieved by monitoring the ambient temperature just outside the inlet vent; when the ambient temperature was greater than the setpoint for three consecutive readings (at 16 second intervals), the vents were shut. The cold water sprays were then used to control the DBT within the kiln. Thus, as the DBT inevitably increased on hot days, so did the humidity, so that drying essentially stopped until the ambient temperature dropped below setpoint again so that the kiln control strategy could return to normal. Kiln conditions were continually monitored so that their effect on the wood could be examined with **KilnSched**.

Fig. 6.5.1 shows the temperature response inside the kiln when the ambient (external) temperature rose above the DBT setpoint twice. The wet bulb depression decreases to approximately 0.1-0.2°C before the kiln DBT rises above setpoint. This effectively prevents drying, so that the timber does not collapse. Note the power failure at approximately 108 hours.

This strategy is not an optimal solution to the problem of over-temperature control; it substantially decreases drying rate, and creates problems with mathematical modelling of the drying process when the surface dries below FSP, as absorption then occurs (in **KilnSched**, the wood surface is assumed to act as a free water surface above FSP).

Ideally, kilns need to be equipped with cooling capacity to restrict DBT during drying to FSP of collapse prone woods.

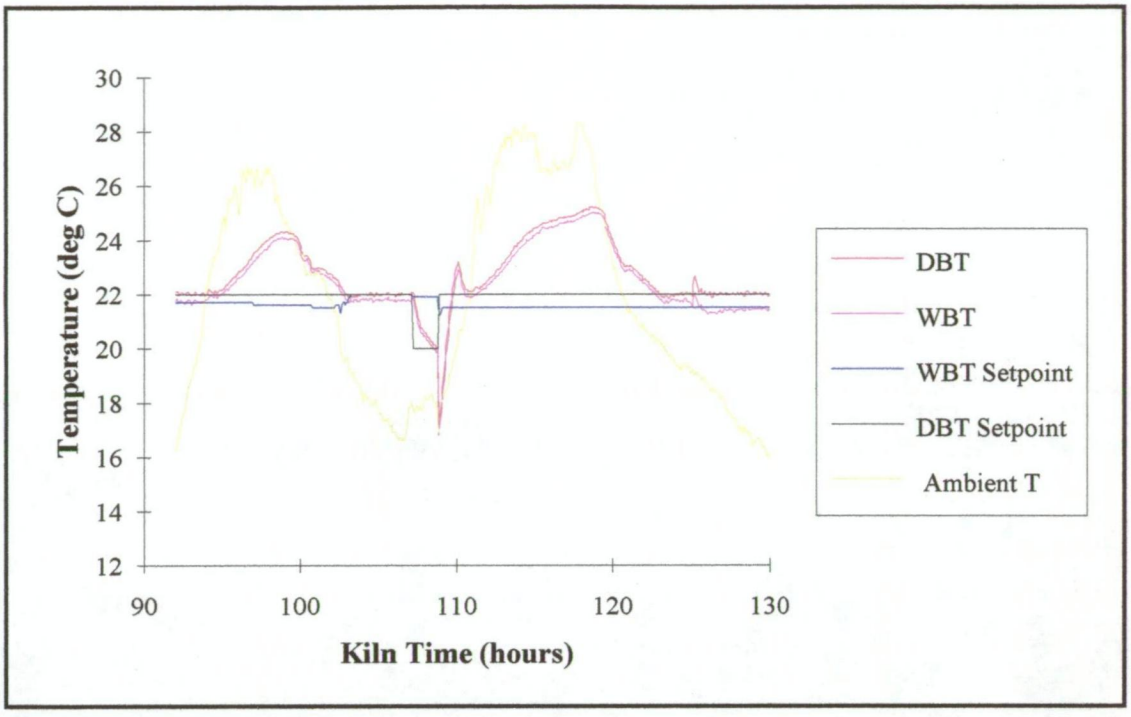

Figure 6.5.1 Response of kiln after addition of over-temperature control

Chapter 7 Drying of Karri (*Eucalyptus diversicolor* F.Muell)

As part of the development of the Clever Kiln Controller® (CKC, see Chapter 6), work was undertaken to assess the seasonability of karri. This work was carried out with the assistance of the Western Australian Department of Conservation and Land Management (CALM). A three-month kiln trial was carried out using the CKC to control a $1m^3$ batch kiln at Harvey, WA from September to November 1995. Currently, very little karri is seasoned to appearance grade because of the difficulty in controlling seasoning-induced degrade (Bootle, 1983).

There appear to be three factors limiting the potential drying rate of karri:

- Exposed vessels on the surface appear to be acting as stress-raisers, decreasing the average stress and strain at the surface which correspond to check initiation. Small surface checks are thus very difficult to find, as they form in the bottoms of these exposed vessels.
- High shrinkage; typically karri is seen to undergo approximately 3% collapse shrinkage at FSP.
- Low diffusion coefficient; the diffusion coefficient in the radial direction appears to be of the order of 3E-8 m^2/hour at 20°C, approximately one fifth that of typical Tasmanian eucalypts.

7.1 Stress-raiser effect of exposed vessels at the board surface

Examination of the surface of karri boards revealed exposed vessels which had been cut in half lengthwise by the saw. The width of these vessels was up to approximately 0.25mm measured under 20× magnification. Observation of surface checked karri boards revealed that the checks invariably formed in the bottoms of these exposed vessels. On the basis of this observation, it was hypothesised that the exposed vessels were acting as stress-raisers at the surface of the timber. This was supported by the AE calibrations, which showed that the checking threshold AE for karri was approximately one-third that of other eucalypt timbers (see section 7.2 below), implying that the average instantaneous strain and stress were lower at failure. In this section, attempts have been made to determine a stress concentration factor for the

vessels by looking at plane-strain stress models. Analytical models for a hole in an infinite plate have been formulated for both isotropic and orthotropic material properties; there does not appear to be an analytical solution to the problem of a semi-circular notch in one edge of a semi-infinite plate (the actual problem, in this case). Models corresponding to these have been formulated using a finite element analysis package, Strand6[1]. Results from the analytical and finite element approaches for the problem of a hole in a plate were compared to ensure that valid results were being obtained by Strand6. The stress-raiser factor obtained from the finite element model of a semi-circular notch in a semi-infinite plate was entered into a version of the **KilnSched** stress-strain and drying model, and the predicted instantaneous strain compared to the AE measured during the Harvey kiln trial.

All of the following modelling was carried out under the assumption that the wood is homogeneous, that is, the effects of growth rings, rays etc. are ignored. The justification for this is that the drying model **KilnSched** also uses these assumptions, but provides predictions which agree with AE measurements to within typically 15%.

This modelling also reveals that the incipient checks formed under these conditions of stress concentration are much smaller (and thus more difficult to find) than those formed in other species not subject to the stress concentration effect. The modelling also indicates possible reasons why the stress-raiser effect of exposed surface vessels is not significant in other woods.

7.1.1 Linear elastic isotropic analytic model of a hole in an infinite plate

This solution is attributed to G. Kirsch (1898). It is taken here directly from Timoshenko and Goodier (1951).

Consider an infinite plate with a circular hole of radius a (Fig. 7.1.1):

[1]Strand6.13 1993. Finite element analysis package. G+D Computing. Suite 508, 3 Small Street, Ultimo NSW 2007, Australia.

We can conclude from Saint-Venant's principle that the change in stresses due to the hole are negligible at distances from the hole which are large compared to a, the hole radius.

Using polar coordinates, the stresses at radius b, where b >> a can thus be given by

$$\sigma_r\big|_{r=b} = S\cos^2\theta = \frac{1}{2}S(1+\cos 2\theta)$$
$$\tau_{r\theta}\big|_{r=b} = -\frac{1}{2}S\sin 2\theta \qquad (7.1.1)$$

where σ_r = radial stress

and $\tau_{r\theta}$ = shear stress in tangential direction.

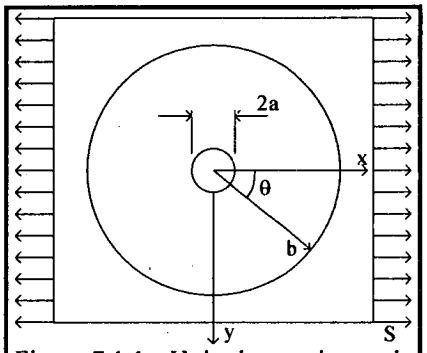

Figure 7.1.1 Hole in an isotropic plate

This stress distribution can be considered as two parts. The first is a constant component ½S. The second part consists of a normal force ½Scos2θ and a shearing force -½Ssin2θ. The stresses arising from the second part may be derived from a stress function of the type:

$$\phi = f(r)\cos 2\theta \qquad (7.1.2)$$

where r is the radius, $a \le r \le b$.

Substituting this into the compatibility equation

$$\left(\frac{\partial^2}{\partial r^2}+\frac{1}{r}\frac{\partial}{\partial r}+\frac{1}{r^2}\frac{\partial^2}{\partial\theta^2}\right)\left(\frac{\partial^2\phi}{\partial r^2}+\frac{1}{r}\frac{\partial\phi}{\partial r}+\frac{1}{r^2}\frac{\partial^2\phi}{\partial\theta^2}\right)=0 \qquad (7.1.3)$$

we get an ordinary differential equation in f(r)

$$\left(\frac{d^2}{dr^2}+\frac{1}{r}\frac{d}{dr}-\frac{4}{r^2}\right)\left(\frac{d^2 f}{dr^2}+\frac{1}{r}\frac{df}{dr}-\frac{4f}{r^2}\right)=0 \qquad (7.1.4)$$

The general solution to this equation is given by

$$f(r) = Ar^2 + Br^4 + C\frac{1}{r^2} + D \qquad (7.1.5)$$

where A, B, C, D are constants.

Substituting 7.1.5 into 7.1.2 we get an expression for the stress function

$$\phi = \left(Ar^2 + Br^4 + \frac{C}{r^2} + D\right)\cos 2\theta \qquad (7.1.6)$$

Using the general formulation for polar coordinates, the stress components are then given by

$$\sigma_r = \frac{1}{r}\frac{\partial\phi}{\partial r} + \frac{1}{r^2}\frac{\partial^2\phi}{\partial\theta^2} = -\left(2A + \frac{6C}{r^4} + \frac{4D}{r^2}\right)\cos 2\theta$$

$$\sigma_\theta = \frac{\partial^2\phi}{\partial r^2} = \left(2A + 12Br^2 + \frac{6C}{r^4}\right)\cos 2\theta \qquad (7.1.7)$$

$$\tau_{r\theta} = -\frac{\partial}{\partial r}\left(\frac{1}{r}\frac{\partial\phi}{\partial\theta}\right) = \left(2A + 6Br^2 - \frac{6C}{r^4} - \frac{2D}{r^2}\right)\sin 2\theta$$

We now use boundary conditions 7.1.1 at radius b, and the condition that the edge of the hole be free from external forces to solve for A, B, C, D.

$$2A + \frac{6C}{b^4} + \frac{4D}{b^2} = -\frac{1}{2}S$$

$$2A + \frac{6C}{a^4} + \frac{4D}{a^2} = 0$$

$$2A + 6Bb^2 - \frac{6C}{b^4} - \frac{2D}{b^2} = -\frac{1}{2}S \qquad (7.1.8)$$

$$2A + 6Ba^2 - \frac{6C}{a^4} - \frac{2D}{a^2} = 0$$

When we assume an infinitely large plate (a/b=0) and solve, we get

$$A = -\frac{S}{4},\quad B = 0,\quad C = -\frac{a^4}{4}S,\quad D = \frac{a^2}{2}S \qquad (7.1.9)$$

Substituting into 7.1.7 and adding the uniform tension ½S we get the stress components

$$\sigma_r = \frac{S}{2}\left(1 - \frac{a^2}{r^2}\right) + \frac{S}{2}\left(1 + \frac{3a^4}{r^4} - \frac{4a^2}{r^2}\right)\cos 2\theta$$

$$\sigma_\theta = \frac{S}{2}\left(1 + \frac{a^2}{r^2}\right) - \frac{S}{2}\left(1 + \frac{3a^4}{r^4}\right)\cos 2\theta \qquad (7.1.10)$$

$$\tau_{r\theta} = -\frac{S}{2}\left(1 - \frac{3a^4}{r^4} + \frac{2a^2}{r^2}\right)\sin 2\theta$$

We can now find the stresses at the edge of the hole by putting r = a

$$\sigma_r = \tau_{r\theta} = 0,\quad \sigma_\theta = S - 2S\cos 2\theta \qquad (7.1.11)$$

σ_θ is clearly highest at $\theta = \pi/2$ and $\theta = 3\pi/2$, where we get $\sigma_\theta = 3S$.

That is, the stress concentration factor for a round hole in a linear elastic isotropic infinite plate is 3.

7.1.2 Finite element model of a hole in an isotropic linear elastic infinite plate

A finite element model equivalent to the analytical model of 7.1.1 was set up in Strand6. Some of the output results are shown in Figs 7.2.1 and 7.2.2. The model was set up in SI units and a uniform tension stress of 2MPa applied in the horizontal (X) direction. Material properties used were: E = 250MPa, μ = 0.5. The lower left node was fully restrained, the other corner nodes were free in the x direction, but otherwise fixed. All other nodes were fixed against translation in the z direction, and against rotation. Fig. 7.2.1 shows a stress-raiser of 3.1, a close approximation to the analytical result of 3.0.

7.1.3 Analytical model of a hole in an orthotropic infinite plate

Oliver (1995a) adapted a solution from Savin (1961), which dealt with the problem of stress concentration around elliptical holes in plates. Oliver (1995b) implemented the solution in a Pascal computer program. The stress concentration factor computed by the program was 3.4. See Appendix C for the solution. The results listing also shows that the area affected by the stress concentration is very small (this result is corroborated by the Strand6 results). This indicates that surface checks are very small when they first form, and that they form in the bottom of the exposed vessels, making them very difficult to find.

7.1.4 Finite element model of a hole in an orthotropic linear elastic infinite plate

A plane strain finite element model equivalent to the analytical model of 7.1.3 was set up in Strand6. The material properties used were the same as those in the analytic model (Appendix C), that is:

μ_{tz} = 0.035; μ_{tr} = 0.379; μ_{rz} = 0.052; μ_{rt} = 0.718; μ_{zr} = 0.495;
μ_{zt} = 0.632; E_t = 250MPa E_r = 500MPa E_Z = 5GPa

Strand6 requires the coefficients of the C matrix for

$$\{\sigma\} = [C]\{\varepsilon\} \tag{7.1.12}$$

For a linearly elastic orthotropic material we have the following Hooke's equations:

$$\varepsilon_x = \frac{\sigma_x}{E_x} - \frac{\mu_{yx}\sigma_y}{E_y} - \frac{\mu_{zx}\sigma_z}{E_z} \tag{7.1.13}$$

$$\varepsilon_y = -\frac{\mu_{xy}\sigma_x}{E_x} + \frac{\sigma_y}{E_y} - \frac{\mu_{zy}\sigma_z}{E_z} \tag{7.1.14}$$

$$\varepsilon_z = -\frac{\mu_{xz}\sigma_x}{E_x} - \frac{\mu_{yz}\sigma_y}{E_y} + \frac{\sigma_z}{E_z} \tag{7.1.15}$$

$$\gamma_{yz} = \frac{1}{G_{yz}}\tau_{yz} \tag{7.1.16}$$

$$\gamma_{zx} = \frac{1}{G_{zx}}\tau_{zx} \tag{7.1.17}$$

$$\gamma_{xy} = \frac{1}{G_{xy}}\tau_{xy} \tag{7.1.18}$$

where γ = shear strain

τ = shear stress

G = shear modulus

and x, y, z are the three principal directions.

The equations 7.1.13 to 7.1.18 are summarised in matrix form

$$\begin{vmatrix} \varepsilon_x \\ \varepsilon_y \\ \varepsilon_z \\ \gamma_{yz} \\ \gamma_{zx} \\ \gamma_{xy} \end{vmatrix} = \begin{vmatrix} s_{11} & s_{12} & s_{13} & 0 & 0 & 0 \\ s_{21} & s_{22} & s_{23} & 0 & 0 & 0 \\ s_{31} & s_{32} & s_{33} & 0 & 0 & 0 \\ 0 & 0 & 0 & s_{44} & s_{45} & s_{46} \\ 0 & 0 & 0 & s_{54} & s_{55} & s_{56} \\ 0 & 0 & 0 & s_{64} & s_{65} & s_{66} \end{vmatrix} \begin{vmatrix} \sigma_x \\ \sigma_y \\ \sigma_z \\ \tau_{yz} \\ \tau_{zx} \\ \tau_{xy} \end{vmatrix} \tag{7.1.19}$$

Where the coefficients s_{ij} correspond to the coefficients of equations 7.1.13 to 7.1.18.

Using the plane strain assumption ($\varepsilon_Z = 0$) in equation 7.1.15 and substituting into equations 7.1.13 and 7.1.14, and acknowledging that out of plane shears are zero, equation 7.1.19 can be simplified and rewritten

$$\begin{vmatrix} \varepsilon_x \\ \varepsilon_y \\ \gamma_{xy} \end{vmatrix} = \begin{vmatrix} s_{11} - \frac{s_{13}s_{31}}{s_{33}} & s_{12} - \frac{s_{13}s_{32}}{s_{33}} & 0 \\ s_{21} - \frac{s_{31}s_{23}}{s_{33}} & s_{22} - \frac{s_{23}s_{32}}{s_{33}} & 0 \\ 0 & 0 & s_{66} \end{vmatrix} \begin{vmatrix} \sigma_x \\ \sigma_y \\ \tau_{xy} \end{vmatrix} \qquad (7.1.20)$$

Comparing equation 7.1.12 with 7.1.20, it is clear that

$$[C] = \begin{vmatrix} s_{11} - \frac{s_{13}s_{31}}{s_{33}} & s_{12} - \frac{s_{13}s_{32}}{s_{33}} & 0 \\ s_{21} - \frac{s_{31}s_{23}}{s_{33}} & s_{22} - \frac{s_{23}s_{32}}{s_{33}} & 0 \\ 0 & 0 & s_{66} \end{vmatrix}^{-1} \qquad (7.1.21)$$

Substituting the material properties, we get

$$[C] = \begin{vmatrix} 0.3719 & 0.2946 & 0 \\ 0.2946 & 0.7465 & 0 \\ 0 & 0 & 0.1117 \end{vmatrix} GPa \qquad (7.1.22)$$

These are the coefficients required by Strand6.

The global restraints applied to the model consisted of rotational and z-translational restraints on all nodes, the lower left node was fully restrained, and the other three corner nodes were free to move in the x-direction only. The infinite plate was approximated by a plate seven diameters square, with the hole in the middle. The local effects resulting from the corner restraints appear not to have affected the stress distribution around the hole. A uniform tension of 2MPa was applied in the x direction. The stress distributions are shown in Figs 7.2.3 and 7.2.4. Only the area near the hole is shown for clarity.

To check for convergence, the model was run again with each plate element subdivided into four. The predicted stresses changed by less than 3%. On the basis of this, the grid shown was selected as giving a reasonable compromise between computation time and accuracy.

Fig 7.2.3 shows a stress-raiser factor of 2.9, somewhat lower than the analytical prediction of 3.4 for an internal hole in an orthotropic material. This level of agreement provides satisfactory support for the results from the finite element model. A finite element model for the problem of a semi-circular notch at a surface (for which there appears to be no analytical solution) was thus formulated.

7.1.5 Finite element model of a semi-circular notch in an orthotropic linear elastic semi-infinite plate

The model presented above in section 7.1.4 was cut in half to model the problem in question, that is, a semi circular notch in a semi-infinite plate, corresponding to a part of a vessel lying exposed on the surface of a board. Model parameters, loads and restraints are all as above. Results are shown in Figs 7.2.5 and 7.2.6. Note that the plate was modelled to a distance of three diameters from the notch; the output displays show only the area around the notch.

Fig 7.2.5 shows a stress-raiser of 3.1. This solution did not converge as well on subdivision of the basic grid as did the solution for a hole in an infinite plate. Further subdivision of the grid gave a solution which appeared to be subject to round-off problems. The uncertainty in the stress-raiser factor appears to be approximately ± 0.3.

7.1.6 Effect of size of notch on stress concentration factor

A model of a 0.1mm diameter semi-circular notch in a linear elastic orthotropic semi infinite plane was set up in Strand6 for comparison with the model presented above, which was identical except that the notch was 0.25mm in diameter. Results are shown in Figs 7.2.7 and 7.2.8.

Comparison of these results with Figs 7.2.5 and 7.2.6 shows that the stress concentration factor for the 0.1mm diameter notch is approximately 15% lower than that for the 0.25mm diameter notch, although this may be affected by grid size. As well as this, the area subject to high stress from the concentration is much smaller in the case of the 0.1mm notch. This means that a check will be much smaller on formation, and once formed will be less likely to run. A smaller vessel occupies a lower proportion of that part of the thickness of the board subjected to tension during drying to FSP.

Thus, it is thought that this stress concentration effect does not occur in other species of eucalypts (*E. regnans, E. delegatensis, E. globulus, E. marginata*) because the vessels are so much smaller than those in karri. It is likely that the effect will occur in

other species which have wide vessels. The effect of saw damage is likely to complicate the issue; small vessels more fragile than those in karri may not provide any stress concentration at all if they are destroyed by the saw. The saw itself may cause local stress concentrations, but this is thought to be unlikely as boards are usually sawn across their faces perpendicular to their length, thus any notches will be parallel to the direction of surface stress due to drying.

7.2 Graphical output from the Strand6 finite element analysis program

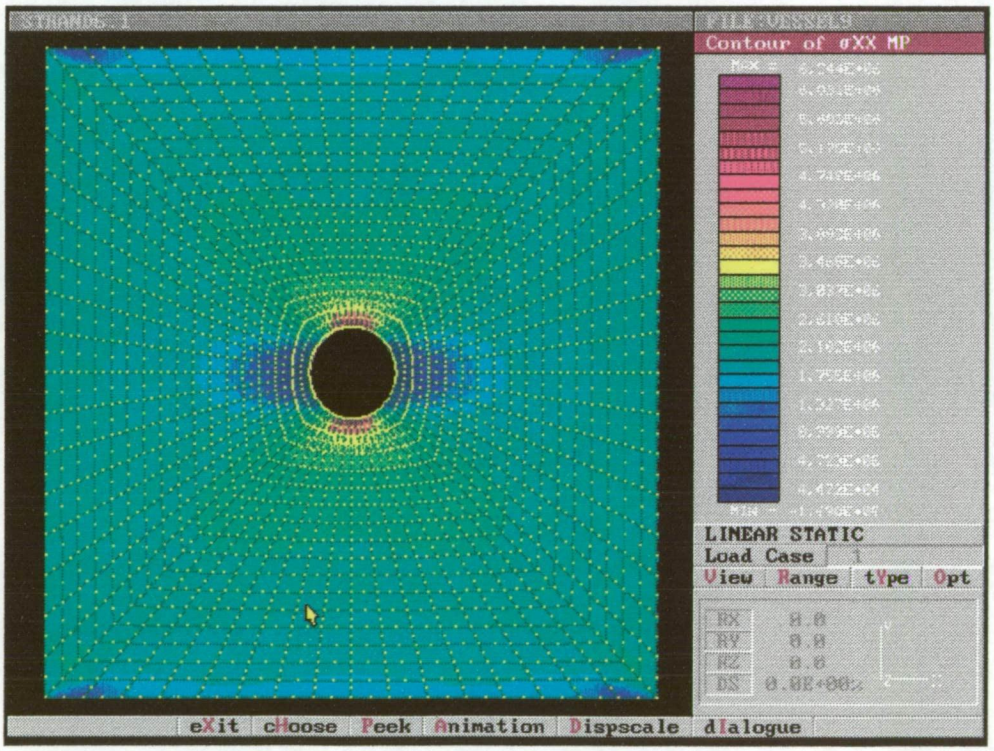

Figure 7.2.1 σ_{XX} plot for 0.25mm hole in linear elastic isotropic infinite plate subjected to 2 MPa tension in the x (horizontal) direction

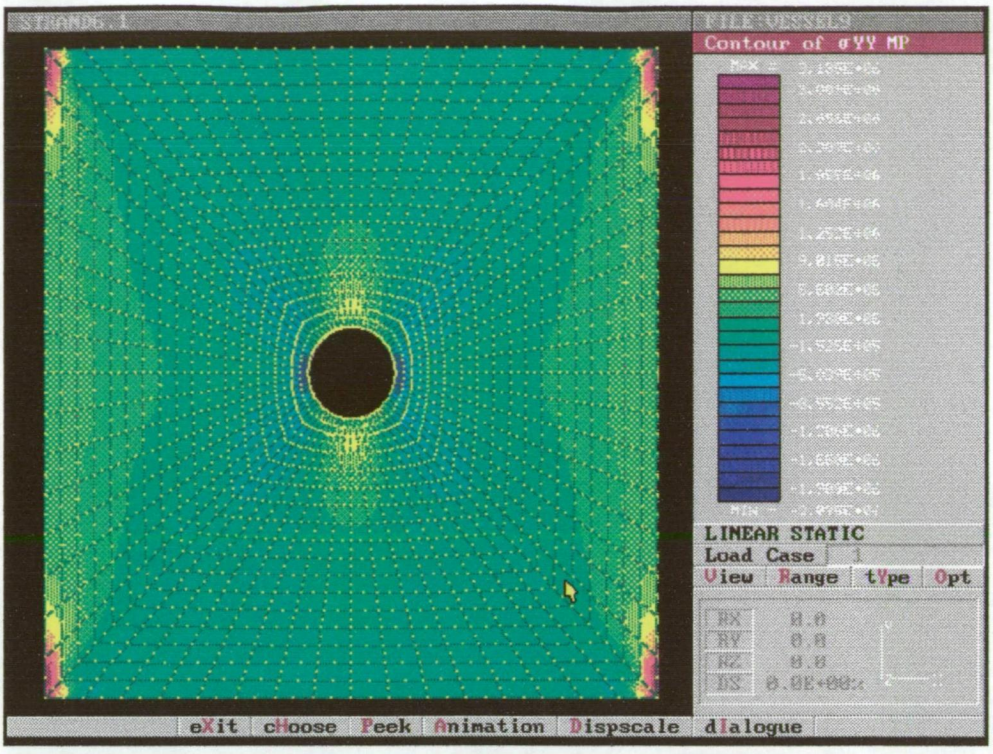

Figure 7.2.2 σ_{yy} plot for 0.25mm hole in linear elastic isotropic infinite plate subjected to 2 MPa tension in the x direction

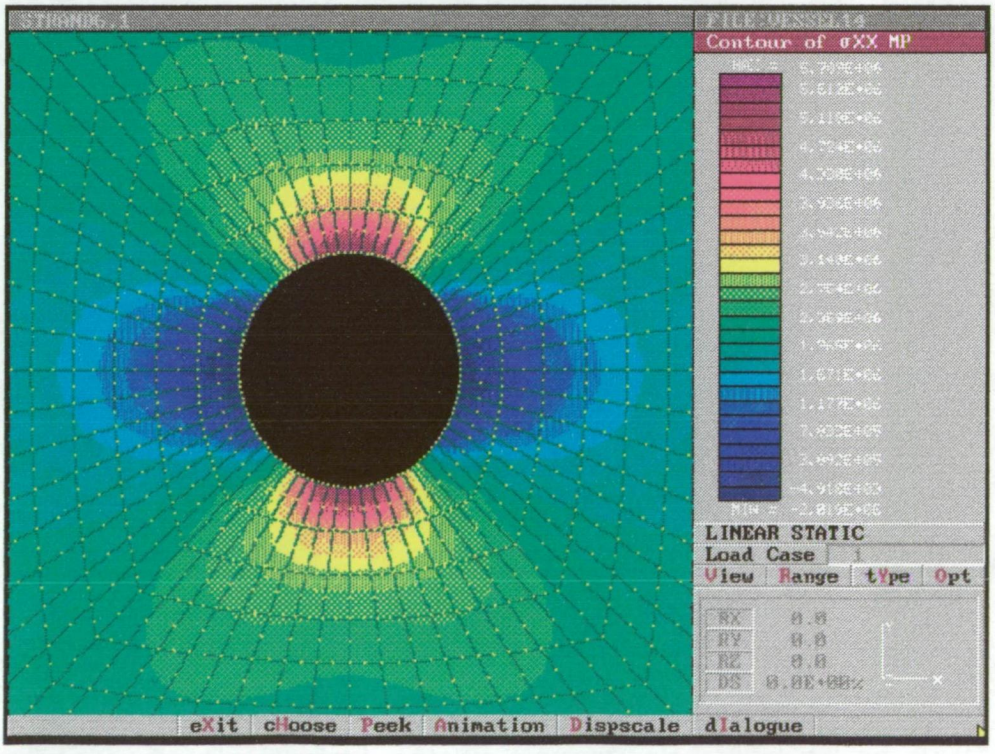

Figure 7.2.3 σ_{xx} plot for 0.25mm hole in linear elastic orthotropic infinite plate subjected to 2 MPa tension in the x direction

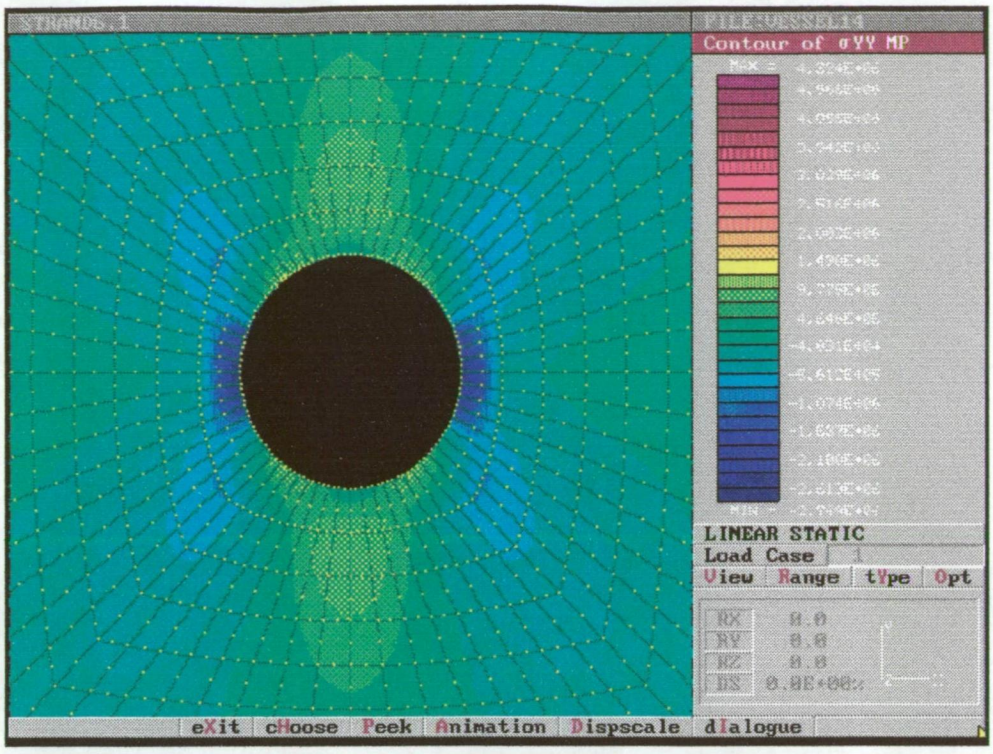

Figure 7.2.4 σ_{yy} plot for 0.25mm hole in linear elastic orthotropic infinite plate subjected to 2 MPa tension in the x direction

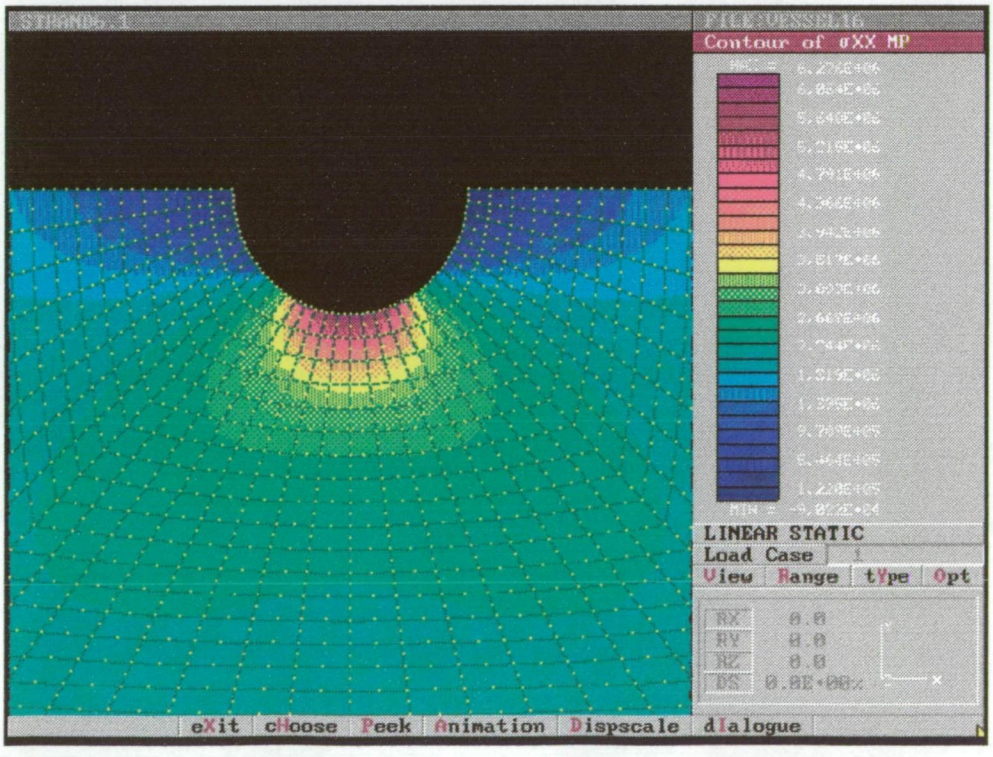

Figure 7.2.5 σ_{xx} plot for 0.25mm semi-circular notch in orthotropic semi-infinite plate subjected to 2 MPa tension in the x direction

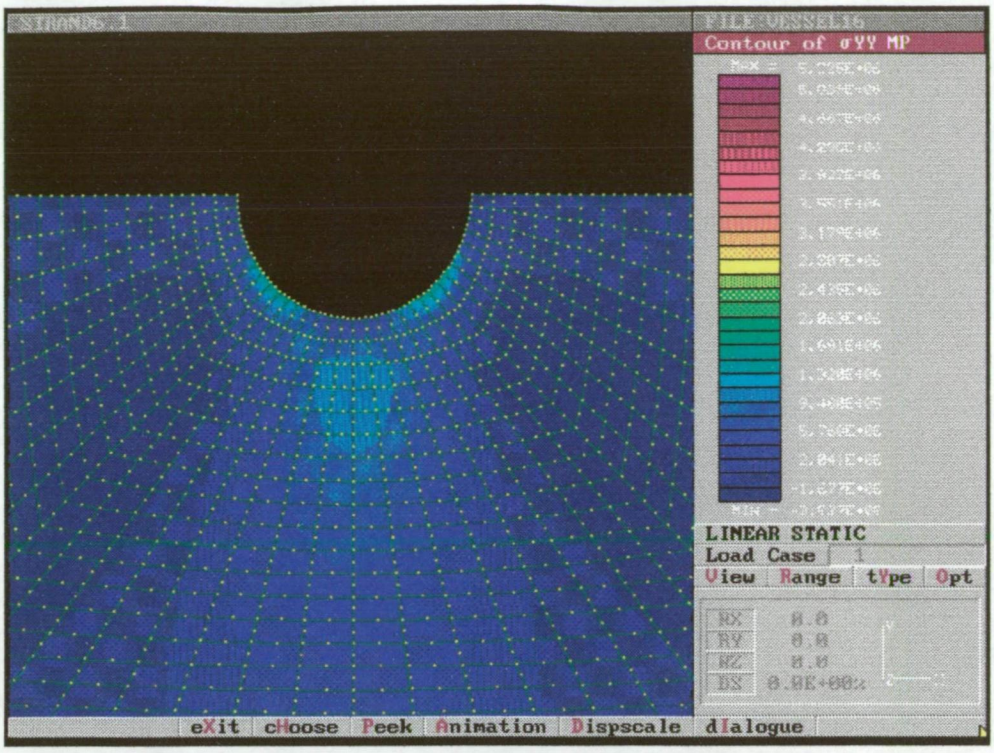

Figure 7.2.6 σ_{yy} plot for 0.25mm diameter semi-circular notch in orthotropic semi-infinite plate subjected to 2 MPa tension in the x direction

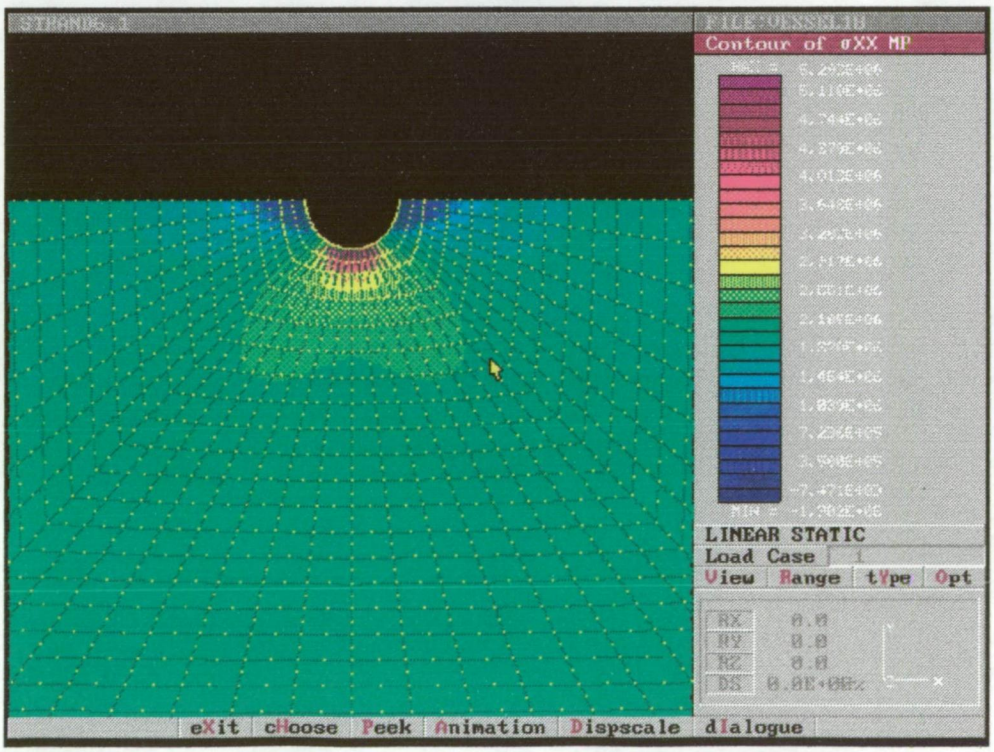

Figure 7.2.7 σ_{xx} plot for 0.1mm diameter semi-circular notch in orthotropic semi-infinite plate subjected to 2 MPa tension in the x direction

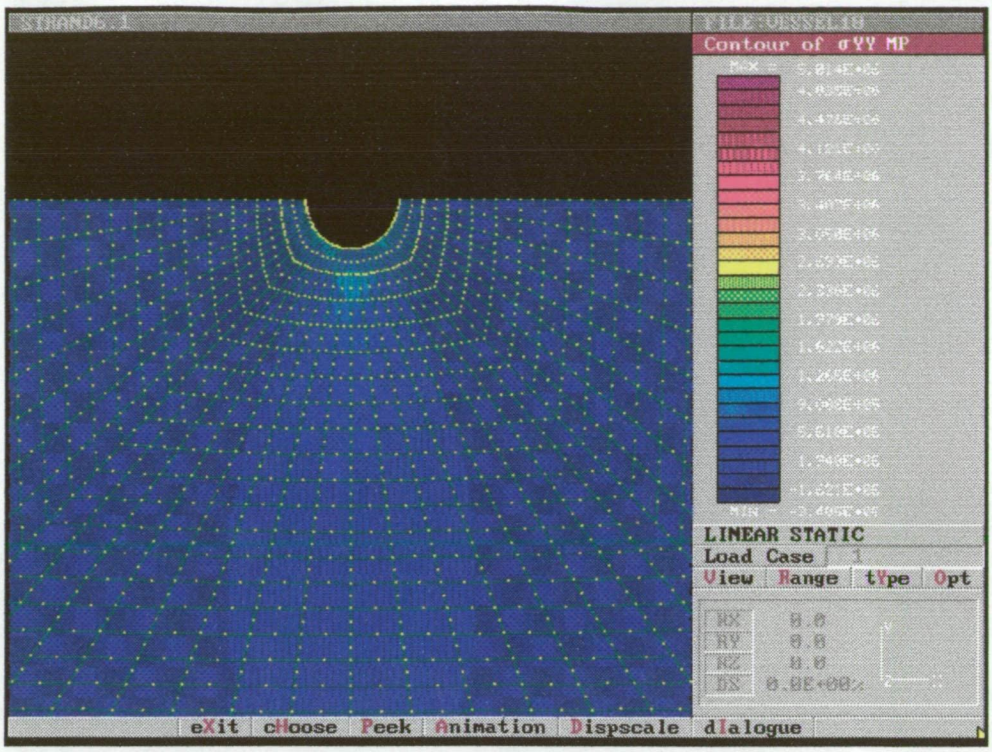

Figure 7.2.8 σ_{yy} plot for 0.1mm semi-circular notch in orthotropic semi-infinite plate subjected to 2 MPa tension in the x direction

7.3 Acoustic Emission (AE) properties of karri

7.3.1 AE and stress concentration

Booker (1994a; 1994c) hypothesised that the AE from drying timber was due to crystalline slips in the crystalline cellulose component of the wood. This hypothesis led to the conclusion that the checking threshold AE should be independent of wood species, since the proportion of crystalline cellulose is near constant for all woods. This conclusion, however, is subject to several assumptions. For example, it is assumed that there are no other substantial sources of AE from the drying timber. In fact, Booker (1994a) measured AE from *Pinus radiata* which did not support this assumption; he attributed this behaviour to "brittle failure in the resin canals, structural elements not present in the eucalyptus genus". It is also assumed that the average surface instantaneous strain corresponding to surface check formation is independent of species. This assumption appears to be valid for the various eucalypts

studied by Booker and others (Booker, 1994a; 1994b; *E. regnans*, *Tristania conferta* studied in this thesis). However, in the case of karri, it appears that the average surface instantaneous strain (and thus stress) corresponding to surface check formation is decreased by a stress-raiser effect around exposed vessels, as discussed above. The result was a substantial decrease in the checking threshold AE for karri as compared to that found for other eucalypts.

7.3.2 Transducer calibration

Two separate batches of karri were sent to Hobart from WA, each batch cut from one tree. This timber was used for AE calibration, shrinkage and basic density determination, and preliminary kiln trials in Hobart. The timber used for the drying trial in WA was from a third batch. Thus some idea of the variation in timber properties of karri was gained from the trials.

The AE transducers to be used for the WA karri trial were calibrated on the samples of karri sent to Hobart. The aim of calibration is to determine the checking threshold level of AE, that is, the level of AE which corresponds to the onset of surface checking in the wood (Booker, 1994a). The transducers were all clamped on a section of green board, which was then left to dry. The drying conditions were restricted in such a way that the AE built up to a peak over a period of several hours. The AE was then allowed to die off gradually, whilst some drying was maintained, so that there was still significant tension stress at the surface of the board to continue opening to visible size any checks which had formed. It was often necessary to mark possible checks, and then leave the board out to dry further, observing later whether the marked faults were in fact checks. A 10× magnifying glass was usually needed to find the checks. When surface checks were observed to have formed on the test board section, it was concluded that the checking threshold AE was lower than the highest measured peak. This technique is now a standard procedure.

This process was repeated with progressively lower peak AE levels until the board section under test was observed to be free of surface checks. The peak AE from this test was then taken to be the checking threshold AE. This level was confirmed and refined by further tests.

The default checking threshold output from the AE hardware is set to 1.5V in the CKC software. This level then corresponds to an AE reading of 100%. 1.5V is a typical value of the checking threshold AE for Tasmanian eucalypt timbers. At the completion of AE testing, the software is normalised so that the checking threshold becomes equivalent to 100% AE. The percentage AE quoted in Table 7.3.1 is thus relative to 1.5V hardware output.

The first problem to become obvious with AE testing of karri was control of the drying rate. Initially, the tests were performed with the boards exposed to the laboratory atmosphere. When the resultant drying rate was found to be too high, subsequent test boards with transducers attached were partially covered with plastic, and the air gaps progressively blocked with each new AE test to further slow the drying rate. When this was still found to be causing the boards to dry too rapidly, they were placed in a sealed chamber, then covered in plastic, to minimise the effect of air currents in the room. When this too was found to provide inadequate control of the drying rate, subsequent AE tests were performed with the board sitting on blocks over a saturated solution of potassium chloride, covered in plastic and in a sealed chamber. The KCl solution provided an RH at room temperature of approximately 85%. This gave maximum AE from the timber of approximately 59%, 53%, and 52% on channels AE1, AE2 and AE3 respectively over a 160 hour trial. When this AE level was found to be still above the checking threshold for karri, the boards were sealed in a plastic garbage bag. The bag was perforated to allow some drying to occur. Variation in the number of perforations provided sufficient control over drying conditions to determine the checking threshold.

A major problem slowing down the AE testing was finding incipient checks. The checks appear to form almost exclusively in the bottoms of vessels, giving rise to the idea of the vessels as stress-raisers. Thus the checks are virtually impossible to detect until they have grown. They are also much smaller on formation than those usually seen in other timbers, as the stress concentration effect results in only a very small amount of wood being at a high stress. This is probably also the reason why the stress concentration effect does not result in internal checks starting at vessels within the bulk of the timber: even if the stress concentration effect results in a local stress high enough to induce formation of a micro crack, the crack will not be able to run as the average tensile stress will be much lower internally than at the surface (subject of course to the possibility of severe collapse-inducing drying conditions).

One further possible problem in determining a repeatable checking threshold AE is that the threshold AE we are looking for is generated in the bottom of the vessels, where the checks form, which is up to approximately 0.13mm below the surface of the timber. Whether the surface AE we are measuring is a reliable indication of AE at the bottom of the vessels is thus somewhat uncertain; however, the surface AE will at least be a true reflection of average surface stress, which will be closely related to stress at the bottom of the vessels which form the highest stress-raisers, and will thus be the most likely sites for check initiation.

In this case, upper bounds for the threshold AE can be defined, but a least upper bound cannot, as the AE corresponding to incipient check formation is likely to be lower than that corresponding to check growth to visible size. However, since checks not visible to the naked eye cannot be considered to be significant seasoning degrade, it is sufficient to keep surface stress levels below that which eventually cause formation of visible checks, even if microscopic incipient checks do form.

See table 7.3.1 for a summary of the AE tests performed. The "Board" column refers to the timber batch under test - either the first or second batch sent to Hobart.

Test ID	AE Peaks AE1/AE2/AE3	Duration (hrs)	Board	Surface condition
AE1	89.4/105/117	22.5	1	Checked[1]
AE2	86.6/86.8/53.4	23	1	Checked[1]
AE3	71.8/80.7/86.1	22.3	1	Checked[2]
AE4	92.1/87.1/66.6	27	1	Trial aborted
AE5	117/50.9/92.4	0.7	1	Trial aborted
AE6	59.4/98.3/90.2	65	1	Checked[1]
AE7	121/65/134	5	1	Trial aborted
AE8	High	3	1	Trial aborted
AE9	60.4/75.7/60.1	156	1	Checked[1]
AE10	74.9/64.5/62.8	20.2	1	Checked[2]
AE11	54.9/48.7/53.9	25.4	1	Clear[2]
AE12	57/57.5/83.8[3]	23.6	1	Clear[2]
AE13	36.5/39.9/36.6	20.7	1	Clear[2]
AE14	52.5/71.6/292[4]	68.4	1	Checked[2]
AE15	50.5/52.9/33.4	29.9	1	Clear[2]
AE16	48.3/40.4/33.2	22.2	1	Clear[2]
AE17	59.2/52.7/52.2	138	1	Checked[2]

AE18	36.3/57.8/55.7	44.5	1	Checked[2]
AE19	69.2/76.7/64.5	115.4	1	Checked[2]
AE20	17.6/16.8/18.4	188	1	Clear[2]
AE21	24.3/21.2/24.1	240	1	Clear[2]
AE22	65.1/348/42.3	9.2	2	Trial aborted
AE23	36.3/30.9/50	154.7	2	Checked[1]
AE24	45/42/25	88	2	Checked[1]
AE25	31/30.8/29.6	190.7	1	Clear[2]

Table 7.3.1 AE test results

Notes

1 Refers to a surface which was obviously checked at the end of the AE trial.

2 Refers to a surface which was examined after drying, possible checks marked, then left out in the laboratory for possible checks to grow.

3 The peak in AE3 appears to be spurious, this was one reading only, not indicative of a buildup to a peak. This is observed occasionally on all channels. Such readings have been disregarded in the later AE trials.

4 Channel 3 was run through a new AE processing circuit for this trial only.

Note that a diagnosis of "Clear" is not necessarily a completely reliable indication of a lower bound for the checking threshold. It appears that it may take several days for checks to grow to a size which can be recognised in this timber (eg. test AE17). Thus, although tests AE11, 12, and 15 were diagnosed "Clear", it appears possible that they do not provide reliable lower bounds for the checking threshold since test AE17 which was run over a much longer duration was eventually surface checked at a similar level of AE.

On the basis of the above measurements, particularly tests AE21 and AE25, the checking threshold was selected to be 30% (0.45 V), and the software modified appropriately. Thus the checking threshold for karri was found to be lower than that for other eucalypts by a factor of approximately 3.3.

A new AE signal processing box was calibrated against the original hardware. This was achieved by connecting one of the three AE transducers on a board to the new box, and comparing the output from the new box with that from the old. The signal from the new box was consistently five times higher than that from the old box, linear between approximately 20% and 200% of failure AE. The higher output level from

the new hardware made it more appropriate for use at Harvey, as electrical noise then formed a less significant part of the signal.

7.4 Shrinkage properties

Shrinkage measurements were taken on the two batches of timber sent to Hobart, as well as on the timber used for the Harvey trial. Shrinkage was measured directly on wafers of wood approximately 0.8mm thick. Total shrinkage was measured on L-T slices, normal shrinkage was measured on R-T slices, (see Section 3.2.1). Representative graphs are shown in Figs 7.4.1 to 7.4.10.

The total shrinkage curves all show some collapse (ie. there is significant shrinkage occurring above FSP). An attempt was made to find collapse threshold temperatures for batch 1 and batch 2 of karri; see Figs 7.4.5, 7.4.6, 7.4.7 and 7.4.8. No significant decrease in the collapse shrinkage for either batch was found by dropping the temperature from 18°C to 5°C. Thus it is concluded that the collapse threshold temperatures for both batch 1 and batch 2 were below 5°C. Similar attempts at collapse threshold temperature determination were not made for the Harvey timber, as there was no provision for drying at temperatures below ambient temperature, so such measurements would be pointless.

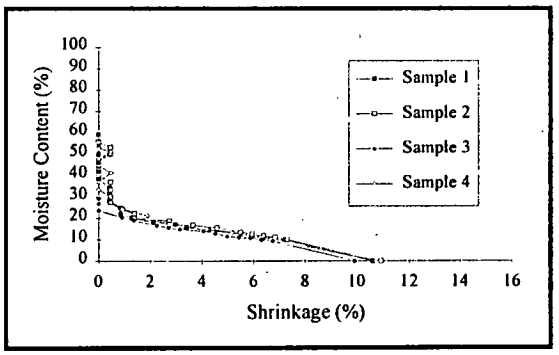

Figure 7.4.1 Normal shrinkage, batch 1, 20°C.

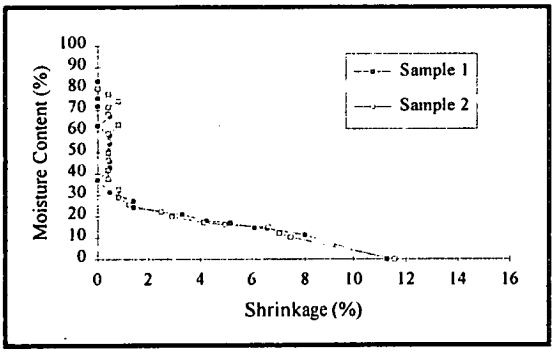

Figure 7.4.2 Normal shrinkage, batch 2, 18°C.

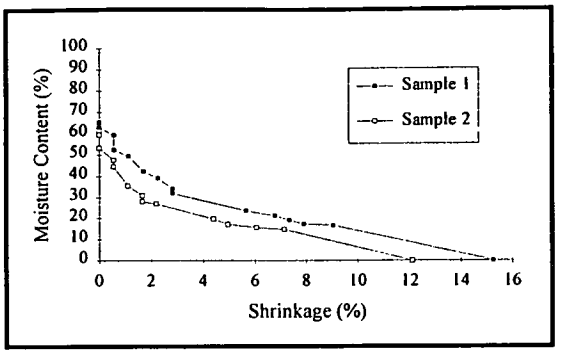

Figure 7.4.3 Total shrinkage, batch 1, 18°C.

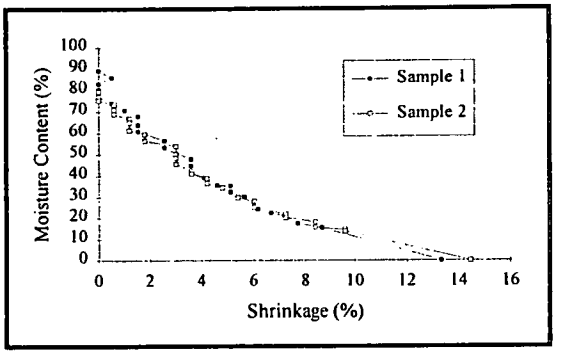

Figure 7.4.4 Total shrinkage, batch 2, 18°C.

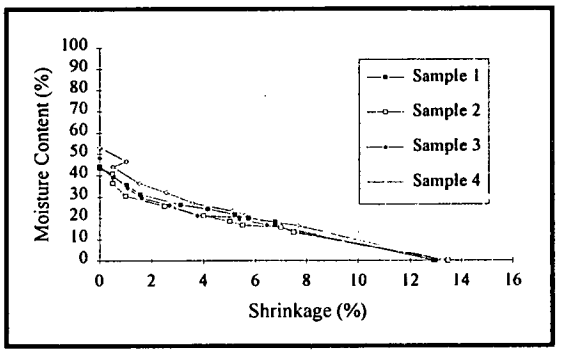

Figure 7.4.5 Total shrinkage, batch 1, 12°C.

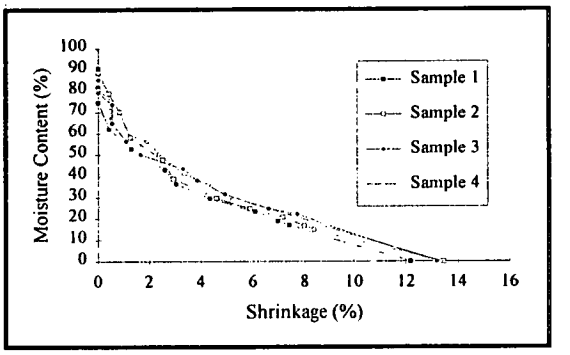

Figure 7.4.6 Total shrinkage, batch 2, 12°C.

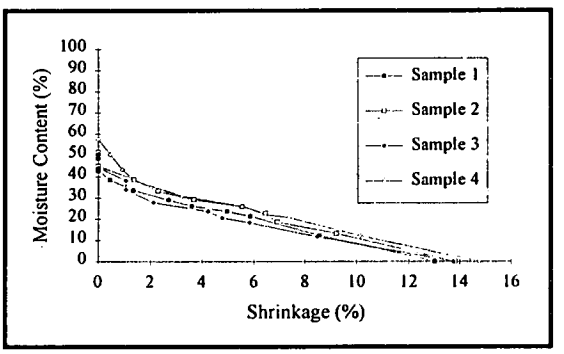

Figure 7.4.7 Total shrinkage, batch 1, 5°C.

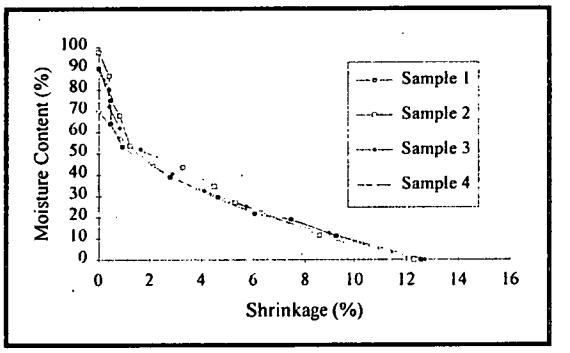

Figure 7.4.8 Total shrinkage, batch 2, 5°C.

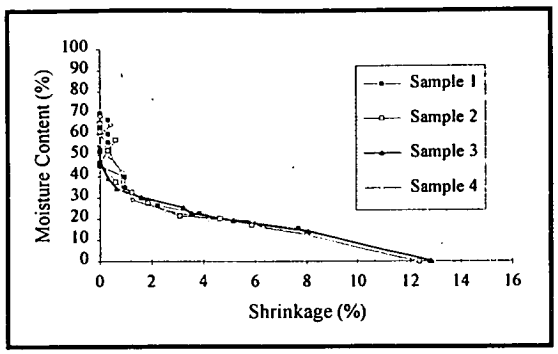

Figure 7.4.9 Normal shrinkage, Harvey timber, 18°C.

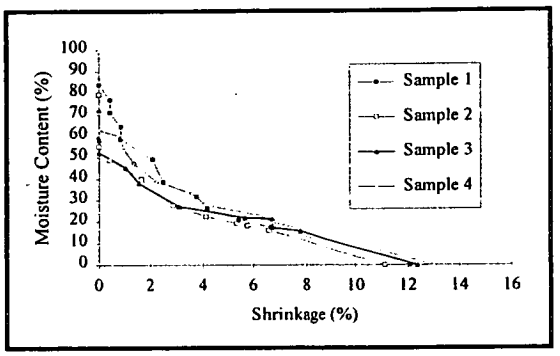

Figure 7.4.10 Total shrinkage, Harvey timber, 18°C.

In each figure, the individual shrinkage curves are generally very similar to each other. This is unusual, as normally L-T slices will show significant variation in total shrinkage due to differences between earlywood and latewood (see Chapter 4). This provides a clue to a possible explanation for the lack of internal checking or washboarding observed in karri, despite the collapse which is obviously occurring. It appears possible that the component of the wood which is less prone to collapse (probably the latewood) is insufficiently stiff, or insufficiently thick to decrease the shrinkage observed in the wafer below the total shrinkage caused by the collapsing component of the wafer. That is, the non-collapsing component of the wafer provides insignificant restraint. Another possible explanation is that the earlywood and latewood have approximately the same propensity for collapse, and collapse a similar amount. Whatever the explanation for the shrinkage behaviour of the wafers, the important result is that there does not appear to be significant differential shrinkage within the wood, probably not enough to precipitate the formation of internal checking. Thus the effect of collapse on the drying of karri is to increase surface stress, similarly to a timber which undergoes a large normal shrinkage (although clearly the collapse shrinkage which occurs above FSP has an effect earlier in the drying process than does normal shrinkage). This is good news for the CKC as an AE based kiln controller, as the limiting factor for drying rate will be surface stress, which is what the AE transducers measure (Booker, 1994b).

The Harvey timber showed substantial normal shrinkage at FSP - of the order of 1.5% (Fig 7.4.9). This was approximately half the total shrinkage at FSP (Fig 7.4.10). Modelling of the unconfined shrinkage of karri for the Harvey trial was derived from Fig 7.4.10, on the basis that the total shrinkage of the uncut fibres was likely to be most representative of the unconfined shrinkage occurring in the timber.

7.5 Harvey kiln trial

A trial of the Clever Kiln Controller® (CKC) was run at the Harvey Wood Utilisation Research Centre (WURC) of the Western Australian Department of Conservation and Land Management (CALM) from September to November 1995. The kiln was a $1m^3$ timber capacity batch kiln of overhead fan type.

7.5.1 Timber Properties

The timber supplied was clear prime karri. The timber was block stacked and wrapped immediately after sawing, and as a result the initial moisture profile was uniform at approximately 75% MC, with virtually no surface drying having occurred. Boards were end-coated with PVA sealer before drying.

Basic density of the timber was measured on four samples from one representative board. Green volume was determined by water immersion. Samples were dried in an oven at 104°C. Basic density was found to be 744 ± 20 kg/m^3.

Tangential shrinkage was measured on eight L-T slices and four R-T slices. Representative curves are shown in Figs 7.4.9 and 7.4.10. Some collapse shrinkage is obvious; the normal shrinkage curve also exhibits significant shrinkage at FSP, approximately 1.5%. This shrinkage appears to be typical for karri, and combined with the apparent stress-raiser effect of the vessels along the board surface and the low diffusion coefficient explain the slow drying and high degrade usually experienced when seasoning karri.

7.5.2 Harvey experimental batch kiln

The kiln accepts a stack of 150mm × 38mm × 2.4m boards seven wide and 12 high. The timber capacity was thus approximately $1.1m^3$. The kiln is of the overhead fan type, with electrical heating and water sprays for humidification. The inlet vent draws air from within a large shed housing the kiln, and the exhaust vents blow out via ducts

to outside the shed. The kiln has a large inlet plenum (stack height by approximately 1.5m in the direction of air flow) and diffuser screens on both upstream and downstream sides of the stack. The air enters the plenum through two jets of approximately $0.15m^2$ total area. The racking sticks were 19mm thick, and the air velocity between the boards was measured with a hot wire anemometer to be 0.3m/s, so that the jets had a mean velocity of approximately 1m/s. The resultant turbulence in the inlet plenum was expected to induce reasonably uniform drying conditions. Time restrictions did not allow a traverse of kiln conditions to be measured to confirm this.

At the request of CALM staff, four average MC boards were included in the stack, for comparison of drying rate between the CKC system and a conventional CALM karri schedule. These boards were periodically removed according to standard CALM procedure, and sections taken for average MC determination.

The stacking arrangement for the kiln trial is shown in Fig 7.5.1. Note that the layer of the stack which houses the AE and moisture profile boards has one less board than the others, due to the extra width taken up by the AE transducer clamping mechanisms. The racking sticks had slots cut out of them immediately above the average MC and the moisture profile sample boards to allow the boards to slide easily out of the stack.

7.5.3 Installation of the CKC at Harvey

The CKC equipment was wired up in place of the existing "μmac" controller with few problems. Temperature probes which had been calibrated in Hobart were used with the CKC. The existing wick-wetting system was used for the wet bulb sensor. This included a vacuum system drawing kiln air over the wick at approximately 5m/s (the ASTM specified velocity).

The vents were controlled by a 2V-10V analogue signal, but the inlet vent required inverse logic to the exhaust vents. That is, a 2V signal to all vents would make the inlet vent open, but shut the exhausts, whilst a 10V signal would have the opposite effect. To solve this problem, the inlet and exhaust vents were controlled by separate channels from the control computer. The PC30B has only four analogue output

channels, so that one of the existing outputs had to be disconnected. The fan was chosen, its speed was set directly from the μmac controller, which otherwise had only a monitoring role. Thus the four outputs from the CKC were used to control heaters, sprays, inlet vent, and exhaust vents. The inlet vent was controlled directly in software to have as its output value (100 - exhaust vent)%. The user interface was modified to account for this change.

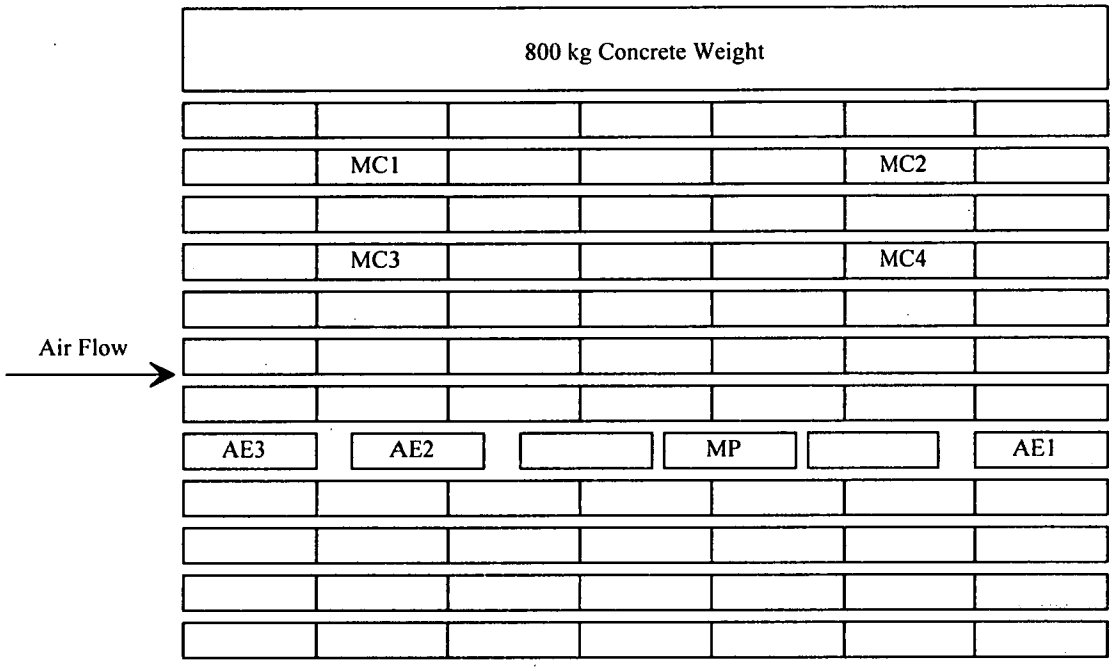

Figure 7.5.1 End view of boards in the stack. MC1..4 are CALM MC boards, AE1..3 are boards with AE transducers attached, MP is moisture profile board.

The "new" design AE box which had been calibrated against the old design (Section 7.2.2) was used at Harvey. The low output from the old design at the checking threshold led to electrical noise problems in the semi-industrial environment.

7.5.4 Running the Kiln

After approximately one and a half days of PID tuning of the controller to the kiln, the trial was started. A graph of kiln conditions vs time is presented in Fig 7.5.2. It shows an overshoot of approximately 1.3°C after starting the kiln. After approximately 8 hours the kiln had settled to its setpoints, controlling to within about 0.2°C of the DBT setpoint, and ±0.1°C of the wet bulb depression setpoint.

A potential problem evident from Fig 7.5.2 is the slow rise of the humidity in the kiln. This is due to the kiln hardware, not the tuning parameters of the CKC. During the warm-up period, the maximum heater setting attained was only approximately 30% (see Fig 7.5.3), whereas the sprays reached 100% shortly after startup. This did not cause any problems during the initial kiln setup, as harsher kiln conditions are acceptable to green wood for a couple of hours, until significant shrinkage occurs at the surface and the surface stress increases. However, if the kiln were to stop for any reason during the trial and had to be restarted from cold, the heater should be limited to approximately 20%.

A couple of spikes are evident in the AE traces presented in Fig 7.5.4. This is commonly seen, and is thought to be due to stress relief at local weak points. After some drying, these peaks cease to occur.

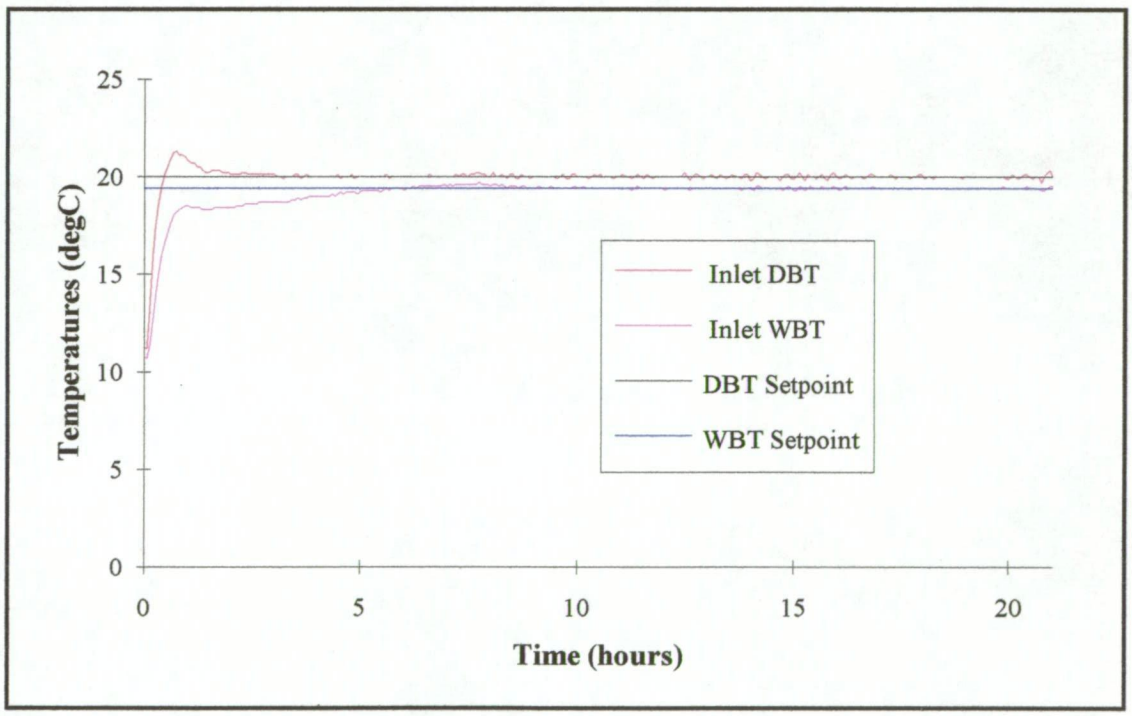

Figure 7.5.2 Temperature response of kiln on startup of trial.

7.5.5 Trial results

After monitoring the trial for three days, it was left under the care of CALM staff at Harvey. Approximately twelve days after the start of the trial, the controller was

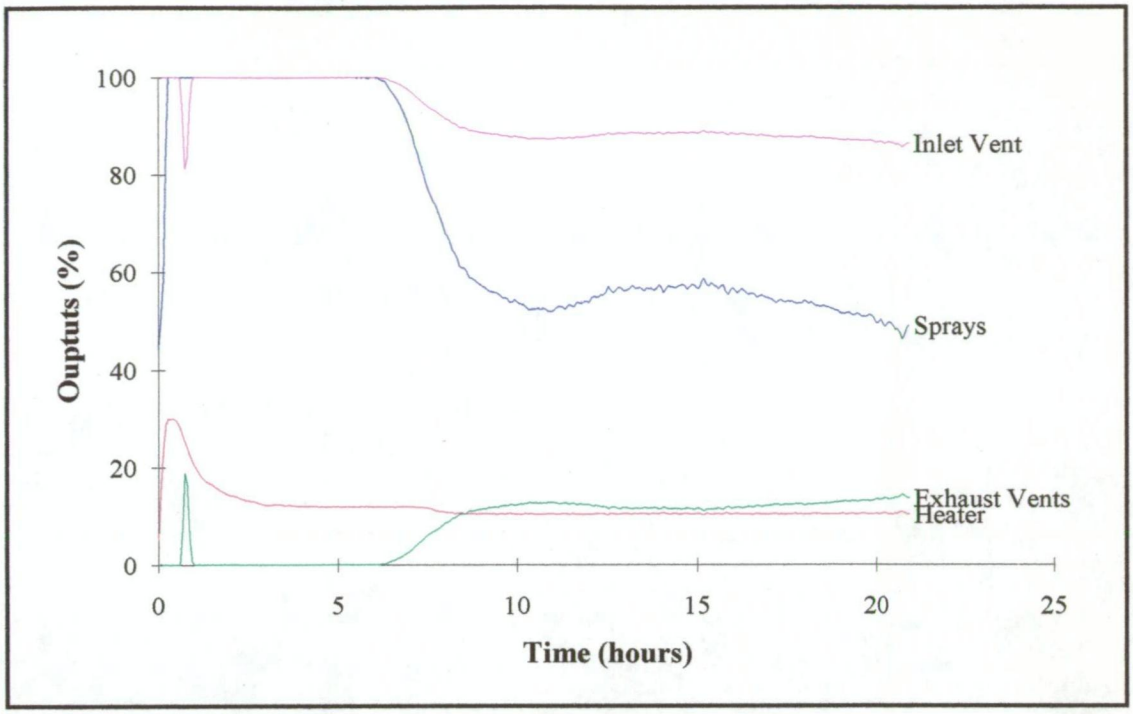

Figure 7.5.3 Controller response on startup of kiln. Note that "Inlet Vent" = 100-"Exhaust Vents". "Exhaust Vents" is actual vent opening.

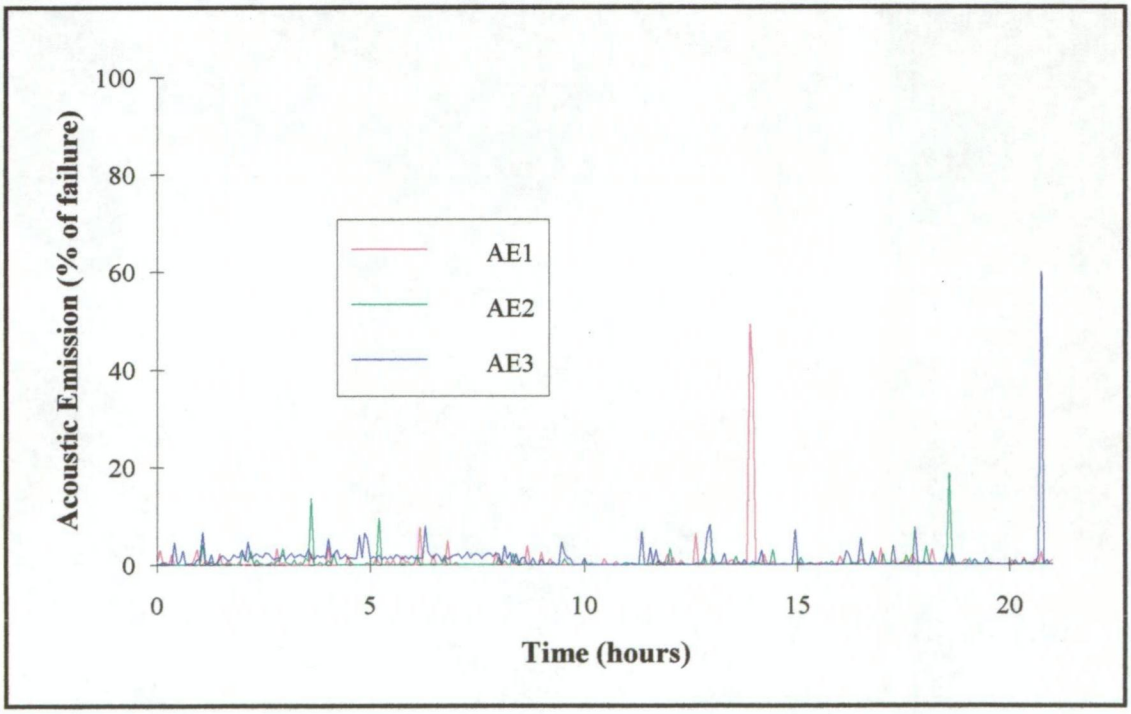

Figure 7.5.4 Acoustic emission recorded from the start of the kiln trial.

switched from fixed setpoint control to AE control. Fig 7.5.6 shows the control AE level varying after this time, and the monitored AE following a similar pattern. This sawtooth control AE level is necessary to prevent overshoot of the AE (see Section 6.4.2). For example, if we wish to restrict AE to approximately 60% then it is

necessary to start slowing drying when the AE reaches perhaps 30%, as there will be a time lag between changing kiln setpoints, and the kiln conditions reacting sufficiently to decrease the AE. This strategy appears to have been reasonably successful here.

Unfortunately, the power supply at Harvey proved to be somewhat unreliable, with five interruptions during the 77 day trial. These can be seen in Fig 7.5.5 at approximately 362, 494, 800, 1000, and 1704 hours. Fig 7.5.6 shows the resultant spikes in AE corresponding to the fluctuations in kiln conditions. The upwards spike in temperature at 362 hours appears to be due to overshoot after a power failure. It seems that the heater was not responding to the controller's output for approximately 2.5 hours, after which time the heater suddenly started working again, the high heater setting then resulting in the overshoot. Fortunately, the heater output from the controller had been restricted to 30%, which limited the overshoot. The controller maintained the humidity sufficiently well to not increase the drying rate, so that there is no corresponding spike in the AE readings. The spike to 140% on AE1 at 292 hours appears to be one of the local stress relief events mentioned earlier.

If the temperature drops rapidly, the AE is often seen to rise. Modelling of this effect by **KilnSched** revealed that a sudden drop in temperature causes the surface of the wood to stiffen, thus decreasing the thickness of that part of the board under tension. This increases the surface tensile stress, which is reflected in the measured AE. This effect has been dubbed the "sea breeze" effect, as cool sea breezes have been observed to cause surface checking. The power failures at 494 and 800 hours allowed the temperature to drop far enough to cause a "sea breeze" effect. This shows how modelling can produce logical explanations of apparently anomalous effects.

The power interruption at 988 hours caused the control computer to lose its setup information for the D/A board channelling, so that it recorded zero data on all channels until 1130 hours, and reverted to default setpoints. Conditions in the kiln during this time are not known.
Unfortunately, the loss of data meant that the **SmartKiln** predictive simulation program could not be run. Normally the kiln would be controlled to a schedule specified by **SmartKiln** with AE feedback used as an override in case of poor modelling. This strategy dries the timber more quickly than controlling on AE alone, as AE control results in oscillatory kiln conditions (see Fig 7.5.5).

At 1295 hours the kiln DBT setpoint was changed to 25°C. This was done as an experiment to see if the extra collapse shrinkage induced by the higher temperature

would induce surface checking (see section 7.4) at a similar drying rate. It does not appear to have done so.

An uninterruptable power supply (UPS) was connected to the control computer and interface box to the kiln after 1130 hours kiln time. A power failure at 1704 hours caused the temperature in the kiln to drop, but the controller boosted the humidity as a response to the rising AE, avoiding the sea breeze effect seen at 494 and 800 hours. In those two cases, the AE rose to very high levels on restart as the controller had been off, and thus unable to boost humidity in the kiln.

The high AE following the power failures highlighted the care which is needed in restarting a kiln under conventional (setpoint) control after a power failure. Oliver (1995c) gives a qualitative description of what is likely to occur during a power failure and fan restart, and makes some recommendations for a restart procedure. This is summarised below.

> When the fan cuts out, it takes a few minutes for the air to become still. After this occurs, the wet wood and still air in the stack move toward equilibrium, with the result that the wood surface moisture concentration rises. As soon as the fans are started, the air in contact with the wood rapidly increases in moisture concentration. There is thus an increase in moisture concentration gradient across the boundary layer, and hence more rapid drying of the surface of the wood. This results in an increase in moisture concentration gradient within the wood near the surface, which can easily lead to surface checking.
>
> If the dry bulb temperature of the air in the plenum reduces below that of the air in the stack, then this effect does not occur. However, if the dry bulb temperature in the plenum becomes significantly lower than the wet bulb temperature of the air in the stack (which is approximately equal to the wood temperature), then restarting the fans will result in a "sea breeze" effect which is likely to result in checking. The restarting technique recommended by Oliver (1995c) is to first switch on the water sprays (assuming that kiln humidification is by water spray in the plenum at entry to the stack). The fans should then be started slowly, either by using the speed controller if it provides sufficiently low fan speed, or by running the fans for short bursts only every few minutes until the moisture concentration and temperature gradients have been restored to their values before the shutdown.

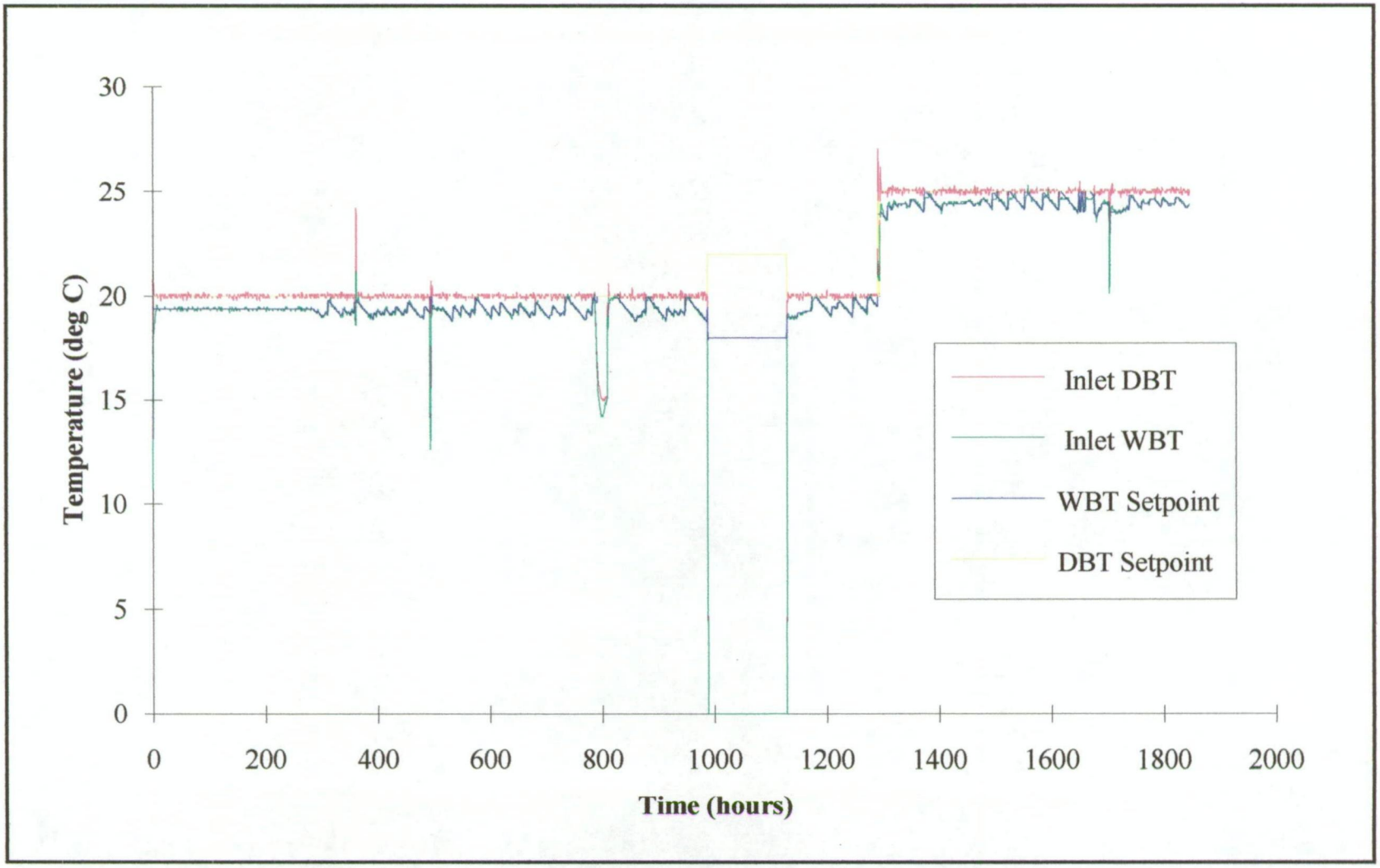

Figure 7.5.5 Logged kiln temperatures and setpoints for the duration of the trial

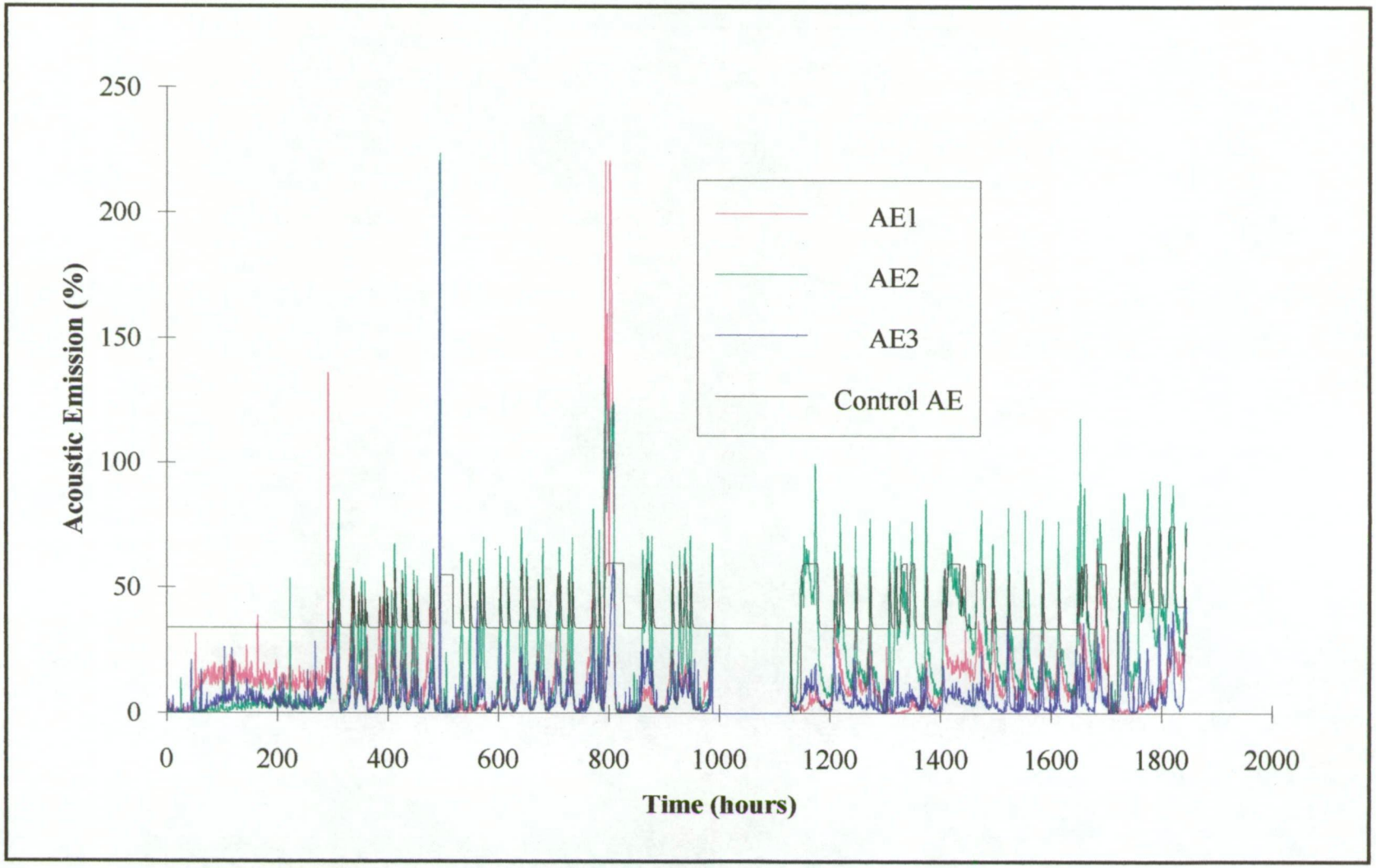

Figure 7.5.6 Logged acoustic emission for the duration of the kiln trial.

The CKC avoids the necessity to do this provided that it is powered via a UPS and it is tuned to respond quickly enough to avoid checking. Even so, manually switching on the sprays prior to starting the fans is recommended. It may still be necessary in some situations to start the fans gradually; automating this could be a useful future addition to the CKC.

Apart from the power interruptions, the kiln control by the CKC was near perfect. The DBT was nearly always within 0.1°C of setpoint. The WBT was also very close to its setpoint, except when the setpoint changed very rapidly which led to some lag. This lag probably contributed somewhat to the amplitude of the oscillations of the WBT setpoint. The trial showed that the CKC is capable of drying karri free of surface checks, given a reliable power supply.

7.5.6 Timber after the trial

The stack was pulled down by CALM personnel at Harvey after approximately 11 weeks drying. Half of the moisture profile and AE2 boards were docked to 300mm lengths and sent to Hobart.

MC in the centre of the moisture profile board was 69%. This is a loss of only 6% from the green centre MC. The very slow rate of drying is a result of the need to avoid surface check formation, and the oscillatory nature of kiln conditions resulting from the AE control mode, so that the drying rate was significantly less than the optimum.

There was only one surface check visible on the board sent to Hobart (see Fig. 7.6.1). This check formed directly adjacent to the AE sensor. This is thought to be due to acceleration of the airflow around the AE sensor. The velocity distribution around a cylinder in a fluid stream with a free stream velocity U (see Fig. 7.5.7) is given by Vennard and Street (1982) as:

$$V_r = U\left(1 - \frac{R^2}{r^2}\right)\cos\theta \qquad (7.5.1)$$

$$V_t = U\left(1 + \frac{R^2}{r^2}\right)\sin\theta \qquad (7.5.2)$$

Substituting $r = R$ and $\theta = 90°$ in equation 7.5.2, we find that the flow velocity adjacent to the sides of the cylinders is double the free stream velocity. In the case of an AE sensor attached to a board surface, the effect on drying will be more complex than that due to a simple doubling of the air velocity, due to the local three dimensional flow pattern caused by distortion of the boundary layer on the board surface. However, it seems reasonable to expect that the local drying rate at the sides of the AE sensor is higher than that over the rest of the board surface, so that the average surface instantaneous stress measured by the probes is somewhat higher than that over the rest of the boards.

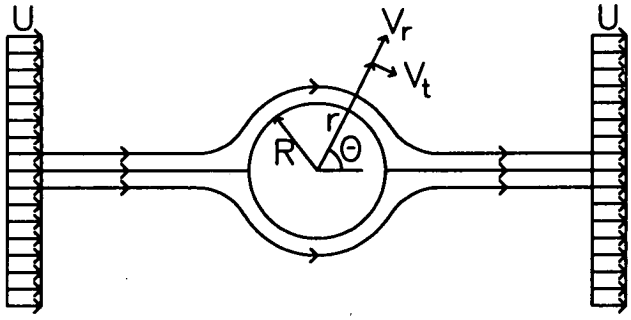

Figure 7.5.7 Cylinder in uniform flow

Thus it appears likely that even if the AE shows readings substantially above the checking threshold, a large proportion of the stack could remain check free. This also means that the stack could safely be dried faster. The problem could probably be reduced, by use of smaller AE sensors which would probably cause less disturbance of the boundary layer. The sensors and clamps currently in use (Fig. 7.6.2) sit above the level of the racking sticks, thus requiring the board directly above the AE board to be docked, leaving a gap for the sensor. The AE board cannot be placed edge to edge with adjacent boards in the same row of the stack as the clamps protrude beyond the width of the board (Fig. 7.6.2), disturbing the boundary layer development through the stack. An appropriate smaller sensor (Physical Acoustics Corp. AD09) has been tested alongside the sensors currently in use (Physical Acoustics Corp. R6I) and found to perform satisfactorily.

7.6 Use of the stress concentration factor in modelling of the drying process, and comparison with measured AE

A stress concentration factor of 3.0 was included in the **SmartKiln** timber seasoning model (see Section 6.4.3). The factor was actually included as a raiser of instantaneous strain. Clearly, for linear elastic analysis, a stress-raiser and a strain raiser are the same thing. The problem is significantly complicated by non-linear

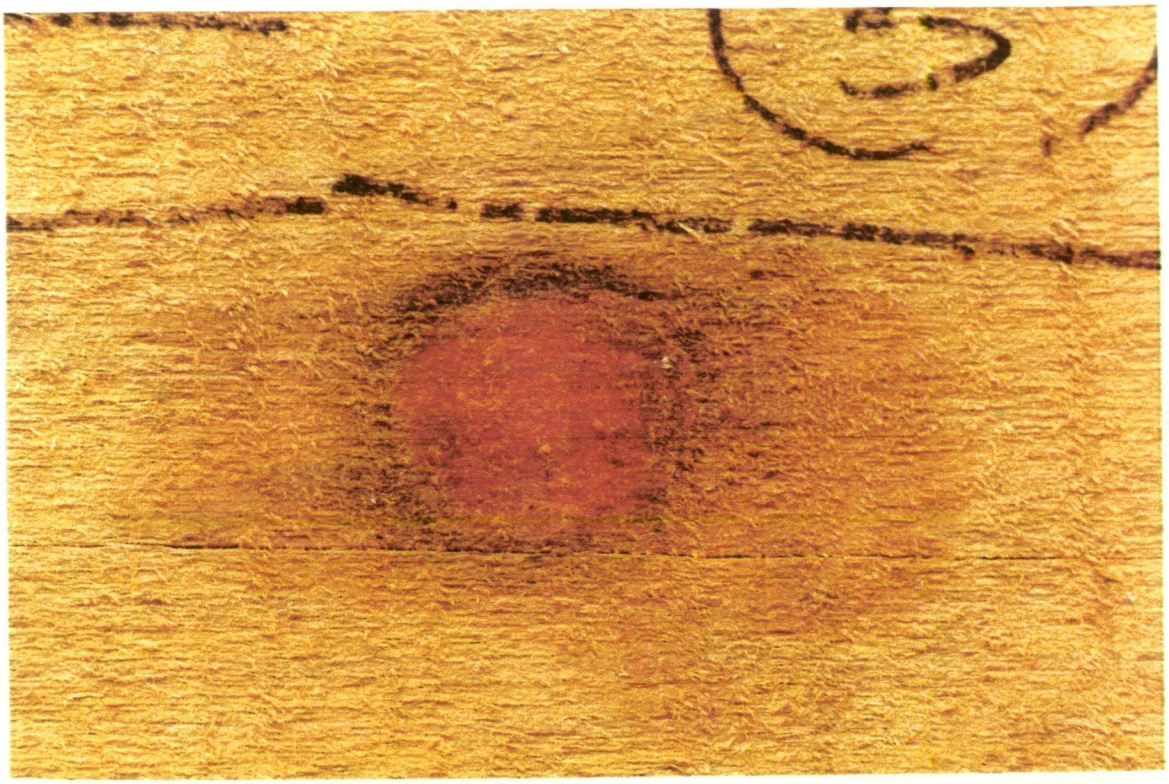

Figure 7.6.1 Photograph showing surface check adjacent to AE sensor

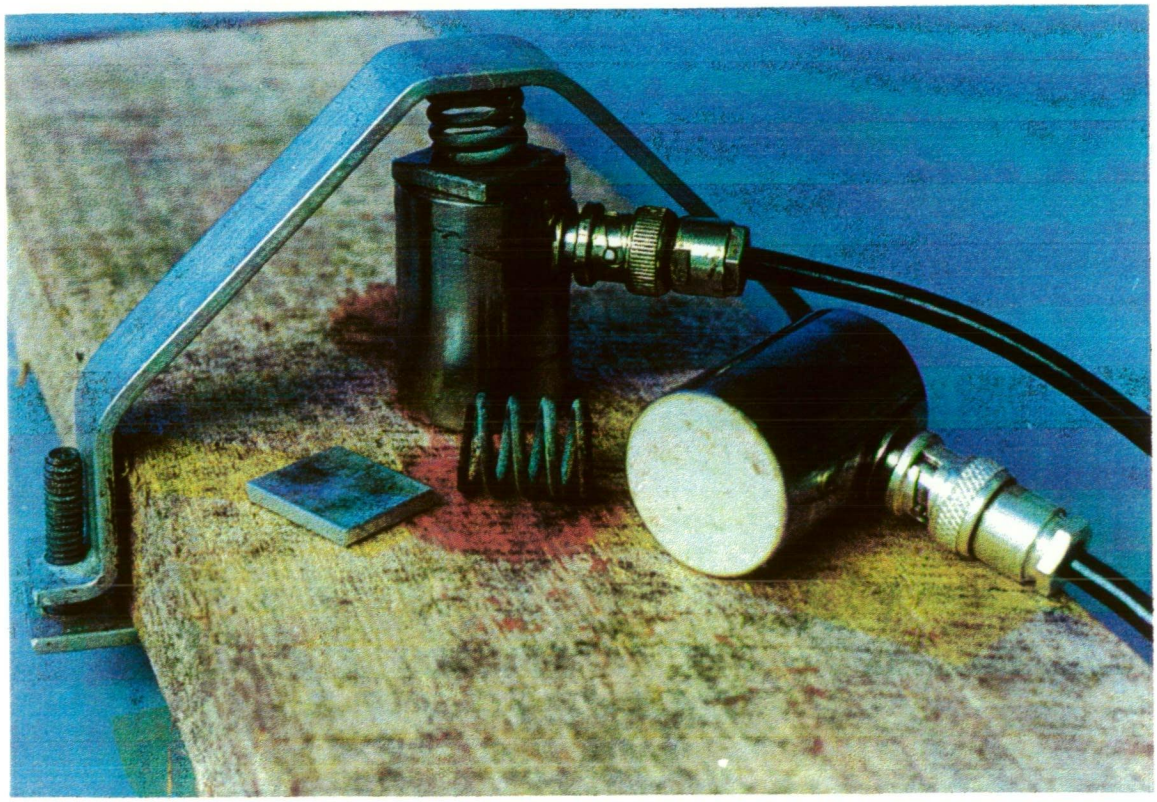

Figure 7.6.2 AE transducer with retaining clamp and spring

material properties, but there is no analytical solution, and Strand6 does not have the capability to model non-linear orthotropic materials.

The results shown in Fig 7.6.3 come from **SmartKiln** run in the CKC. Figure 7.6.3 shows very good agreement between the measured AE whilst it is rising and the predicted instantaneous strain from **SmartKiln**. This indicates that the stress concentration factor used predicts the modification of the behaviour of the surface under tension reasonably well.

The agreement between stress analysis, **SmartKiln** modelling and measured AE provides strong evidence for a surface stress-raiser effect from the vessels in karri. It is likely that such an effect could also be found in other species which have large, well defined vessels visible on sawn board surfaces. Such species would be identified by their propensity to form surface checks in the bottom of exposed vessels. The stress raiser effect will need to be accounted for in modelling of the stress development during drying of these species.

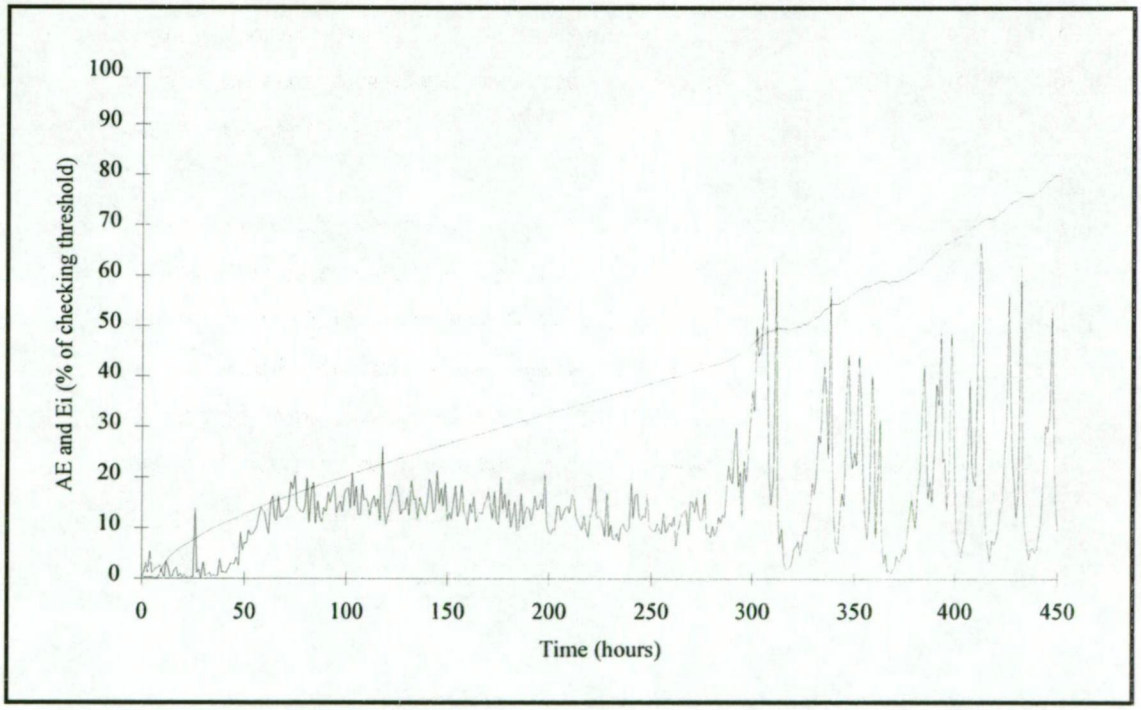

Figure 7.6.3 Sensed acoustic emission and surface instantaneous strain calculated by **SmartKiln** based on the first 450 hours of the Harvey kiln trial.

The stress concentration effect observed here calls into doubt the practice of rough machining sawn boards before seasoning. Machining is expected to have more of a tendency to leave exposed open vessels than sawing, and thus appears more likely to

cause the stress concentration effect. However, it will also affect the airflow over the board surfaces by the removal of most of the roughness generating features of sawn boards. This roughness also affects the response of the board surface to drying stresses, and hence the propensity of the board to form surface checks. Its overall effect is thus uncertain.

The drying work described here was repeated on brushbox (*Tristania conferta*). Results are contained in Appendix B.

Chapter 8 Conclusions

The work on collapse in this thesis has added to the base of knowledge behind the Clever Kiln Controller (CKC). Previous work on the CKC has focused on the optimisation of drying rate to produce seasoned sawn timber free of surface checks. This work has shown how to avoid collapse induced checking both internally and at the board surfaces.

The work began with a new stress-strain model of a single collapse prone fibre under conditions of internal tension. This model considered anatomical data such as cell wall construction and size, as well as material property variation with temperature and moisture content. It predicted that failure is precipitated at the inner fibre wall, and that collapse is very sensitive to temperature, in confirmation of previous suggestions. The temperature sensitivity is related to that of stiffness of the wood.

The temperature sensitivity prediction of the single fibre model was supported by similar predictions from modelling of the drying process by **KilnSched** (see Section 4.1), and by acoustic emission (AE) measurements. The concept of a collapse threshold temperature was introduced, a temperature below which collapse does not occur. This concept was verified by several drying trials. A standard technique was developed to identify collapse prone wood.

The formation of internal and surface checking associated with collapse was examined by use of a stress and drying model which considers wood as a heterogeneous material. This model demonstrated that checks form in response to differential shrinkages arising from localised collapse. It showed that the best way of avoiding collapse checking is to dry with conditions which do not induce collapse shrinkage.

Industry information suggested that the collapse threshold temperature of a board changes as drying progresses. Modelling indicated that this was unlikely to be due to creep or mechano-sorptive strain relaxation or the decrease of water surface tension with increase of temperature. An examination of the effect of the bulk stress in the board due to drying on the stress distribution in individual fibres indicated that the centre section of the board which was subject to compression was less prone to collapse than sections not subject to compression. The part of the board subject to compression during drying roughly corresponds to the part of the board still at moisture content above fibre saturation, and thus vulnerable to collapse. Quantitative modelling of the effect is not possible at this point in time, due to lack of appropriate

two-dimensional stress and drying models. Dry bulb temperature schedules during drying to fibre saturation point (FSP) can currently best be determined by experimental drying trials.

Work on the seasonability of karri (*E. diversicolor*) and brushbox (*Tristania conferta*) was completed as part of the commercialisation program of the CKC. The work on karri revealed that large vessels lying along the board surfaces act as stress-raisers. Modelling of the stress-raiser effect predicted a stress concentration factor of approximately three. AE calibrations yielded a checking threshold AE level of approximately one-third of the checking threshold level for other eucalypts. Addition of a stress concentration factor of three in **KilnSched** provided modelling of the karri kiln trial which agreed closely with measured AE. This stress concentration effect is likely to occur in other timbers.

The thesis demonstrates how mathematical modelling leads to a greater understanding of the processes involved in problems such as timber seasoning. For example, modelling explained the apparently anomalous behaviour of wood which formed surface checks under the influence of a cool breeze (see Section 7.5.5).

It is no longer necessary to completely dry a wood sample to FSP to establish a kiln schedule which will ensure zero drying degrade. The work on karri and brushbox have shown how sufficient information on a new species can be obtained in several weeks to allow an appropriate schedule to be determined.

8.1 Suggestions for continuing work

- Further investigation into the variation of the collapse threshold temperature during drying would enable the determination of schedules by modelling. At present, the most effective way of determining appropriate dry bulb temperature schedules for drying to FSP appears to be by running small-scale kiln trials.

- The next aspect of the CKC which needs to be addressed is automation of high temperature final drying. This involves the gathering of high temperature timber properties necessary for modelling of the effect. The final drying process should

leave the timber free of residual stresses, as well as drying it to the correct (uniform) moisture content.

- The work on karri in this thesis revealed a possible new mechanism for the mechano-sorptive effect (see Section 5.2). This needs further investigation, and the results incorporated into **KilnSched** and the CKC.

Amin, M. 1982. Ascent of sap in plants by means of electrical double layers. J. Biol. Phys. 10: 103-109.

Amos, G.L. 1954. Radial fissures in the early wood of conifers. Aust. J. Bot. 2: 22-34.

Armstrong, L.D. 1972. Deformation of wood in compression during moisture movement. Wood Sci. 5(2): 81-86.

Armstrong, L.D. 1983. Mechano-sorptive deformations in collapsible and non-collapsible species of wood. J. Inst. Wood Sci. 9: 200-211.

Armstrong, L.D., and Kingston, R.S.T. 1960. The effect of moisture changes on creep in wood. Nature 185: 862.

Armstrong, L.D., and Kingston, R.S.T. 1962. The effect of moisture content changes on the deformation of wood under stress. Aust. J. Appl. Sci. 13(4): 257-276.

Banks, W.H., and Barkas, W.W. 1946. Collapse of capillaries in the drying of porous gels. Nature 158: 341-342.

Bariska M. 1975. Collapse phenomena in Beechwood during and after NH_3 impregnation. Wood Sci. and Technol. 9: 293-306.

Berthelot, M. 1950. Ann. Chim. Phys. 3(30): 232-237.

Bisset, I.J.W. and Ellwood, E.L. 1951. The relation of differential collapse and shrinkage to wood anatomy in *Euclyptus regnans* F.v.M. and *E.gigantea* Hook.F. Aust. J. Appl. Sci. 2(1): 175-183.

Booker, J.D. 1990. Kiln control by acoustic emission. BE Hons thesis, Faculty of Engineering, University of Tasmania, Australia.

Booker, J.D. 1994a. The use of Acoustic Emission in improving hardwood timber seasoning productivity. PhD thesis, Faculty of Engineering, University of Tasmania, Australia.

Booker, J.D. 1994b. Acoustic emission related to instantaneous strain in Tasmanian eucalypt timber during seasoning. Wood Sci. and Technol. 28: 249-259.

Booker, J.D. 1994c. Acoustic emission and surface checking in *Eucalyptus regnans* boards during drying. Holz als Roh- und Werkstoff 52: 383-388.

Booker, J.D. 1995. Acoustic emission related to strain energy during drying of *Eucalyptus regnans* boards. Wood Sci. and Technol. 29: 145-156.

Booker, R.E. 1994. Internal checking and collapse - which comes first? Paper presented at 4th IUFRO international wood drying conference August 9-13 1994 Rotorua, New Zealand.

Bootle, K.R. 1983. Wood in Australia, Types, properties and uses. McGraw-Hill Sydney.

Briggs, L.J. 1950. J. Appl. Phys. 21: 721-722.

Bryan, E.L. 1960. Collapse and its removal in Pacific Madrone. For. Prod. J., 10: 598-604.

Campbell, G.S. 1960. Presteaming cuts drying time of "Ash" eucalypts. CSIRO Forest Products Newsletter No. 263

Campbell, G.S. unknown date. Wood, the material. Stage 2: Lesson 7 - Collapse and recovery. CSIRO, Timber Seasoning Correspondence Course.

Chafe, S.C. 1985. The distribution and interrelationship of collapse, volumetric shrinkage, moisture content and density in trees of *Eucalyptus regnans* F.Muell. Wood Sci. and Technol. 19: 329-345.

Chafe, S.C. 1986a. Collapse, volumetric shrinkage, specific gravity and extractives in *Eucalyptus* and other species. Part 1: The shrinkage/specific gravity ratio. Wood Sci. and Technol. 20: 293-307.

Chafe, S.C. 1986b. Radial variation of collapse, volumetric shrinkage, moisture content and density in *Eucalyptus regnans* F.Muell. Wood Sci. and Technol. 20: 253-262.

Chafe, S.C. 1990. Effect of brief presteaming on shrinkage, collapse and other wood-water relationships in *Eucalyptus regnans* F.Muell. Wood Sci. and Technol. 24: 311-326.

Chafe, S.C. 1993. The effect of boiling on shrinkage, collapse and other wood-water properties in core segments of *Eucalyptus regnans* F. Muell. Wood Sci. and Technol. 27: 205-217.

Choong, E.T., Mackay, J.F.G., Stewart, C.M. 1973. Collapse and moisture flow in kiln-drying and freeze-drying of woods. Wood Sci. 6(2): 127-135.

Clarke, S.A. 1927. The seasoning of Western Australian hardwoods. Forests Dept. Western Australia, Bull. 40.

Cowen, D.J. 1978. Comparison of the pilodyn and torsiometer methods for the rapid assessment of wood density of living trees. N.Z. J. For. Sci. 8(3): 384-391.

Cronshaw, J. 1960. The fine structure of the pits of *Eucalyptus regnans* (F. Muell.) and their relation to the movement of liquids into the wood. Aust. J. Bot., Vol.8, No.1.

Cuevas, L.E. 1969. Shrinkage and collapse studies on *Eucalyptus viminalis*. J. Inst. Wood Sci., 23: 29-38.

Dixon, H.H. 1909. Proc. Roy. Dublin Soc., 12: 60-65.

Dixon, H.H. 1914. Transpiration and the ascent of sap in plants. Macmillan, London.

Doe, P.E., Oliver, A.R., Booker, J.D. 1994. A non-linear strain and moisture content model of variable hardwood drying schedules. Paper presented at 4th IUFRO International Wood Drying Conference, August 9-13 1994, Rotorua New Zealand.

Doe, P.E., Booker, J.D., Innes, T.C., Oliver, A.R. 1996. Optimal lumber seasoning using acoustic emission sensing and real time strain modelling. Paper presented at 5th IUFRO International Wood Drying Conference, Quebec City, Canada, August 13-17.

Donny F.M.L. 1846. Ann. Chim. Phys. 3(16): 167-190.

Dorsey, N.E. 1968. Properties of ordinary water substance. Hafner Publishing Company, New York.

Ellwood, E.L., Ecklund, B.A., and Zavarin, E. 1963a. The effect of organic liquids on collapse and shrinkage of wood. 1. Effect of degree of replacement. For. Prod. J., 13: 291-298.

Ellwood, E.L., Ecklund, B.A., and Zavarin, E. 1963b. The effect of organic liquids on collapse and shrinkage of wood. 2. Effect of drying temperature. For. Prod. J., 13: 350-354.

Ellwood, E.L., Ecklund, B.A., and Zavarin, E. 1963c. The effect of organic liquids on collapse and shrinkage of wood. 3. Chemical influences. For. Prod. J., 13: 401-404.

Gerum, E., Straub, J., and Grigull, U. 1977. Examination of the metastable state of liquids. In: Heat Transfer in Boiling, E. Hahne & U. Grigull, editors. Academic Press.

Gibson, E.J. 1965. Creep of wood: role of water and effect of a changing moisture content. Nature 206: 213-215.

Gottstein, J.W. and McCombe, B. 1956. Recent studies on "ash" type hardwoods - collapse intensified by heating while green. CSIRO Forest Products Newsletter No. 216, March 1956.

Greenhill, W.L. 1938. Collapse and Its Removal: Some Recent Investigations with *Eucalyptus regnans*. Commonwealth of Australia Council for Scientific and Industrial Research, Division of Forest Products - Technical Paper No. 24.

Hasan, O. 1994. Unpublished data.

Hattori, Y., Kanagawa, Y. and Terazawa, S. 1981. Liquid-tension collapse of cells in concentrated polymer solution. Mokuzai Gakkaishi 27(4): 256-262.

Hearmon R.F.S. and Paton, J.M. 1964. Moisture content changes and creep of wood. Forest Prod. J. 14(8): 357-359.

Hillis, W.E. 1978. Wood quality and utilization. In Hillis, W.E. and Brown, A.G. (Eds) Eucalypts for wood production. Melbourne, CSIRO, 259-289.

Hillis, W.E. and Rozsa, A.N. 1978. The softening temperatures of wood. Holzforschung 32: 68-73.

Holbrook, N.M., Burns, M.J., Field, C.B. 1995. Negative xylem pressures in plants: a test of the balancing pressure technique. Science 270: 1193-1194.

Huber, B. and Schmidt, E. 1936. Weitere thermo-elektrische Untersuchungen über den Transpirationsstrom der Bäume. Tharandt Forst Jb 87: 369-412.

Ilic, J. 1987. Personal communication cited by Oliver (1991).

Ilic, J. 1990. Personal communication with A.R. Oliver.

Ilic, J. 1991. CSIRO Atlas of Hardwoods. Crawford House Press in association with the CSIRO.

Ilic, J. 1993. The effect of prefreezing on collapse, internal check development and drying rate in *Eucalyptus regnans* F.Muell. Paper 3/10 presented at the 24th Forest Products Research Conference, 15-18 November 1993 CSIRO Melbourne.

Ilic, J. and Chafe, S.C. 1986. The relationship between collapse, pulse resistance and depth of electrode penetration in trees of *Eucalyptus regnans* F.Muell. Aust. For. Res. 16: 291-299.

Ilic, J. and Hillis, W.E. 1986. Prediction of collapse in dried eucalypt wood. Holzforschung 40: 109-112.

Innes, T.C. 1992. Mechanical properties of Tasmanian Oak relevant to seasoning. B.E. Hons thesis, Department of Civil and Mechanical Engineering, University of Tasmania.

Kauman, W.G. 1960. Contribution to the theory of cell collapse in wood: investigations with *Eucalyptus regnans*. Aust. J. Appl. Sci. 11(1): 122-145.

Kauman, W.G. 1961. Effect of thermal degradation on shrinkage and collapse of wood from 3 Australian species. For. Prod. J., 11(9): 445-452.

Kauman, W.G. 1965a. Cell Collapse in Wood Part 1: Process Variables and Collapse Recovery. Holz als Roh- und Werkstoff 22(5): 183-196.

Kauman, W.G. 1965b. Cell Collapse in Wood Part 2: Prevention, Reduction and Prediction of Collapse - Recent Results.. Holz als Roh- und Werkstoff 22(12): 465-472.

Kemp, A.E. 1959. Collapse in aspen during kiln drying. For. Prod. J., 9: 124-130.

Keylwerth, R. 1951. Die Kammertrocknung von Schnittholz. Betriebsblatt 1. Holz als Roh- und Werkstoff, 9: 289-292.

Kingston, R.S.T, and Clarke, L.N. 1961. Some aspects of the rheological behaviour of wood. Aust. J. Appl. Sci. 12: 211-240.

Kollmann, F.F.P. 1950. Untersuchungen über die Ursachen von Schäden bei der Trocknung von grünem Eschenholz. Svenska Träforskninginstitutet, Trätekn. avd., Medd. 21, Stockholm.

Kollmann, F.F.P., and Côté, W.A., Jr. 1984. Principles of Wood Science and Technology. Vol 1. Solid Wood. Springer Verlag.

Lee, M. 1993. Personal communication.

Lekhnitskii S.G. 1937. The two-dimensional static problem of the theory of the elasticity of the anisotropic body, Prikl. mat. mekh., Nov ser., 1(1).

Love, A.E.H. 1944. A treatise on the mathematical theory of elasticity. 4th edition, Dover Publications, New York.

Lutz, H.J. 1952. Ocurrence of clefts in the wood of living white spruce in Alaska. J. For. 50(2): 99.

Milburn, J.A. 1973a. Cavitation in *Ricinus* by Acoustic Detection: Induction in Excised Leaves by Various Factors. Planta 110: 253-265.

Milburn, J.A. 1973b. Cavition Studies on Whole *Ricinus* Plants by Acoustic Detection. Planta 112: 333-342.

Milburn, J.A. and Johnson, R.P.C. 1966. The conduction of sap II. Detection of vibrations produced by sap cavitation in *Ricinus* xylem. Planta 69: 43-52.

Miller, W. and Simpson, I. 1992 Collapse-associated internal checking in radiata pine. Proc. 3rd IUFRO drying conference Vienna 1992.

Mühlethaler, K. 1960. Die Feinstruktur der Zellulosemikrofibrillen. Beih. Zeit. Schweiz. Forstv. 30: 55-65.

Mühlethaler, K. 1965. The fine structure of the cellulose microfibril. In: Cellular Ultrastructure of Woody Plants, W.A. Côté, Jr., Editor. Syracuse Univ. Press, Syracuse, New York.

Muskhelishvili, N.I. 1935. Some basic problems of the mathematical theory of elasticity. Izd. Akad. Nauk SSSR.

Nelson, R.M. 1983. A model for sorption of water vapour by cellulosic materials. Wood and Fiber Sci. 15: 8-22.

Oliver, A.R., Mills, R., and Ralph, K. 1986. Pascal program DRYWOOD. Tasmanian Timber Promotion Board.

Oliver, A.R. 1991. A model of the behaviour of wood as it dries (with special reference to Eucalypt materials). Research Report CM91-1, Civil and Mechanical Engineering Department, University of Tasmania.

Oliver, A.R. 1993b. Computer program labs.p. Unpublished.

Oliver, A.R. 1995a. Unpublished work.

Oliver, A.R. 1995b. Computer program Vessels.p. Unpublished.

Oliver, A.R. 1995c. Recovery from power failure to drying kiln. Unpublished.

Oliver, A.R. 1996. Personal communication.

Palin, M.A. and Petty, J.A. 1981. Permeability to water of the cell wall material of spruce heartwood. Wood Sci. and Technol. 15: 161-169.

Pankevicius, E.R. 1960. Recent studies on collapse. CSIRO Forest Products Newsletter 260.

Pankevicius, E.R. 1961. Influence of position in tree on recoverable collapse in wood. Forest Products Journal, 11: 131-132.

Panshin, A.J. and de Zeeuw, C. 1980. Textbook of wood technology. McGraw-Hill New York.

Parsons, T. 1989. Acoustic Emissions from drying timber. BE Hons thesis, Department of Civil and Mechanical Engineering, University of Tasmania.

Pentoney, R.E. 1953. Mechanisms affecting tangential vs radial shrinkage. Forest Products Journal, June 1953.

Plumb, R.C. and Bridgman, W.B. 1972. Ascent of sap in trees. Science 176: 1129-1131.

Pockman, W.T., Sperry, J.S. and O'Leary, J.W. 1995. Sustained and significant negative water pressure in xylem. Nature 378: 715-716.

Ranta-Maunus, A. 1994. Computation of moisture transport and drying stresses by a 2_D FE programme. Paper presented at 4th IUFRO International Wood Drying Conference, August 9-13 1994, Rotorua New Zealand.

Renner O. 1915. Theoretisches und Experimentelles zur Kohäsionetheorie der Wasserbewegung. Jb Wiss Bot 56: 617-667.

Rohsenow, W.M. and Choi, H.Y. 1961. Heat, mass and momentum transfer. Prentice-Hall, Englewood Cliffs.

Savin, G.N. 1961. Stress concentration around holes. Pergamon Press.

Schaffner, R.D. 1981. Fundamental aspects of timber seasoning. MEngSci thesis, Research Report CM81/1, Mechanical Engineering Department, Faculty of Engineering, University of Tasmania.

Schaffner, R.D. and Doe, P.E. 1981. An application of an orthotropic Fickian diffusion model to timber drying. Paper presented at 20th Forest Products Research Conference, Melbourne Australia, November 1981.

Scholander, P.F., Hammel H.T., Bradstreet, E.D. and Hemmingsen, E.A. 1965. Sap Pressure in Vascular Plants. Science 148: 339-346 April 1965.

Shigo, A.L. and Shigo, A. 1974. Detection of discoloration and decay in living trees and utility poles. US For. Serv., North-eastern For. Exp. Stn Res. Pap. No. NE -294.

Siau, J.F. 1984. Transport Processes in Wood. Springer-Verlag Berlin Heidelberg.

Slatyer, R.O. 1967. Plant-Water Relationships. Academic Press London and New York.

Stamm, A.J. 1929. J. Phys. Chem. 5: 398.

Stamm, A.J. 1964. Wood and Cellulose Science. The Ronald Press Company, New York.

Stamm, A.J. and Loughborough, W.K. 1942. Variation in shrinkage and swelling of wood. Amer. Soc. Mech. Eng., Trans. 64: 379-386.

Tiemann, H.D. 1906. Effect of moisture upon the strength and stiffness of wood. US Dep Agric For Serv Bull 70, 144pp.

Tiemann, H.D. 1915. Principles of kiln drying. Lumber World Review, January 15 and September 25.

Timoshenko, S, Goodier, J.N. 1951. Theory of Elasticity. McGraw-Hill.

Trevena, D.H. 1987. Cavitation & Tension in Liquids. Adam Hilger, Bristol and Philadelphia.

Tyree, M.T. and Dixon, M.A. 1983. Cavitation Events in *Thuja occidentalis* L.? Plant Phys. 72: 1094-1099.

Ursprung A. 1915. Über die Kohäsion des Wassers im Farnanulus. Ber Dtsch Bot Ges 33: 153-162.

Valentin, G. 1837. Reportium für Anatomie und Physiologie. Berlin.

Vennard and Street 1982. Elementary fluid mechanics sixth edition. John Wiley and Sons.

Vermaas, H.F. and Bariska M. 1994. Collapse during low temperature drying of *Eucalyptus grandis* W.Hill and *Pinus silvestris* L. Paper presented at 4th IUFRO International Wood Drying Conference, August 9-13 1994, Rotorua New Zealand.

Volmer, M. 1939. Kinetik der Phasenbildung, Verlag T. Steinkopff, Dresden.

Wardrop, A.B. 1964a. The structure and formation of the cell wall in xylem. In: The formation of wood in forest trees. M.H. Zimmermann, Editor. Academic Press Inc., New York. 87-134.

Wardrop, A.B. and Dadswell, H.E. 1955. The nature of reaction wood. Aust. J. Bot. 3: 177-189.

Weast, R.C. 1981 editor: CRC handbook of chemistry and physics. CRC press, Boca Raton, Florida.

West, D.W. and Gaff, D.F. 1976. Xylem cavitation in excised leaves of *Malus sylvestris* Mill. and measurement of leaf water status with the pressure chamber. Planta 129: 15-18.

Wilkilns, A.P. and Wilkes, J. 1987. Observations on the mechanism of collapse in wood. J. Inst. Wood Sci. 11(2): 89-92.

Wright, G.W. 1967. Pre-freezing as a drying treatment. CSIRO Forest Products Newsletter 337, Jan-Feb 1967.

Wu Qinglin 1989. An investigation of some problems in drying of Tasmanian Eucalypt timbers. MEngSci thesis, Faculty of Engineering, University of Tasmania, Australia.

Yang, Jun Li (1994). Unpublished x-ray densitometry plots.

Zimmermann, M.H. 1983. Xylem Structure and the Ascent of Sap. Springer-Verlag Berlin.

Appendix A. Notation

A,a	constants
AMC	absolute moisture concentration (kg water/m^3 wet wood)
A_k	activation energy (J)
b	a constant
BD	basic density (kg/m^3)
C	total collapse, constant
CF	collapse factor
C_L	liquid tension collapse
D	density of a liquid (kg/m^3), area of cross section of dry wood (m^2), diffusion coefficient (m^2/hour)
DBT	dry bulb temperature (°C)
D_0	reference diffusion coefficient (m^2/hour)
e	strain
E	Young's modulus (Pa)
E^*	instantaneous modulus, that is, ratio between increments of instantaneous stress and strain (Pa)
EMC	Equilibrium Moisture Content (kg water/kg dry wood)
EW	earlywood
f	a stress (Pa)
FSP	Fibre Saturation Point
G	area of cross section of green wood (m^2), shear stiffness (Pa)
J	frequency of bubble formation
k	Boltzmann's Constant
k_L	deformation coefficient
K	constant
LW	latewood
L-T	longitudinal-tangential slice
m	mass of a molecule, mass of water (kg)
M	molecular mass of a liquid
MC	moisture content (kg water/kg dry wood)
MC0	initial moisture content (kg water/kg dry wood)
P, p	pressure (Pa)
q	moisture concentration (kg water/m^3 wet wood)
R	Universal Gas Constant
RH	relative humidity
R-T	radial-tangential slice

s	stress (Pa)
S_0	collapse free shrinkage
R,r	radius (m)
t	time (s)
T	temperature (°C)
T_k	temperature (K)
u	radial displacement of the fibre wall at a specified radius (m)
V	volume (m^3)
WBT	wet bulb temperature (°C)
x	direction in Cartesian coordinate system
y	direction in Cartesian coordinate system
z	direction in Cartesian coordinate system
Z_1	number of molecules per unit volume
Δ	change in a variable
δ	signifies an increment
ε	local instantaneous strain
γ	shear modulus (Pa)
λ	latent heat of vaporisation per molecule (J)
μ	Poisson's ratio
θ	angle for Polar coordinate system
ρ	density (kg/m^3)
σ	local instantaneous stress (Pa) or surface tension (N/m)
τ	a time constant, shear stress (Pa)

Subscripts

green	refers to a property of the material in its "green" or saturated condition, that is, with a MC greater than FSP.
i	instantaneous
k	a critical value
r	radial direction
t	tangential direction
u	ultimate
w	property of water
wr	water removed
y	proportional limit
z	longitudinal direction

0	initial value of a variable
1	value of a variable at the fibre inner wall
2	value of a variable at the fibre inner wall

Appendix B Drying of Brushbox (*Tristania conferta* R.Br.)

As part of the development of the CKC (chapter 6), work was undertaken to determine the seasoning properties of brushbox. Measurements were made of its shrinkage, basic density and AE properties. A kiln trial was then run over 32 days in the 0.25m^3 experimental tunnel kiln in Hobart.

B.1 Materials

The tree sampled was approximately eighty years old, from the Chichester region near Dungog in New South Wales. A 28mm thick slab was cut from approximately half way between the pith and bark, then sawn into 100mm wide boards. The boards were docked to 485mm length, then immediately wrapped in plastic and transported to the Hobart laboratory.

B.2 Seasoning properties

B.2.1 Basic density

Basic density was measured on three 100×25×25mm blocks. Green volume was determined by water displacement, then the blocks were oven dried. Basic density was 708±15 kg/m^3.

Initial average moisture content was approximately 80%.

B.2.2 Shrinkage and collapse threshold temperature

Tangential shrinkage was measured directly on slices following the method specified in Section 3.2.1. The measurements were carried out in a temperature and humidity controlled room.

Measurements were taken on L-T slices at temperatures between 17°C and 30°C, and on R-T slices at 22°C. The measured shrinkage curves are shown in Figs. B.2.1 to B.2.6.

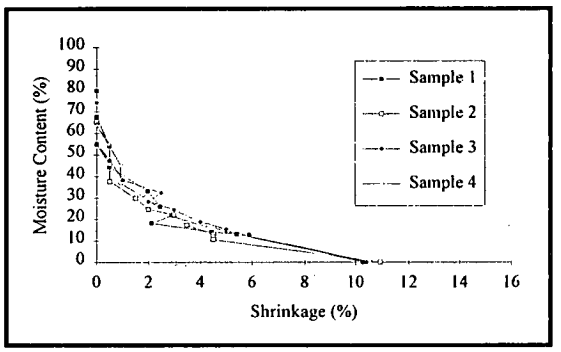

Figure B.2.1 Total shrinkage 17°C

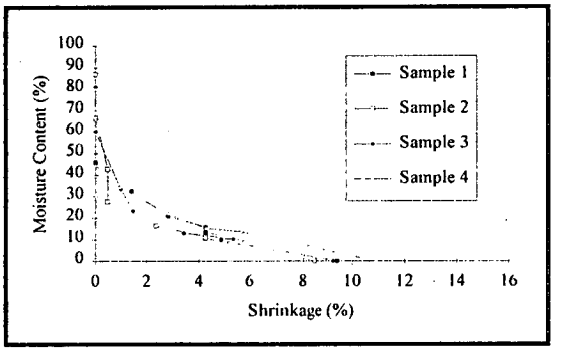

Figure B.2.2 Total shrinkage 20°C

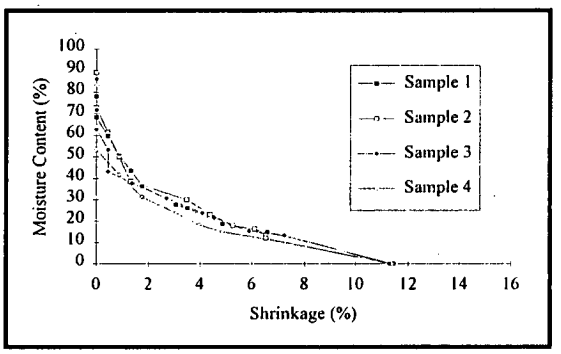

Figure B.2.3 Total shrinkage 22°C

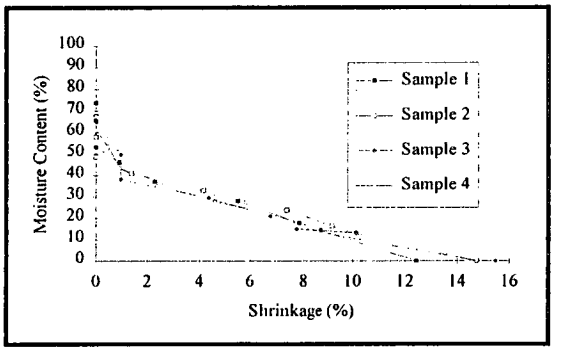

Figure B.2.4 Total shrinkage 25°C

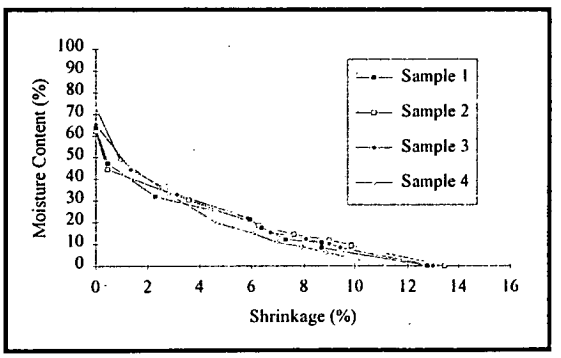

Figure B.2.5 Total shrinkage 30°C

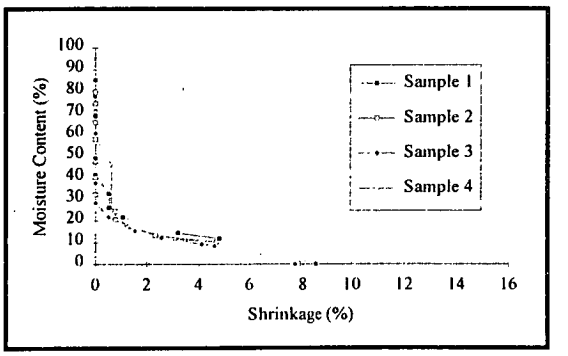

Figure B.2.6 Normal shrinkage

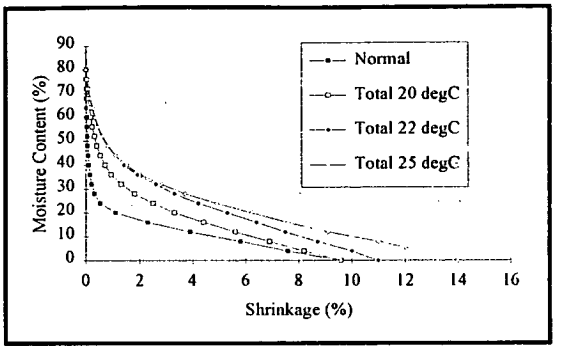

Figure B.2.7 Fits to shrinkage data

Hyperbolas were fitted by eye to the shrinkage curves shown in Figs. B.2.1 to B.2.6. These fits are shown in Fig. B.2.7. The fit to the shrinkage measured at 30°C was the same as that for 25°C, and the fit for 17°C was the same as that for 20°C.

The shrinkage fits show an increase of collapse shrinkage with temperature between 20°C and 25°C. Further softening of the fibre walls by increase of temperature did not appear to result in an increase of collapse shrinkage. Decreasing the temperature below 20°C did not result in a lessening of collapse shrinkage. The extra shrinkage at FSP of the L-T slices dried at 17°C and 20°C over normal shrinkage measured on R-T slices was probably due to loss of bound water from ray or vessel cells above FSP in the L-T slices. Free water dries very quickly out of R-T slices, so that FSP is reached before significant bound water is lost from vessel or ray cells. Note that the oven dry shrinkage of the L-T slices at 17°C and 20°C was the same as the oven dry normal shrinkage. The collapse threshold temperature of this timber was thus approximately 20°C.

B.2.3 AE calibrations

The three AE transducers to be used in the kiln trial were calibrated on brushbox samples using the procedure described in 7.3.2. The transducers had already been calibrated on eucalypt samples; the calibrations on brushbox returned the same calibration factor. To prevent surface checking, the test board had to be mostly enclosed within a plastic bag; exposure to the environmental conditions of the laboratory caused surface checking in several hours.

B.2.4 Diffusion coefficient

The diffusion coefficient was determined by comparing MC distributions predicted by the model **MCProfiles** with measured profiles (see Section 6.3). The surface MC gradients of the measured and predicted profiles measured after the first three days drying were found to agree closely when the reference diffusion coefficient used in the model was 1.0E-8m^2/hour at 20°C (see Fig. B.2.8).

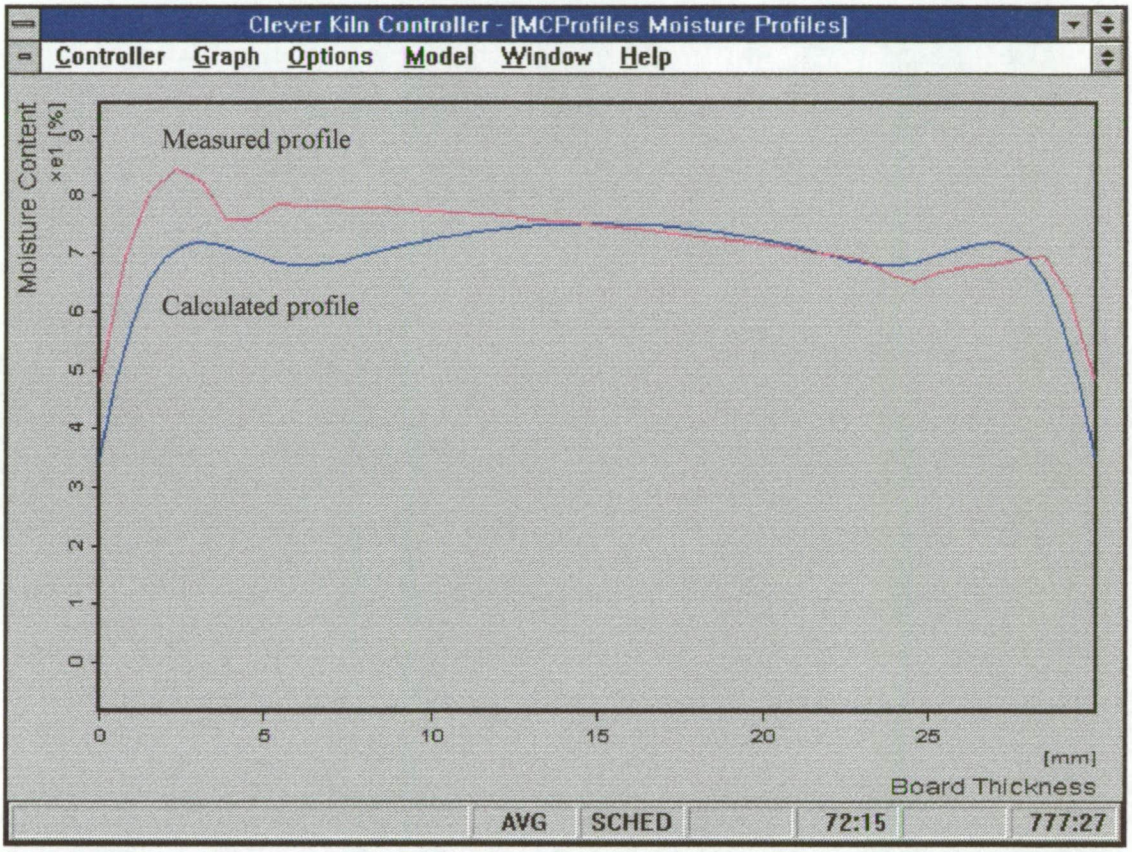

Figure B.2.8 **MCProfiles** comparison of calculated and measured moisture profiles through board thickness after 72 hours drying; left hand side is upper board surface

Fig. B.2.8 shows the measured MC profile to be unsymmetrical. This is a common situation in boards green off saw, but can also result from different drying rates from the top and bottom surfaces. The initial moisture profile is averaged by **MCProfiles** for use in the modelling; all of the modelling is carried out for a half board thickness. The diffusion coefficient is chosen by matching the calculated and measured MC gradients near the board surface. Note that the gradients at the surfaces in Fig. B.2.8 are well matched on both the upper and lower surfaces of the board, although there are differences in the magnitude of the MC.

B.3 Kiln trial

A kiln trial was run in the 0.25m^3 timber capacity experimental tunnel kiln at the Hobart laboratory. The kiln is of insulated aluminium construction. It has a high velocity jet into a large plenum upstream of diffuser screens and the stack to ensure that kiln conditions are as close to uniform as possible. Heating is by electrical element, humidity is controlled by vents both upstream and downstream of the fan and cold water sprays. A more complete description of the kiln is given by Booker (1994b).

The brushbox available was used to fill two rows at half stack height. The rest of the kiln was filled with dummy boards (partially dried Tasmanian Oak) to maintain uniform airflow. The layout of AE and moisture profile (MP) boards is shown in Fig. B.3.1. The three AE sensors (Physical Acoustics Corporation R6I) were placed on three different boards to provide some indication of the importance of variation of drying conditions within the stack. The boards could not quite be stacked edge to edge because the clamps holding the AE sensors protrude from the sides of the board, and also because the MP board needed space on either side so that it could be removed for measurements.

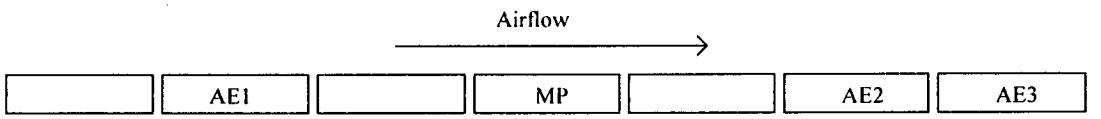

Figure B.3.1 Layout of AE and MP boards

The kiln DBT was set to 22°C and the air velocity between the boards to 0.5m/s. Unfortunately, the temperature outside the kiln for the first part of the kiln trial often exceeded 22°C during the day. The strategy for preventing collapse due to an increase in temperature was to close the vents and increase the spray setting when the ambient temperature exceeded the kiln DBT setpoint (see Section 6.5). This strategy effectively prevented collapse when the kiln temperature rose above setpoint, but dramatically slowed drying by increasing humidity (see Fig. B.3.2).

B.3.1 Results of drying trial

The trial was stopped after approximately 32 days. The two layers of brushbox were removed from the kiln charge and inspected. No surface checking was visible on any of the board surfaces. No collapse was visible at the board surfaces, and cross cutting of several boards revealed no internal checking. The temperature and AE data recorded during the trial are shown in Figs. B.3.2 and B.3.3. A software bug meant that approximately 50 hours of data was lost between 220 and 270 hours; during this time the kiln controller behaved normally.

The CKC was run in setpoint control mode for approximately the first 20 hours, between 110 and 130 hours, and for the last 150 hours. Apart from this, the CKC controlled in AE mode. Unfortunately, a power failure at approximately 110 hours resulted in the recording of discontinuous temperature data; this then meant the **SmartKiln** modelling program could not be run, so that the CKC could not be run in AE/**SmartKiln** mode.

Note that AE1 was consistently higher than the other two AE channels. This is probably due to the air near the inlet of the stack being drier than that further through the stack, so that boards near the stack entrance dry faster than those nearer the exit (see Table B.3.1). Note however, that the free stream velocity of the kiln air increases through the stack due to the boundary layer growth on the board surfaces, which can increase drying rate through the stack. Some of the differences in MC of the three boards may be due to the variability of the material, as demonstrated in the shrinkage curves B.2.1 to B.2.6.

Note the response of the kiln when the ambient temperature rose above the DBT setpoint. The strategy effectively halted drying, and restricted the DBT to some extent (see Section 6.5). There are several spikes in the DBT response which do not appear to be connected with the ambient temperature behaviour. These spikes appear to be due to the choice of PID parameters, resulting in relatively large increases in heater setting for some combinations of DBT error over three consecutive readings.

Figs. B.3.4 and B.3.5 show the initial and final MC profiles of the moisture profile board (Fig. B.3.1) respectively. The centre MC had not changed substantially over the course of the kiln trial. The final average MC of the MP board was 74%.

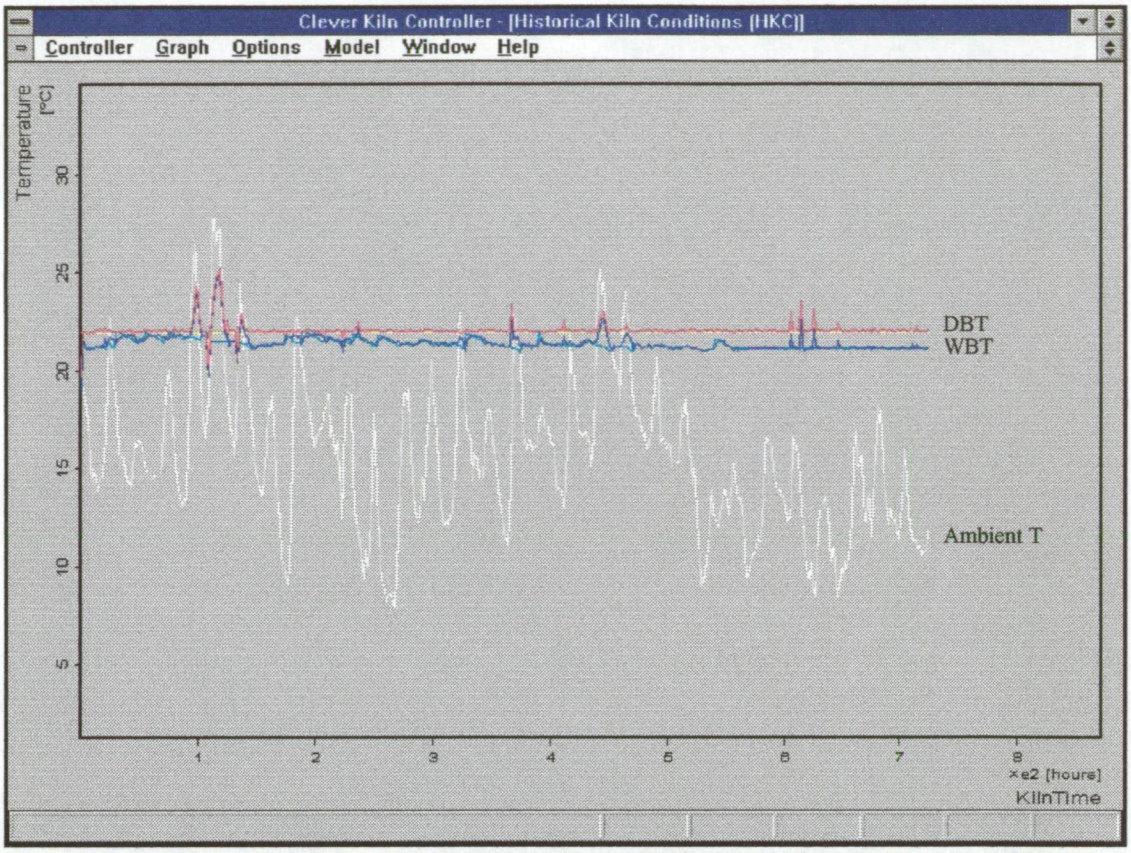

Figure B.3.1 Log of temperatures recorded during the kiln trial

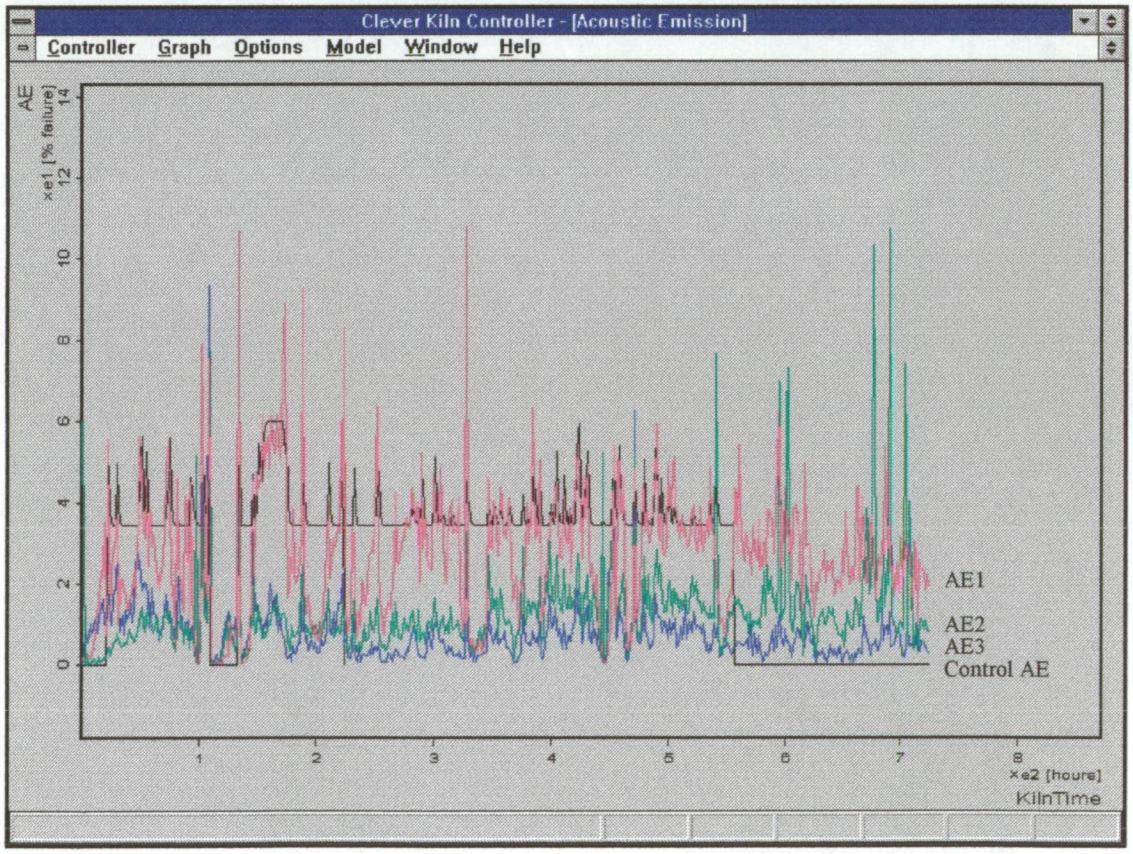

Figure B.3.2 Log of acoustic emissions recorded during the kiln trial

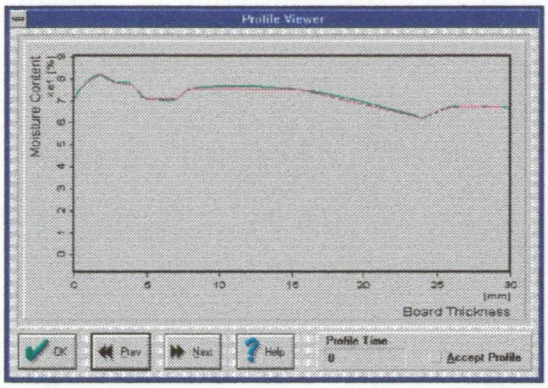

Figure B.3.4 Initial moisture content profile

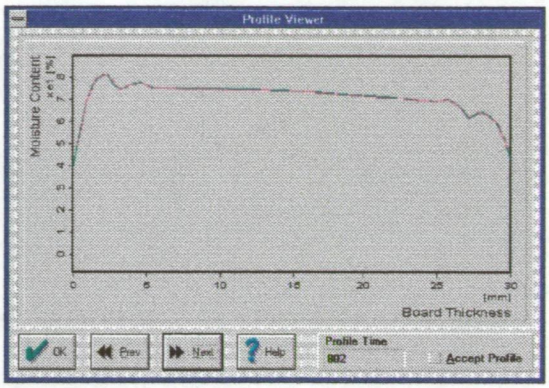

Figure B.3.3 Final moisture content profile

Average MC was also measured for the three AE boards at the end of the kiln trial; results are shown in Table B.3.1.

	AE1	AE2	AE3
MC	68.3%	74.3%	77.4%

Table B.3.1 MC of AE boards following kiln trial

Table B.3.1 shows that average MC of each board progressively increased through the stack from inlet to outlet. When the kiln trial was stopped, significant condensation was observed on the roof and walls of the kiln, particularly toward the outlet side of the stack. Some of this condensation had dripped onto the boards; such condensation was not observed on the board AE1. It appears that the low airspeed combined with the moist kiln conditions and low outside temperature resulted in significant condensation on the kiln walls increasing from the inlet to the outlet to the stack, and significant gradient in drying conditions. This situation is not expected to occur to the same degree in larger kilns. For this kiln, it appears advisable to locate the AE boards as close as possible to the MP board so that the change in drying conditions over the four boards is decreased.

In this trial the rate of drying of the stack was limited by the AE from board AE1. Table B.3.1 shows that this board had dried substantially more than the other AE boards or the MP board, although it still experienced no drying induced degrade. This indicates that the board AE1 dried at a rate much closer to the optimum than did the other boards.

B.4 Drying simulation

The measured shrinkage and diffusion coefficient were used in the predictive timber drying simulation model SmartKiln (see Section 6.4.3). Graphical results are shown in Fig. B.4.1.

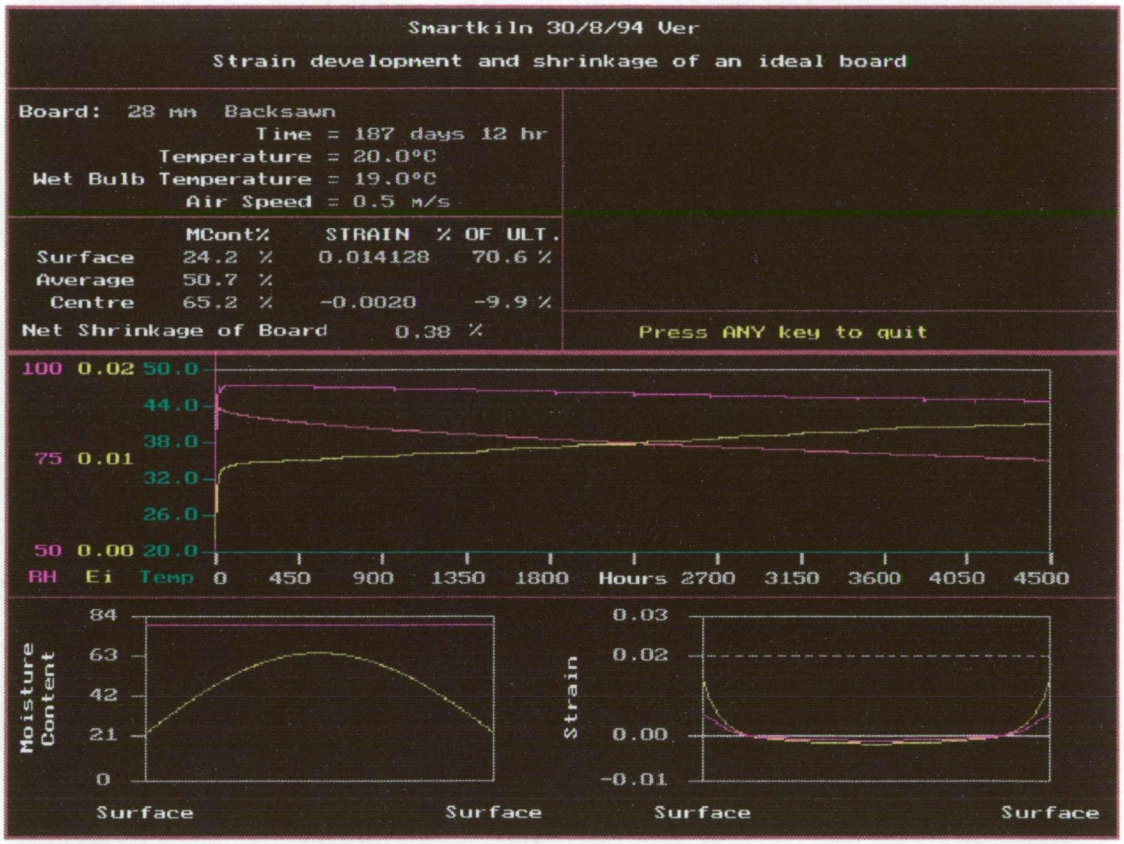

Figure B.4.1 **SmartKiln** drying simulation predictions

The top two left hand boxes of the **SmartKiln** output (Fig. B.4.1) show summary data of the present simulated board state. The central graph shows the variation with time of the dry bulb temperature (green), relative humidity (magenta), surface strain (yellow) and average moisture content (red). Scale of the average moisture content graph is 0 to 100%. The lower left hand graph shows the predicted moisture content distribution (yellow) and the initial moisture content (magenta). The graph at lower right shows the predicted instantaneous strain distribution (yellow) and stress distribution (magenta). Scale of the stress distribution graph is -1.7 to +5 MPa.

The simulation predicted that, even after six months' drying, the average MC would still be approximately 50% with a centre MC of approximately 65%. Significantly more drying would be necessary before high temperature final drying could be

performed. Experience has shown that drying with the surface at an instantaneous strain closer to the ultimate value does not greatly reduce seasoning time.

B.5 Conclusions

Properties of brushbox needed for seasoning simulation were collected, and a kiln trial run over 32 days. Simulation predicted that drying of this timber free of surface checks will be a very slow process. Racking out the timber in a semi-controlled environment such as a "curing shed" may be a more viable financial option than kiln drying.

Appendix C Analytical model of a round hole in an orthotropic infinite plate

This analysis was performed by Oliver (1995a). The solution is largely taken from Savin (1961).

We use the method of stress functions to find an analytical solution to this problem. The Airy stress function U(x,y) is defined in plane stress situation by

$$\sigma_x = \frac{\partial^2 U}{\partial y^2}$$

$$\sigma_y = \frac{\partial^2 U}{\partial x^2} \tag{1}$$

$$\tau_{xy} = -\frac{\partial^2 U}{\partial x \partial y}$$

so that any values of U satisfy the equations of statics

$$\frac{\partial \sigma_x}{\partial x} + \frac{\partial \tau_{xy}}{\partial y} = 0$$

$$\frac{\partial \sigma_y}{\partial y} + \frac{\partial \tau_{xy}}{\partial x} = 0 \tag{2}$$

We now assume that a condition of plane strain exists (which seems reasonable far from the ends of a drying board). The strain components can then be defined in terms of the components of displacement u and v in the x and y directions

$$\varepsilon_x = \frac{\partial u}{\partial x}$$

$$\varepsilon_y = \frac{\partial v}{\partial y} \tag{3}$$

$$\gamma_{xy} = \frac{\partial u}{\partial y} + \frac{\partial v}{\partial x}$$

A third equation, the equation of compatibility, is required to define the three components of strain

$$\frac{\partial^2 e_x}{\partial y^2} + \frac{\partial^2 e_y}{\partial x^2} = \frac{\partial^2 \gamma_{xy}}{\partial x \partial y} \tag{4}$$

Timber can be regarded as being orthotropic, so its properties in the three principal directions (radial, tangential and longitudinal) are described by

$$\varepsilon_r = \frac{\sigma_r}{E_r} - \frac{\mu_{tr}\sigma_t}{E_t} - \frac{\mu_{zr}\sigma_z}{E_z} \tag{5}$$

$$\varepsilon_t = -\frac{\mu_{rt}\sigma_r}{E_r} + \frac{\sigma_t}{E_t} - \frac{\mu_{zt}\sigma_z}{E_z} \tag{6}$$

$$\varepsilon_z = -\frac{\mu_{rz}\sigma_r}{E_r} - \frac{\mu_{tz}\sigma_t}{E_t} + \frac{\sigma_z}{E_z} \tag{7}$$

When we assume plane stress (σ_Z = constant) and plane strain ($\varepsilon_Z = 0$), equations 5 and 6 become

$$\varepsilon_r = \left(1 - \mu_{zr}\mu_{rz}\right)\frac{\sigma_r}{E_r} - \left(\mu_{tr} + \mu_{zr}\mu_{tz}\right)\frac{\sigma_t}{E_t} \tag{8}$$

$$\varepsilon_t = -\left(\mu_{rt} + \mu_{zt}\mu_{rz}\right)\frac{\sigma_r}{E_r} + \left(1 - \mu_{zt}\mu_{tz}\right)\frac{\sigma_t}{E_t} \tag{9}$$

For the general two-dimensional plane stress/plane strain situation, we resolve from the r-t axes to the x-y axes, and introduce shear strains. Following Savin (1961) we have

$$\varepsilon_x = a_{11}\sigma_x + a_{12}\sigma_y + a_{13}\tau_{xy} \tag{10}$$

$$\varepsilon_y = a_{21}\sigma_x + a_{22}\sigma_y + a_{23}\tau_{xy} \tag{11}$$

$$\gamma_{xy} = a_{31}\sigma_x + a_{32}\sigma_y + a_{33}\tau_{xy} \tag{12}$$

From the concept of strain energy, the matrix of coefficients must be symmetric (Love 1927), ie

$$a_{ij} = a_{ji} \tag{13}$$

Comparison of this condition to equations 8 and 9 yields the condition

$$\frac{\mu_{rt} + \mu_{zt}\mu_{rz}}{E_r} = \frac{\mu_{tr} + \mu_{zr}\mu_{tz}}{E_t} \tag{14}$$

Substituting equations 1 into equations 10 to 12, applying the results to the compatibility equation 4 and making use of the condition 13, we get

$$a_{22}\frac{\partial^4 U}{\partial x^4} - 2a_{23}\frac{\partial^4 U}{\partial x^3 \partial y} + \left(2a_{12} + a_{33}\right)\frac{\partial^4 U}{\partial x^2 \partial y^2} - 2a_{13}\frac{\partial^4 U}{\partial x \partial y^3} + a_{11}\frac{\partial^4 U}{\partial y^4} = 0 \tag{15}$$

The general solution to this differential equation depends on the roots of the characteristic equation

$$a_{11}s^4 - 2a_{13}s^3 + \left(2a_{12} + a_{33}\right)s^2 - 2a_{23}s + a_{22} = 0 \tag{16}$$

The general solution can now be written

$$U(x,y) = F_1\left(x + s_1 y\right) + F_2\left(x + s_2 y\right) + F_3\left(x + s_3 y\right) + F_4\left(x + s_4 y\right) \tag{17}$$

where s_i are the roots of equation 16. Lekhnitskii (1937) as cited in Savin (1961) showed that, on the basis of energy considerations, these roots cannot be purely real, and so may be replaced by

$$s_1 = \alpha_1 + i\beta_1 \quad s_2 = \alpha_2 + i\beta_2 \quad s_3 = \alpha_3 + i\beta_3 \quad s_4 = \alpha_4 + i\beta_4 \tag{18}$$

Without loss of generality, we can write

$$z_1 = x + s_1 y \text{ and } z_2 = x + s_2 y \tag{19}$$

and a general solution of equation 15 can be written

$$U(x,y) = F_1(z_1)z_1 + F_2(z_2) + \overline{F_1(z_1)} + \overline{F_2(z_2)} \tag{20}$$

where the over-bar denotes the complex conjugate.

Two new functions are introduced

$$\phi(z_1) = \frac{\partial F_1}{\partial z_1} \text{ and } \varphi(z_2) = \frac{\partial F_2}{\partial z_2} \tag{21}$$

By inserting equation 20 into equation 1 and considering equation 21 we obtain the stress components as expressions of the functions $\phi(z_1)$ and $\varphi(z_2)$

$$\begin{aligned} \sigma_x &= 2\,\mathrm{Re}\left[s_1^2\phi'(z_1) + s_2^2\varphi'(z_2)\right] \\ \sigma_y &= 2\,\mathrm{Re}\left[\phi'(z_1) + \varphi'(z_2)\right] \\ \tau_{xy} &= -2\,\mathrm{Re}\left[s_1\phi'(z_1) + s_2\varphi'(z_2)\right] \end{aligned} \tag{22}$$

where Re denotes the real part of the expression.

Equation 16 is simplified for the case of timber by transferring from the general x-y plane to r-t coordinates. This puts $a_{13} = a_{23} = a_{31} = a_{32} = 0$. Equation 16 then becomes

$$a_{11}s^4 + (2a_{12} + a_{33})s^2 + a_{22} = 0 \tag{23}$$

Typical values of the structural properties of green eucalypts are:

$\mu_{tz} = 0.035$; $\mu_{tr} = 0.379$; $\mu_{rz} = 0.052$; $\mu_{rt} = 0.718$; $\mu_{zr} = 0.495$;

$\mu_{zt} = 0.632$; $E_t = 250\text{MPa}$ $E_r = 500\text{MPa}$ $E_z = 5\text{GPa}$

Equation 13 imposes restrictions on these values, viz

$$\begin{aligned} a_{21} &= -\frac{(\mu_{rt} + \mu_{zt}\mu_{rz})}{E_r} = -1.502E-9 \\ a_{12} &= -\frac{(\mu_{tr} + \mu_{zr}\mu_{tz})}{E_t} = -1.585E-9 \end{aligned} \tag{24}$$

The difference is small, and may be due to experimental error. An average value is used, so that

$$a_{21} = a_{12} = -1.544E-9 \tag{25}$$

We also get

$$a_{11} = 1.949E-9 \text{ and } a_{22} = 3.912E-9 \tag{26}$$

Consideration of a pure shearing strain in this situation leads to the relation

$$a_{33} = \frac{1}{G} = \frac{1+\mu_{rt}}{E_r} + \frac{1+\mu_{tr}}{E_t} = 8.952E-9 \tag{27}$$

Equation 23 then becomes

$$1.949E-9s^4 + 5.865E-9s^2 + 3.912E-9 = 0 \tag{28}$$

The solutions to which are

$$s^2 = -2.013 \text{ or } -0.997 \tag{29}$$

Hence, in equation 18 we have

$$\alpha_1 = \alpha_2 = 0 \quad \beta_1 = 1.419 \quad \beta_2 = 0.988 \tag{30}$$

and thus from equation 19 we get

$$z_1 = x + \beta_1 y \text{ and } z_2 = x + \beta_2 y \tag{31}$$

and from equations 22 we get

$$\sigma_x = 2\,\mathrm{Re}\left[-\beta_1^2\phi'(z_1) - \beta_2^2\varphi'(z_2)\right]$$
$$\sigma_y = 2\,\mathrm{Re}\left[\phi'(z_1) + \varphi'(z_2)\right] \qquad (32)$$
$$\tau_{xy} = -2\,\mathrm{Re}\left[i\beta_1\phi'(z_1) + i\beta_2\varphi'(z_2)\right]$$

The solution to the problem presented by Savin (1961) involves mapping the area outside the hole in question onto the area inside a unit circle. He presents a general solution for elliptical holes in an infinite plate, but we will here consider a specific solution for a circular hole.

A cylindrical vessel is described in the physical (z = x + iy) plane by a circle of radius a, but a solution of equations 21 (and thus the stress distributions from equations 22) requires analysis of behaviour in the z_1 and z_2 planes of equation 31. In these planes, the contour of the hole in the physical plane is described by ellipses, as shown in equation 31. The ellipses have one axis of length a in the x direction, and the other of length a/β_1 and a/β_2 in the y direction.

An ellipse with axes a and b in the x and y directions respectively in the z plane is mapped onto the unit circle $\varsigma = \exp(i\theta)$ in the ς plane, and the area outside the ellipse in the z plane is mapped onto the area inside the circle in the ς plane by the conformal transformation

$$z = \frac{1}{2}(a-b)\varsigma + \frac{1}{2}\frac{(a+b)}{\varsigma} \qquad (33)$$

In this case, the transformation becomes

$$z = \frac{1}{2}a\left(1+\frac{i}{\beta}\right)\exp(i\theta) + \frac{1}{2}a\left(1-\frac{i}{\beta}\right)\exp(-i\theta) \qquad (34)$$

The general solutions for $\phi(z_1)$ and $\varphi(z_2)$ of equations 21 are written

$$\phi = \phi_0 + \phi_1 \text{ and } \varphi = \varphi_0 + \varphi_1 \qquad (35)$$

where the subscript 1 denotes that part of the function which describes its behaviour away from the edge of the hole, and the subscript 0 denotes that part of the function which ensures that the resultant stress is zero at the edge of the hole.

The problem in which we are interested in this case is that of uniform tension in the x-direction so that as $z \to \infty$ we want

$$\sigma_x\big|_\infty = p \text{ and } \sigma_y\big|_\infty = \tau_{xy}\big|_\infty = 0 \qquad (36)$$

The general solutions for $\phi(z_1)$ and $\varphi(z_2)$ can be written

$$\phi_1(z_1) = A_1\ln(z_1) + (B_1 + iC_1)z_1$$
$$\varphi_1(z_2) = A_2\ln(z_2) + (B_2 + iC_2)z_2 \qquad (37)$$

The constants A_1 and A_2 are both zero as they do not contribute to the stresses as z tends to infinity. We then find the other constants in equations 37 using equations 22 and 31

$$B_1 = -\frac{p}{2(\beta_1^2 - \beta_2^2)} \quad B_2 = \frac{p}{2(\beta_1^2 - \beta_2^2)} \quad C_1 = C_2 = 0 \tag{38}$$

We now need to determine ϕ_0 and φ_0 to satisfy the condition of zero net stress around the circle $\varsigma = \sigma$. On this circle we have

$$\begin{aligned} 2\,\mathrm{Re}\left[\phi(z_1) + \varphi(z_2)\right] &= \int_0^s Y_n ds = f_1 = 0 \\ 2\,\mathrm{Re}\left[s_1\phi(z_1) + s_2\varphi(z_2)\right] &= \int_0^s X_n ds = f_2 = 0 \end{aligned} \tag{39}$$

After mapping the ellipses onto the circle $\varsigma = \sigma$, equations 39 become

$$\begin{aligned} 2\,\mathrm{Re}\left[\phi_2(\sigma) + \varphi_2(\sigma)\right] &= f_1(\theta) \\ 2\,\mathrm{Re}\left[s_1\phi_2(\sigma) + s_2\varphi_2(\sigma)\right] &= f_2(\theta) \end{aligned} \tag{40}$$

To find the functions $\phi(\varsigma)$ and $\varphi(\varsigma)$ which apply within the unit circle $\varsigma = \exp(i\gamma)$ and satisfy 40 around the boundary of the circle, Savin (1961) uses the Schwartz formula (citing Muskhelishvili 1935)

$$F(\varsigma) = \frac{1}{2\pi i}\int_\gamma U(\theta)\frac{\sigma+\varsigma}{\sigma-\varsigma}\frac{d\sigma}{\sigma} \tag{41}$$

Savin (1961) thus obtains

$$\begin{aligned} \phi_2(\varsigma) + \varsigma_2(\varsigma) &= \frac{1}{4\pi i}\int_\gamma f_1(\theta)\frac{\sigma+\varsigma}{\sigma-\varsigma}\frac{d\sigma}{\sigma} \\ s_1\phi_2(\varsigma) + s_2\varsigma_2(\varsigma) &= \frac{1}{4\pi i}\int_\gamma f_2(\theta)\frac{\sigma+\varsigma}{\sigma-\varsigma}\frac{d\sigma}{\sigma} \end{aligned} \tag{42}$$

and hence, using the results of 18 and 30

$$\begin{aligned} \phi_2(\varsigma) &= \frac{1}{4\pi(\beta_1 - \beta_2)}\int_\gamma \left[i\beta_2 f_1^0(\theta) - f_2^0(\theta)\right]\frac{\sigma+\varsigma}{\sigma-\varsigma}\frac{d\sigma}{\sigma} \\ \varphi_2(\varsigma) &= -\frac{1}{4\pi(\beta_1 - \beta_2)}\int_\gamma \left[i\beta_1 f_1^0(\theta) - f_2^0(\theta)\right]\frac{\sigma+\varsigma}{\sigma-\varsigma}\frac{d\sigma}{\sigma} \end{aligned} \tag{43}$$

Savin then uses equations 38 and 40 to write

$$\begin{aligned} f_1^0 &= -2\,Re\left[B_1 z_1 + B_2 z_2\right] \\ f_2^0 &= -2\,Re\left[i\beta_1 B_1 z_1 + i\beta_2 B_2 z_2\right] \end{aligned} \tag{44}$$

Next, he uses the known results for Cauchy integrals

$$\int_\gamma \sigma\frac{\sigma+\varsigma}{\sigma-\varsigma}\frac{d\sigma}{\sigma} = 4\pi i\varsigma \text{ and } \int_\gamma \frac{1}{\sigma}\frac{\sigma+\varsigma}{\sigma-\varsigma}\frac{d\sigma}{\sigma} = 0 \tag{45}$$

to give

$$\phi_2(\varsigma) = \frac{-\varsigma}{2(\beta_1 - \beta_2)} \text{ and } \varphi_2(\varsigma) = \frac{\varsigma}{2(\beta_1 - \beta_2)} \tag{46}$$

The inverse of the mapping function 34 gives

$$\varsigma = z_1 - \frac{\sqrt{z_1^2 - (1-\beta_1^2)}}{1-\beta_1} \text{ or } \varsigma = z_2 - \frac{\sqrt{z_2^2 - (1-\beta_2^2)}}{1-\beta_2} \tag{47}$$

whence

$$\frac{d\varsigma}{dz_1} = \frac{1}{(1-\beta_1)}\left(1 - \frac{z_1}{\sqrt{z_1^2 - (1-\beta_1^2)}}\right) \text{ and}$$

$$\frac{d\varsigma}{dz_2} = \frac{1}{(1-\beta_2)}\left(1 - \frac{z_2}{\sqrt{z_2^2 - (1-\beta_2^2)}}\right) \tag{48}$$

from which it follows that

$$\phi_2'(z_1) = -\frac{1}{2(\beta_1 - \beta_2)}\frac{1}{(1-\beta_1)}\left(1 - \frac{z_1}{\sqrt{z_1^2 - (1-\beta_1^2)}}\right) \text{ and}$$

$$\varphi_2'(z_2) = \frac{1}{2(\beta_1 - \beta_2)}\frac{1}{(1-\beta_2)}\left(1 - \frac{z_2}{\sqrt{z_2^2 - (1-\beta_2^2)}}\right) \tag{49}$$

and finally, equations 22 yield

$$\sigma_x = 1 + \frac{1}{\beta_1 - \beta_2}\left[\frac{\beta_1^2}{1-\beta_1}\text{Re}\left(1 - \frac{z_1}{\sqrt{z_1^2 - (1-\beta_1^2)}}\right) - \frac{\beta_2^2}{1-\beta_2}\text{Re}\left(1 - \frac{z_2}{\sqrt{z_2^2 - (1-\beta_2^2)}}\right)\right]$$

$$\sigma_y = \frac{1}{\beta_1 - \beta_2}\left[\frac{1}{1-\beta_1}\text{Re}\left(1 - \frac{z_1}{\sqrt{z_1^2 - (1-\beta_1^2)}}\right) - \frac{1}{1-\beta_2}\text{Re}\left(1 - \frac{z_2}{\sqrt{z_2^2 - (1-\beta_2^2)}}\right)\right]$$

$$\tau_{xy} = \frac{1}{\beta_1 - \beta_2}\left[\frac{\beta_1}{1-\beta_1}\text{Im}\left(1 - \frac{z_1}{\sqrt{z_1^2 - (1-\beta_1^2)}}\right) - \frac{\beta_2}{1-\beta_2}\text{Im}\left(1 - \frac{z_2}{\sqrt{z_2^2 - (1-\beta_2^2)}}\right)\right]$$

where Im means the imaginary part of the argument.

This solution was implemented in a Pascal program written by Oliver (1995b). A complete results listing is provided below. The main result is the tangential stress ratio at x = 0, y = 1 radius. This is the highest stress in the x-direction, and has a value of 3.4. This is the stress concentration factor for the hole in this case. The results listing also shows that the area of material around the hole affected by the stress concentration is very small (this result is corroborated by the Strand6 results).

HOLLOW CYLINDER IN LINEARLY ELASTIC ORTHOTROPIC MATERIAL A/G SAVIN							
DATA							
5.0E+08=Erad 2.5E+08=Etang 0.632=Muzt 0.495=Muzr 0.718=Murt 0.052=Murz							
0.379=Mutr 0.035=Mutz							
1.4186=BETA1 0.9987=BETA2 -5.690E+00=D1 1.904E+03=D2 3.4174=PEAK OF ST							
STRESS RATIOS IN BACKSAWN MATERIAL							
(A21=ALPHA1-THETA1; A22=ALPHA2-THETA2)							
1.000=Y							
TANG.	RADIAL	SHEAR	PHI	PSI	A21	A22	X
3.4174	0	0	2.3817	2.3817	-1.09E-11	-5.46E-12	0
3.2515	-0.047	-0.3157	2.2645	2.3116	6.92E-02	-2.45E-04	0.1
2.8497	-0.1472	-0.506	1.9672	2.1144	1.27E-01	-4.63E-04	0.2
2.3944	-0.2275	-0.5479	1.5975	1.825	1.68E-01	-6.32E-04	0.3
2.0079	-0.2495	-0.4959	1.2382	1.4877	1.92E-01	-7.44E-04	0.4
1.7244	-0.2171	-0.4128	0.927	1.1441	2.03E-01	-8.01E-04	0.5
1.5299	-0.1527	-0.3367	0.6721	0.8248	2.06E-01	-8.12E-04	0.6
1.3975	-0.0786	-0.2821	0.4689	0.5475	2.01E-01	-7.90E-04	0.7
1.3039	-0.0098	-0.2495	0.3091	0.3189	1.93E-01	-7.45E-04	0.8
1.2332	0.0463	-0.2336	0.1842	0.1379	1.83E-01	-6.88E-04	0.9
1.1758	0.0876	-0.2283	0.0872	-0.0004	1.71E-01	-6.26E-04	1
1.1269	0.1149	-0.2285	0.012	-0.1029	1.59E-01	-5.64E-04	1.1
1.0838	0.1307	-0.2306	-0.0459	-0.1766	1.48E-01	-5.04E-04	1.2
1.0456	0.1375	-0.2326	-0.0902	-0.2277	1.36E-01	-4.50E-04	1.3
1.0117	0.1377	-0.2331	-0.1238	-0.2615	1.25E-01	-4.00E-04	1.4
0.9819	0.1334	-0.2319	-0.149	-0.2824	1.15E-01	-3.55E-04	1.5
1.100=Y							
TANG.	RADIAL	SHEAR	PHI	PSI	A21	A22	X
2.5661	-0.2148	0	1.7542	1.969	-9.10E-12	-5.46E-12	0
2.5046	-0.2212	-0.1175	1.6998	1.9209	4.47E-02	-1.85E-04	0.1
2.3435	-0.2323	-0.2008	1.5519	1.7842	8.46E-02	-3.53E-04	0.2
2.1354	-0.2323	-0.2369	1.347	1.5792	1.16E-01	-4.89E-04	0.3
1.9292	-0.2107	-0.2355	1.1225	1.3332	1.39E-01	-5.87E-04	0.4
1.7515	-0.1679	-0.2154	0.9054	1.0733	1.53E-01	-6.46E-04	0.5
1.609	-0.1118	-0.1927	0.71	0.8218	1.60E-01	-6.71E-04	0.6

1.4975	-0.0522	-0.176	0.5414	0.5936	1.62E-01	-6.67E-04	0.7
1.409	0.0032	-0.168	0.3998	0.3967	1.60E-01	-6.44E-04	0.8
1.3366	0.0496	-0.1677	0.2829	0.2333	1.55E-01	-6.08E-04	0.9
1.2751	0.0852	-0.1724	0.1873	0.102	1.48E-01	-5.64E-04	1
1.2214	0.1103	-0.1796	0.1098	-0.0005	1.41E-01	-5.17E-04	1.1
1.1736	0.1259	-0.1872	0.0474	-0.0785	1.32E-01	-4.70E-04	1.2
1.1308	0.1339	-0.1939	-0.0026	-0.1365	1.24E-01	-4.26E-04	1.3
1.0925	0.1359	-0.1988	-0.0424	-0.1783	1.15E-01	-3.83E-04	1.4
1.0584	0.1336	-0.2016	-0.0738	-0.2074	1.07E-01	-3.45E-04	1.5
1.200=Y							
TANG.	RADIAL	SHEAR	PHI	PSI	A21	A22	X
2.0943	-0.2909	0	1.3641	1.6549	-9.10E-12	-5.46E-12	0
2.0687	-0.2864	-0.0385	1.3344	1.6209	3.11E-02	-1.43E-04	0.1
1.9987	-0.272	-0.0678	1.2513	1.5232	5.98E-02	-2.75E-04	0.2
1.9011	-0.2454	-0.084	1.129	1.3744	8.42E-02	-3.85E-04	0.3
1.7942	-0.2064	-0.0889	0.9853	1.1916	1.03E-01	-4.70E-04	0.4
1.6912	-0.1573	-0.088	0.8356	0.993	1.17E-01	-5.26E-04	0.5
1.5987	-0.1031	-0.0868	0.6912	0.7943	1.26E-01	-5.57E-04	0.6
1.518	-0.0491	-0.0887	0.5586	0.6076	1.30E-01	-5.65E-04	0.7
1.4477	0.0003	-0.0949	0.4408	0.4404	1.32E-01	-5.56E-04	0.8
1.3857	0.0423	-0.1047	0.3385	0.2962	1.30E-01	-5.34E-04	0.9
1.3302	0.0755	-0.1169	0.2511	0.1757	1.27E-01	-5.05E-04	1
1.2797	0.0998	-0.1298	0.1774	0.0776	1.23E-01	-4.71E-04	1.1
1.2335	0.1163	-0.1422	0.1158	-0.0005	1.17E-01	-4.35E-04	1.2
1.1911	0.1259	-0.1531	0.0646	-0.0613	1.11E-01	-3.99E-04	1.3
1.1523	0.13	-0.162	0.0223	-0.1077	1.05E-01	-3.64E-04	1.4
1.1172	0.1299	-0.1686	-0.0123	-0.1422	9.87E-02	-3.31E-04	1.5
1.300=Y							
TANG.	RADIAL	SHEAR	PHI	PSI	A21	A22	X
1.806	-0.3108	0	1.0996	1.4104	-7.28E-12	-5.46E-12	0
1.7948	-0.3039	-0.0044	1.0817	1.3856	2.28E-02	-1.13E-04	0.1
1.7633	-0.2834	-0.0074	1.0306	1.3141	4.41E-02	-2.18E-04	0.2
1.7171	-0.2507	-0.0089	0.953	1.2037	6.31E-02	-3.08E-04	0.3
1.6628	-0.2081	-0.0098	0.8575	1.0655	7.88E-02	-3.81E-04	0.4
1.6058	-0.1589	-0.012	0.753	0.9119	9.11E-02	-4.33E-04	0.5

1.5497	-0.1072	-0.0169	0.6469	0.7542	9.99E-02	-4.65E-04	0.6
1.4961	-0.0569	-0.0254	0.5447	0.6016	1.06E-01	-4.80E-04	0.7
1.4455	-0.0109	-0.0374	0.4497	0.4607	1.09E-01	-4.80E-04	0.8
1.3977	0.0286	-0.0521	0.3638	0.3352	1.09E-01	-4.69E-04	0.9
1.3523	0.0607	-0.0681	0.2875	0.2268	1.09E-01	-4.50E-04	1
1.3091	0.0852	-0.0844	0.2208	0.1356	1.06E-01	-4.26E-04	1.1
1.2682	0.1028	-0.0999	0.1632	0.0603	1.03E-01	-3.99E-04	1.2
1.2295	0.1143	-0.1139	0.1138	-0.0005	9.90E-02	-3.70E-04	1.3
1.1932	0.1206	-0.1258	0.0718	-0.0488	9.47E-02	-3.42E-04	1.4
1.1595	0.1228	-0.1355	0.0364	-0.0864	9.00E-02	-3.14E-04	1.5
1.400=Y							
TANG.	RADIAL	SHEAR	PHI	PSI	A21	A22	X
1.6174	-0.3066	0	0.9096	1.2163	-7.28E-12	-5.46E-12	0
1.6125	-0.2997	0.0106	0.8981	1.1978	1.73E-02	-9.04E-05	0.1
1.5987	-0.2796	0.0202	0.8646	1.1443	3.37E-02	-1.75E-04	0.2
1.5774	-0.248	0.0274	0.8127	1.0607	4.86E-02	-2.51E-04	0.3
1.5508	-0.2078	0.0314	0.7469	0.9547	6.15E-02	-3.12E-04	0.4
1.5208	-0.1621	0.0311	0.6724	0.8345	7.21E-02	-3.59E-04	0.5
1.4887	-0.1145	0.0262	0.594	0.7084	8.03E-02	-3.91E-04	0.6
1.4554	-0.068	0.017	0.5155	0.5835	8.62E-02	-4.09E-04	0.7
1.4214	-0.0252	0.004	0.4399	0.4651	9.01E-02	-4.15E-04	0.8
1.387	0.0123	-0.0116	0.3692	0.3569	9.21E-02	-4.11E-04	0.9
1.3523	0.0436	-0.0287	0.3043	0.2607	9.26E-02	-4.00E-04	1
1.3178	0.0684	-0.0461	0.2458	0.1774	9.19E-02	-3.84E-04	1.1
1.2836	0.0871	-0.063	0.1939	0.1067	9.02E-02	-3.64E-04	1.2
1.2503	0.1003	-0.0786	0.1481	0.0478	8.78E-02	-3.42E-04	1.3
1.2182	0.1087	-0.0925	0.1082	-0.0005	8.49E-02	-3.19E-04	1.4
1.1875	0.1131	-0.1043	0.0736	-0.0394	8.16E-02	-2.97E-04	1.5
1.500=Y							
TANG.	RADIAL	SHEAR	PHI	PSI	A21	A22	X
1.4876	-0.2921	0	0.7675	1.0596	-7.28E-12	-5.46E-12	0
1.4857	-0.286	0.0169	0.7596	1.0456	1.35E-02	-7.36E-05	0.1
1.4803	-0.2681	0.0321	0.7367	1.0047	2.64E-02	-1.43E-04	0.2
1.4715	-0.24	0.044	0.7004	0.9404	3.83E-02	-2.06E-04	0.3
1.4597	-0.2042	0.0515	0.6536	0.8578	4.89E-02	-2.59E-04	0.4

1.4451	-0.1635	0.0539	0.5993	0.7628	5.80E-02	-3.01E-04	0.5
1.4281	-0.1207	0.0512	0.5405	0.6612	6.53E-02	-3.31E-04	0.6
1.4088	-0.0786	0.0437	0.48	0.5586	7.10E-02	-3.50E-04	0.7
1.3874	-0.0391	0.0321	0.4201	0.4592	7.51E-02	-3.60E-04	0.8
1.3639	-0.0039	0.0177	0.3624	0.3662	7.78E-02	-3.61E-04	0.9
1.3389	0.0263	0.0014	0.308	0.2817	7.92E-02	-3.56E-04	1
1.3126	0.0511	-0.0156	0.2577	0.2066	7.95E-02	-3.45E-04	1.1
1.2855	0.0706	-0.0325	0.2119	0.1413	7.89E-02	-3.31E-04	1.2
1.258	0.0851	-0.0485	0.1706	0.0855	7.76E-02	-3.15E-04	1.3
1.2308	0.0952	-0.0632	0.1338	0.0385	7.58E-02	-2.97E-04	1.4
1.204	0.1016	-0.0761	0.1012	-0.0004	7.35E-02	-2.78E-04	1.5
1.600=Y							
TANG.	RADIAL	SHEAR	PHI	PSI	A21	A22	X
1.3947	-0.2736	0	0.6578	0.9314	-7.28E-12	-5.46E-12	0
1.3942	-0.2684	0.019	0.6522	0.9206	1.07E-02	-6.07E-05	0.1
1.3929	-0.2531	0.0363	0.6358	0.8888	2.11E-02	-1.19E-04	0.2
1.3904	-0.229	0.0504	0.6096	0.8386	3.08E-02	-1.71E-04	0.3
1.3865	-0.198	0.0601	0.5754	0.7734	3.96E-02	-2.17E-04	0.4
1.3808	-0.1625	0.0648	0.5349	0.6974	4.73E-02	-2.54E-04	0.5
1.373	-0.1248	0.0644	0.4902	0.615	5.38E-02	-2.82E-04	0.6
1.3629	-0.0871	0.0592	0.4432	0.5303	5.91E-02	-3.02E-04	0.7
1.3504	-0.0512	0.0501	0.3955	0.4467	6.31E-02	-3.13E-04	0.8
1.3354	-0.0184	0.0378	0.3486	0.367	6.60E-02	-3.18E-04	0.9
1.3181	0.0103	0.0233	0.3033	0.2931	6.79E-02	-3.16E-04	1
1.2989	0.0346	0.0077	0.2606	0.226	6.89E-02	-3.10E-04	1.1
1.2782	0.0543	-0.0082	0.2207	0.1664	6.90E-02	-3.01E-04	1.2
1.2564	0.0697	-0.0237	0.1841	0.1144	6.86E-02	-2.88E-04	1.3
1.234	0.0812	-0.0384	0.1508	0.0696	6.75E-02	-2.75E-04	1.4
1.2115	0.0892	-0.0517	0.1207	0.0315	6.61E-02	-2.60E-04	1.5
1.700=Y							
TANG.	RADIAL	SHEAR	PHI	PSI	A21	A22	X
1.326	-0.2542	0	0.571	0.8251	-7.28E-12	-5.46E-12	0
1.3262	-0.2498	0.0191	0.5669	0.8166	8.70E-03	-5.07E-05	0.1
1.3268	-0.2368	0.0367	0.5548	0.7916	1.72E-02	-9.93E-05	0.2
1.3275	-0.2164	0.0514	0.5354	0.7518	2.52E-02	-1.44E-04	0.3

1.3278	-0.19	0.0622	0.5097	0.6997	3.25E-02	-1.83E-04	0.4
1.3271	-0.1594	0.0685	0.4789	0.6383	3.91E-02	-2.16E-04	0.5
1.3249	-0.1265	0.0702	0.4444	0.5709	4.48E-02	-2.42E-04	0.6
1.3207	-0.0932	0.0673	0.4075	0.5007	4.96E-02	-2.61E-04	0.7
1.3142	-0.0609	0.0606	0.3694	0.4302	5.34E-02	-2.74E-04	0.8
1.3053	-0.0308	0.0507	0.3311	0.3619	5.64E-02	-2.80E-04	0.9
1.2941	-0.0039	0.0385	0.2935	0.2974	5.85E-02	-2.82E-04	1
1.2807	0.0195	0.0248	0.2574	0.2379	5.98E-02	-2.79E-04	1.1
1.2654	0.0391	0.0104	0.2231	0.184	6.05E-02	-2.73E-04	1.2
1.2486	0.055	-0.004	0.1909	0.136	6.06E-02	-2.64E-04	1.3
1.2308	0.0674	-0.018	0.1612	0.0938	6.01E-02	-2.53E-04	1.4
1.2122	0.0765	-0.0311	0.1339	0.0573	5.93E-02	-2.42E-04	1.5
1.800=Y							
TANG.	RADIAL	SHEAR	PHI	PSI	A21	A22	X
1.2738	-0.2352	0	0.5009	0.7361	-7.28E-12	-5.46E-12	0
1.2743	-0.2315	0.0183	0.4978	0.7293	7.17E-03	-4.27E-05	0.1
1.2759	-0.2206	0.0353	0.4887	0.7093	1.42E-02	-8.39E-05	0.2
1.2781	-0.2034	0.0498	0.474	0.6774	2.08E-02	-1.22E-04	0.3
1.2805	-0.181	0.061	0.4543	0.6353	2.71E-02	-1.56E-04	0.4
1.2825	-0.1548	0.0683	0.4305	0.5853	3.27E-02	-1.85E-04	0.5
1.2835	-0.1263	0.0714	0.4035	0.5297	3.77E-02	-2.09E-04	0.6
1.283	-0.097	0.0705	0.3741	0.4711	4.20E-02	-2.27E-04	0.7
1.2806	-0.0681	0.066	0.3434	0.4115	4.55E-02	-2.40E-04	0.8
1.276	-0.0408	0.0585	0.3121	0.3529	4.84E-02	-2.48E-04	0.9
1.2693	-0.0159	0.0485	0.2809	0.2967	5.06E-02	-2.51E-04	1
1.2604	0.0063	0.0369	0.2504	0.244	5.21E-02	-2.51E-04	1.1
1.2495	0.0254	0.0243	0.2209	0.1956	5.31E-02	-2.47E-04	1.2
1.237	0.0413	0.0113	0.1929	0.1516	5.36E-02	-2.41E-04	1.3
1.2232	0.0542	-0.0017	0.1666	0.1125	5.36E-02	-2.33E-04	1.4
1.2083	0.0642	-0.0141	0.1421	0.0779	5.32E-02	-2.24E-04	1.5
1.900=Y							
TANG.	RADIAL	SHEAR	PHI	PSI	A21	A22	X
1.2333	-0.2173	0	0.4434	0.6607	-5.46E-12	-5.46E-12	0
1.234	-0.2142	0.0171	0.441	0.6552	5.99E-03	-3.64E-05	0.1
1.2359	-0.2051	0.033	0.434	0.6391	1.19E-02	-7.15E-05	0.2

1.2388	-0.1906	0.047	0.4226	0.6132	1.75E-02	-1.04E-04	0.3
1.2422	-0.1716	0.0581	0.4072	0.5788	2.28E-02	-1.34E-04	0.4
1.2456	-0.1492	0.0658	0.3885	0.5377	2.76E-02	-1.60E-04	0.5
1.2484	-0.1245	0.07	0.3671	0.4916	3.20E-02	-1.81E-04	0.6
1.2501	-0.0989	0.0706	0.3435	0.4424	3.58E-02	-1.98E-04	0.7
1.2503	-0.0733	0.068	0.3186	0.3919	3.91E-02	-2.11E-04	0.8
1.2487	-0.0486	0.0625	0.2928	0.3415	4.18E-02	-2.19E-04	0.9
1.2452	-0.0257	0.0546	0.2668	0.2925	4.39E-02	-2.24E-04	1
1.2397	-0.005	0.045	0.241	0.246	4.56E-02	-2.25E-04	1.1
1.2323	0.0133	0.0342	0.2158	0.2025	4.67E-02	-2.24E-04	1.2
1.2233	0.029	0.0227	0.1916	0.1626	4.75E-02	-2.20E-04	1.3
1.2128	0.042	0.0111	0.1684	0.1264	4.78E-02	-2.15E-04	1.4
1.2011	0.0525	-0.0004	0.1466	0.094	4.78E-02	-2.08E-04	1.5
2.000=Y							
TANG.	RADIAL	SHEAR	PHI	PSI	A21	A22	X
1.2012	-0.2007	0	0.3955	0.5963	-5.46E-12	-5.46E-12	0
1.2019	-0.1981	0.0157	0.3937	0.5918	5.06E-03	-3.12E-05	0.1
1.2039	-0.1905	0.0305	0.3882	0.5787	1.00E-02	-6.15E-05	0.2
1.207	-0.1783	0.0436	0.3792	0.5574	1.48E-02	-8.99E-05	0.3
1.2108	-0.1621	0.0543	0.367	0.5291	1.93E-02	-1.16E-04	0.4
1.2148	-0.1429	0.0622	0.3521	0.495	2.35E-02	-1.39E-04	0.5
1.2185	-0.1216	0.0671	0.3349	0.4565	2.74E-02	-1.58E-04	0.6
1.2215	-0.0992	0.0688	0.3158	0.415	3.08E-02	-1.74E-04	0.7
1.2234	-0.0766	0.0677	0.2954	0.372	3.37E-02	-1.86E-04	0.8
1.2238	-0.0545	0.0639	0.274	0.3285	3.63E-02	-1.95E-04	0.9
1.2225	-0.0336	0.0578	0.2523	0.2859	3.84E-02	-2.01E-04	1
1.2196	-0.0143	0.0501	0.2304	0.2448	4.00E-02	-2.03E-04	1.1
1.2149	0.0029	0.041	0.2089	0.2059	4.13E-02	-2.03E-04	1.2
1.2086	0.0181	0.0311	0.1878	0.1698	4.21E-02	-2.01E-04	1.3
1.2009	0.031	0.0208	0.1675	0.1366	4.27E-02	-1.98E-04	1.4
1.192	0.0417	0.0104	0.1482	0.1065	4.29E-02	-1.92E-04	1.5
2.100=Y							
TANG.	RADIAL	SHEAR	PHI	PSI	A21	A22	X
1.1754	-0.1856	0	0.3552	0.5409	-5.46E-12	-5.46E-12	0
1.1761	-0.1834	0.0143	0.3538	0.5372	4.31E-03	-2.70E-05	0.1

1.178	-0.177	0.0279	0.3494	0.5263	8.55E-03	-5.32E-05	0.2
1.1811	-0.1666	0.04	0.3422	0.5088	1.27E-02	-7.80E-05	0.3
1.1849	-0.1529	0.0502	0.3324	0.4853	1.66E-02	-1.01E-04	0.4
1.1891	-0.1364	0.0581	0.3204	0.4568	2.02E-02	-1.21E-04	0.5
1.1932	-0.118	0.0633	0.3064	0.4244	2.36E-02	-1.39E-04	0.6
1.1969	-0.0985	0.0659	0.2908	0.3892	2.66E-02	-1.54E-04	0.7
1.1997	-0.0785	0.0659	0.2739	0.3524	2.93E-02	-1.65E-04	0.8
1.2014	-0.0587	0.0635	0.2561	0.3148	3.17E-02	-1.74E-04	0.9
1.2017	-0.0397	0.059	0.2378	0.2776	3.36E-02	-1.80E-04	1
1.2006	-0.022	0.0529	0.2193	0.2413	3.53E-02	-1.83E-04	1.1
1.198	-0.0058	0.0454	0.2008	0.2066	3.65E-02	-1.85E-04	1.2
1.1939	0.0086	0.037	0.1826	0.174	3.75E-02	-1.84E-04	1.3
1.1884	0.0212	0.028	0.1648	0.1436	3.82E-02	-1.82E-04	1.4
1.1817	0.0319	0.0187	0.1477	0.1158	3.86E-02	-1.78E-04	1.5
2.200=Y							
TANG.	RADIAL	SHEAR	PHI	PSI	A21	A22	X
1.1543	-0.1719	0	0.321	0.4928	-5.46E-12	-5.46E-12	0
1.1549	-0.17	0.013	0.3198	0.4898	3.71E-03	-2.35E-05	0.1
1.1568	-0.1646	0.0254	0.3162	0.4808	7.36E-03	-4.63E-05	0.2
1.1597	-0.1557	0.0366	0.3104	0.4661	1.09E-02	-6.81E-05	0.3
1.1634	-0.144	0.0462	0.3025	0.4465	1.43E-02	-8.83E-05	0.4
1.1675	-0.1299	0.0538	0.2926	0.4225	1.75E-02	-1.07E-04	0.5
1.1717	-0.1139	0.0592	0.2811	0.3951	2.05E-02	-1.22E-04	0.6
1.1757	-0.0968	0.0624	0.2682	0.3651	2.32E-02	-1.36E-04	0.7
1.179	-0.0792	0.0632	0.2542	0.3334	2.56E-02	-1.47E-04	0.8
1.1815	-0.0616	0.0619	0.2393	0.3009	2.78E-02	-1.56E-04	0.9
1.1829	-0.0444	0.0588	0.2239	0.2683	2.96E-02	-1.62E-04	1
1.183	-0.0282	0.054	0.2081	0.2362	3.12E-02	-1.66E-04	1.1
1.1819	-0.0132	0.0479	0.1922	0.2053	3.25E-02	-1.68E-04	1.2
1.1795	0.0005	0.0409	0.1764	0.1759	3.35E-02	-1.68E-04	1.3
1.1758	0.0126	0.0331	0.1608	0.1482	3.42E-02	-1.67E-04	1.4
1.1709	0.0231	0.025	0.1457	0.1225	3.48E-02	-1.65E-04	1.5
2.300=Y							
TANG.	RADIAL	SHEAR	PHI	PSI	A21	A22	X
1.1369	-0.1594	0	0.2915	0.4509	-5.46E-12	-5.46E-12	0

1.1375	-0.1578	0.0118	0.2905	0.4484	3.21E-03	-2.05E-05	0.1
1.1391	-0.1532	0.0231	0.2876	0.4408	6.39E-03	-4.06E-05	0.2
1.1418	-0.1456	0.0334	0.2829	0.4285	9.48E-03	-5.98E-05	0.3
1.1453	-0.1356	0.0424	0.2764	0.4119	1.25E-02	-7.77E-05	0.4
1.1492	-0.1234	0.0497	0.2682	0.3916	1.53E-02	-9.40E-05	0.5
1.1533	-0.1095	0.0551	0.2587	0.3683	1.79E-02	-1.08E-04	0.6
1.1573	-0.0946	0.0586	0.248	0.3426	2.03E-02	-1.21E-04	0.7
1.1609	-0.079	0.0601	0.2362	0.3152	2.25E-02	-1.31E-04	0.8
1.1639	-0.0633	0.0597	0.2237	0.287	2.45E-02	-1.40E-04	0.9
1.1659	-0.0479	0.0576	0.2105	0.2584	2.62E-02	-1.46E-04	1
1.167	-0.0331	0.054	0.197	0.2301	2.77E-02	-1.50E-04	1.1
1.1669	-0.0192	0.0491	0.1833	0.2025	2.90E-02	-1.53E-04	1.2
1.1658	-0.0064	0.0432	0.1696	0.1759	3.00E-02	-1.54E-04	1.3
1.1635	0.0052	0.0367	0.156	0.1508	3.08E-02	-1.54E-04	1.4
1.1601	0.0154	0.0296	0.1426	0.1272	3.14E-02	-1.52E-04	1.5
2.400=Y							
TANG.	RADIAL	SHEAR	PHI	PSI	A21	A22	X
1.1223	-0.1481	0	0.266	0.4141	-5.46E-12	-5.46E-12	0
1.1228	-0.1468	0.0107	0.2652	0.412	2.81E-03	-1.81E-05	0.1
1.1243	-0.1428	0.021	0.2628	0.4056	5.58E-03	-3.58E-05	0.2
1.1268	-0.1363	0.0304	0.2589	0.3952	8.28E-03	-5.28E-05	0.3
1.1299	-0.1276	0.0388	0.2535	0.3811	1.09E-02	-6.87E-05	0.4
1.1336	-0.1171	0.0457	0.2467	0.3638	1.34E-02	-8.33E-05	0.5
1.1375	-0.105	0.0511	0.2388	0.3438	1.57E-02	-9.64E-05	0.6
1.1415	-0.0919	0.0547	0.2297	0.3217	1.79E-02	-1.08E-04	0.7
1.1451	-0.0782	0.0567	0.2198	0.298	1.99E-02	-1.18E-04	0.8
1.1483	-0.0642	0.057	0.2092	0.2733	2.17E-02	-1.26E-04	0.9
1.1508	-0.0503	0.0557	0.198	0.2482	2.33E-02	-1.32E-04	1
1.1524	-0.0368	0.0531	0.1863	0.2232	2.47E-02	-1.36E-04	1.1
1.1532	-0.024	0.0493	0.1745	0.1985	2.59E-02	-1.39E-04	1.2
1.1529	-0.0121	0.0445	0.1625	0.1746	2.69E-02	-1.41E-04	1.3
1.1517	-0.0012	0.0389	0.1506	0.1518	2.77E-02	-1.41E-04	1.4
1.1495	0.0086	0.0328	0.1388	0.1302	2.84E-02	-1.41E-04	1.5
2.500=Y							
TANG.	RADIAL	SHEAR	PHI	PSI	A21	A22	X

1.1099	-0.1379	0	0.2438	0.3817	-5.46E-12	-5.46E-12	0
1.1104	-0.1367	0.0097	0.2431	0.3798	2.46E-03	-1.60E-05	0.1
1.1118	-0.1333	0.019	0.2411	0.3744	4.90E-03	-3.17E-05	0.2
1.114	-0.1277	0.0277	0.2378	0.3655	7.29E-03	-4.68E-05	0.3
1.1169	-0.1202	0.0355	0.2333	0.3535	9.59E-03	-6.10E-05	0.4
1.1203	-0.111	0.042	0.2276	0.3387	1.18E-02	-7.42E-05	0.5
1.124	-0.1005	0.0472	0.2209	0.3215	1.39E-02	-8.61E-05	0.6
1.1277	-0.089	0.051	0.2133	0.3023	1.59E-02	-9.66E-05	0.7
1.1313	-0.0769	0.0532	0.2049	0.2817	1.77E-02	-1.06E-04	0.8
1.1345	-0.0644	0.054	0.1958	0.2602	1.93E-02	-1.13E-04	0.9
1.1372	-0.0519	0.0534	0.1862	0.2381	2.08E-02	-1.19E-04	1
1.1393	-0.0396	0.0516	0.1762	0.2158	2.21E-02	-1.24E-04	1.1
1.1405	-0.0279	0.0487	0.1659	0.1938	2.33E-02	-1.27E-04	1.2
1.141	-0.0168	0.0448	0.1555	0.1723	2.42E-02	-1.29E-04	1.3
1.1406	-0.0066	0.0402	0.145	0.1515	2.50E-02	-1.30E-04	1.4
1.1393	0.0028	0.035	0.1345	0.1318	2.57E-02	-1.30E-04	1.5
0.000=Y							
TANG.	RADIAL	SHEAR	PHI	PSI	A21	A22	X
0	0.7058	0	-1.6789	-2.3847	0.00E+00	0.00E+00	1
-0.0362	0.4787	0	-1.4914	-1.9702	0.00E+00	0.00E+00	1.1
-0.0253	0.3253	0	-1.3298	-1.6551	0.00E+00	0.00E+00	1.2
0.011	0.2197	0	-1.1903	-1.41	0.00E+00	0.00E+00	1.3
0.0602	0.1461	0	-1.0695	-1.2156	0.00E+00	0.00E+00	1.4
0.1149	0.0942	0	-0.9646	-1.0588	0.00E+00	0.00E+00	1.5
0.1708	0.0572	0	-0.8732	-0.9305	0.00E+00	0.00E+00	1.6
0.2255	0.0308	0	-0.7934	-0.8241	0.00E+00	0.00E+00	1.7
0.2776	0.0118	0	-0.7233	-0.7351	0.00E+00	0.00E+00	1.8
0.3267	-0.0019	0	-0.6616	-0.6597	0.00E+00	0.00E+00	1.9
0.100=Y							
TANG.	RADIAL	SHEAR	PHI	PSI	A21	A22	X
-0.0095	0.6655	0.0642	-1.6487	-2.3142	7.02E-02	-2.45E-04	1
-0.0322	0.4564	0.0049	-1.4656	-1.922	5.79E-02	-1.85E-04	1.1
-0.0149	0.3132	-0.0277	-1.3078	-1.621	4.81E-02	-1.43E-04	1.2
0.0241	0.2137	-0.0448	-1.1715	-1.3852	4.04E-02	-1.13E-04	1.3
0.0738	0.1435	-0.0528	-1.0536	-1.1971	3.41E-02	-9.02E-05	1.4

0.1281	0.0937	-0.0556	-0.9511	-1.0448	2.90E-02	-7.34E-05	1.5
0.1831	0.0579	-0.0552	-0.8618	-0.9196	2.49E-02	-6.05E-05	1.6
0.2367	0.0321	-0.0532	-0.7836	-0.8156	2.15E-02	-5.05E-05	1.7
0.2877	0.0134	-0.0503	-0.7149	-0.7283	1.86E-02	-4.26E-05	1.8
0.3357	-0.0002	-0.047	-0.6544	-0.6542	1.62E-02	-3.62E-05	1.9
0.200=Y							
TANG.	RADIAL	SHEAR	PHI	PSI	A21	A22	X
-0.0264	0.5573	0.0935	-1.5589	-2.1162	1.34E-01	-4.63E-04	1
-0.0146	0.396	-0.0073	-1.3889	-1.7849	1.11E-01	-3.52E-04	1.1
0.0188	0.2807	-0.0629	-1.2426	-1.5233	9.24E-02	-2.74E-04	1.2
0.0639	0.1974	-0.092	-1.1163	-1.3137	7.78E-02	-2.17E-04	1.3
0.1148	0.1369	-0.1054	-1.0067	-1.1436	6.59E-02	-1.75E-04	1.4
0.1674	0.0926	-0.1096	-0.9114	-1.004	5.63E-02	-1.43E-04	1.5
0.2195	0.06	-0.1084	-0.828	-0.888	4.83E-02	-1.18E-04	1.6
0.2697	0.0359	-0.1042	-0.7548	-0.7907	4.18E-02	-9.90E-05	1.7
0.3174	0.0181	-0.0984	-0.6903	-0.7084	3.63E-02	-8.36E-05	1.8
0.3621	0.0049	-0.0919	-0.6333	-0.6382	3.17E-02	-7.13E-05	1.9
0.300=Y							
TANG.	RADIAL	SHEAR	PHI	PSI	A21	A22	X
-0.0214	0.4133	0.0686	-1.4125	-1.8258	1.85E-01	-6.32E-04	1
0.0304	0.3148	-0.0454	-1.2648	-1.5796	1.54E-01	-4.89E-04	1.1
0.0815	0.2368	-0.109	-1.1376	-1.3744	1.30E-01	-3.85E-04	1.2
0.1325	0.1758	-0.142	-1.0275	-1.2033	1.10E-01	-3.08E-04	1.3
0.1827	0.1286	-0.1566	-0.9316	-1.0602	9.34E-02	-2.50E-04	1.4
0.2316	0.0921	-0.1601	-0.8477	-0.9398	8.01E-02	-2.05E-04	1.5
0.2785	0.0641	-0.1572	-0.7738	-0.8379	6.90E-02	-1.71E-04	1.6
0.3231	0.0424	-0.1505	-0.7086	-0.7511	5.99E-02	-1.44E-04	1.7
0.3652	0.0258	-0.142	-0.6508	-0.6766	5.22E-02	-1.22E-04	1.8
0.4046	0.013	-0.1327	-0.5994	-0.6124	4.58E-02	-1.04E-04	1.9
0.400=Y							
TANG.	RADIAL	SHEAR	PHI	PSI	A21	A22	X
0.0368	0.2717	-0.0067	-1.216	-1.4878	2.21E-01	-7.44E-04	1
0.1169	0.2336	-0.1067	-1.0997	-1.3333	1.86E-01	-5.87E-04	1.1
0.1786	0.1928	-0.1632	-0.9988	-1.1916	1.57E-01	-4.69E-04	1.2

0.2304	0.1548	-0.192	-0.9104	-1.0653	1.34E-01	-3.80E-04	1.3
0.2762	0.1216	-0.2036	-0.8327	-0.9543	1.15E-01	-3.12E-04	1.4
0.3182	0.0936	-0.2046	-0.7637	-0.8573	9.93E-02	-2.58E-04	1.5
0.3573	0.0704	-0.1992	-0.7024	-0.7728	8.61E-02	-2.16E-04	1.6
0.394	0.0514	-0.1902	-0.6477	-0.6991	7.50E-02	-1.83E-04	1.7
0.4285	0.0361	-0.1793	-0.5986	-0.6347	6.57E-02	-1.56E-04	1.8
0.4609	0.0237	-0.1676	-0.5544	-0.5782	5.78E-02	-1.34E-04	1.9
0.500=Y							
TANG.	RADIAL	SHEAR	PHI	PSI	A21	A22	X
0.0326	0.1181	0.0018	-1.0692	-1.1873	2.83E-01	-1.00E-03	0.9
0.1658	0.1623	-0.1088	-0.9815	-1.1438	2.40E-01	-8.01E-04	1
0.2513	0.1693	-0.1777	-0.904	-1.0733	2.04E-01	-6.46E-04	1.1
0.3104	0.1582	-0.2172	-0.8348	-0.993	1.75E-01	-5.26E-04	1.2
0.355	0.1394	-0.2365	-0.7725	-0.9118	1.51E-01	-4.32E-04	1.3
0.3913	0.1183	-0.2426	-0.716	-0.8343	1.30E-01	-3.58E-04	1.4
0.423	0.0978	-0.24	-0.6647	-0.7625	1.13E-01	-3.00E-04	1.5
0.4517	0.0791	-0.2321	-0.6179	-0.697	9.89E-02	-2.53E-04	1.6
0.4785	0.0626	-0.2211	-0.5753	-0.6379	8.68E-02	-2.16E-04	1.7
0.5039	0.0484	-0.2085	-0.5364	-0.5848	7.64E-02	-1.85E-04	1.8
0.600=Y							
TANG.	RADIAL	SHEAR	PHI	PSI	A21	A22	X
0.2509	0.0226	-0.1553	-0.7603	-0.7829	2.83E-01	-9.87E-04	0.9
0.3598	0.0977	-0.2055	-0.7268	-0.8245	2.44E-01	-8.12E-04	1
0.4268	0.1297	-0.2403	-0.6922	-0.8219	2.11E-01	-6.70E-04	1.1
0.4697	0.1372	-0.2606	-0.6573	-0.7945	1.83E-01	-5.56E-04	1.2
0.4992	0.1316	-0.2694	-0.6227	-0.7543	1.59E-01	-4.64E-04	1.3
0.5214	0.1195	-0.2695	-0.589	-0.7085	1.39E-01	-3.90E-04	1.4
0.5398	0.1048	-0.2637	-0.5564	-0.6612	1.22E-01	-3.30E-04	1.5
0.5563	0.0896	-0.254	-0.5252	-0.6149	1.07E-01	-2.82E-04	1.6
0.572	0.0752	-0.2419	-0.4956	-0.5707	9.49E-02	-2.41E-04	1.7
0.5873	0.0619	-0.2285	-0.4675	-0.5295	8.41E-02	-2.08E-04	1.8
0.700=Y							
TANG.	RADIAL	SHEAR	PHI	PSI	A21	A22	X
0.436	-0.1395	-0.2727	-0.4186	-0.2791	3.06E-01	-1.10E-03	0.8

0.5335	-0.0044	-0.2637	-0.4553	-0.4509	2.68E-01	-9.33E-04	0.9
0.5917	0.0732	-0.2703	-0.4742	-0.5475	2.35E-01	-7.89E-04	1
0.6246	0.113	-0.2792	-0.4809	-0.5939	2.06E-01	-6.67E-04	1.1
0.6425	0.129	-0.2847	-0.479	-0.608	1.82E-01	-5.64E-04	1.2
0.652	0.1306	-0.2855	-0.4713	-0.6019	1.60E-01	-4.79E-04	1.3
0.6574	0.1242	-0.2817	-0.4596	-0.5838	1.42E-01	-4.08E-04	1.4
0.6612	0.1135	-0.2742	-0.4453	-0.5588	1.26E-01	-3.50E-04	1.5
0.6649	0.101	-0.2639	-0.4294	-0.5304	1.12E-01	-3.01E-04	1.6
0.6691	0.0881	-0.2519	-0.4126	-0.5007	9.95E-02	-2.60E-04	1.7
0.800=Y							
TANG.	RADIAL	SHEAR	PHI	PSI	A21	A22	X
0.7898	-0.2461	-0.4228	0.0347	0.2808	3.00E-01	-1.10E-03	0.7
0.8074	-0.0959	-0.3404	-0.0955	0.0004	2.70E-01	-9.78E-04	0.8
0.8203	0.0078	-0.3046	-0.1848	-0.1926	2.43E-01	-8.57E-04	0.9
0.8241	0.0735	-0.2915	-0.2456	-0.3191	2.18E-01	-7.44E-04	1
0.8203	0.111	-0.2876	-0.2862	-0.3972	1.95E-01	-6.43E-04	1.1
0.8117	0.1288	-0.2859	-0.3122	-0.441	1.74E-01	-5.55E-04	1.2
0.8008	0.1336	-0.2832	-0.3276	-0.4612	1.56E-01	-4.79E-04	1.3
0.7897	0.1303	-0.2783	-0.3353	-0.4656	1.40E-01	-4.14E-04	1.4
0.7796	0.1223	-0.2712	-0.3373	-0.4596	1.25E-01	-3.59E-04	1.5
0.7711	0.1117	-0.262	-0.3353	-0.447	1.12E-01	-3.13E-04	1.6
0.900=Y							
TANG.	RADIAL	SHEAR	PHI	PSI	A21	A22	X
1.4846	-0.3585	-0.6736	0.8298	1.1883	2.72E-01	-1.00E-03	0.5
1.2821	-0.2552	-0.4956	0.5288	0.7839	2.63E-01	-9.88E-04	0.6
1.1719	-0.1423	-0.3826	0.3093	0.4516	2.48E-01	-9.33E-04	0.7
1.1066	-0.0443	-0.3188	0.1485	0.1928	2.31E-01	-8.57E-04	0.8
1.0614	0.0306	-0.2869	0.0304	-0.0001	2.13E-01	-7.73E-04	0.9
1.0247	0.0821	-0.273	-0.0564	-0.1385	1.95E-01	-6.88E-04	1
0.9921	0.1141	-0.2679	-0.1199	-0.234	1.78E-01	-6.07E-04	1.1
0.962	0.1309	-0.2659	-0.1661	-0.297	1.62E-01	-5.34E-04	1.2
0.9345	0.1369	-0.2641	-0.199	-0.3359	1.47E-01	-4.68E-04	1.3
0.9098	0.1355	-0.261	-0.222	-0.3575	1.34E-01	-4.11E-04	1.4

Appendix D Computer programs

D.1 Cyl_A and Cyl_B

The single fibre stress analysis of Chapter 2 was written by this author as the Turbo Pascal program **Cyl_A**.pas. This program was modified and extended to include creep and mechano-sorptive strains, and to allow for variable external stress to be read from a file (calculated by KilnSched). The new version was called **Cyl_B**.pas, and corresponds to Chapter 5. Critical sections of code from both programs have been listed; a block diagram of **Cyl_B**.pas is also supplied.

Block letters are used in the listings and block diagram to identify procedure names. Code enclosed within braces in the listings is comment.

An explanation of some of the identifier names in the code listings:

First letter:

R	radius
S	stress
E	strain
Y	instantaneous Young's modulus
d	change in value of a variable
Error	error in resultants during iteration using method of bisection

Second (lower case) letters:

r	radial
t	tangential
in	change in variable over an increment

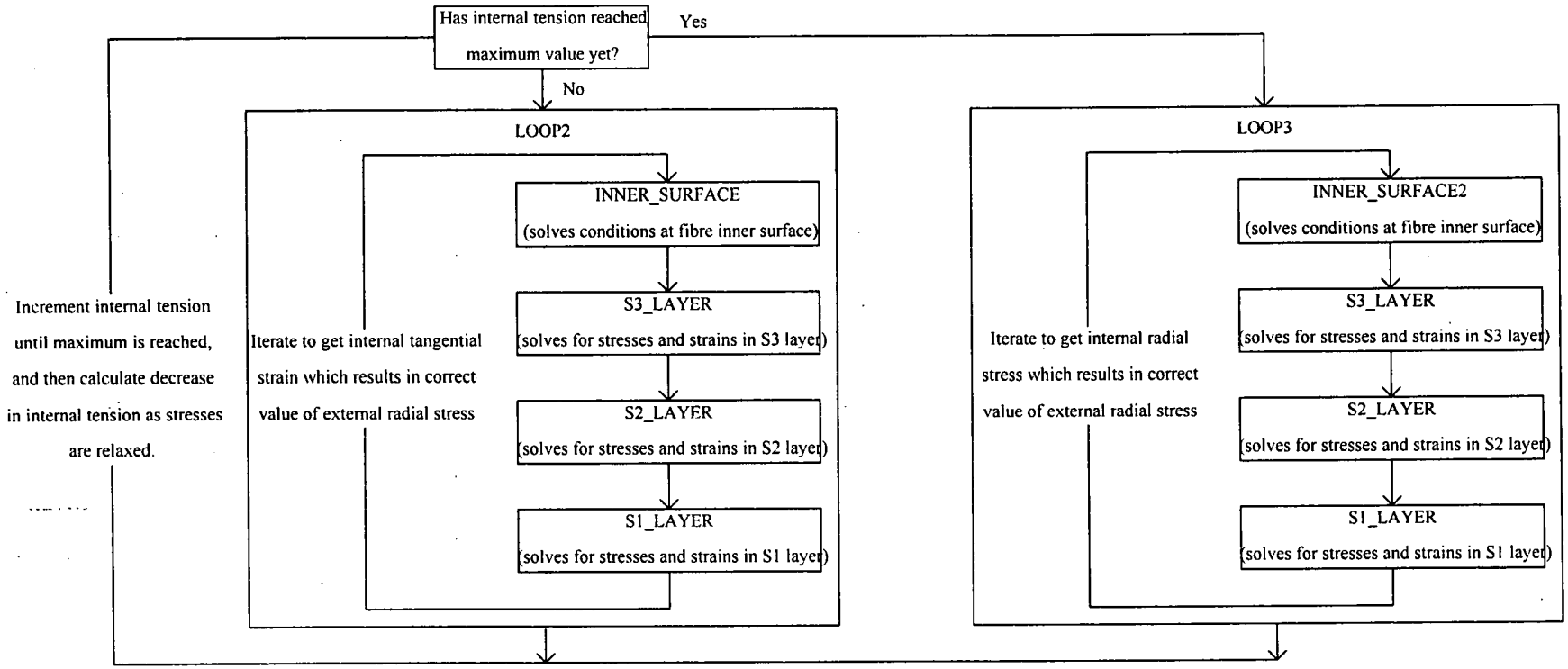

Figure D.1 Block diagram for program **Cyl_B**.pas

Cyl_A.pas follows the same block diagram as Figure D.1, except that there is no LOOP3. The program terminates when the internal tension reaches the maximum value (input by the user).

```
PROCEDURE S3Layer;
{This procedure calculates the stress distribution through the S3 layer.
This is done in an incremental manner using the equation for static equilibrium}
VAR
 Ro2,Rin,Srin,Srina,Srinb,Srinc,Stin,Rn2,Er2,Yzr32,Ytt32,dEr3,dEt3,
 SSUM2,Et2,Ytt32a,Yzr32a,Errora,Errorb,Errorc : REAL;  {"in" is for increment of radius}
 Count,Counta : Integer;
BEGIN
 SSUM2:=Sr[0]+St[0]; {Sum of stresses from INNER_SURFACE}
 Rin:=(Radius2-Radius1)/NRS3; {No. of increments of radius for layer}
 FOR Count := 1 TO NRS3 DO {Increment Count through S3 layer using NumberRadiusSteps3
                            increments}
 BEGIN
  Ro2:=Radius1+Count*Rin; {Radius for this calculation}
  Rad[Count]:=Ro2;
  {Use method of bisection to find Srin and satisfy force equilibrium}
  Srin:=(St_last[Count]-St_last[Count-1])/2;
  Srin:=Rin*(St[Count-1]+Srin-Sr[Count-1])/Ro2;
  IF NOT(Srin_last[3]=0.0) THEN
   IF (ABS(Srin/Srin_last[3])<0.7) THEN
    Srin:=Srin_last[3];
  {Change in radial stress over radius increment}
  Srin_last[3]:=Srin;
  Srina:=-0.8*Srin; {Guesses for method of bisection}
  Srinb:=3*Srin;
  Sr[Count]:=Sr[Count-1]+Srina;{Radial stress for this radius increment}
  St[Count]:=SSUM2-Sr[Count];{Tangential stress for this radius increment}
  Errora:=(St[Count]+St[Count-1])/2-Sr[Count-1];
  Errora:=Errora-(Ro2-Rin)/Rin*(Sr[Count]-Sr[Count-1]);
  Sr[Count]:=Sr[Count-1]+Srinb;{Radial stress for this radius increment}
  St[Count]:=SSUM2-Sr[Count];{Tangential stress for this radius increment}
  Errorb:=(St[Count]+St[Count-1])/2-Sr[Count-1];
  Errorb:=Errorb-(Ro2-Rin)/Rin*(Sr[Count]-Sr[Count-1]);
  Counta:=0;
  WHILE ABS(Errora)>100 DO
   BEGIN
    Counta:=Counta+1;
    IF Counta>100 THEN
    BEGIN
     Writeln('Counta>100, Count=',Count); {Limit iterations of bisection loop to 100 in case of }
     Sound(220);                          {divergence}
     Delay(200);
     NoSound;
     Readln;
     Halt;
    END;
    Srinc:=(Srina+Srinb)/2; {Bisection}
    Sr[Count]:=Sr[Count-1]+Srinc;{Radial stress for this radius increment}
    St[Count]:=SSUM2-Sr[Count];{Tangential stress for this radius increment}
    Errorc:=(St[Count]+St[Count-1])/2-Sr[Count-1];
    Errorc:=Errorc-(Ro2-Rin)/Rin*(Sr[Count]-Sr[Count-1]);
    IF Errorc*Errora>0 THEN
    BEGIN
     Srina:=Srinc;
     Errora:=Errorc;
    END;
```

```
  IF Errorc*Errora<0 THEN
  BEGIN
   Srinb:=Srinc;
   Errorb:=Errorc;
  END;
 END;{WHILE}
IF SetMaxMin AND ((Sr[Count]>k2*Yzr3L(Temp)) OR (St[Count]>k2*Ytt3L(Temp))) THEN
BEGIN
 Writeln('Stress too high S3'); {Stress has exceeded ultimate value}
 ReadLn;
 Halt;
END;
Yzr3(Sr[Count],Yzr32); {Local modulus in r and z directions}
Ytt3(St[Count],Ytt32); {Local modulus in t direction}
Yzr3(Sr_last[Count],Yzr32a); {Local modulus in r and z directions}
Ytt3(St_last[Count],Ytt32a); {Local modulus in t direction}
Yzr32:=(Yzr32a+Yzr32)/2; {Average modulus for current and previous stress increment}
Ytt32:=(Ytt32a+Ytt32)/2; {Average modulus for current and previous stress increment}
{Increments of strains from increments of stresses}
dEt3:=-(Sr[Count]-Sr_last[Count])/Yzr32*MUzrt3*(1+MUrz3);
dEt3:=dEt3+(St[Count]-St_last[Count])/Ytt32*(1-MUzrt3*MUtzr3);
dEr3:=(Sr[Count]-Sr_last[Count])/Yzr32*(1-SQR(MUrz3));
dEr3:=dEr3-(St[Count]-St_last[Count])/Ytt32*MUtzr3*(1+MUrz3);
Et[Count]:=Et_last[Count]+dEt3; {New strains}
Er[Count]:=Er_last[Count]+dEr3;
Rn2:=Ro2*(1+Et[Count]); {New radius}
IF Creep THEN {Carry out creep calculations}
BEGIN
 SUltimateR:=Kult*Yzr3L(Temp); {Ultimate radial stress}
 DEiR:=Er[Count]-Er_last[Count]; {Change in instantaneous radial strain}
 DELTA_ECREEP(Sr[Count],SUltimateR,CreepRatioR[Count],Count,DCreepRatioR[Count]);
                                        {Calculate change in radial creep ratio}
 EcreepR[Count]:=EcreepR_last[Count]+PrevCreepRatioR[Count]*DEiR;
 EcreepR[Count]:=EcreepR[Count]+Er[Count]*DCreepRatioR[Count]; {New value of radial
                                                          creep ratio}
 SUltimateT:=Kult*Ytt3L(Temp); {Repeat for tangential direction}
 DEiT:=Et[Count]-Et_last[Count];
 DELTA_ECREEP(St[Count],SUltimateT,CreepRatioT[Count],Count,DCreepRatioT[Count]);
 EcreepT[Count]:=EcreepT_last[Count]+PrevCreepRatioT[Count]*DEiT;
 EcreepT[Count]:=EcreepT[Count]+Et[Count]*DCreepRatioT[Count];{DEC=EI.DE + DEI*E}
END; {IF}
IF Mech_sorp THEN {Carry out mechano-sorptive strain calculations}
BEGIN
 IF Sr[Count]<0 THEN MSM:=MSMsame ELSE MSM:=MSMopp; {Mechano-sorptive strain
        multipliers for stress and shrinkage in same and opposite directions respectively}
 DEm_sR[Count]:=MSM*dMCdef/MC0*Sr[Count]/Yzr3L(Temp); {Change in radial mechano-
                                                          sorptive strain}
 Em_sR[Count]:=Em_sR[Count]+DEm_sR[Count]; {New radial mechano-sorptive strain}
 IF St[Count]<0 THEN MSM:=MSMsame ELSE MSM:=MSMopp; {Repeat for tangential
                                                          direction}
 DEm_sT[Count]:=MSM*dMCdef/MC0*St[Count]/Ytt3L(Temp);
 Em_sT[Count]:=Em_sT[Count]+DEm_sT[Count];
END;
IF SetMaxMin THEN {Store maximum and minimum values}
BEGIN
IF Sr[Count]>SrMax THEN SrMax:=Sr[Count];
IF St[Count]>StMax THEN StMax:=St[Count];
IF Er[Count]>ErMax THEN ErMax:=Er[Count];
```

```
    IF Et[Count]>EtMax THEN EtMax:=Et[Count];
    IF Sr[Count]<SrMin THEN SrMin:=Sr[Count];
    IF St[Count]<StMin THEN StMin:=St[Count];
    IF Er[Count]<ErMin THEN ErMin:=Er[Count];
    IF Et[Count]<EtMin THEN EtMin:=Et[Count];
    IF EcreepR[Count]>EcreeprMax THEN EcreeprMax:=EcreepR[Count];
    IF EcreepT[Count]>EcreeptMax THEN EcreeptMax:=EcreepT[Count];
    IF EcreepR[Count]<EcreeprMin THEN EcreeprMin:=EcreepR[Count];
    IF EcreepT[Count]<EcreeptMin THEN EcreeptMin:=EcreepT[Count];
    IF Et[Count]*Ro2>Umax THEN Umax:=Et[Count]*Ro2;
    IF Et[Count]*Ro2<Umin THEN Umin:=Et[Count]*Ro2;
    END;
  END;{FOR}
END;{S3 layer}
```

Listing D.1 Typical code for stress and strain calculation in secondary cell wall layer, including creep and mechano-sorptive calculations

```
PROCEDURE CREEP_R0 (VAR R0 :REAL);{T temperature deg C}
BEGIN
 R0 := 105.6-3.46*Temp+0.0319*Temp*Temp;
END;

PROCEDURE CREEP_RS (VAR RS :REAL);
BEGIN
 RS := 60-1.99*Temp+0.019*Temp*Temp;
END;

PROCEDURE CREEP_R (S,SU :REAL; VAR R :REAL);
VAR
 R0,RS : REAL;
BEGIN
 CREEP_R0(R0);
 CREEP_RS(RS);
 R := R0-RS*ABS(S/SU);
END;

PROCEDURE CREEP_B1 (S,SU :REAL; VAR B1 :REAL);
VAR
 R0,RS : REAL;
BEGIN
 CREEP_R0(R0);
 CREEP_RS(RS);
 B1 := 0.5*((1+A2_MULT)*R0-RS*ABS(S/SU));
END;

PROCEDURE CREEP_A (S,SU :REAL; VAR A :REAL);
VAR
 R0,RS,B1 : REAL;
BEGIN
 CREEP_R0(R0);
 CREEP_RS(RS);
 CREEP_B1(S,SU,B1);
 A:=1/(B1+SQRT(CREEP_K2-A2_MULT*R0*(R0-RS*ABS(S/SU))+B1*B1));
END;

PROCEDURE DELTA_ECREEP(S,SU,PrevE :REAL; Posn :INTEGER; VAR DeltaEc :REAL);
```

```
VAR
 A : REAL;
BEGIN
 CREEP_A(S,SU,A);
 CreepA[Posn]:=A;
 DeltaEc:=CREEP_K1*(0.5*(A+LastCreepA[0])PrevE)*DTIME
         /(1+0.5*CREEP_K1*DTIME);
END;
```

Listing D.2 Code for creep calculations

Only procedure DELTA_ECREEP is called externally; this uses the other creep procedures and calculates the change in creep ratio. Mechano-sorptive calculations are carried out in the procedures INNER_SURFACE through to S1_LAYER; see Listing D.1.

D.2 HetLabS

The modelling of wood as a heterogeneous material covered in Chapter 4 was written by this author as the Turbo Pascal program **HetLabS**.pas. It is a modification of **LabS**, a later version of **KilnSched** which uses variable grid spacing in the board thickness. This allows use of extra grid points to correspond to the position of earlywood and latewood bands. This model was also translated to C++ for use as part of the Clever Kiln Controller.

HetLabS has been presented here in block diagram format with listings of important sections of code which constitute the modifications for modelling wood as a heterogeneous material. Block letters indicate procedure names.

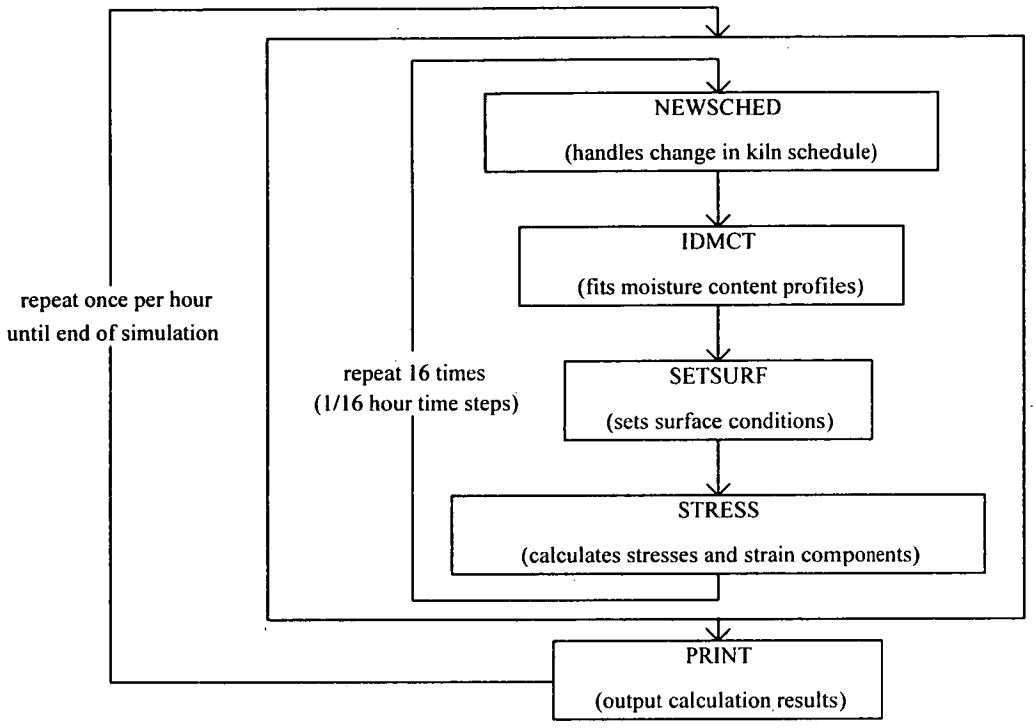

Figure D.2 Block diagram of LabS

The modifications to **LabS** to model wood as being heterogeneous consisted of several extra procedures and modifications to the procedure STRESS. Some of the critical sections of code are listed below.

```
IF AYTYPE[I]=TRUE THEN  {Earlywood}
 IF ((ATEMP[I]>CTTEW) AND (CTTEW_EXCEEDED_ALREADY[I]=FALSE)) THEN
 {CTTEW is collapse threshold temperature of earlywood}
 BEGIN  {Just started to collapse}
  COLLAPSE_TIME[I]:=ITIME;
  CTTEW_EXCEEDED_ALREADY[I]:=TRUE;
  SET_PROPORTION_OF_COLLAPSE(I);
  COLLAPSE;
  SHRINK;
  EU:=APROPORTION_OF_COLLAPSE[I]*EU_COLLAPSE
      + (1-APROPORTION_OF_COLLAPSE[I])*EU_NORMAL;
 END
 ELSE
 BEGIN  {Already been collapsing}
  COLLAPSE;
  SHRINK;
  EU:=APROPORTION_OF_COLLAPSE[I]*EU_COLLAPSE
      + (1-APROPORTION_OF_COLLAPSE[I])*EU_NORMAL;
 END
ELSE  {Latewood}
```

Listing D.3 Modification to procedure STRESS

The modification to STRESS accounts for the different shrinkages undergone by earlywood and latewood under conditions which cause collapse in either or both. There is a corresponding section dealing with latewood. The procedure COLLAPSE calculates the amount of total shrinkage for earlywood from a hyperbola based on three total shrinkage points. The array APROPORTION_OF_COLLAPSE stores the proportion of collapsing fibres at each grid point, calculated in the procedure SET_PROPORTION_OF_COLLAPSE (see Listing D.5).

```
PROCEDURE ADJUST_LWMC; {Adjusts LW MC to actual value}
BEGIN
 FSPEW:=FSP/100*RHOEW; {FSP in EW}
 FSPLW:=FSPEW*RHOLW/RHOEW; {FSP in LW}
 IF MC>FSPEW THEN
 BEGIN
  MC:=(MC0LW-FSPLW)/(MC0EW-FSPEW)*MC+FSPLW-FSPEW*(MC0LW-
FSPLW)/(MC0EW-FSPEW); {MC0 is initial moisture content}
 END
 ELSE {MC<FSP}
 BEGIN
  MC:=FSPLW/FSPEW*MC;
 END
END;
```

Listing D.4 Additional procedure in HetLabS

The procedure ADJUST_LWMC adjusts the moisture concentration in the latewood following the reasoning set out in Section 4.2.3.

```
PROCEDURE SET_PROPORTION_OF_COLLAPSE(GRID_LOCATION:INTEGER);
{Sets the proportion of fibres which collapse}
BEGIN
 IF AYTYPE[GRID_LOCATION]=FALSE THEN {Latewood}
 BEGIN
  ADJUST_LWMC;
  APROPORTION_OF_COLLAPSE[GRID_LOCATION]:=(MC-FSPLW)/(MC0LW-
FSPLW)
 END
 ELSE
  APROPORTION_OF_COLLAPSE[GRID_LOCATION]:=(MC-FSPEW)/(MC0EW-
FSPEW);
 IF APROPORTION_OF_COLLAPSE[GRID_LOCATION]<0 THEN {Put limits on}
  APROPORTION_OF_COLLAPSE[GRID_LOCATION]:=0; {proportion of collapse}
 IF APROPORTION_OF_COLLAPSE[GRID_LOCATION]>1 THEN
  APROPORTION_OF_COLLAPSE[GRID_LOCATION]:=1;
END;
```

Listing D.5 Additional procedure for HetLabS

Procedure SET_PROPORTION_OF_COLLAPSE calculates the proportion of fibres which collapse at each grid point based on the moisture content at which collapse begins (due to the local temperature becoming higher than the relevant collapse

threshold temperature). This is calculated as the proportion of fibres which are likely to be at MC above FSP.